

Assessing climate change impacts on wind energy financing

Von der Fakultät Nachhaltigkeit
der Leuphana Universität Lüneburg zur Erlangung des Grades

Doktor der Naturwissenschaften
- Dr. rer. nat. -

genehmigte Dissertation von
Thomas Remke

geboren am 20. Mai 1987 in Georgsmarienhütte

Eingereicht am: 28. Mai 2019

Mündliche Verteidigung (Disputation) am: 20. Januar 2020

Erstbetreuerin und Erstgutachterin: Prof. Dr. Daniela Jacob

Zweitgutachter: Prof. Dr. Günter Groß

Drittgutachter: Prof. Dr. Ulf Moslener

Erschienen unter dem Titel: Assessing climate change impacts on wind energy financing

Druckjahr: 2020

Abstract

Wind energy is expected to become the largest source of electricity generation in Europe's future energy mix with offshore wind energy in particular being considered as an essential component for secure and sustainable energy supply. As a consequence, future electricity generation will be exposed to an increasing degree to weather and climate. With planning and operational lifetimes of wind energy infrastructure reaching climate time scales, adaptation to changing climate conditions is of relevance to support secure and sustainable energy supply. Premise for success of wind energy projects is the ability to service financial obligations over the project lifetime. Though, revenues (via electricity generation) are exposed to changing climate conditions affecting the wind resource, operating conditions or hazardous events interfering with the wind energy infrastructure. For the first time, a procedure is presented to assess such climate change impacts specifically for wind energy financing.

At first, a generalised financing chain for wind energy is prepared to (qualitatively) trace the exposure of individual cost elements to physical climate change. In this regard, the revenue through wind power production is identified as the essential component within wind energy financing being exposed to changing climate conditions. This implies the wind resource to be of crucial interest for an assessment of climate change impacts on the financing of wind energy.

Therefore, secondly, a novel high-resolution experimental modelling framework with the non-hydrostatic extension of the regional climate model REMO is set up to generate physically consistent climate and climate change information of the wind resource across wind turbine operating altitudes. With this setup, enhanced simulated intra-annual and inter-annual variability across the lower planetary boundary layer is achieved, being beneficial for wind energy applications, compared to state-of-the-art regional climate model configurations. In addition, surrogate climate change experiments with this setup disclose vertical wind speed changes in the lower planetary boundary layer to be indirectly affected by temperature changes through thermodynamically-induced atmospheric stability alterations. Moreover, air density changes are

identified to occasionally exceed the net impact of wind energy density changes originating from changes in wind speed. This supports the consideration of air density information (in addition to wind speed) for wind energy yield assumptions.

Thirdly, the generated climate and climate change information of the wind resource are transferred to a simplified but fully-fledged financial model to assess the financial risk of wind energy project financing with respect to changing climate conditions. Sensitivity experiments for an imaginary offshore wind farm located in the German Bight reveal the long-term profitability of wind energy project financing not to be substantially affected by changing wind resource conditions, but incidents with insufficient servicing of financial obligations experience changes exceeding -10% to 14% .

The integration of wind energy-specific climate and climate change information into existing financial risk assessment procedures would illustrate a valuable contribution to enable climate change adaptation for wind energy. In particular information about intra-annual and inter-annual variability change of the wind resource originating from changing climate conditions permit the quantification of additional financial risk associated to debt repayment obligations and, subsequently, enable the development of suitable preventive economic measures. Though, additional efforts in combination with future technical development are necessary to provide essential additional information about the bandwidth of climate change and uncertainties associated to such sector-specific climate and climate change information.

Contents

Abstract	iv
Contents	vi
1 Introduction	1
1.1 Critical Energy Infrastructure and Climate Change Adaptation	2
1.2 Wind Energy	3
1.3 Motivation and Objective	5
2 Climate Change Impacts on Wind Energy Financing	7
2.1 The Wind Energy Financing Chain	8
2.2 Climate Change Impacts on the Wind Energy Financing Chain	12
2.3 Conclusions	16
3 Climate Change Information for Wind Energy	19
3.1 Boundary Layer Meteorology and Wind Energy	20
3.2 Regional Climate Modelling	23
3.3 The Regional Climate Models REMO and REMO-NH	26
3.4 Methodology	31
3.4.1 Surrogate Climate Change Experiments	32
3.4.2 Simulation Setup	40
3.5 Results and Discussion	48
3.5.1 Simulated Wind Conditions in the Planetary Boundary Layer	49
3.5.2 High Resolution Surrogate Climate Change Experiments	60
3.5.3 Wind and Wind Energy Characteristics under Surrogate Climate Change	62
3.6 Conclusions	75

4	Financial Modelling of Wind Energy Project Financing	79
4.1	Introduction	80
4.2	Methodology	81
4.2.1	Description of the Financial Model	82
4.2.2	Economic Assessment Criteria	86
4.2.3	Simulation Setup	89
4.3	Results and Discussion	95
4.3.1	Simulation of Wind Energy Project Financing Cash Flows	97
4.3.2	Impact of Climate Change on Wind Energy Project Financing	103
4.4	Conclusions	111
5	Conclusions and Outlook	113
	References	117
	List of Abbreviations	129
	List of Figures	131
	List of Tables	135
A	Appendix	137
	Acknowledgements	165

1 Introduction

Objective of this thesis is to develop a framework for assessing climate change impacts on wind energy financing. This very first chapter introduces the relevance for climate change adaptation of the energy sector - being in transition to low-carbon electricity generation - and of wind energy in particular. In Section 1.1, the energy sector is described as critical infrastructure, and its role for climate change mitigation as well as adaptation is illustrated. The significance of (offshore) wind energy in future energy mix scenarios is highlighted in Section 1.2. Finally, the motivation to conduct this topic as well as the thesis' objective is formulated in Section 1.3.

1.1 Critical Energy Infrastructure and Climate Change Adaptation

Critical infrastructures are facilities of special importance for countries and broader economic regions. Their interruption can result in severe consequences for associated sectors, economy and society as a whole. As such, the energy sector is regarded as critical infrastructure (*Cortekar and Groth, 2015*) and referred to as *critical energy infrastructure* in the following. Its protection and secured operation is of superior interest (*Council of the European Union, 2008*). Planning and operational lifetimes of energy infrastructure projects usually span several years to multiple decades (*Cortekar and Groth, 2015*). Therefore, climate and climate change information is needed for risk management and to support secure and sustainable energy supply in light of a changing climate (*Groth et al., 2018*).

Aiming to reduce greenhouse gas emissions, the entire energy sector is undergoing a transition to low-carbon electricity generation, associated with growing power production from renewables and decreasing electricity generation from conventional energy sources. The European Union (EU) implemented binding (national) targets set under the *Renewable Energy Directive (2009)* to accelerate this transition. Recently, the 2030-target has been renewed to accomplish a share of energy from renewable sources of at least 32% of the gross final consumption from all European member states (*European Commission, 2016, 2018*). EU's long-term perspective envisages 75% of the gross energy consumption to be provided from renewable sources by the middle of the 21st century (*European Commission, 2012*). According to the latest official annual assessment report outlining the deployment progress of renewable energy sources in the EU, the share of electricity generation by renewable energy sources is estimated to account 17.4% in 2017 across all European member states (*EEA, 2018*). In Germany, renewable energy sources contributed for 40.4% to the (regulated) net public electricity generation in 2018 (i.e. the electricity mix fed into the public power grid; *Fraunhofer ISE, 2019*).

Renewable energy generation depends on the availability of renewable resources. In contrast to conventional electricity generation, the renewable resource is (mostly) cost-free but naturally expresses variable in space and time. With larger shares of renewables in the energy system, not only the infrastructure and facilities themselves but as well the energy generation through renewable resources is exposed to weather and climate. Regarding planning and operational lifetimes of critical energy infrastructure, usually spanning several years to multiple decades, this might result in enhanced vulnerability of the energy sector under changing climate conditions

(Groth *et al.*, 2018). Therefore, the incorporation of measures to adapt to expected changing climate conditions is proposed for future energy infrastructure activities to support a secure and sustainable energy supply in light of a transforming energy sector (Groth *et al.*, 2018). In this regard, the energy sector as a critical infrastructure is also of special importance as it combines aspects of climate change mitigation and adaptation.

1.2 Wind Energy

According to the EU Energy Roadmap 2050 (European Commission, 2012), wind power is estimated to contribute more electricity than any other technology by the middle of the 21st century, regarding a decarbonisation scenario conforming to the EU's emission reduction targets (cf. Section 1.1). However, recently recorded levels deviate considerably from estimates of future energy mix scenarios: According to *WindEurope* (2018a), 11.6% of the EU's average annual electricity demand has been covered by wind energy in 2017. Nevertheless, distinctly higher shares are already present for individual European member states (e.g. 44.4% for Denmark or 20.8% for Germany). The corresponding installed wind power capacity in 2017 is quantified to 168.7 GW of which about 15.8 GW are accounted to offshore wind (*WindEurope*, 2018a). Referring to this, Germany is assigned as the European member state with the largest installed wind power capacity amounting to 56.1 GW (about 5.4 GW offshore wind; *WindEurope*, 2018b), producing approximately 102.8 TWh of wind energy in 2017 (about 17.4 TWh from offshore wind generated primarily in the North Sea; *Fraunhofer ISE*, 2019).

Electricity generation from offshore wind is characterised by more stable and higher wind energy output compared to onshore sites (Emeis, 2013; *Fraunhofer IWES*, 2017). This is primarily due to less pronounced diurnal variations in atmospheric stability and a smoother surface roughness offshore resulting in less turbulence, less vertical wind shear and higher wind speeds across altitudes where wind turbines operate at (see Section 3.1). Because of its ability to provide energy more stable and continuous compared to onshore wind energy, European future energy mix scenarios consider wind energy from offshore sites as operating reserve and, therefore, essential for secure and sustainable energy supply (*Fraunhofer IWES*, 2017).

Offshore wind energy is a relatively young and agile market being in transition from development stage towards reaching commercial viability and price competitiveness on energy markets. The development and market potential of offshore wind energy is reflected in rapidly growing and projected continuous increases of additional installed capacity: For Europe, *WindEurope* (2018b)

expects an installed capacity of 25 GW to be available by 2020 and 50 to 100 GW by 2030, with most of the offshore wind expansion occurring in the North Sea. At the moment, Germany is the only country committing offshore wind capacity extensions manifested within the German Renewable Energy Sources Act (EEG) until 2030 (*WindEurope*, 2018b). According to this, *Fraunhofer IWES* (2017) estimates that 28% of the total renewable electricity generation in Germany could be provided from offshore wind energy by the middle of the 21st century - corresponding to a share of 36% on total wind energy generation - assuming optimal utilisation of renewable energy resources.

Along with the projected market development of offshore wind energy over the next decades, cost reduction goals are promoted by manufacturers. For example, *Siemens* (2016) is targeting to lower costs by more than one third of 2016-levelised costs of electricity until 2025. Moreover, offshore wind turbine technology holds potential for development and capacity for innovation. Prognoses of future turbine technology portrait rated capacities of 20 MW with hub heights of 150 m and rotor diameters of 250 m to be feasible (*Fichaux et al.*, 2011), thus, well exceeding dimensions of most-recent installed offshore wind turbines reaching rated capacities of 8 to 9 MW with hub heights of about 100 m and rotor diameters spanning around 160 m (*BMW*i**, 2018). This emphasises the potential for cost reduction and market competitiveness as well as incessant commercial attractiveness for deployment of offshore wind energy in particular.

Besides political efforts to foster the installation of additional offshore wind energy capacity, its market potential and expected technical development, sufficient long-term experience and empirical value are lacking since the first commercially installed offshore wind farms only recently reached their expected lifetimes (*Ørsted*, 2016; *Vattenfall*, 2016). Moreover, only limited meteorological and oceanographic observational records are available. In particular spatially comprehensive and sufficiently long climatologies about wind speed, turbulence and wind shear across altitudes where offshore wind turbines operate are rare - though crucial to evaluate a project's technical and economic feasibility. Analogously, climate change information of sufficient high resolution and specific for wind energy applications are almost non-existent. In this regard, research demand is identified to facilitate vulnerability assessments supporting climate change adaptation (*UBA*, 2015).

1.3 Motivation and Objective

Wind energy is expected to become the largest source of electricity generation in Europe's future energy mix with offshore wind energy in particular being considered as an essential component for secure and sustainable energy supply. As a consequence, future electricity generation will be exposed to an increasing degree to weather and climate. Taking into account planning and operational lifetimes of wind energy infrastructure (see Section 2.1), typical climate time scales comprising 30 years are reached. Therefore, climate and climate change information become generally of relevance to identify and quantify climate related impacts on wind energy.

Wind energy is a capital intensive technology for which large initial expenses, accounting to about half of the total project costs, incur upfront project realisation and, thus, before generating any return (see Section 2.1). Cash obligations get refinanced solely through revenues generated by the wind energy project during its operational lifetime (see Section 4.1; *Böttcher*, 2012, 2013). Accordingly, economic feasibility (as part of a projects' due diligence) is evaluated and project financing plans get prepared on the basis of assumptions of expected yield (*Böttcher*, 2010).

Commonly, wind energy yield assessments are based solely on (available) retrospective observational records and/or reanalysis data (*Böttcher*, 2012; *IEC-61400*, 2015). This circumstance limits assumptions for yield assessments, utilised for project financing plans, to be representative for current climate conditions only. However, several research studies analysed and quantified potential climate change impacts on the wind energy resource and subsequent wind power production, providing (consistent) evidence of an exposure of the wind energy resource to changing climate conditions for Europe (see Section 2.2; *Pryor et al.*, 2005, 2012; *Pryor and Barthelmie*, 2010; *Barstad et al.*, 2012; *Hueging et al.*, 2013; *Reyers et al.*, 2014, 2016; *Tobin et al.*, 2015, 2016; *Moemken et al.*, 2018). In addition, wind turbine operating conditions might be reduced due to projected variability and wind speed distribution changes (*Moemken et al.*, 2018). And projected climatic changes might impact extreme and fatigue load characteristics, to which the wind energy infrastructure is exposed (*Pryor et al.*, 2005, 2012; *Pryor and Barthelmie*, 2010, 2013).

Until now, consequences for wind energy being related to changing climate conditions have not been investigated specifically with regard to wind energy financing. This research gap is addressed in this thesis and guided by the following research questions:

- *Which cost elements of wind energy financing are affected most by changing climate conditions?*
- *How do changing climate conditions affect the financial risk of wind energy financing?*

- *Should climate change impacts be considered as an additional influencing factor on wind energy financing?*

Along with these guiding research questions, a methodological procedure is presented to assess such climate change impacts for wind energy financing. This procedure is applied for the case of offshore wind energy because of its important role as operating reserve, its comparably high rate of additional installed capacity being expected for the decades to come and to support gain of empirical value - but is likewise transferable to onshore wind energy.

The thesis is structured as follows; A generalised financing chain for wind energy is presented and the exposure of individual elements to physical climate change is traced in Chapter 2. After introducing principles of wind energy meteorology and regional climate modelling, the methodology to generate climate change information of high resolution and specific for wind energy with the regional climate model REMO as well as results of simulated wind characteristics is covered in Chapter 3. How the generated climate change information impacts on wind energy project financing is investigated through a financial modelling exercise being presented in Chapter 4. While a comprehensive discussion is provided for each chapter individually, summarising concluding remarks and an outlook are given in Chapter 5.

2 Climate Change Impacts on Wind Energy Financing

Wind energy projects are complex ventures consisting of various individual (but interconnected) operations. The financial costs of these individual operations can be arranged in confined categories and assigned to their temporal occurrence. In combination with the balancing financial income through electricity generation, the different cost positions can be structured to a comprehensive wind energy financing chain. The breakdown of a total wind energy investment to different cost origins and their temporal occurrence allows to trace and evaluate their exposure to physical climate change. In this regard, direct as well as indirect climate change impacts on wind energy financing can be identified and the most significant quantities can be determined.

Objective of this chapter is to specify elements of the wind energy project financing chain, which are potentially subject to physical climate change, and estimate the most impacted elements in a qualitative manner. A definition and overview of the financing chain for wind energy is provided in Section 2.1. Potential direct and indirect impacts related to changing climate conditions associated to individual elements of this wind energy financing chain are elaborated in Section 2.2. This chapter is completed by concluding remarks given in Section 2.3.

2.1 The Wind Energy Financing Chain

Wind energy projects can be arranged in a pre-operational phase, an operational phase and decommissioning (*Krohn et al.*, 2009, Fig. 2.1). The pre-operational phase comprises all initial investment (or capital) costs which are due prior to the commissioning of the power plant. Depending on the size of the wind farm, this phase comprises up to five or more years of planning and construction. Variable (or operational) costs are present during the operational phase of the project and appear to be erratic over the project lifetime, spanning at least 20 to 25 years (*BMWi*, 2018; *Krohn et al.*, 2009). Expenditures for decommissioning are usually accounted as securities which are due with the commissioning of the power plant or as variable cost position over the operational phase - depending on the financing design and regulatory framework - even though those costs are required subsequent to the project lifetime. All expenses to be incurred get solely balanced through revenues generated by the wind energy project during the operational phase. In this regard, the revenue through wind power production is gained from the cost-free renewable wind resource.

A wind energy financing chain is developed according to cost and income positions (see Fig. 2.2). The different components and their share with respect to the investment are described in the following. Cost structures are different for onshore and offshore wind energy investments, especially because of diverging requirements regarding the technical infrastructure and logistics as well as for operation and maintenance (e.g. *Blanco*, 2009; *Böttcher*, 2012, 2013; *Hau*, 2014). Lacking experience depicts an additional cost driver for offshore wind energy. As the focus of this thesis is on offshore wind energy, factual information raised in this section refer to offshore wind energy (if not specified differently).

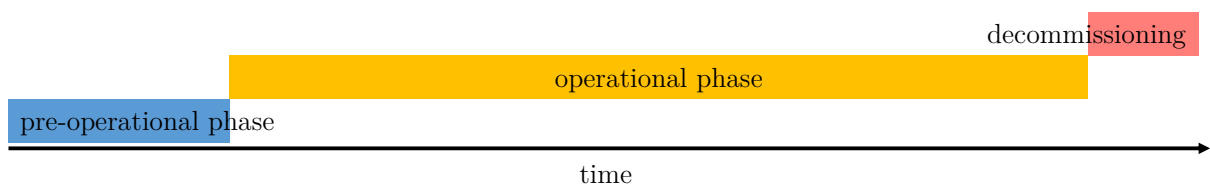


Figure 2.1: Schematic of different phases of wind energy projects over their lifetime. The size of the bars provide a rough estimate of the relative time frame of the different phases even though they are given as indistinct. In this regard, the operational phase extends to about four to six times the horizon of the pre-operational phase. Decommissioning is intended to account about a third up to a half of the horizon of the pre-operational phase.

Capital Costs

Wind energy is a capital intensive technology for which large initial expenses, accounting to about half of the total costs, incur upfront project realisation and, thus, before generating any return. Overall, a share of up to 80% of the levelised costs of electricity can be related to capital costs (*Blanco, 2009*). Pre-operational investment costs comprise costs for initial planning, logistics, technical infrastructure, technology, assembly and commissioning as well as administrative, financial and legal costs. According to *Blanco (2009)* and *Krohn et al. (2009)*, the largest share of the capital costs (about 50%) can be accounted to wind turbine technology. About 40% of the capital costs can be related to technical infrastructure, which divide to equal parts into costs for foundations and connection to the grid. The remaining 10% of the initial investment are mainly associated to project management, assembly, commissioning and administration. Logistics are already included in the costs for technology and technical infrastructure but can be estimated to account to about 10 to 15% of the capital costs. Actual capital costs and their shares vary among projects as they depend on the specific geotechnical conditions at the site of the wind farm. In this regard, the distance from the coast, the water depth and seabed conditions are substantial cost drivers for offshore wind energy projects. All presented values are meant to provide an estimate only. For completeness, subsidising deployment policies (e.g financial incentives or other subsidies) might be accounted with fulfilment of certain milestone agreements already during the pre-operational phase.

Variable Costs

Variable costs over the lifetime of a wind energy project are rather uncertain and oscillate around a share of 20% of the levelised costs of electricity for onshore sites, but might reach higher values for offshore wind farms (*Blanco, 2009*). Only limited comprehensive and representative information about operational costs for offshore wind energy are available because of lacking long-term experience. *Hau (2014)* assumes operational expenses to be higher by one third for nearshore and by one half for offshore wind energy compared to onshore sites, referring to prognosis prepared for the amendment of the EEG as of 2004. Taking this into account, operation and maintenance costs reach about 5% of the initial investment per year (including regular service, repair and spare parts; *Blanco, 2009; Hau, 2014*). This would relate to about 25% of the variable costs. Costs for insurance are determined to account to about 10% to 25% of the variable costs (*Blanco, 2009; Böttcher, 2013*). Remaining operational costs are associated to land lease, grid premiums

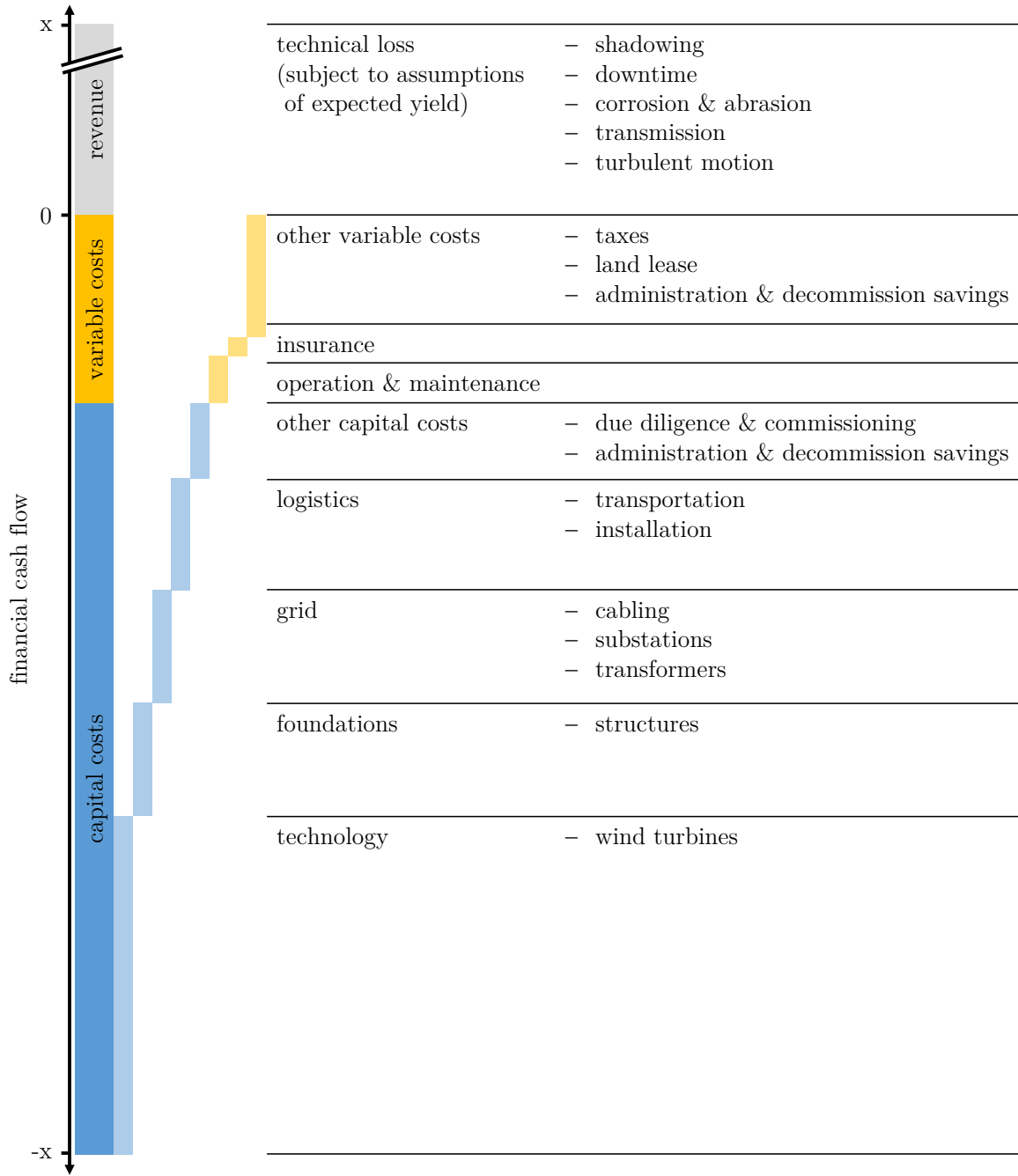


Figure 2.2: Schematic of the wind energy financing chain. Capital costs and variable costs get solely balanced through the revenue generated by the wind energy project during the operational phase. Financial costs of individual operations are arranged in confined elements and assigned to their temporal occurrence (cf. Fig. 2.1). The size of the bars reflect the relative share of capital costs and variable costs (relating to levelised costs of electricity). Moreover, the relative shares of the different cost positions with respect to capital costs and variable costs are indicated. No resource costs incur to the generated revenue but technical losses are subject to yield assumptions based on manufacturers' wind turbine power curves. Information is distilled and harmonised from *Blanco (2009)*, *Krohn et al. (2009)* and *Hau (2014)*.

and administration. Nominal accumulated variable costs over the entire project lifetime for offshore wind energy are accounted to equal the total investment costs (*Böttcher*, 2013). However, expenditures for operation and maintenance as well as for insurance depend on the conditions of service contract agreements - which are an invariable part of purchase contracts with wind turbine manufacturers - and, therefore, vary among projects. In this regard, *Böttcher* (2013) estimates accumulated operation and maintenance costs to reach even up to 60% of the variable costs, revealing a large bandwidth with respect to operation and maintenance cost assumptions.

Revenue

Contrary to conventional energy based on fossil fuels, wind energy - as a renewable energy - utilises cost-free energy resources. Because no costs for the resource prevail as additional variable cost position for wind energy, the levelised costs of electricity are dominated by capital costs (see above). This is why in particular technology-intensive renewable energy projects, such as wind energy, require large amounts of capital costs prior to the project realisation (*Blanco*, 2009). Because planned lifetimes of such projects span at least 20 to 25 years (*BMW*, 2018; *Krohn et al.*, 2009), most large-scale wind power plant projects are based on long-term financing and are realised through project financing (*Böttcher*, 2013, 2012, ; the author refers to Section 4.1 for an introduction to financing of wind energy). With project financing, cash obligations of capital costs and variable costs are refinanced solely through revenues generated by the wind energy project during the operational phase. Thus, the project success is intimately connected with the extracted energy from wind and, in turn, primarily wind climate determines this revenue.

Mechanical limitations restrict the extraction of kinetic energy contained in the wind by wind turbines to a specific maximum portion, according to *Betz's law* (*Hau*, 2014). Turbine manufacturers provide individual wind turbine power curves describing the energy output taking this effect into account. Moreover, technical losses are present reducing the conversion to power and, thus, abating the resulting revenue. These losses incorporate wind turbine shadowing effects within farm structures, downtime (other than originating from regular service or wind conditions outside the operational wind speed range), corrosion and abrasion, losses related to transmission of energy and others. This technical loss can account to about 10 to 15% of the actual revenue (*Blanco*, 2009). For completeness, regulation acts as well as the market for power trading are non-attributable risks being subject to the revenue generated through wind power production.

2.2 Climate Change Impacts on the Wind Energy Financing Chain

Individual elements of the wind energy financing chain (see Section 2.1 and Fig. 2.2) are externally exposed to weather and climate. Because atmospheric conditions and the sea state might get altered through changing climate conditions, elements of the wind energy financing chain are potentially affected by physical climate change. To evaluate such climate change impacts on the wind energy financing chain, meteorological and oceanographic variables, which are subject to variations with changing climate conditions, are determined and assigned to individual elements of the wind energy financing chain. In this regard, direct as well as indirect impacts are incorporated. In order to trace and determine the most considerable quantities, the exposure of individual elements to climate change is reflected in the context of climate time scales. In this regard, capital costs arise at a relatively early instance in time (i.e. foreseeable future with respect to the planning phase), whereas variable costs are present over the entire lifetime of the project.

According to cost and income positions the wind energy financing chain is based upon (see Section 2.1), potential climate change impacts on individual elements of the wind energy financing chain are described in the following. Only few research has been conducted addressing individual components of wind energy in the context of climate change specifically (e.g. *Pryor and Barthelmie*, 2010, 2013; *IPCC SR*, 2012; *IPCC*, 2014, and references therein). Available assessments are referred to in the subsequent paragraphs to the author's best knowledge. An overview of assigned potential climate change impacts on individual elements of the wind energy financing chain are provided in Fig. 2.3.

Capital Costs

Wind turbines are mechanical constructions. Weather and climate affect the performance and lifetime of the turbines through wear and tear. The material and mechanical components are exposed to fatigue loads and gradual stress, primarily determined by mean wind speed conditions and turbulence intensity (*Pryor and Barthelmie*, 2010; *Hau*, 2014). Moreover, extreme loads, arising mainly from rare events associated with extreme atmospheric motion, could cause malfunction or even force demolition when exceeding critical loads (*Hau*, 2014). These extremes comprise - among others - extreme wind speed and wind gusts, abrupt wind direction changes, extreme vertical wind shear as well as coherent extreme gusts with direction changes during operation (*Pryor and Barthelmie*, 2013; *IEC-61400*, 2015). Offshore wind turbines are exposed

to sea level variations, combinations of wind and wave loads and (drifting) sea ice, which produce mechanical stress on towers and foundation structures (*Pryor and Barthelmie, 2013*). Cold and hot temperature extremes might affect the physical properties of materials, the hydraulic system or electronic components (*Pryor and Barthelmie, 2010*). Nonetheless, *Pryor and Barthelmie (2010, 2013)* evaluate the vulnerability of the wind turbine design with respect to projected European climate change and extreme events to be covered by the conservative estimate range of the *IEC-61400 (2015)* wind turbine design industry standard. However, other regions might be impacted though (as changes in amplitudes or frequencies of extreme events appear heterogeneous) and only limited research is conducted covering compound events and wind-wave loading.

The connection of an offshore wind farm to the grid comprises the internal cabling between turbines, substations, sea transmission cables and transformer stations (e.g. *Hau, 2014*). Weather and climate could evoke extreme loads causing malfunction or even force demolition to some of those components. Analogous to wind turbine towers and foundation structures, offshore substations are primarily exposed to load through sea level, waves and (drifting) sea ice (*Hau, 2014*). Because transformer stations are usually located onshore, variations in sea level and storm surges represent potential impacts. The author is not aware of any study that investigated design load cases on substations and transformers in the context of changing climate conditions. Nevertheless, the *IEC-61400 (2015)* wind turbine design industry standard is harmonised with industry standards for onshore and offshore structures (such as rigs), which is why conservative estimate ranges valid for substations and transformers can be regarded to cover projected magnitudes of European climate change and extreme events (cf. *Pryor and Barthelmie, 2010, 2013*).

Logistics for the transport and installation of offshore wind components are prone to weather conditions as well as to the sea state (*Blanco, 2009*). During the deployment phase of an offshore wind farm, site access and assembly is limited to well-defined weather conditions due to technical feasibility and safety regulations (*Hau, 2014*). In this regard, critical wind speed and wave height as well as sea ice and restricted visibility as a result of marine fog depict limiting circumstances (*Pryor and Barthelmie, 2010; Hau, 2014*). Potential changes in these variables impact the occurrence or duration of operational weather windows. Even though installation vessels are usually chartered several years in advance for dedicated time slots, logistics remain adjustable to changing climate conditions and are regarded as flexible with respect to climate time scales. Moreover, premium products exist which provide reinsurance solutions for guarantee obligations, thus, enabling to abandon the financial risk of a delayed commissioning due to adverse weather or sea state conditions (*MunichRE, 2018*).

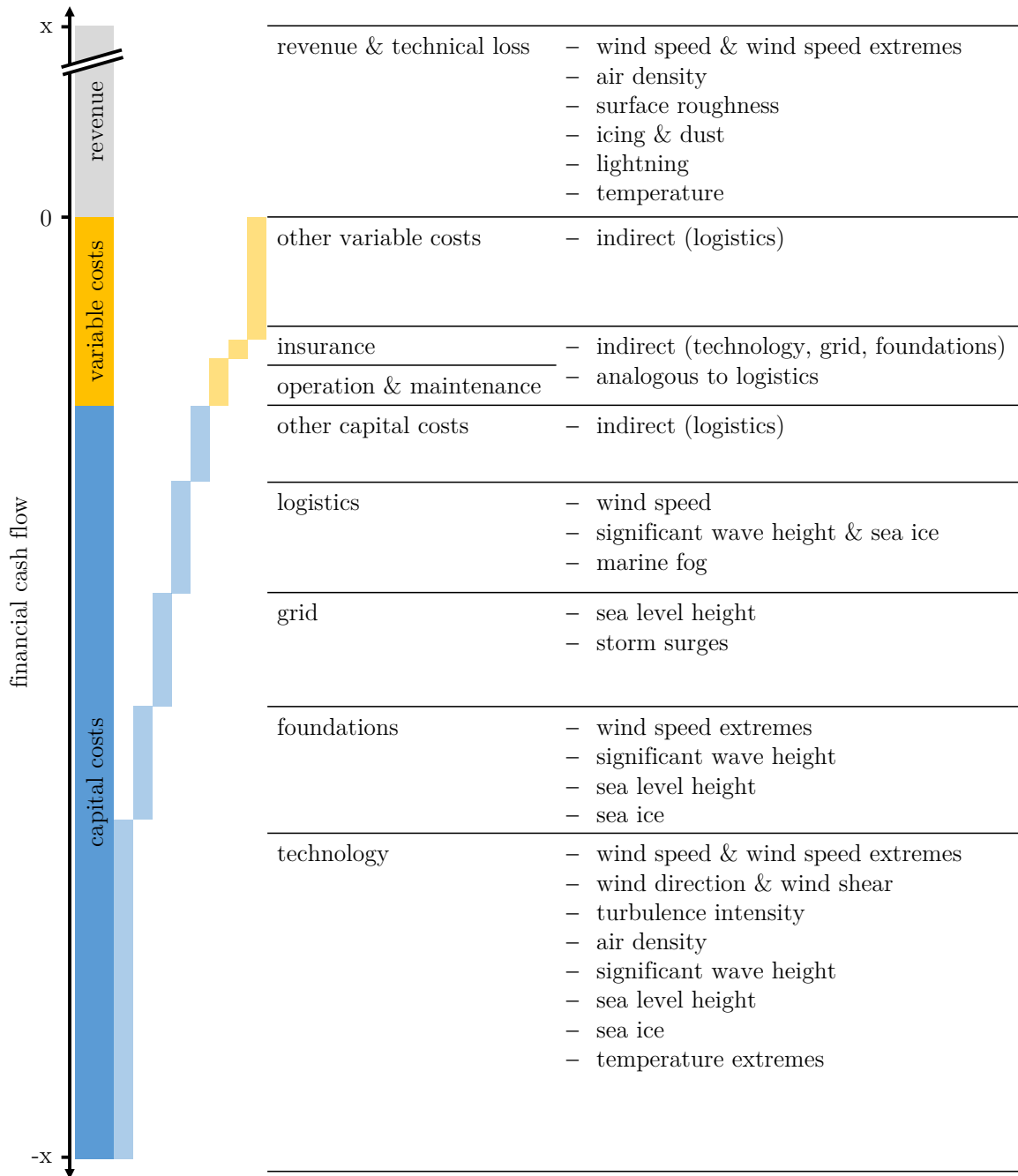


Figure 2.3: Schematic of climate change impacts on the wind energy financing chain. Meteorological and oceanographic variables, which are subject to variations with changing climate conditions, are determined and assigned to individual elements of the wind energy financing chain. In addition to directly exposed quantities, indirect impacts are incorporated. Analogous to Fig. 2.2, financial costs of the confined elements are assigned to their temporal occurrence (cf. Fig. 2.1). The size of the bars reflect the relative share of capital costs and variable costs (relating to levelised costs of electricity). Moreover, the relative shares of the different cost positions with respect to capital costs and variable costs are indicated.

Variable Costs

Operation and maintenance is tied primarily to wear and tear of the wind turbines and to a minor extent to the technical infrastructure (Hau, 2014). Potential changes in mean wind speed conditions and turbulence intensity, which primarily determine fatigue loads and gradual stress (Pryor and Barthelmie, 2010; Hau, 2014), could evoke the necessity for additional maintenance intervals or unscheduled service to assure performance and operating lifetime of the turbines. The durability - limited through wear and tear - is directly related to the engineering of wind turbines. As the wind turbine design is evaluated to cover projected magnitudes of European climate change and extreme events within the conservative estimate range of the *IEC-61400* (2015) wind turbine design industry standard, the design of wind turbines is regarded to reflect durability against wear and tear under changing climate conditions as well (Pryor and Barthelmie, 2010, 2013).

Furthermore, potential impacts on the operation and maintenance of offshore wind farms are present with respect to logistics. Because the accessibility is limited to well-defined weather conditions and the sea state, potential changes in the occurrence or duration of operational weather windows might impact regular maintenance intervals and unscheduled service. However, analogous to logistics during the deployment phase (see previous paragraph), logistics for operation and maintenance remain adjustable to changing climate conditions and are regarded as flexible with respect to climate time scales.

Additional interdependencies among elements of the wind energy financing chain and variable costs can be established. The potential impacts on operation and maintenance raised above might indirectly feed back on insurance products as changes in (perceived) long term risk on wind turbines, technical infrastructure or logistics will likely be reflected in insurance premiums. Furthermore, estimated costs and savings for decommission might be affected indirectly through logistics.

Revenue

Revenues generated during the operational phase of a wind energy project depend primarily on the wind climate. The harvestable wind energy resource being potentially available to wind turbines is a function of the wind speed and air density (cf. Eq. 3.14; e.g. Hau, 2014). Several research studies analysed and quantified potential climate change impacts on the wind energy resource and subsequent wind power production for Europe (Pryor *et al.*, 2005, 2012; Pryor and Barthelmie, 2010; Barstad *et al.*, 2012; Hueging *et al.*, 2013; Reyers *et al.*, 2014, 2016; Tobin *et al.*,

2015, 2016; *Moemken et al.*, 2018). Even though limitations persist in how climate information is translated to match wind energy relevant height levels and planetary boundary layer conditions (cf. Section 3.1) or how changes in air density are treated (cf. Section 3.5), these studies provide (consistent) evidence of an exposure of the wind energy resource to changing climate conditions. Most of the studies agree on an increase of the annual mean wind energy resource over northern and parts of central Europe under changing climate conditions, even though uncertainty with respect to the magnitude and the sign of change is present among climate change projections. More robust changes are projected for seasons: In particular during winter, increasing values are projected, while a decrease is analysed during summer. This provides evidence of an intensification of the intra-annual variability for most of Europe. However, significant changes are expected to evolve earliest during the second half of the 21st century. Nonetheless, wind turbine operating conditions might be reduced due to projected variability and wind speed distribution changes (i.e. wind speed below cut-in or above cut-out wind speed ranges of wind turbines; *Moemken et al.*, 2018).

In addition to climate change impacts affecting the wind energy resource and subsequent revenue, the wind power production is subject to technical losses, which are again potentially impacted by climate change. Extreme wind events could force automatic shutdowns or even foster disruptions or outages of facilities leading to unscheduled downtime (*Pryor et al.*, 2005, 2012; *Pryor and Barthelmie*, 2010, 2013). Moreover, changes in the frequency of lightning might cause damage to wind turbine blades as well as to other mechanical or electronic components (*Pryor and Barthelmie*, 2013). Icing on wind turbine blades - primarily at higher altitudes and/or mid to high latitudes - alter their aerodynamic efficiency and could even evoke unscheduled downtime (*Dalili et al.*, 2009). However, the frequency for such occurrences is estimated to decline with increasing atmospheric temperatures under changing climate conditions (*Pryor and Barthelmie*, 2010). Moreover, the aerodynamic efficiency of wind turbines gets degraded through blade soiling with lifetime of the turbines (*Dalili et al.*, 2009). Finally, projected increasing temperature conditions result in increasing electricity transmission losses (*Troccoli*, 2008; *Troccoli et al.*, 2014).

2.3 Conclusions

Arising financial costs and expected income of wind energy projects are structured to a comprehensive wind energy financing chain (see Fig. 2.2). External climate variables, which are subject to variations with changing climate conditions, are determined and assigned to individual

elements of this wind energy financing chain (see Fig. 2.3). In order to trace and determine the most affected elements, their exposure to climate change is reflected in the context of climate time scales and prioritised in a qualitative manner.

Capital costs depict the largest cost component comprising up to 80% of the levelised costs of electricity, but arise at a relatively early instance in time in foreseeable future with respect to the planning phase. The largest share in capital costs is generated by wind turbine technology and the technical infrastructure, for which the vulnerability with respect to projected European climate change and extreme events is evaluated to be covered by conservative estimate ranges of industry standards. In addition, logistics are regarded as flexible with respect to climate time scales and, thus, examined as adjustable to changing climate conditions. This leads to the conclusion that potential changes in climate variables affecting capital cost components remain manageable.

Variable costs are present over the entire operational phase of the project, spanning at least 20 to 25 years. They are subject to (economic) uncertainty as some future expenses can only be (roughly) estimated. However, variable costs are quantified to oscillate around 20% of the levelised costs of electricity, thus, well below capital cost amounts. Operation and maintenance interferes strongly with the design of wind turbines. As conservative estimate ranges of industry standards are evaluated to cover the vulnerability with respect to projected European climate change and extreme events, the design of wind turbines is regarded to reflect durability against wear and tear under changing climate conditions. Logistics for operation and maintenance are regarded as flexible with respect to climate time scales and, therefore, examined as adjustable to changing climate conditions. Moreover, insurance premiums will likely reflect changes in (perceived) risk due to potential climate change impacts, however, costs for insurance represent an ancillary cost component of the wind energy financing chain. This leads to the conclusion that variable cost components are not substantially exposed to potential changes in climate variables.

Cash obligations for wind energy projects are usually refinanced solely through the revenues generated from the power production during the operational phase. In turn, the wind energy power production is primarily determined by the wind climate. Even though methodological limitations are present and uncertainties are subject to climate change projections, current research provides (consistent) evidence of an exposure of the wind energy resource to changing climate conditions in terms of the mean state and variability. Because the entire wind energy project investment relies on generated revenues, the exposure of the wind energy revenue to projected climate change is concluded to be essential for wind energy financing.

The qualitative comparison of climate change impacts on capital costs, variable costs and wind energy revenue leads to the conclusion that the revenue needs to be regarded as the essential component of the wind energy financing chain being exposed to changing climate conditions. This implies the wind resource through variables determining the wind climate (see Section 2.2 and Fig. 2.2) to be the crucial climate variables of interest for an assessment of climate change impacts on the financing of wind energy.

3 Climate Change Information for Wind Energy

Dimensions of most-recent installed offshore wind turbines comprise turbines of the 8 MW or 9 MW class, reaching turbine hub heights of about 100 m and rotor diameters spanning more than 160 m (*BMW*, 2018). Prognoses of future offshore wind turbine technology portrait turbine classes reaching 12 MW or more by 2025, with hub heights of 120 m and rotor diameters of about 200 m (*BMW*, 2018). *Fichaux et al.* (2011) even illustrate feasible scenarios for 20 MW wind turbines reaching hub heights of 150 m and rotor diameters of 250 m. These dimensions and expected technical development indicate the lowest 300 m of the atmosphere as relevant for wind turbine energy generation. Therefore, atmospheric conditions and characteristics of this part of the atmosphere, the planetary boundary layer, need to be taken into account. As large-scale wind power plant projects comprise planning and operational horizons of at least 20 to 25 years (*BMW*, 2018; *Krohn et al.*, 2009), climate and climate change information are of potential interest and relevance for such infrastructure projects.

This chapter describes relevant theoretical aspects in meteorology for wind energy, associated challenges in generating wind energy-specific climate and climate change information and covers a methodological modelling framework aiming to achieve such information. Furthermore, thermodynamically induced changes in wind climate and wind characteristics are assessed. A brief introduction to the theory of boundary layer meteorology and the relevance for wind energy is provided in Section 3.1. Subsequently, regional climate modelling is presented as a tool to generate climate information and ongoing development in this field of research are outlined in Section 3.2. The regional climate model REMO and its recently developed non-hydrostatic extension REMO-NH, which are used in the frame of this thesis, are introduced in Section 3.3. Section 3.4 presents the methodological concept of surrogate climate change experiments as well as adjustments introduced to the REMO model and the simulation setup with the purpose

to generate wind energy-specific climate information. The results of realised experiments are illustrated in Section 3.5 and comprised by concluding remarks in Section 3.6.

3.1 Boundary Layer Meteorology and Wind Energy

Wind power production is determined by atmospheric conditions and characteristics of the planetary boundary layer. Therefore, theoretical aspects of boundary layer meteorology and their relevance for wind energy as well as their consideration in the generation process of wind climate information are of interest for wind power applications.

Theoretical Aspects of Boundary Layer Meteorology

The troposphere extends to an average altitude of about 11 km. Almost all weather conditions take place in this part of the atmosphere, but just the lowest few kilometres get modified by the underlying surface. Among a variety of more or less similar definitions, *Stull* (1988) defines this planetary boundary layer (PBL; also referred to as atmospheric boundary layer or simply boundary layer) as the part of the troposphere which is influenced directly by the presence of the Earth's surface and associated processes forced by heat, moisture and momentum transfer on a timescale of about an hour or less. In this regard, the temporal scale is regarded as the time frame with the ability to trigger a differing planetary boundary layer (PBL) equilibrium state initiated by atmospheric variations. These characteristics can be summarised to a well defined and recurring structure of the PBL evolving with the diurnal cycle (*Stull*, 1988; *Foken*, 2008). The structure of the PBL is driven by the surface energy budget. The energy budget is determined by incoming shortwave and outgoing longwave solar radiation, while the energy of the shortwave radiation is transferred in terms of heat, moisture and momentum resulting in warming, evaporation and friction, respectively (e.g. *Etling*, 2008).

The thickness of the PBL is variable in time and space and ranges from a couple of hundred metres to a few kilometres (*Stull*, 1988). While over land the PBL depth amounts to about 1 to 2 km, over ocean surface it is usually less thick amounting to about 0.5 km. In addition, the PBL depth varies relatively slowly in space and time over ocean surface (*Stull*, 1988). This is primarily because of a comparably smooth surface as well as the ocean's slow response to atmospheric variation and its capacity to absorb large amounts of heat, thus, dampening turbulent transport of heat, moisture and momentum (*Stull*, 1988; *Foken*, 2008). However, the PBL depth varies considerably with stratification and stability (or turbulence intensity) (*Foken*, 2008).

Within the PBL wind speed increases non-linearly with height, from lower values at the friction dominated surface until geostrophic wind speed is reached at the interface of the PBL and the free troposphere (*Foken, 2008*). In theoretical meteorology, this observable characteristic is explainable by the setting of acting forces. Based on this theoretical construct, the PBL is further subdivided into three distinct layers (*Etling, 2008*). The viscous sublayer amounts to just a few millimetres and the energy transport within this layer is subject to molecular forces only. As such it is free of turbulence and does not influence PBL dynamics (*Etling, 2008*). The surface layer (also referred to as Prandtl layer or constant flux layer) is defined as the lowest 10% of the PBL reaching an altitude of approximately 20 to 50 m under unstable stratification and a few meters under stable stratification (*Stull, 1988; Foken, 2008*). Friction and gravitation (or pressure gradient) are the dominating forces in the surface layer. An important assumption for the theoretical concept of the PBL structure are constant vertical turbulent energy fluxes within the surface layer (*Foken, 2008*). Primarily because the frictional stress decreases with distance from the Earth's surface, the wind speed increases with height resulting in a characteristic logarithmic profile (*Etling, 2008*). Above the surface layer follows the Ekman layer (also referred to as upper layer) covering the remaining 90% of the PBL (*Stull, 1988*). In this layer the Coriolis acceleration contributes to the acting forces in addition to friction and gravity. The presence of the Coriolis force is the reason why the Ekman layer is characterised by a clockwise rotation (on the Northern Hemisphere; counterclockwise on the Southern Hemisphere) of the wind direction with height towards the superimposed geostrophic wind. This concept is referred to as the Ekman spiral (*Stull, 1988; Etling, 2008*). Nonetheless, the wind speed remains relatively stable across the Ekman layer (*Etling, 2008*). At the top of the Ekman layer the frictional force diminishes such that a geostrophic equilibrium prevails between gravitational and Coriolis force.

Relevance of Boundary Layer Meteorology for Wind Energy

The PBL is the part of the troposphere where wind turbines harvest energy from wind. Thus, the vertical profile of wind speed and wind direction as well as the wind shear, atmospheric stability and turbulence within the PBL are of interest since those quantities determine the wind resource. As state-of-the-art wind turbines for offshore wind energy purposes reach hub heights of about 100 m and rotor diameters of more than 160 m (*BMWi, 2018*), the lowest 300 m of the atmosphere present the relevant altitudes for wind energy production. Those altitudes cover the entire surface layer and regularly entrain deeply into the Ekman layer, depending on prevailing atmospheric stability (*Emeis, 2013, 2014, 2015*).

The availability of physically consistent climate and climate change information across these altitudes is limited. Regularly, just information about near surface wind speed are accessible or provided. Therefore, methodologies exist to extrapolate near surface wind speed values to wind turbine hub heights. One procedure, which is widely applied, is the logarithmic wind profile (e.g. Troccoli *et al.*, 2014; Emeis, 2014). The logarithmic wind profile (see Eq. 3.1) can be derived from the Navier-Stokes equations of motion under the assumption of constant turbulent momentum energy fluxes with height (e.g. Etling, 2008). Because this assumption holds just for the surface layer, the logarithmic wind profile is just valid for this lower part of the PBL. Furthermore, the logarithmic wind profile does not describe a uniform function but comprises a term to correct the profile for atmospheric stability conditions. Information needed to solve this stability function are of more complex nature and usually not available. Therefore, the logarithmic wind profile is commonly applied in a simplified form without the stability correction term. While this results in a conformal solution for neutral atmospheric conditions (as the stability correction drops out), this is not the case for unstable or stably stratified atmospheric conditions. That is why the logarithmic wind profile does, strictly speaking, provide physically consistent solutions only under neutral stratification in the Prandtl layer (Etling, 2008) and does not match predominant and mean atmospheric conditions (Emeis, 2015).

Even though empirical methodologies are developed to compensate for erroneous representations of unstable or stably stratified atmospheric conditions across the Prandtl and Ekman layers (e.g. Gryning *et al.*, 2007; Peña *et al.*, 2010a,b; Emeis, 2013), a dynamical simulation through the Navier-Stokes equations of motion would, from a theoretical point of view, represent a physically consistent description of heat, moisture and momentum transport in the PBL and, thus, vertical wind speed profiles, which are of interest with respect to wind energy. Furthermore, when it comes to climate change assessments, a climate change signal associated to the near surface wind speed is assumed to prevail invariable with altitude when extrapolating this signal to hub heights. This might not necessarily be correct due to non-linearity and since changes in the atmospheric temperature profile might evolve non-uniform, thus, affecting atmospheric thermodynamics resulting in altered atmospheric stability conditions.

For completeness, another prominent methodology applied for extrapolation of near surface wind speed values to wind turbine hub heights is the empirical power law. However, the same limitations as for the logarithmic wind profile apply.

$$\bar{v} = \frac{u_*}{\kappa} \left[\ln \left(\frac{z}{z_0} \right) + \psi(z, z_0, L_*) \right] \quad (3.1)$$

where

- \bar{v} : wind speed
- u_* : frictional velocity
- κ : von Kármán constant
- z : height
- z_0 : surface roughness length
- ψ : stability function
- L_* : Monin-Obukhov length (see Eq. 3.12)

Dynamical climate models solve the Navier-Stokes equations of motion and, thus, provide a physically consistent description of atmospheric motion and velocity. However, the suitability of such models, especially in terms of vertical and horizontal resolution as turbulence is not explicitly resolved but parameterised, needs to be reassessed for the aim to generate climate and climate change information for the purpose of wind energy. Even though large eddy simulation (LES) models exist, which are potentially a more sophisticated tool to simulate PBL characteristics as those models simulate at a significantly higher resolution compared to climate models and are capable to numerically resolve large eddy turbulent flow, dynamical climate models represent the ultimate tool developed to interactively simulate climate time scales. This is why climate modelling is harnessed in the frame of this thesis, for the purpose to generate wind energy-specific climate and climate change information.

3.2 Regional Climate Modelling

Climate models, in general, are based on fundamental laws of nature (i.e. conservation of mass, momentum and energy) being expressed in differential equations. Global climate models (or general circulation models; GCMs) solve this system of differential equations numerically in a three-dimensional grid space, thus, being used to simulate the Earth's climate on a global scale for the past, present and future (e.g. *Warner, 2011; IPCC, 2013, ch. 9* and references therein). Information on regional climate could be directly obtained from these simulations (*IPCC, 2013, ch. 9*). However, state-of-the-art GCMs from the latest Coupled Model Intercomparison Project Phase 5 (CMIP5) comprise an average latitudinal resolution of about 1.3° (in the atmosphere)

corresponding to a horizontal grid spacing of approximately 145 km (*Taylor et al.*, 2012). This is too coarse to admit for certain small and fine scale dynamical processes being important on a regional scale or beyond (*Laprise et al.*, 2008; *Rummukainen*, 2010, 2016). Thus, regional climate models (RCMs) have been developed with the purpose to better resolve physical processes of relevance to the climate for a specific region applicable all over the globe (*IPCC*, 2013, ch. 9).

Principles of Regional Climate Modelling

The basic approach of regional climate modelling is to force RCMs with large-scale climate information over a limited area. In this model domain, the RCMs simulate weather and climate at high resolution. Thus, the spatial and temporal resolution can be significantly increased while preserving computational costs, compared to a GCM (*Warner*, 2011). State-of-the-art RCMs simulate at a resolution of approximately 12 to 50 km (*Giorgi et al.*, 2009). The forcing data are usually provided by a GCM or some other gridded data set - such as reanalysis data - and get supplied to the RCM as regular lateral and lower boundary information and as initial conditions. This procedure is referred to as dynamical downscaling (*Warner*, 2011).

RCMs are based on a dynamical core comparable to GCMs describing the fundamental physical-dynamical processes. As the climate system is characterised by processes acting on different spatial and temporal scales, the enhanced resolution of a RCM allows for an advanced representation of particular processes being important on a regional scale, compared to a GCM. Thus, RCMs are able to represent small and fine scale processes in a physically consistent manner and generate small and fine scale detail (*Denis et al.*, 2002; *Laprise et al.*, 2008). Especially an improved representation of the distinct model orography (i.e. topography, coastline and surface properties) allows for fine scale dynamical processes that can only be resolved at the higher resolution of a RCM (*Rummukainen*, 2016). Notably, an enhanced resolution is beneficial for the simulation of synoptic and mesoscale systems or extremes (*Laprise*, 2008; *Rummukainen*, 2010, 2016).

Several studies have been conducted to investigate the performance of RCMs with respect to its driving GCM, endorsing regional climate modelling as a useful tool to add value to GCM results (e.g. *Laprise et al.*, 2008; *Di Luca et al.*, 2012, 2013; *Jacob et al.*, 2014; *Kotlarski et al.*, 2015; *Torma et al.*, 2015; *Giorgi et al.*, 2016; *Rummukainen*, 2016). More precisely, improved simulation of temperature, precipitation, wind and extremes has been reported (*Rummukainen*, 2016; *IPCC*, 2013, ch. 9 and references therein). Nonetheless, a RCM is not an ultimate solution to the limitations a GCM is exposed to when simulating climate characteristics on a regional to local scale. Even though, RCMs enhance the resolution compared to GCMs, they are limited by

unresolved subgrid-scale processes, which can not be represented explicitly due to limitations in their spatial or temporal resolution, or due to their extensive computational costs (e.g. turbulence or cloud microphysics, *Warner, 2011*). These unresolved processes need to be described through a conceptual model, a parameterisation, providing an approximation. So, RCMs push unresolved processes further towards finer scales but still do not encompass them fully (*Rummukainen, 2010*). Regional climate modelling is a relatively young discipline within climate sciences, being applied since about 25 to 30 years (*Dickinson et al., 1989; Giorgi, 1990*). However, several RCMs have since been developed, their performance assessed and evaluated (e.g. *Laprise et al., 2008; Jacob et al., 2012; Kotlarski et al., 2014*). Nowadays, RCMs are frequently used to simulate past, present and future climate over various regions of the world (*Giorgi et al., 2009*), while finding application within fundamental research as well as for impact, vulnerability and adaptation research (e.g. *Jacob et al., 2014; IPCC, 2013, 2014*). More recently, the field of climate services, which focuses on developing and providing science-based user- and sector-specific tailored climate information, makes use of and relies on RCM simulation data (e.g. *European Commission, 2015; Hewitt et al., 2012*).

Future climate change projections are assessed with RCMs downscaling GCM results under certain representative concentration pathways describing future atmospheric greenhouse gas and aerosol emissions as defined for example by *Moss et al. (2010)*. In addition, historical climate simulations under pre-industrial greenhouse gas conditions are performed to deduce climate change signals. Besides projections aiming at investigating future climate development, regional climate modelling is applied to simulate present-day climate. For this purpose, retrospective analyses data - an observation-based best-estimate of the state of the atmosphere in space and time - are used for downscaling. Present-day climate simulations are used to assess the model performance (*Kotlarski et al., 2014*) as well as to conduct high resolved hindcast simulations serving as reference and for impact modelling purposes (*Warner, 2011; Lucas-Picher et al., 2013*).

Recent Developments in Regional Climate Modelling

With progressing computer performance, opportunities for computationally more intensive climate model setups evolved over time. Next generation GCMs participating in the Coupled Model Intercomparison Project Phase 6 (CMIP6) will reach horizontal resolutions of approximately 50 km in the atmosphere (*Haarsma et al., 2016*), thus, approaching the mesoscale. This trend is happening similarly with respect to RCMs. Currently, RCMs reaching convection-permitting scales of just a few kilometres are developed (*Prein et al., 2015, Section 3.3*). This depicts not just

a progress towards the microscale by the next generation of RCMs but furthermore demonstrates opportunities for local-scale climate information in the near future (*Rummukainen, 2016*). This is not just of interest for fundamental science but as well for the broad field of climate impact, vulnerability and adaptation research as well as for climate services.

Besides the structural development of climate models also the ability to generate and efficiently manage and analyse larger amounts of quantitative climate simulation data has increased with progressing computer performance and storage capacity. This allows for more advanced and profound exploration of uncertainties (*Rummukainen, 2016*). Even though information of future climate from climate model simulations will remain uncertain, uncertainties with respect to the model, scenario assumptions and internal variability can be assessed by considering an ensemble of simulations comprising multiple scenarios (*Knutti et al., 2010*). To tackle this in an organised manner, coordinated international projects ensuring standardised and comparable model configurations are initiated. Similar to model intercomparison projects designed for the global scale (i.e. CMIPs, *Taylor et al., 2012; Haarsma et al., 2016*), coordinated modelling efforts for the regional scale have been performed within the last decade. With a regional focus on Europe, the projects PRUDENCE (*Christensen et al., 2002*) and ENSEMBLES (*Hewitt and Griggs, 2004*), or the ongoing WCRP COordinated Regional Climate Downscaling Experiment (CORDEX, *Giorgi et al., 2009*) with its European branch EURO-CORDEX (*Jacob et al., 2014*) contribute to produce multi-model RCM ensembles allowing the assessment of uncertainties.

Several research has been performed analysing future wind conditions under a changing climate considering a RCM ensemble approach. Besides approaches comprising experiment setups of single RCM ensembles (*Barstad et al., 2012; Pryor et al., 2012; Reyers et al., 2014, 2016*), multi-model multi-scenario RCM ensembles are analysed in the recent future (*Hueging et al., 2013; Tobin et al., 2015, 2016; Moemken et al., 2018*).

3.3 The Regional Climate Models REMO and REMO-NH

The regional climate model REMO (REgional MOdell) is a three-dimensional hydrostatic regional atmospheric circulation model (*Jacob and Podzun, 1997; Jacob, 2001*). It was developed based on the former numerical weather prediction model operated by the German Weather Service (DWD), the EUROPA-MODELL (*Majewski, 1991*), using its physical-dynamical core while, complementary, the physical parameterisation scheme of the general circulation model ECHAM4 (*Roeckner et al., 1996*) of the Max-Planck-Institute for Meteorology was adopted. REMO was

continuously developed analogues to ECHAM's model development and, in addition, several modifications were made (*Jacob et al.*, 2001, 2007; *Semmler*, 2002; *Pfeifer*, 2006; *Kotlarski*, 2007; *Rechid*, 2009; *Teichmann*, 2009).

REMO, as a regional model, is getting forced by lateral and lower boundary conditions. The prognostic variables used as driving information at the lateral boundary are surface pressure, horizontal wind components, temperature, specific humidity and cloud water content. According to the formulation of *Davies* (1976), they get harmonised to the model following a relaxation scheme where the large scale information prescribed at the lateral boundaries of the model domain decays exponentially over eight grid boxes towards the center of the domain (*Jacob and Podzun*, 1997). In addition to the lateral boundary conditions, surface characteristics are prescribed determining the atmospheric lower boundary conditions. Over sea, the sea surface temperature (SST) and sea ice distribution are prescribed. Over land, the surface roughness length, surface albedo, vegetation ratio and leaf area index are prescribed as well as surface temperature and moisture. REMO has its own soil scheme computing the surface temperature and moisture from initial conditions throughout the simulation without any additional external forcing. The surface albedo, vegetation ratio and leaf area index are prescribed on an annual cycle (*Rechid and Jacob*, 2006; *Rechid*, 2009). The roughness length over land is kept constant with time. In addition, REMO uses a fractional surface cover for the representation of subgrid-scale processes of land, water as well as sea ice and inland ice (*Semmler*, 2002; *Kotlarski*, 2007). The top boundary does not receive any prognostic variables.

The prognostic variables are calculated for every model timestep. This is realised by a leap-frog scheme with semi-implicit correction and Asselin-filter (*Asselin*, 1972). REMO uses a rotated spherical (latitude-longitude) coordinate system such that the equator passes through the middle of the defined model domain. This is due to reasons of numerical optimisation. The horizontal is discretised using an Arakawa-C grid (see Fig. 3.1). Here, the scalar variables (φ in Fig. 3.1) are located at the box centres, while the horizontal wind components (u and v in Fig. 3.1 representing the zonal and meridional wind component, respectively) are located at the box edges. The vertical direction is discretised using a hybrid σ -coordinate system (see Fig. 3.2). Here, the lowest levels close to the surface follow the model topography, while this effect diminishes with height, resulting in pure pressure levels (isobars) at the topmost level extending up to 25 hPa. The scalar variables (φ in Fig. 3.2) are located at the center of the layers (at full-levels), while the vertical velocities (ω in Fig. 3.2) are located at the layer boundaries (at half-levels) (*Teichmann*, 2009).

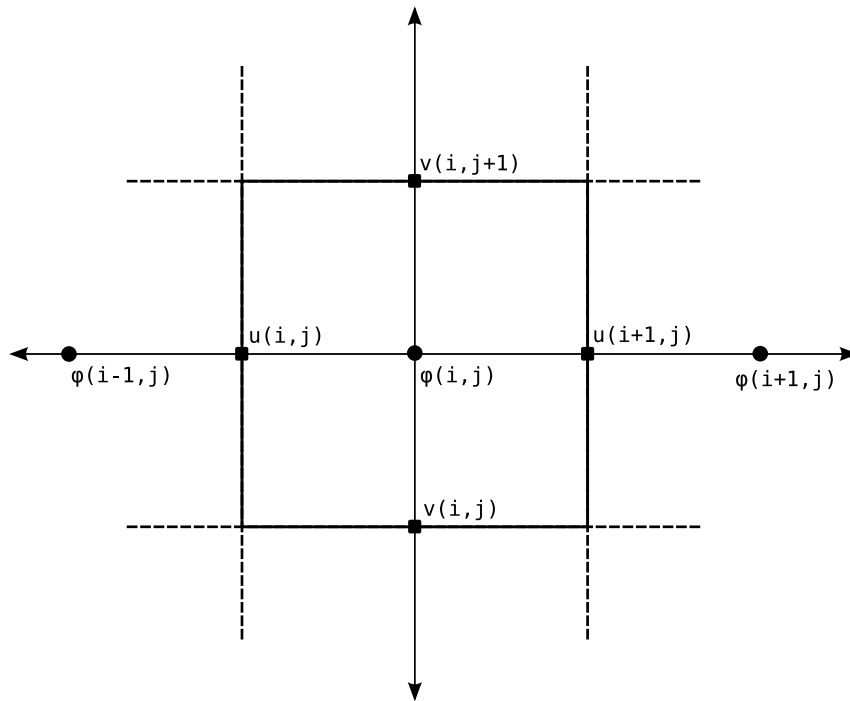


Figure 3.1: Schematic of an Arakawa-C grid. A schematic of the horizontal discretisation on an Arakawa-C grid is shown (taken from *Teichmann, 2009*). Scalar values (φ) are defined in the center of the grid boxes. The wind-vector components (u, v) are located at the edge of the grid box.

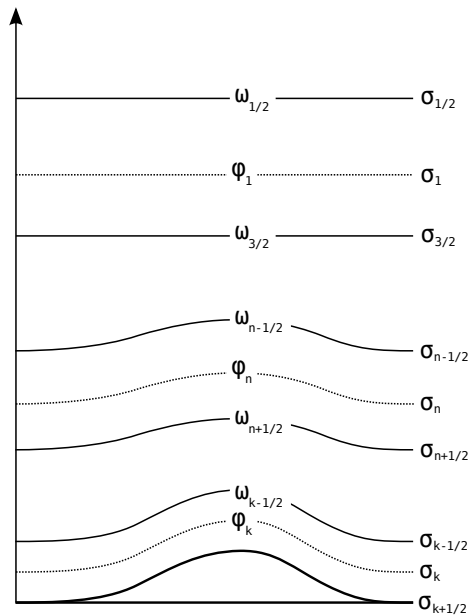


Figure 3.2: Schematic of a σ -coordinate system. A schematic of the vertical discretisation in a hybrid coordinate system is shown (taken from *Teichmann, 2009*). Scalar values (φ) are defined in the center of the layers (at full-levels; dotted line). The vertical velocities (ω) are located at the border of the layer (at half-levels; solid line).

Vertical Diffusion in REMO

Because of the relevance of the turbulent PBL for wind energy (see Section 3.1), the vertical diffusion scheme used by REMO representing turbulent exchange of energy at the surface and vertical turbulent transfer of energy across the PBL and the remaining atmosphere is briefly described in the following. The turbulent exchange of energy in terms of momentum, heat, moisture and cloud water is realised through a higher order closure scheme (*Roeckner et al.*, 1996). This parameterisation is expressing energy fluxes through turbulent transfer coefficients derived solely from surface conditions and atmospheric values. These transfer coefficients are then used by the prognostic equations. The depth of the PBL is defined using a combination of convective and dynamic criteria. Above this turbulent layer, the vertical diffusion scheme is only operating under statically unstable atmospheric conditions.

The turbulent exchange of energy at the surface is realised following Monin-Obukhov similarity theory (e.g. *Stull*, 1988), assuming constant fluxes in the lowest model level according to the concept of the surface layer (see Section 3.1). Here, turbulent transfer coefficients for momentum and heat are solved through universal functions approximated following an analytic expression (*Louis*, 1979). Applying Dyer-Businger relations (e.g. *Stull*, 1988) as modified by *Louis* (1979), these transfer coefficients are based on individual empirical functions differentiating between near neutral, stable and unstable atmospheric cases.

Above the lower boundary, the similarity theory for surface fluxes is extended by a mixing length approach. Atmospheric fluxes are solved using the concept of eddy diffusivity and expressed in eddy diffusion coefficients solved as functions of the turbulent kinetic energy (*Blackadar*, 1962; *Brinkop* and *Roeckner*, 1995). In the atmosphere, moisture and cloud effects on stability are considered by reformulating the Richardson number to include cloud processes on the buoyancy term expressed in a moist Richardson number (*Brinkop* and *Roeckner*, 1995).

While the eddy diffusion coefficients depend on wind shear, Richardson number and mixing length, the turbulent transfer coefficients for momentum and heat depend on Richardson number and roughness length. The roughness length is prescribed and constant over land, while it is solved iterative over sea according to Charnock's relation (*Charnock*, 1955; *Stull*, 1988). The whole turbulence scheme as well as the formulation of the prognostic equations incorporating the turbulent transfer coefficients is described in detail by *Roeckner et al.* (1992, 1996).

Non-hydrostatic REMO

Initially, REMO is a hydrostatic model. An important assumption of hydrostatic models is the hydrostatic approximation. This simplifies the vertical equation of motion by assuming absolute vertical acceleration in the atmosphere to be negligible (as compared to horizontal acceleration). However, this physical assumption limits hydrostatic models to horizontal resolutions finer than 10 km where the hydrostatic approximation is no longer valid (*Prein et al.*, 2015). To enable kilometre scale climate simulations, the hydrostatic model version of REMO has been complemented by a non-hydrostatic extension. This latest development of the REMO model is referred to as REMO-NH if used in the non-hydrostatic model setup.

The non-hydrostatic extension was implemented by *Göttel* (2009) based on an idea of *Laprise* (1992) and following an alternative approach by *Janjic et al.* (2001) for hydrostatic numerical weather prediction models using a mass-based vertical σ -coordinate system. This approach comprises a modular extension of the hydrostatic formulation by higher-order corrections for vertical acceleration through the non-hydrostatic equations of motion (*Göttel*, 2009; *Janjic et al.*, 2001). The main advantage of this modular approach is the option to switch between the hydrostatic and non-hydrostatic formulations, thus, simulating climate optionally either in a hydrostatic or non-hydrostatic regime while retaining the existing model infrastructure. Especially keeping the terrain-following pressure-based vertical hybrid σ -coordinate system REMO is structurally based on is particularly advantageous. With this development, REMO-NH allows for simulations at convective-permitting resolutions with explicit convection.

Climate simulation setups on a kilometre scale require suitable large scale information used as boundary conditions. As a rule of thumb, the spatial resolution of such driving data should not exceed the RCM's resolution by a factor of ten to avoid numerical problems (*Warner*, 2011). A direct dynamical downscaling of GCM or reanalyses data might, therefore, be inappropriate. However, a downscaling strategy comprising a double-nesting approach could be considered as a solution to this problem, where a step-wise downscaling is performed (e.g. *Warner*, 2011; *Prein et al.*, 2015).

REMO is - as all RCMs and GCMs - solving Reynolds-averaged Navier-Stokes equations, in which all turbulent kinetic energy and turbulent fluxes remain unresolved. The same applies to REMO-NH, thus, turbulence needs to be parameterised to incorporate their influence on variables at the mean grid-scale. For simulations in a non-hydrostatic regime, this is treated the same way as for simulations in a hydrostatic regime, by solving the vertical diffusion scheme as described above. With convection-permitting RCMs, scales are about to be reached where energy is produced by

the largest turbulent motions (*Prein et al.*, 2015). Even though parameterisations of turbulent fluxes are intentionally not designed for these scales, most of these models still rely on traditional parameterisation approaches designed for the mesoscale, because of historical and practical reasons (*Prein et al.*, 2015). *Prein et al.* (2015) discussed the importance of the parameterisation of turbulent fluxes and their challenges with respect to convection-permitting RCMs in more detail. However, the design of turbulence schemes for the kilometre scale of convection-permitting RCMs is a relatively new direction and subject to ongoing research. Therefore it is not discussed further in this thesis.

Overall, the regional climate model REMO is a sophisticated and mature tool being widely-used for a variety of applications within climate research and in climate services, such as long-term climate projections, impact assessment and climate adaptation. Among others, *Jacob et al.* (2012) and *Teichmann et al.* (2013) investigated and demonstrated the capability of REMO to simulate climate for various regions of the globe. *Kotlarski et al.* (2014) evaluated the model performance in the setting of a RCM ensemble for European climate. As well, REMO is evaluated with respect to wind climate for European mid-latitudes (*Larsén et al.*, 2010) and it is part of several RCM ensemble simulation studies analysing wind and wind energy in a changing climate (e.g. *Hueging et al.*, 2013; *Tobin et al.*, 2015, 2016).

3.4 Methodology

As concluded in Chapter 2, the wind resource - intimately connected with the wind energy revenue - is determined as the essential component within wind energy financing being exposed to changing climate conditions. Therefore, a novel high-resolution experimental modelling framework with the non-hydrostatic extension of the regional climate model REMO is set up to generate physically consistent climate and climate change information of the wind resource across wind turbine operating altitudes. In this regard, regional climate model simulations are carried out within a surrogate climate change experimental design. For the first time, this set up enables to study thermodynamically induced changes in wind climate, wind characteristics and wind energy conditions in the lower part of the PBL with the regional climate model REMO. In the following, the methodological procedure to perform surrogate climate change experiments with REMO is described. Moreover, the downscaling strategy and simulation setup to generate high-resolution climate information with the non-hydrostatic REMO-NH is presented, in addition to specific adjustments concerning wind climate information in the PBL introduced to the REMO model.

3.4.1 Surrogate Climate Change Experiments

At the moment, long-term climate projections spanning several decades are economically not feasible with convection-permitting RCMs. So far, most published convection-permitting RCM studies do not exceed 10 years of simulation or focus on single years or events (*Prein et al.*, 2015). However, a sophisticated and sound climate change assessment requires at least 30 years of simulation data to distinguish climate change signals from natural climate variability (*WMO*, 2017). Nonetheless, methodologies exist to estimate the impact of climate change on atmospheric processes and quantities in more generalised experimental settings. A technique to do so are surrogate climate change (or pseudo global warming) experiments as initially designed by *Schär et al.* (1996).

The concept of surrogate climate change experiments is to mimic a future climate by artificially adjusting the boundary conditions according to a large-scale climate change temperature signal while retaining relative humidity and circulation. The methodological approach proposed by *Schär et al.* (1996) is simple to implement and physically consistent. Recently, this method got extended by *Kröner et al.* (2017) for vertically variable temperature change signals, thus, taking stratification effects into account. This is beneficial, because under climate change, the upper troposphere is projected to warm at a faster rate than lower levels and the surface (e.g. *Keller et al.*, 2018; *IPCC*, 2013, ch. 12 and references therein), thus, modifying atmospheric and surface energy fluxes. *Kröner et al.* (2017) demonstrate the importance of this physical characteristic for European mid-latitude climate by separating the climate change signal into thermodynamic, stratification (or lapse-rate) and circulation changes, quantifying stratification effects to explain up to one third of the near surface temperature change signal.

Surrogate climate change experiments address thermodynamic effects, while the large-scale circulation imposed through the lateral boundary conditions remains unchanged. Changes in atmospheric circulation as simulated by GCMs are uncertain (*IPCC*, 2013). This is especially true for mid-latitudes because of diverging projections of the future development of storm tracks (*IPCC*, 2013). This is, among others, a dominating factor why robust information with respect to wind and wind extremes and, thus, wind energy are uncertain as well (*Reyers et al.*, 2014, 2016). Even though changes in circulation are worth to investigate and a necessary component for a complete climate change assessment, studying thermodynamic effects separately could procure more certainty in terms of assessing climate change impacts on wind energy. Thus, in the frame of this thesis, the surrogate climate change methodology of *Schär et al.* (1996) and its extension

by *Kröner et al.* (2017) is adopted to perform sensitivity experiments with the regional climate model REMO. In contrast to a height-based vertical coordinate system used in *Kröner et al.* (2017), the methodology is adjusted to conform with REMO's hybrid σ -pressure-based coordinate system. In this regard, better compliance with mass balance is assured (even though rated as negligible; *Kröner et al.*, 2017). The methodological procedure is described in the following.

Surrogate Climate Change Experiments with REMO

In this thesis, climate change signals for atmospheric temperature from the regional climate model REMO are extracted. The REMO simulations were carried out within the EURO-CORDEX framework, receiving their lower and lateral boundary conditions from the global climate model MPI-ESM of the Max Planck Institute for Meteorology following pre-industrial greenhouse gas forcing conditions as well as three different representative concentration pathway scenarios analogous to a radiative forcing of 2.6, 4.5 and 8.5 Wm^{-2} at the end of the 21st century (*Moss et al.*, 2010). The REMO version used for these simulations is REMO2009 (*Jacob et al.*, 2012) while the first realisation of MPI-ESM's climate projections is downscaled (see Tab. A.1). Here, the climate change signals of just a single RCM is regarded because information across the atmosphere in the vertical are required which are not publicly available (e.g. through the Earth System Grid Foundation (ESGF) distributing state-of-the-art CORDEX RCM ensemble simulation data). However, the temperature profiles extracted from the REMO model simulations used are evaluated against those at pressure levels at 850 hPa and 500 hPa of the most recent EURO-CORDEX ensemble at this instant of time (see Tab. A.1, and Figs. 3.3 and 3.4 as well as Figs. A.1 and A.2). At first, a climatological time series of daily mean atmospheric temperature of these simulations is generated for every vertical model level separately, by horizontally averaging across an area covering the German Bight, which matches the simulation domain of interest for the surrogate climate change experiments (see Fig. 3.5 b). The daily time series cover the 30-year periods of 1971 to 2000 for historical climate and 2071 to 2100 for future climate, respectively.

To incorporate variability of the temperature change signals with the seasons, annual cycles are approximated based on these time series. A spectral reconstruction of the climatological annual cycle by a superposition of harmonics is performed on these time series according to *Narapusetty et al.* (2009) and *Bosshard et al.* (2011). The latter authors demonstrate the superior representation of climatological mean values derived from spectral methods compared to moving mean estimates. Expressed in sine and cosine terms, the spectral reconstruction reads:

$$\bar{x}(t_i) = a_0 + \sum_{k=1}^H [a_k \cos(\omega_k t_i) + b_k \sin(\omega_k t_i)] \quad (3.2)$$

where

- \bar{x} : spectrally filtered variable (in this case temperature)
- t_i : time t_i (with $i = [1, 2, \dots, N]$ and length N of time series)
- k : order of harmonics
- H : truncation parameter
- a_k, b_k : regression coefficients
- ω_k : $\frac{2\pi k}{P_0}$ with base period P_0

Here, the regression coefficients a_k and b_k are least square estimates derived through the discrete Fourier transform (e.g. *von Storch and Zwiers, 1999; Narapusetty et al., 2009*) from the daily time series. This is a standard regression problem with the following solution:

$$z = (A^T A)^{-1} A^T \bar{x} \quad (3.3)$$

with A being the $N \times (2H + 1)$ matrix of sinusoidal values, and z being the $(2H + 1)$ -dimensional vector of amplitudes containing the regression coefficients a_k and b_k :

$$A = \begin{pmatrix} 1 & \cos(\omega_1 t_1) & \cdots & \cos(\omega_H t_1) & \sin(\omega_1 t_1) & \cdots & \sin(\omega_H t_1) \\ 1 & \cos(\omega_1 t_2) & \cdots & \cos(\omega_H t_2) & \sin(\omega_1 t_2) & \cdots & \sin(\omega_H t_2) \\ \vdots & \vdots & \ddots & \vdots & \vdots & \ddots & \vdots \\ 1 & \cos(\omega_1 t_N) & \cdots & \cos(\omega_H t_N) & \sin(\omega_1 t_N) & \cdots & \sin(\omega_H t_N) \end{pmatrix} \quad z = \begin{pmatrix} a_0 \\ a_1 \\ \vdots \\ a_H \\ b_1 \\ \vdots \\ b_H \end{pmatrix}$$

The fact, that the area of the German Bight, where the temperature is extracted from and horizontally averaged over, is considerably smaller than the global or continental scale considered by *Narapusetty et al. (2009)*, results in higher natural variability. This is the reason, why higher orders of harmonics as considered by *Narapusetty et al. (2009)* are utilised to prevent overfitting. Therefore, consistent with *Bosshard et al. (2011)*, a value of 3 is chosen for the truncation parameter H as a trade-off between sufficient detail and overfitting. As REMO is

using a Gregorian calendar, a base period P_0 of 365.25 days is used to account for leap years (Narapusetty *et al.*, 2009). Subsequently, the derived filtered and smoothed reconstruction of the annual cycle is scaled to match a standard year of 365 days. Thereafter, an annual temperature cycle is generated for every simulation and each individual model level. From these annual cycles, the climate change signal of temperature is computed by subtracting annual cycles based on historical time series data from annual cycles based on climate projection time series data. This is done for each climate scenario and each model level individually.

Finally, these climate change signals get transposed to an annual time series of vertical atmospheric temperature change profiles. This step is essential, because the time series data are extracted from REMO simulations performed on 27 vertical model levels while the surrogate climate change experiments are realised with REMO-NH on 49 vertical levels (see Section 3.4.2). Thus, higher resolved information across the interfaces of the given model levels is needed. To achieve this, the atmospheric pressure at the full model levels (where temperature as a scalar variable is defined) for the simulation setups of 27 and 49 vertical levels is computed, assuming atmospheric standard pressure of 1013.25 hPa at the surface (see Eq. 3.5 derived from the relation in Eq. 3.4) and using AK and BK values according to Tabs. A.2 and A.3. Now, the climate change signals for every model level are paired with their prevailing atmospheric pressure and their vertical profiles are constructed using spline-fitting for interpolation (see Fig. 3.3). From these vertical atmospheric temperature change profiles, the temperature values for the model levels for the simulation setup of 49 vertical levels are determined by use of their individual atmospheric pressures. Because the lower and upper bound of the atmosphere is distinctly and equally defined for both vertical coordinate systems, interpolation to additional model levels is sufficiently accurate.

$$p_{k-\frac{1}{2}} = AK_{k-\frac{1}{2}} + BK_{k-\frac{1}{2}} p_s \quad (3.4)$$

$$p_k = \frac{1}{2} \left(AK_{k-\frac{1}{2}} + AK_{k+\frac{1}{2}} + \left(BK_{k-\frac{1}{2}} + BK_{k+\frac{1}{2}} \right) (p_s - AK_1) \right) \quad (3.5)$$

where

- $p_{k-\frac{1}{2}}$: pressure at half model level $k - \frac{1}{2}$
- p_k : pressure at full model level k
- p_s : pressure at surface
- AK : AK vertical coordinate
- BK : BK vertical coordinate

Vertical Temperature Change Signals

The resulting vertically variable temperature change signals based on long-term climate change projections following the representative concentration pathways (RCPs) 2.6, 4.5 and 8.5 are shown in Fig. 3.3. Due to the inherent smoothed annual cycle of daily resolution, resulting in slightly diverging change signals for each single day of the year, just snapshot profiles for every 15th day of a month are highlighted. All profiles show a warming of the troposphere and pronounced stratospheric cooling during almost all month of the year. Throughout the troposphere, the warming rate increases with height up to the tropopause, while steepest gradients occur during summer. This is in agreement to previous research (e.g. *Keller et al.*, 2018; *IPCC*, 2013, ch. 12 and references therein). Depending on the season of the year, a distinct gradient in the vicinity of the surface up to about 975 to 950 hPa can be observed. While this characteristic is pronounced in spring, the warming signal is more homogeneous with height during winter.

The shape of the profiles varies with the degree of greenhouse gas forcing. Whereas small and rather homogeneous changes can be observed for the RCP2.6 scenario, the gradual warming within the troposphere as well as stratospheric cooling is more pronounced for RCP4.5 and distinguishable strongest for the highest emission scenario RCP8.5. Throughout the year, near surface temperature change signals vary between about 0.2 and 1.2 K (RCP2.6), 1.0 and 1.6 K (RCP4.5) and 1.4 and 3.0 K (RCP8.5), respectively. In the upper troposphere, these can reach 6.0 K for the highest emission scenario RCP8.5. Within the PBL, gradients in the temperature change signals can extend to more than 1.5 K.

Because just a single RCM could be used to extract climate change information across the atmosphere and to reconstruct vertical temperature change profiles, the profiles are evaluated against temperature change signals at pressure levels of 850 hPa and 500 hPa of the most recent EURO-CORDEX ensemble at this instant of time (see Fig. 3.4). Overall, the REMO simulations lie in the lower part of the full ensemble range and mostly below the ensemble median. This is especially striking for spring and autumn, while REMO is situated within the interquartile range for most of the remaining months. However, the bandwidth of the ensemble of up to about 4.5 K (during summer), indicates large spread among the ensemble members in this region. This uncertainty needs to be regarded in the context of diverging projections of future development of atmospheric circulation regimes in the mid-latitudes among climate models (*IPCC*, 2013). Even though the REMO simulations are situated in the lower part of the full ensemble range, it needs to be highlighted that these simulations represent equally likely evolutions of future climate.

Compared to a climate change signal based on the entire EURO-CORDEX simulation domain,

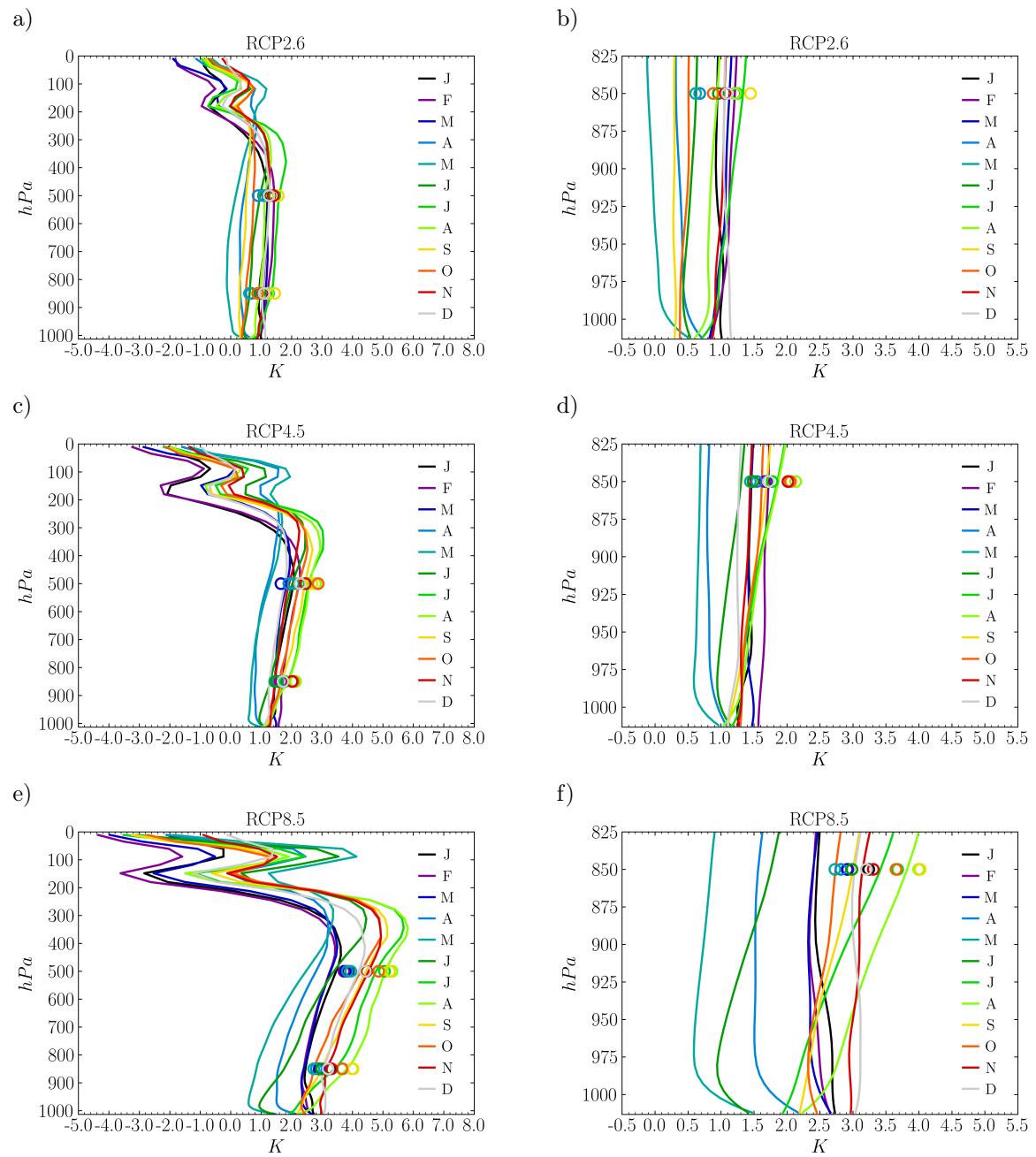


Figure 3.3: Vertical temperature change signals to be used for surrogate climate change experiments. Shown are signals following the emission scenarios RCP2.6 (a-b), RCP4.5 (c-d) and RCP8.5 (e-f) for the entire (a, c, e) and lower atmosphere (b, d, f; up to 825 hPa) as simulated by REMO. The signals are achieved by spatially averaging and spectrally filtering 30-year periods of daily temperature values over the geographical area of the REMO-NH simulation domain (i.e. the German Bight; see Fig. 3.5) to gain smoothed annual temperature cycles for every model level separately. Change signals for the end of the 21st century are computed from these annual cycles and reconstructed to daily-resolved vertical temperature change profiles over a year (only the mid-month days for each month are shown due to visibility reasons). The vertical profiles range from 1013.25 hPa until 25 hPa where REMO's atmospheric top is capped. Circles depict median temperature change values of the EURO-CORDEX ensemble (see Tab. A.1) at 850 hPa and 500 hPa, while the color code matches the monthly scaling.

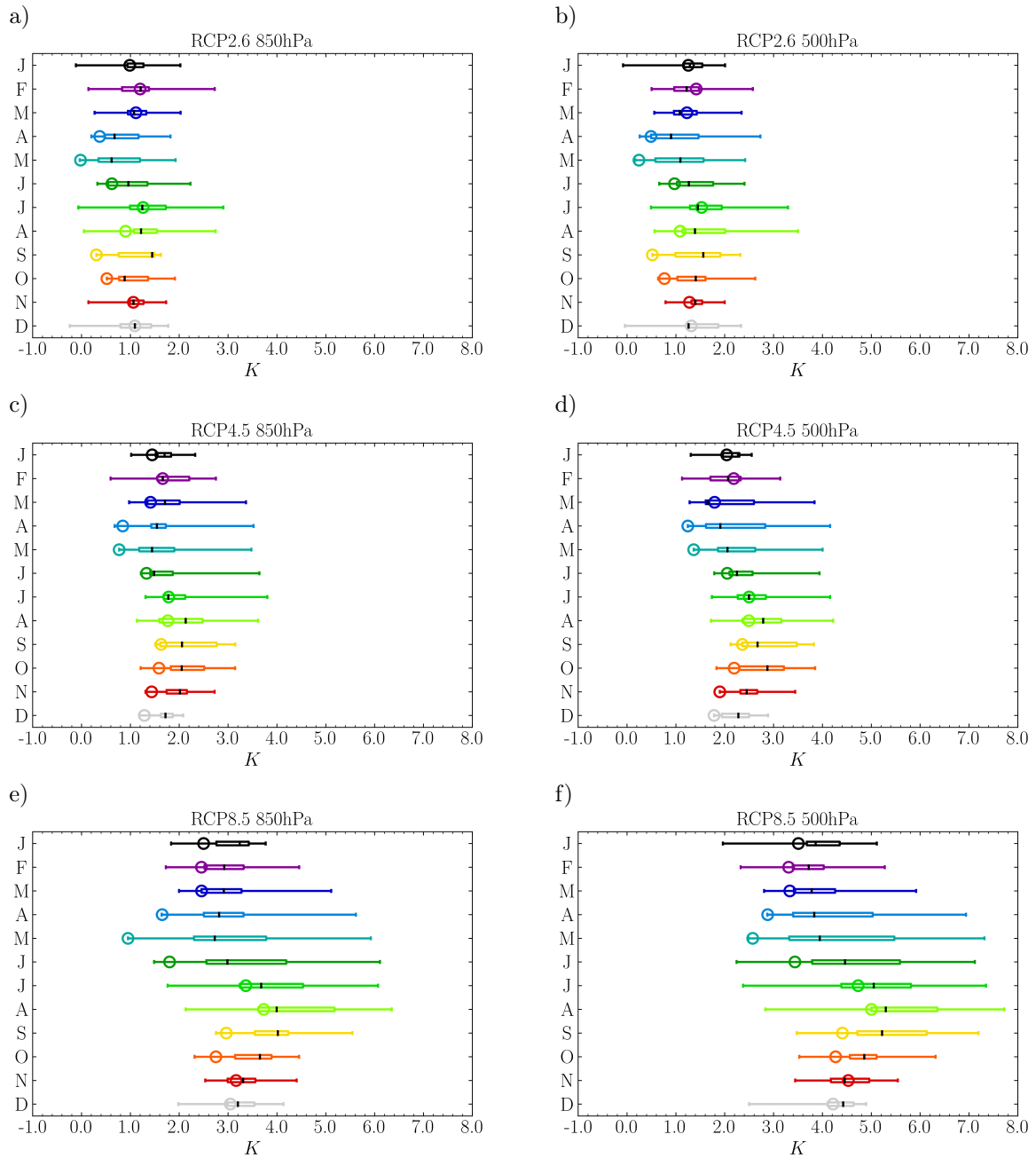


Figure 3.4: Bandwidth of EURO-CORDEX ensemble temperature change signals. Shown are signals at 850 hPa (a, c, e) and 500 hPa (b, d, f) following the emission scenarios RCP2.6 (a-b), RCP4.5 (c-d) and RCP8.5 (e-f) for the end of the 21st century. The methodological procedure is as described in Section 3.4.1 and Fig. 3.3 but applied to the EURO-CORDEX ensemble (see Tab. A.1). Monthly-resolved box and whisker plots indicate the ensemble median (black bars), interquartile range (boxes; i.e. range between 25th and 75th percentile) as well as minimum and maximum values (whisker edges; i.e. full ensemble range). Circles depict the REMO model simulation from which the climate change signals are extracted and used for the surrogate climate change experiments (according to Fig. 3.3).

which is used by *Kröner et al.* (2017) and investigated as well in the frame of this thesis (see Fig. A.1), the signals for the selected region of the German Bight tend to be more variable in space and in time. This originates from the averaging over a significantly smaller geographical area. Thus, when averaging over the entire EURO-CORDEX simulation domain, the vertical temperature profiles are much smoother and distinct over the course of the year. Furthermore, when comparing these temperature signals against pressure at levels of 850 hPa and 500 hPa of the EURO-CORDEX ensemble, the spread among the ensemble members is less pronounced and more homogeneous throughout the year. However, comparing both resulting vertical temperature change profiles indicates that the general behaviour is comparable. The magnitude of change is smaller for the region of the German Bight, while tropospheric gradients are more variable and pronounced with season. This reflects a more regional climate associated to the mid-latitudes of the German Bight, which is why the temperature change signals shown in Fig. 3.3 are chosen for surrogate climate change experiments (see Section 3.4.2) instead of a European-scale representation of the climate change signal.

Perturbation of Boundary Conditions

The temperature change signal of each individual RCP scenario is added to the initial as well as lower and lateral boundary conditions which, subsequently, serve as perturbed boundary conditions for surrogate climate change experiments. While the signal is added to the temperature fields on all model levels in the atmosphere, sea surface and surface skin temperatures as well as soil temperature fields are adjusted using the values of the lowest model level (*Kröner et al.*, 2017, see Eq. 3.7). In addition, the specific humidity is adjusted such that the relative humidity is kept constant. This is performed according to the Clausius-Clapeyron relation describing the temperature dependency of equilibrium vapour pressure at saturation (e.g. *Etling*, 2008). The saturation vapour pressure is computed through the empirical approximation of Eq. 3.6 after *Bolton* (1980). Calculating this for both, the absolute temperatures based on the historical simulation data and the absolute historical temperatures plus the temperature change signal, reveals the ratio at which the specific humidity is adjusted (see Eq. 3.8). Furthermore, the geopotential height needs to be adjusted due to the modification of the temperature and specific humidity fields. This is achieved by integrating the hydrostatic balance from the top of atmosphere down to the surface (see Eq. 3.9). The adjustment of the geopotential height ensures dynamic consistency with the temperature fields (*Schär et al.*, 1996). Because this is a feature already embedded in REMO's preprocessor routine, it is solved along with the preprocessing of the

boundary data. Thus, the boundary information get adjusted before preprocessing them for the simulation setup. A list of the REMO variables which need to get adjusted to perform surrogate climate change experiments can be found in Tab. A.4. For completeness, it needs to be mentioned that for leap years the signals of the previous day is added to the leap day.

$$e_s(T) = 611.2 \exp\left(\frac{17.67T}{T + 243.5}\right) \quad (3.6)$$

where

e_s : saturation vapour pressure [Pa]

T : air temperature [C°]

$$T_{p_k} = T_k + \Delta T_k \quad (3.7)$$

$$q_{p_k} = q_k \left(\frac{e_{s_k}(T_{p_k})}{e_{s_k}(T_k)} \right) \quad (3.8)$$

where

T_{p_k} : perturbed air temperature at model level k

T_k : air temperature at model level k

ΔT_k : air temperature change signal at model level k

q_{p_k} : perturbed specific humidity at model level k

q_k : specific humidity at model level k

e_{s_k} : saturation vapour pressure at model level k (see Eq. 3.6)

$$\Phi_{k+\frac{1}{2}}(p_{k+\frac{1}{2}}) = \int_{p_{k+\frac{1}{2}}}^{p_{k-\frac{1}{2}}} \frac{RT_{p_{k+\frac{1}{2}}}}{p_{k+\frac{1}{2}}} dp_{k+\frac{1}{2}} \quad (3.9)$$

where

$\Phi_{k+\frac{1}{2}}$: geopotential height at model level $k + \frac{1}{2}$

$p_{k+\frac{1}{2}}$: atmospheric pressure at model level $k + \frac{1}{2}$

$T_{p_{k+\frac{1}{2}}}$: perturbed air temperature at model level $k + \frac{1}{2}$

R : gas constant for dry air

3.4.2 Simulation Setup

An experiment design comprising high-resolution surrogate climate change experiments with the non-hydrostatic regional climate model REMO-NH is set up. The purpose is to generate

physically consistent and highly-resolved estimates of climate change, addressing wind conditions in the PBL through sensitivity experiments. The German Bight will serve as a case study region. These information are subsequently used to assess the impact of changing wind conditions, related to climate change signals of different intensity, on wind energy financing. This is illustrated and investigated in Chapter 4.

Experiment Design & Downscaling Strategy

A downscaling strategy is established to assure an appropriate and methodological sound simulation setup. The ERA-Interim reanalysis (*Dee et al.*, 2011), as a representation of current climate, is downscaled serving as a reference climate simulation. The surrogate climate change methodology as described in Section 3.4.1 is applied using the same ERA-Interim boundary conditions in combination with different gradual temperature change profiles, based on different climate change scenarios, to achieve information about changing climate.

The surrogate climate change experiments are solely performed for non-hydrostatic regional climate model simulations with REMO-NH. For the region of interest, the German Bight, a simulation domain is set up with a horizontal resolution of 0.022° (corresponding to approximately 2.5 km) containing 151×151 grid boxes (see Fig. 3.5 b). Adjacent coastal areas and topographic features are taken into account according to best-practice guidelines (*Warner*, 2011). The size of the domain is carefully chosen and in line with recommendations based on sensitivity experiments with convection-permitting RCMs, thus, preventing degradation of large-scale features and large-scale variability as well as stronger deviations of the RCM from its lateral boundary conditions (*Prein et al.*, 2015, and references therein).

The ERA-Interim reanalysis is provided on a spectral horizontal resolution of approximately 0.7° (corresponds to approximately 80 km). An immediate downscaling of ERA-Interim to the target domain could evoke numerical biases (*Warner et al.*, 1997), because of the difference in resolution, exceeding postulated admissible grid ratios of approximately 1 to 12 (*Antic et al.*, 2006; *Denis et al.*, 2003). To compensate for this, a nesting approach (e.g. *Warner*, 2011) is applied: a simulation of coarser resolution is performed in a first attempt which subsequently serves as boundary condition to the higher resolution simulation. The intermediate simulation is achieved by downscaling the ERA-Interim reanalysis to a horizontal resolution of 0.11° (corresponding to approximately 12 km). Simulating a hydrostatic regime is sufficient at this resolution, which is why those simulations are performed with the standard hydrostatic REMO setup. For convenience and to achieve comparability to state-of-the-art regional climate information provided by RCMs,

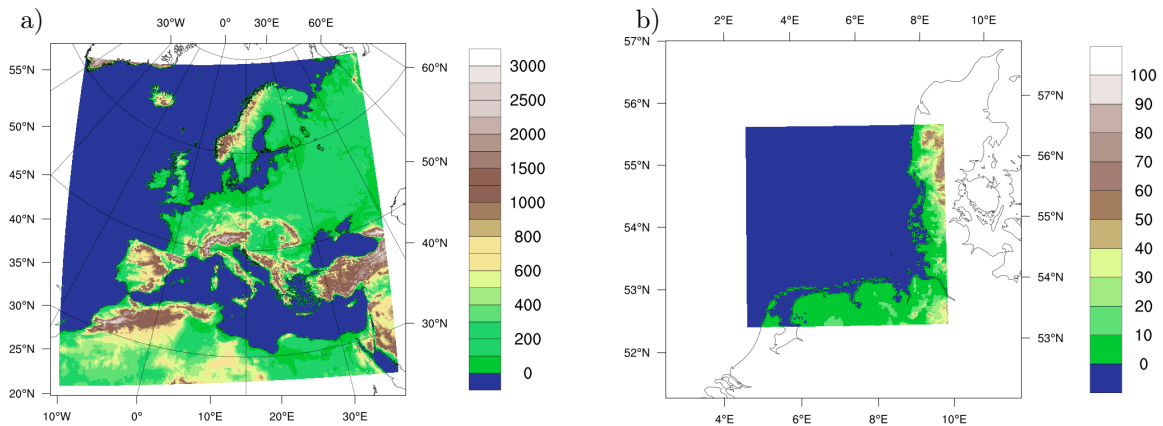


Figure 3.5: Simulation domains for REMO27, REMO49 and REMO-NH. REMO27 and REMO49 simulations cover the entire European continent following the EURO-CORDEX domain at 0.11° horizontal resolution (a) and REMO-NH simulations cover the German Bight at 0.022° horizontal resolution (b). Shown is the model orography in *m*. Compared to the state-of-the-art EURO-CORDEX simulation setup, the high-resolution setup of REMO-NH is capable to resolve coastlines and islands at a finer resolution.

the existing REMO EURO-CORDEX simulation setup is used (e.g. *CORDEX*, 2015; *Jacob et al.*, 2014) covering the entire European continent on a domain of 433×433 grid boxes (see Fig. 3.5 a). Both simulation domains use a rotated spherical grid with the same rotation grade of the pole, which is, through the middle of Europe.

The intermediate hydrostatic REMO simulation is forced with updated lateral and lower boundary conditions of ERA-Interim every 6 hours (cf. Section 3.3). To prevent drift of the inertial soil, a so-called warm start is performed where initial soil variables are replaced with steady state soil conditions spun up over 10 years of pre-simulation. The lateral and lower boundary boundary conditions for nested non-hydrostatic regional climate model simulations with REMO-NH are subsequently provided by the intermediate hydrostatic REMO simulation. Here, the driving boundary information gets passed over every hour, because of the superior performance as compared to 6 hourly update intervals. This is indicated by less deviation of the simulated large-scale pattern from the driving large-scale information expressed in mean sea level pressure (MSLP) differences (see Fig. 3.6). Previous theoretical elaborations as well as sensitivity experiments support this choice of configuration (*Warner et al.*, 1997; *Termonia et al.*, 2009; *Davies*, 2014). The non-hydrostatic REMO simulations get initialised with the first simulation output interval from the intermediate hydrostatic REMO simulation. As the intermediate simulation downscaled

ERA-Interim reanalysis data, large-scale dynamics of retrospective weather patterns are simulated in a high-resolution simulation setup with REMO-NH. These simulations serve as reference to surrogate climate change experiments, which are driven with the same boundary conditions provided by the intermediate simulation but with an added temperature climate change signal as described in Section 3.4.1. In this regard, three signals of different radiative forcing intensities

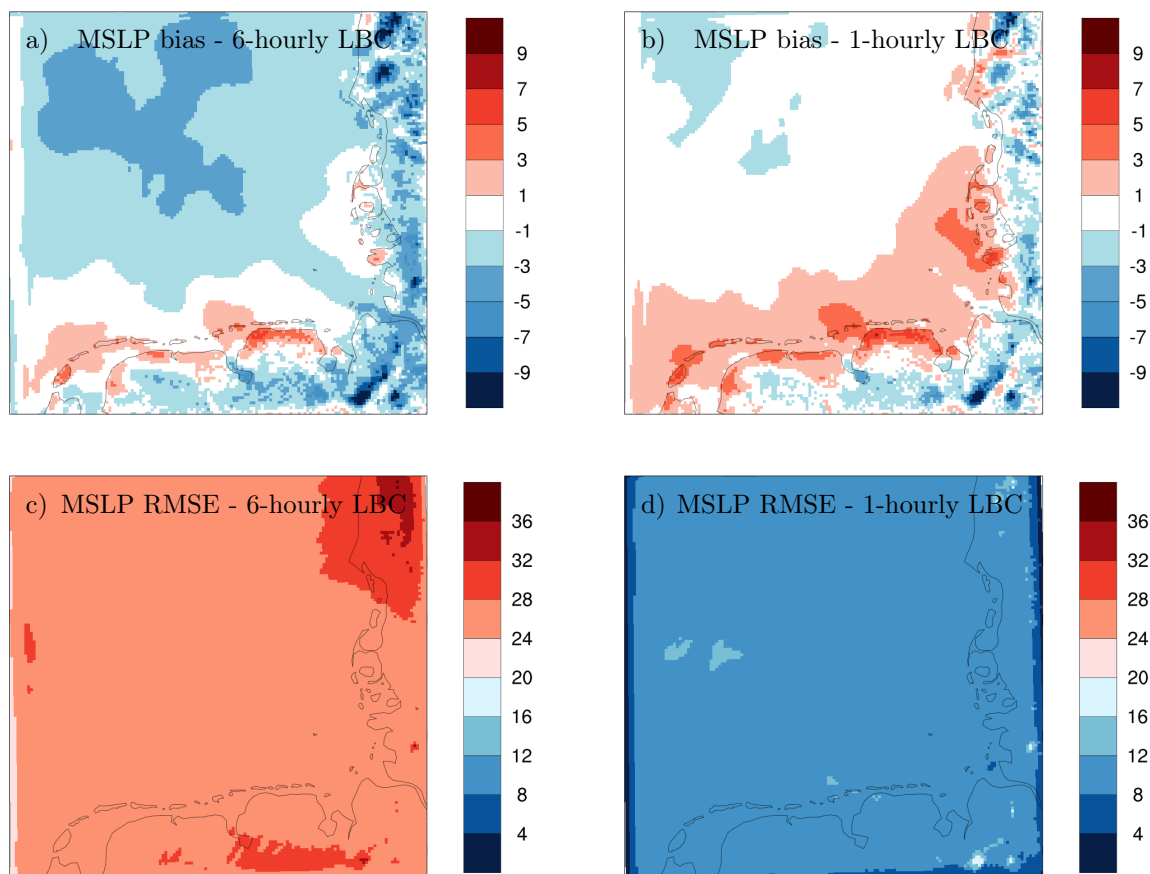


Figure 3.6: Mean sea level pressure (MSLP) sensitivity to lateral boundary condition (LBC) update intervals of 6-hours and 1-hour of the REMO-NH simulation setup. Shown is the bias (a, b) and the root mean square error (RMSE; c, d) for MSLP in hPa of the simulations with respect to hourly-resolved driving data averaged over one month. The REMO-NH simulations are driven by downscaled ERA-Interim reanalysis data according to REMO49 for January 2010. Both simulations are initialised and forced with the same boundary conditions and use the same simulation setup, except for the update interval frequency of the LBC. An increase of the LBC update interval reduces a negative bias in MSLP across large parts of the domain. The spatial and temporal correlation is very high for both setups (> 0.99) but the RMSE is reduced when updating LBCs every hour, thus, indicating less deviation from the large-scale driving fields.

following representative concentration pathway scenarios analogous to a radiative forcing of 2.6, 4.5 and 8.5 Wm^{-2} at the end of the 21st century are used (see Fig. 3.3). In addition, greenhouse gas concentrations of the respective RCP scenario for the end of the 21st century are passed to the model. Thus, the thermodynamic effect of perturbed boundary conditions according to climate change signals as projected for the end of the 21st century can be studied.

The high-resolution non-hydrostatic REMO simulations performed for the German Bight (hereafter referred to as REMO-NH) are performed on a vertical resolution of 49 levels. This depicts REMO's current upper limit due to structural reasons. The desired number of vertical levels prescribe the vertical resolution of the boundary data required by REMO's preprocessor to be equal or greater than the resolution of the target grid. Therefore, the intermediate simulation downscaling ERA-Interim is set up with the same resolution of 49 vertical levels (hereafter referred to as REMO49). Because this increase in vertical model resolution depicts a REMO setup which has not been investigated so far, additional simulations with a well-established REMO configuration used for production runs conducted within the EURO-CORDEX framework are performed for comparison. These REMO simulations comprise a resolution of 27 vertical levels (hereafter referred to as REMO27). Thus, the setup of REMO27 remains the same as REMO49 except for the vertical resolution.

In addition to the overarching objective to generate highly-resolved estimates of climate change (making use of REMO-NH), the three REMO simulation configurations (REMO27, REMO49 and REMO-NH) allow to analyse the impact or value added of spatial (horizontal as well as vertical) resolution on simulated climate from a single-model perspective. Furthermore, this can be related to state-of-the-art climate and climate change information, as REMO27 is configured analogous to the latest regional climate model simulation setup conducted within the EURO-CORDEX framework.

Long-term climate projections spanning several decades are at the moment economically not feasible with convection-permitting RCMs. Therefore, individual years are simulated in the frame of this thesis. Thus, intra-annual variability is covered while computational costs are viable. These simulations cover only the statistics of simulated weather events of a particular year rather than climate. In particular wind is highly variable on time scales ranging from seconds to multiple decades due to its turbulent nature (e.g. *Troen and Lundtang Petersen, 1989*). This variability in the wind resource is reflected in power output by wind turbines and entire farms as well (*Milan et al., 2013*). Therefore, single simulation years are not representative for the respective wind climate and subsequent wind energy production. To address this circumstance, two complete

years with wind energy generation at the more upper and lower range with respect to the previous 10 years of production are deliberately chosen to be simulated. These are the years 2008 and 2010, respectively, according to (IWR, 2018). This is in qualitative agreement with wind energy density amounts computed from near surface wind speed of the ERA-Interim reanalysis data, which serve as forcing (using constant air density of 1.225 kgm^{-3}). A list of the simulations conducted in the frame of this thesis is shown in Tab. A.6.

Adjustments to REMO

The model version used is based on REMO2015 but contains adjustments and additional variable output. With increased vertical levels the lower troposphere is significantly higher resolved (see Tabs. A.2 and A.3). This has implications for the computation of near surface variables which get determined from prognostic values at the surface and of the lowest model level, because the geopotential is variable in space and time due to the nature of the mass-based σ -coordinate system. For the near surface wind speed at 10 m, the geographical height of the second lowest model half-level - the lowest model half-level corresponds to the surface (cf. Fig. 3.2) - can, under certain conditions, fall below this height when the vertical resolution is increased to 49 model levels. Therefore, the computation of the near surface wind speed as implemented in the vertical diffusion scheme is adjusted. Now, when the second lowest model half-level height falls below 10 m, the wind speed value gets determined from the prognostic wind components of the adjacent model levels by linearly interpolating between them. Due to the logarithmic nature of the increase of wind speed with height, a linear interpolation does not represent a perfect description but a sufficient approximation.

Furthermore, additional variable output is introduced in the frame of this thesis, supporting the analysis of wind energy conditions in the lower part of the PBL. A list of those variables is shown in Tab. A.5. To achieve a better impression of the wind conditions at levels where wind turbines actually operate, certain wind variables are computed for the first 300 m above ground at 20 m interval levels. Here, the adjusted computation of the 10 m wind speed as described above is applied to subsequent model half-levels to gain this information on additional height levels. Besides variables which are already inherent to the REMO model but are not considered for the output routine so far, some variables are newly introduced. These are potential temperature (see Eq. 3.10), air density (see Eq. 3.11), Monin-Obukhov length (see Eq. 3.12), turbulent heat flux (see Eq. 3.13) and wind energy density (see Eq. 3.14). Furthermore, the maximum, minimum and standard deviation of wind speed values over the output interval are computed. The wind

direction is not a specific output variable but can get derived directly from the horizontal velocity components according to Eq. 3.15. All additional variables listed in Tab. A.5 are computed interactively and can get stored for every model time step. However, to limit storage capacity, the simulation output is set to 1-hour time intervals.

The potential temperature θ is reformulated within the vertical diffusion scheme and computed for every model level according to Eq. 3.10 (e.g. *Etling*, 2008). Here, a standard reference pressure p_0 of 1000 hPa is used, the gas constant for dry air R is $287.05 \text{ Jkg}^{-1}\text{K}^{-1}$ and the specific heat capacity at constant pressure is $1005.0 \text{ Jkg}^{-1}\text{K}^{-1}$.

$$\theta_k = T_k \left(\frac{p_0}{p_k} \right)^{R/c_p} \quad (3.10)$$

where

- θ_k : potential temperature at model level k
- T_k : temperature at model level k
- p_0 : standard reference pressure of 1000 hPa
- p_k : pressure at model level k
- R : gas constant for dry air
- c_p : specific heat capacity at constant pressure

The computation of the air density ρ (see Eq. 3.11) is implemented as a new routine being derived as the absolute ratio of pressure and geopotential differences between half model levels, while for the lowest model level surface geopotential is used.

$$\begin{aligned} \rho_{k-\frac{1}{2}} &= \left| \frac{p_{k+\frac{1}{2}} - p_{k-\frac{1}{2}}}{\phi_{k+\frac{1}{2}} - \phi_{k-\frac{1}{2}}} \right| \\ &= \left| \frac{AK_{k+\frac{1}{2}} - AK_{k-\frac{1}{2}} + (BK_{k+\frac{1}{2}} - BK_{k-\frac{1}{2}}) (p_s - AK_1)}{\phi_{k+\frac{1}{2}} - \phi_{k-\frac{1}{2}}} \right| \end{aligned} \quad (3.11)$$

where

- $\rho_{k-\frac{1}{2}}$: air density at model level $k - \frac{1}{2}$
- $p_{k-\frac{1}{2}}$: pressure at model level $k - \frac{1}{2}$
- p_s : pressure at surface
- $\phi_{k-\frac{1}{2}}$: geopotential at model level $k - \frac{1}{2}$
- AK : AK vertical coordinate
- BK : BK vertical coordinate

The Monin-Obukhov length L_* (see Eq. 3.12, *Stull*, 1988) is already implemented in REMO as it is used to approximate turbulent kinetic energy. However, since turbulent kinetic energy is just produced when additional energy gets transferred (not dissipated), the Monin-Obukhov length in REMO is defined for positive heat flux values only. Therefore, the computation is adjusted to comprise positive and negative heat flux directions, thus, describing stable as well as unstable atmospheric conditions. A physical interpretation of the Monin-Obukhov length is that the absolute value of this length scale is the atmospheric height at which turbulent kinetic energy production ($L_* < 0$) or loss ($L_* > 0$) is through equal parts by buoyancy forces and dynamic shear production (*Stull*, 1988; *Etling*, 2008; *Foken*, 2008). Furthermore, the Monin-Obukhov length serves as stability indicator. When the ratio of the geometric height z and L_* is negative, unstable atmospheric conditions are characterised, while positive values of z/L_* describe stable atmospheric conditions. Neutral stratification is present for values of z/L_* around zero.

$$L_* = -\frac{\theta u_*^2}{\kappa g \theta_*} \quad (3.12)$$

where

- θ : potential temperature
- u_* : frictional (or shear) velocity
- θ_* : turbulent heat flux
- κ : von Kármán constant
- g : gravitational acceleration

Subsequently, the turbulent heat flux θ_* (see Eq. 3.13) is derived from the previously computed Monin-Obukhov length according to Monin-Obukhov similarity theory (e.g. *Stull*, 1988). According to Monin-Obukhov similarity theory (e.g. *Stull*, 1988), the turbulent heat flux θ_* (see Eq. 3.13) is defined as:

$$\theta_* = \frac{\overline{\omega' \theta'}}{u_*} \quad (3.13)$$

where

- $\overline{\omega' \theta'}$: potential temperature flux (positive upwards)
- u_* : frictional velocity

The energy density of the wind velocity v_p is computed as the power in the wind per unit area (e.g. *Hau*, 2014) and determined within a postprocessing routine according to Eq. 3.14.

$$v_\rho = \frac{P}{A} = \frac{1}{2} \rho v^3 \quad (3.14)$$

where

ρ : density

v : velocity

Likewise, the direction of the wind velocity v_{dir} in polar coordinates (with 0° corresponding to a northward direction) is derived from derotated horizontal wind components within a postprocessing routine according to Eq. 3.15.

$$v_{dir} = \text{atan2}(u, v) \frac{360}{2\pi} + 180 \quad (3.15)$$

where

u : u-velocity component (derotated)

v : v-velocity component (derotated)

3.5 Results and Discussion

A novel high-resolution experimental modelling framework is set up to generate physically consistent climate and climate change information of the wind resource across wind turbine operating altitudes (see Section 3.4). In this regard, regional climate model simulations are carried out within a surrogate climate change experimental design. For the first time, this set up enables to study thermodynamically induced changes in wind climate, wind characteristics and wind energy conditions specifically within the lower part of the PBL with the regional climate model REMO. The experimental design comprises hydrostatic and non-hydrostatic simulations with the regional climate models REMO and REMO-NH on different vertical and horizontal resolutions for the deliberately chosen years of 2008 and 2010 (see Tab. A.6).

The analysis of the individual simulations is supported by horizontal maps, statistics for meridional transects as well as vertical profiles generated from averages over a local area comprising 5×5 grid boxes. To avoid interference imposed by the large-scale driving fields (*Warner, 2011; Prein et al., 2015*), the transect and grid box area are positioned farthest from the domain boundaries: The transect passes through the middle of the simulation domain (see Fig. 3.7 a), while the grid box area is situated central to the domain (see Fig. 3.7 b).

The impact of resolution on simulated wind conditions as well as the benefit of high-resolution

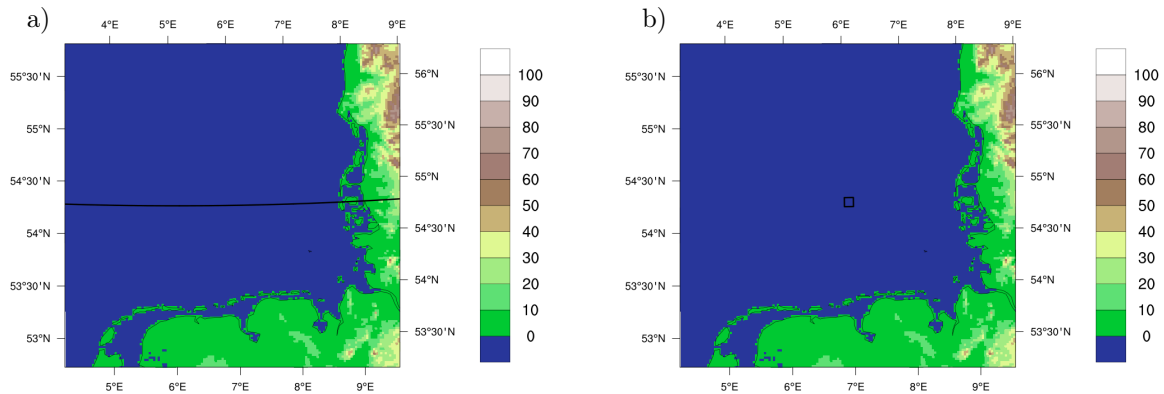


Figure 3.7: Analysis setup for meridional transects and vertical profiles. Meridional transects (a, black horizontal line) and vertical profiles get generated from averages over a local area comprising 5×5 grid boxes (b, black square) of the REMO-NH simulation domain. Shown is the orography in m at 0.022° horizontal resolution. The same degree of latitude is taken to generate meridional transects for REMO27 and REMO49, while vertical profiles are solely illustrated for REMO-NH simulations.

non-hydrostatic modelling for simulating PBL characteristics is illustrated in Section 3.5.1. The subsequent Section 3.5.2 demonstrates the capability of the surrogate climate change methodology to transfer temperature change information and simulate a thermodynamically adjusted atmosphere with REMO-NH. Finally, the analysis of surrogate climate change experiments with respect to thermodynamic effects of perturbed boundary conditions on wind climate - according to climate change signals as projected for the end of the 21st century - is presented in Section 3.5.3. The focus of this analysis is on wind speed and processes affecting wind speed, since this variable is used as primary input for wind power production assumptions for the financial modelling covered in Chapter 4.

3.5.1 Simulated Wind Conditions in the Planetary Boundary Layer

In order to evaluate the influence of an increased vertical and horizontal resolution of REMO on simulated PBL characteristics, wind speed patterns as simulated by REMO49 and REMO-NH are compared to a state-of-the-art regional climate model setup, represented by REMO27. As REMO27 and REMO49 share the same horizontal grid and topography, spatial patterns of both simulation results are directly comparable. Non-hydrostatic high-resolution REMO-NH simulations are evaluated qualitatively on its native resolution to preserve small scale information.

Impact of Resolution on Simulated Wind Speed

The near surface wind speed at 10 m height is a standard model output of REMO. For the domain of interest, the German Bight, annual mean 10 m wind speed is reaching 3 to 5 ms^{-1} over land area, increasing to about 7 to 8 ms^{-1} along the Dutch, German and Danish coast line and up to 10 ms^{-1} offshore. This horizontal wind speed pattern evolves alike for REMO27, REMO49 and REMO-NH (see Fig. 3.8). The wind speed is significantly higher over the ocean due to the comparably smoother surface, while it decreases with increasing roughness producing higher friction over land area. The horizontal gradient is less pronounced with increasing altitude (see Fig. A.3), because of decreasing influence of the surface drag with height. Nonetheless, the vertical wind speed profile in the PBL is determined by the surface roughness (e.g. *Stull*, 1988). Comparing the hydrostatic REMO simulations on 27 and 49 vertical model levels, the difference in their annual mean 10 m wind speed amounts to about $\pm 0.5 \text{ ms}^{-1}$ (not shown). These differences vary strongly in sign and intensity throughout the year, reaching almost $\pm 1.0 \text{ ms}^{-1}$ (see Fig. A.4 a-d). The high-resolution non-hydrostatic REMO-NH simulations significantly increase the representation of coastlines and topography (see Fig. 3.8 e-f): Distinct wind speed pattern and horizontal gradients are resolved in the vicinity of the coast, including the Frisian Islands and bays along the North Sea as compared to REMO27 (see Fig. 3.8 a-b) and REMO49 (see Fig. 3.8 c-d). However, the horizontal wind speed patterns follow those of the hydrostatic REMO simulations.

Comparing the individual simulation years 2010 (see Fig. 3.8 a, c and e) and 2008 (see Fig. 3.8 b, d and f), higher annual mean 10 m wind speed over most of the Dutch and German land area is simulated for 2008, irrespective of the REMO simulation setup. The same is true along the entire coast line and the adjacent offshore area. In this regard, the annual mean 10 m wind speed is about 0.7 ms^{-1} higher over land area and reaches more than 1.0 ms^{-1} along the coast and offshore for the simulation year 2008. This is in agreement with higher observed wind energy generation (*IWR*, 2018) as well as with higher annual mean wind speed and wind energy density of the forcing data of ERA-Interim for 2008 compared to 2010. With increasing vertical resolution from 27 to 49 vertical model levels, the difference in their annual mean 10 m wind speed reveals lower values simulated for 2010 and higher values for 2008 (not shown). Taking into account that these years are characterised by lower (2010) and higher (2008) annual mean wind speed conditions, this potentially indicates a feedback loop as an effect of dynamical processes being modified by a higher resolved atmosphere. However, this hypothesis needs to be proven by an extended evaluation comprising in-situ observations and is outside the scope of this thesis.

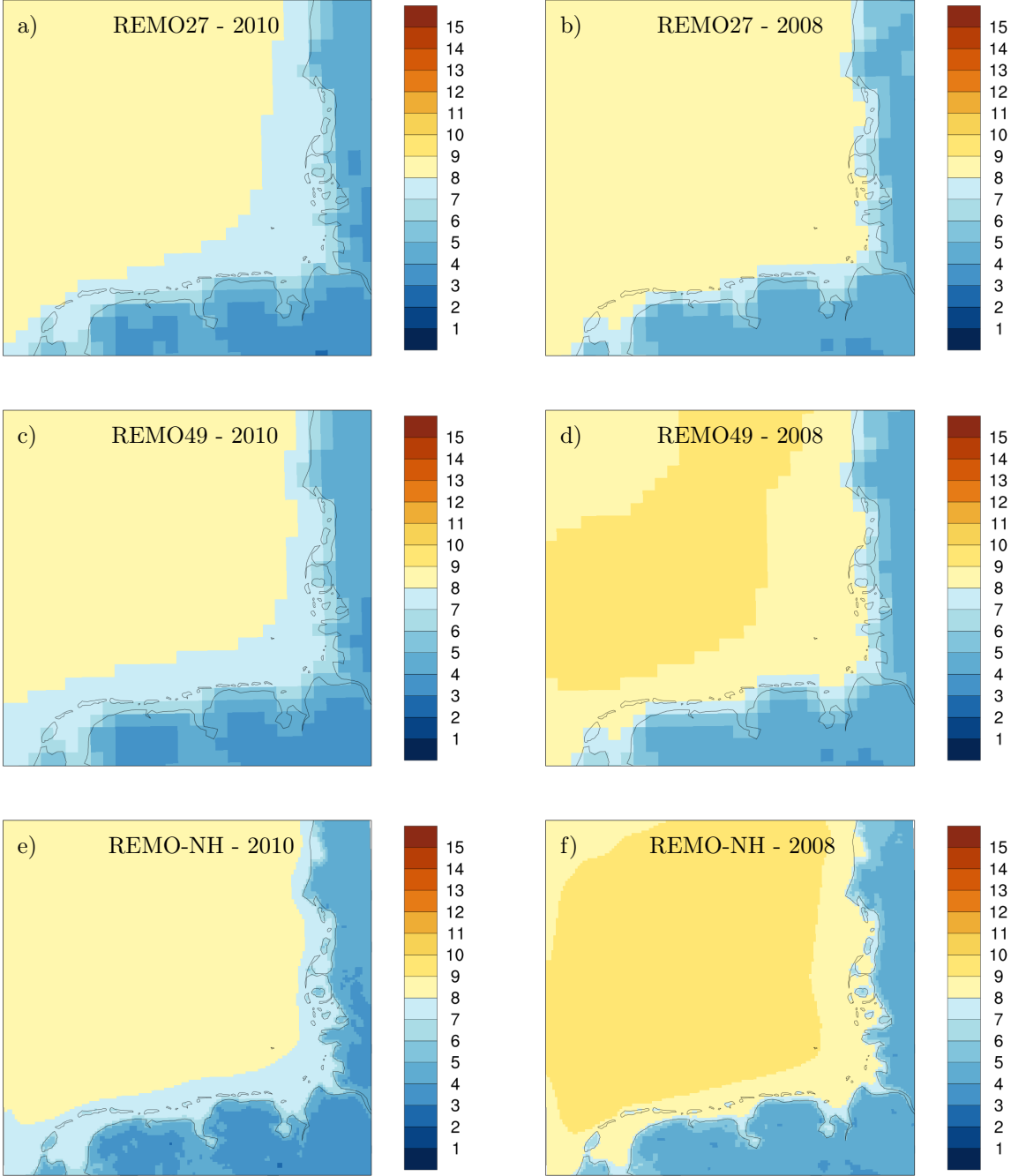


Figure 3.8: Horizontal patterns of annual mean wind speed at 10 m height as simulated for the three different simulation setups. Shown are annual mean absolute values in $m s^{-1}$ for REMO27 (a-b), REMO49 (c-d) and REMO-NH (e-f) for the respective simulation periods covering the year 2010 (a, c, e) and 2008 (b, d, f).

Vertical wind speed information is provided on model levels through the horizontal wind components. Annual mean wind speed for the lowest 1000 m of the atmosphere are visualised as meridional transects (cf. Fig. 3.7 a) in Fig. 3.9. The vertical patterns show lowest wind speed values closest to the surface, reaching 4.0 ms^{-1} over topography to above 9.0 ms^{-1} offshore. Again, the wind speed occurs to be higher over the ocean due to the comparably smoother surface, while it decreases with increasing roughness producing higher friction over land. Wind speed values increase with height because of diminishing surface drag, reaching highest values at about 200 to 500 m altitude (within the lowest 1000 m of the atmosphere).

Increasing the number of atmospheric model levels from 27 to 49 significantly increases the resolution of the lower atmosphere: The mean atmospheric state within the first 1000 m above ground is covered by about 5 to 6 model levels for REMO27 (cf. dashed lines of Fig. 3.9 a-b), while it consists of about 16 to 17 model levels for REMO49 (cf. Fig. 3.9 c-d) and REMO-NH (cf. Fig. 3.9 e-f). As REMO49 and REMO-NH share the same vertical model resolution, their vertical patterns evolve rather similar even though REMO-NH is simulated at a significantly higher horizontal resolution. Because the REMO49 simulation output serves as boundary condition for the REMO-NH simulations, a high spatial correlation is reasonable. The REMO27 simulations generally match the vertical wind speed patterns of REMO49 and REMO-NH but get resolved much poorer. This is expressed in distinct fine-scale vertical gradients being observable for the vertically higher resolved simulations and demonstrate the benefit of an increased vertical model resolution.

Comparing the individual simulation years of 2010 (see Fig. 3.9 a, c and e) and 2008 (see Fig. 3.9 b, d and f), higher annual mean wind speed is present across the PBL for 2008, reaching more than 11.5 ms^{-1} , while 2010 amounts to about 10.0 ms^{-1} . Again, this is in agreement with higher observed wind energy generation as well as with higher annual mean wind speed and wind energy density of the forcing data of ERA-Interim for 2008 as compared to 2010.

With the adjustments introduced to REMO, simulation output of certain wind variables for the first 300 m above ground at 20 m intervals is provided to support the analysis of wind conditions in the lower PBL (see Section 3.4.2). The information provided by the additional height levels are achieved through an interpolation between adjacent model levels with every model time step (cf. Section 3.4.2). Therefore, characteristics of the vertical pattern of annual mean wind speed for the first 300 m above ground shown in Fig. 3.10 follow those of the pure model levels as presented for the meridional transects for the first 1000 m above ground (see previous paragraph and Fig. 3.9). Nonetheless, the high-resolution REMO-NH simulations reveal distinct spatial

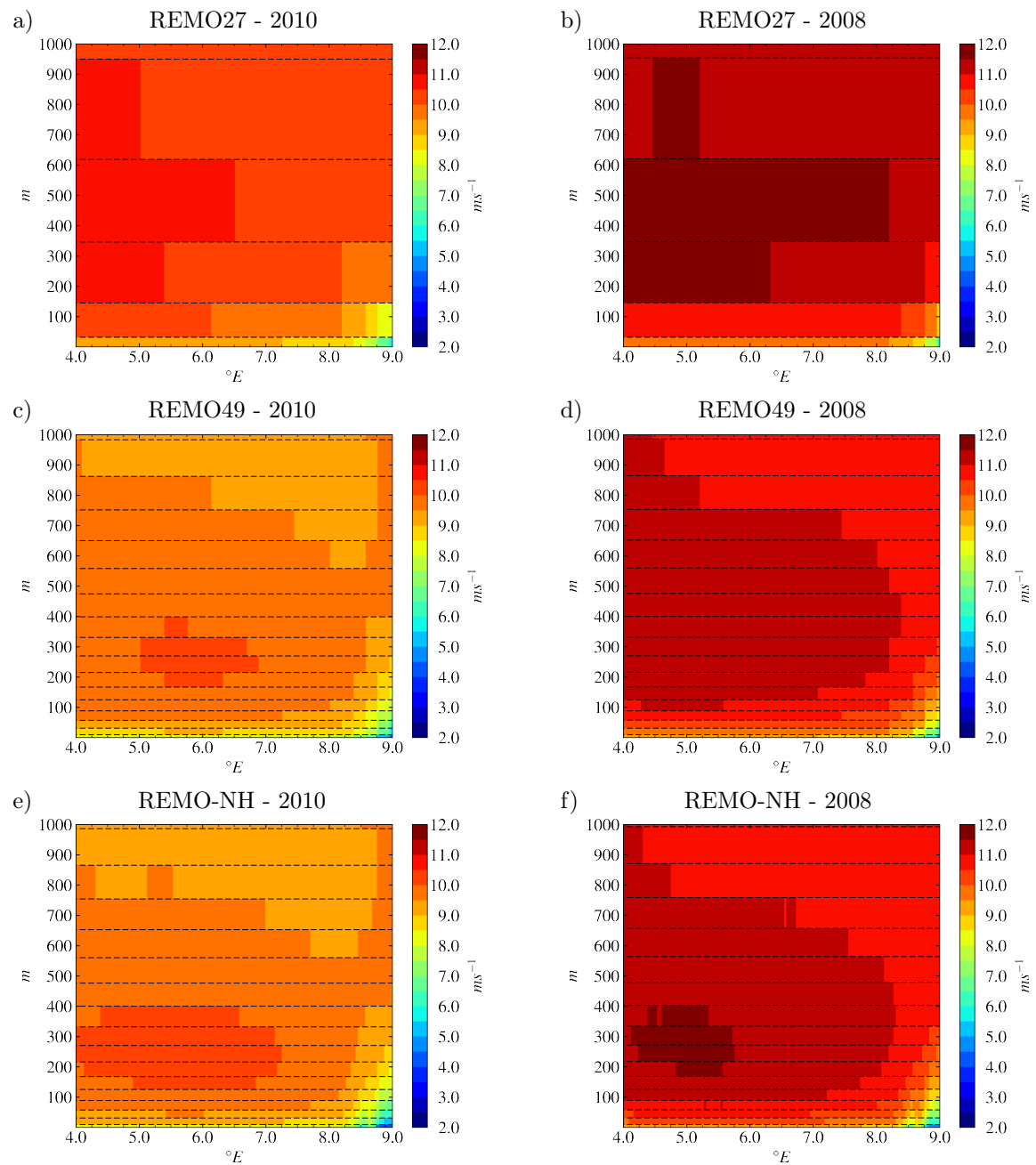


Figure 3.9: Meridional transects of annual mean wind speed for the lowest 1000 m of the atmosphere as simulated for the three different simulation setups. Shown are annual mean absolute values in ms^{-1} for REMO27 (a-b), REMO49 (c-d) and REMO-NH (e-f) for the respective simulation periods covering the year 2010 (a, c, e) and 2008 (b, d, f) for the meridional transect as defined in Fig. 3.7. Dashed black lines indicate the average geometric height of model half-levels of the individual simulations where the horizontal wind components are defined.

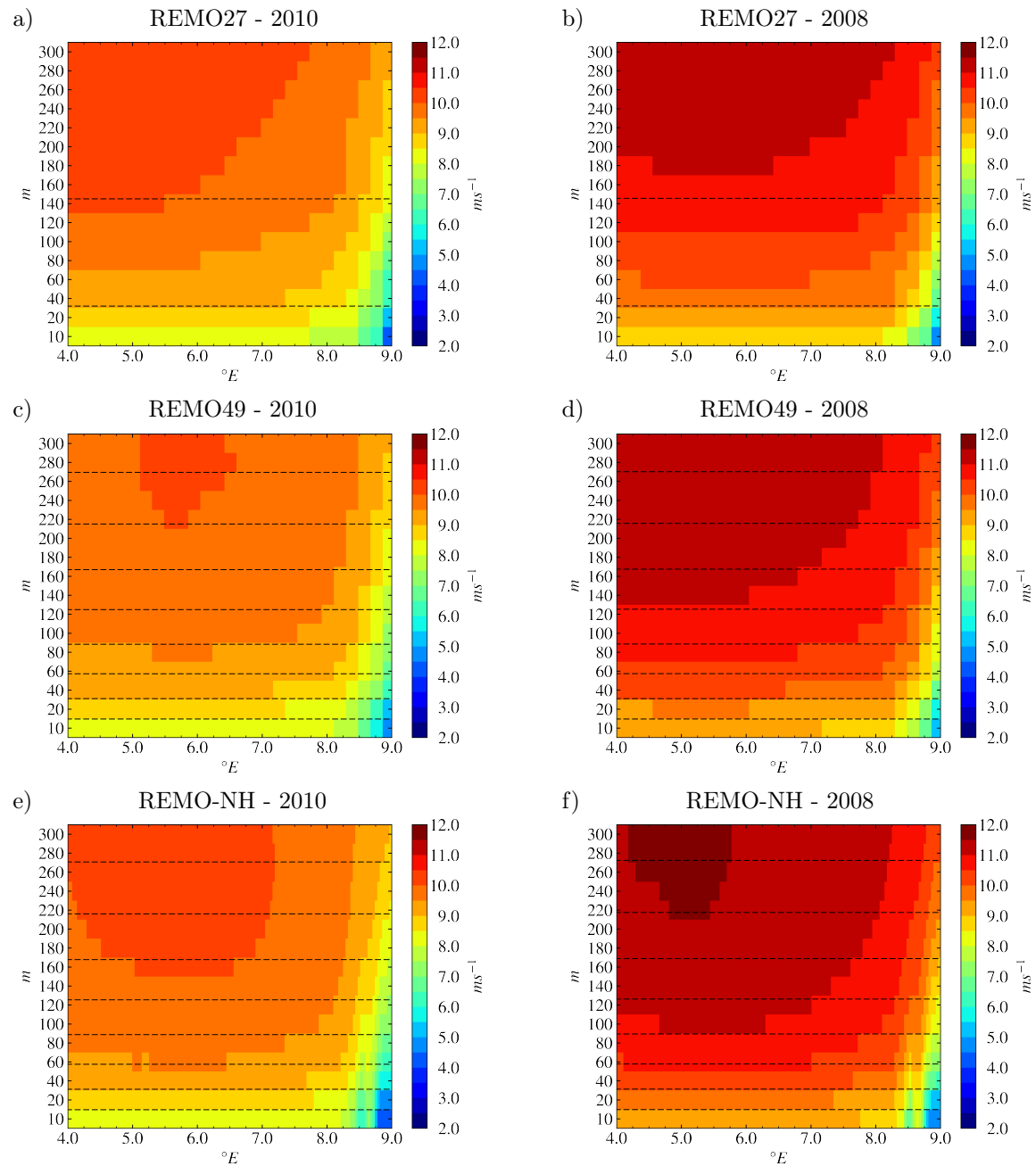


Figure 3.10: Meridional transects of annual mean wind speed for the lowest 300 m of the atmosphere as simulated for the three different simulation setups. Shown are annual mean absolute values in ms^{-1} for REMO27 (a-b), REMO49 (c-d) and REMO-NH (e-f) for the respective simulation periods covering the year 2010 (a, c, e) and 2008 (b, d, f) for the meridional transect as defined in Fig. 3.7. Dashed black lines indicate the average geometric height of model half-levels of the individual simulations where the horizontal wind components are defined.

gradients in the vicinity of the coast (cf. right edges of Fig. 3.10 e-f) as this setup is capable to resolve small islands and land area off the coast. These resolved wind speed patterns are not captured by both, REMO27 (see Fig. 3.10 a-b) and REMO49 (see Fig. 3.10 c-d), due to their more coarse horizontal resolution. In addition to the benefits of an increased vertical resolution as illustrated in the previous paragraph, an increased horizontal resolution is of importance to capture fine-scale information especially with respect to topography.

As REMO49 and REMO27 share the same horizontal grid, their meridional transects for the first 300 m above ground are directly comparable. Their differences in seasonal mean wind speed across this transect are shown in Fig. 3.11. In this manner, seasons do not follow meteorological conventions but are rather defined as quarters of a year corresponding to January to March (JFM), April to June (AMJ), July to September (JAS) and October to December (OND), respectively, since only single years are simulated. While the differences in annual mean wind speed express relatively small and more homogeneous within the range of $\pm 0.4 \text{ ms}^{-1}$ (not shown) as variations throughout the year average out, differences in seasonal mean wind speed can amount to more than $\pm 0.8 \text{ ms}^{-1}$ (corresponding to about $\pm 4.0\%$). Moreover, distinct vertical gradients in these seasonal mean wind speed differences are observable at the interfaces of 10 to 20 m, 40 to 60 m and 120 to 140 m height levels (see Fig. 3.11 a-h). This can be related to the different vertical resolutions of the simulations: The mean atmospheric state within the first 300 m above ground is covered by about 3 model levels for REMO27 (cf. dashed lines of Fig. 3.10 a-b), while it consists of about 9 model levels for REMO49 (cf. Fig. 3.10 c-d). According to the adjustments introduced to REMO's vertical diffusion scheme, information on additional height levels lying within the lowest model level get derived from prognostic variables at the surface and the lowest model level, whereas information above the the lowest model level are the result of a linear interpolation between adjacent model levels. Consequently, the number and thickness of vertical model levels determine the resulting wind speed values on additional height levels. This resolution-dependence causes the distinct vertical gradients visible in the differences between REMO49 and REMO27 at the interfaces of 10 to 20 m, 40 to 60 m and 120 to 140 m shown in Fig. 3.11 a-h. Because the prognostic variables for an increased number of vertical model levels get derived by REMO's vertical diffusion scheme in a physically and numerically consistent way, they provide a better approximation of the atmospheric state of the PBL with increasing vertical resolution. The better representation of simulated wind speed in the lower PBL due to the increased number of vertical model levels is equally valid for REMO-NH, as REMO49 and REMO-NH share the same vertical model resolution.

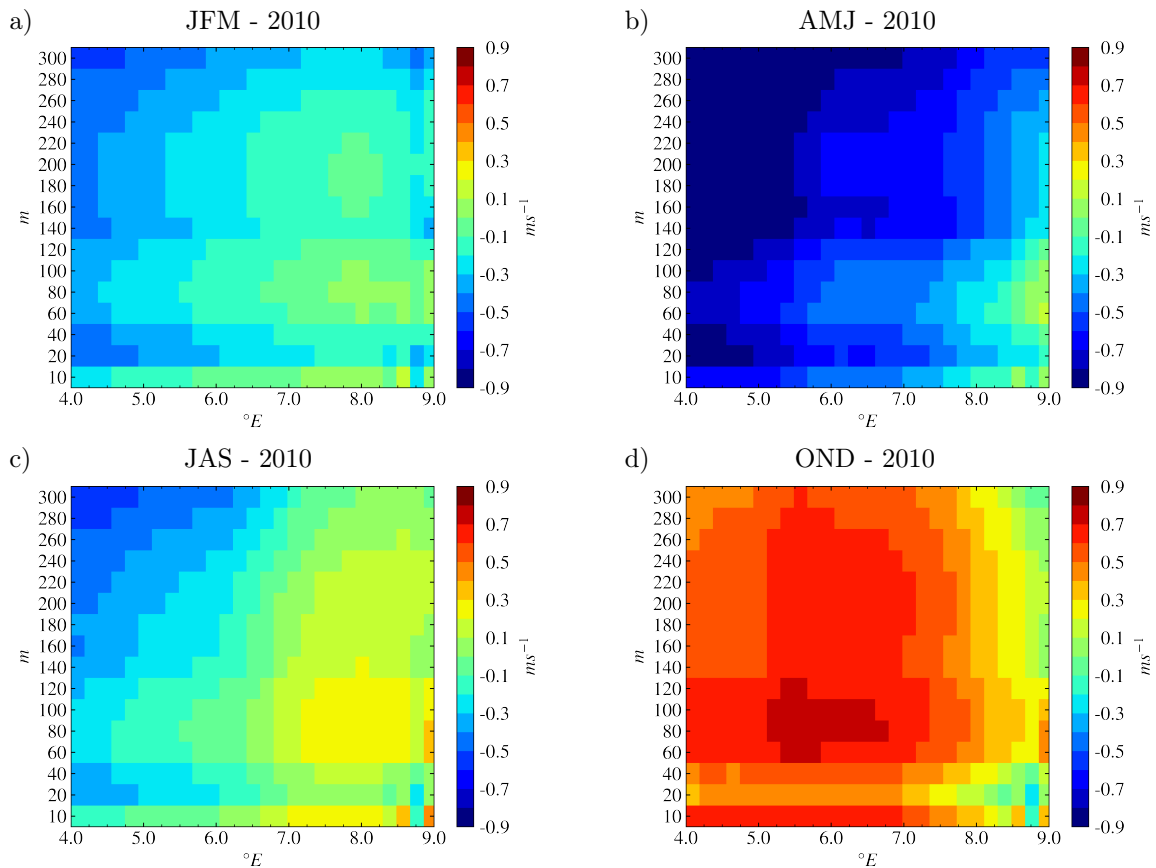


Figure 3.11: Meridional transects of seasonal mean wind speed differences for the lowest 300 m of the atmosphere between REMO49 and REMO27 for the simulation year 2010. Shown are mean absolute differences in ms^{-1} for JFM (a), AMJ (b), JAS (c) and OND (d) for the meridional transect as defined in Fig. 3.7. Analogous, images (e-h) on the next page illustrate seasonal mean wind speed differences for the simulation year of 2008.

Impact of Resolution on Variability of Simulated Wind Speed

Wind speed is highly variable in space and time and characterised by intra-annual and inter-annual variability. This characteristic is inherent to the conducted simulations as well and can be illustrated through seasonal mean wind speed and year-to-year comparison. Variations in seasonal mean wind speed for the first 300 m above ground are shown in Figs. A.5 (REMO27), A.6 (REMO49) and A.7 (REMO-NH), revealing diverging vertical wind speed patterns with seasons irrespective of the REMO simulation. Strongest wind speed and steepest vertical gradients occur during OND (see Figs. A.5, A.6 and A.7 d and h) and JFM (a and e), reaching $15.0 ms^{-1}$, whereas AMJ (b and f) and JAS (c and g) indicate lower mean wind speed of about 8.0 to $10.0 ms^{-1}$ at altitudes beyond 150 m. This is likely because of enhanced cyclone activity during autumn and winter accompanied by high shear velocities as compared to spring and summer.

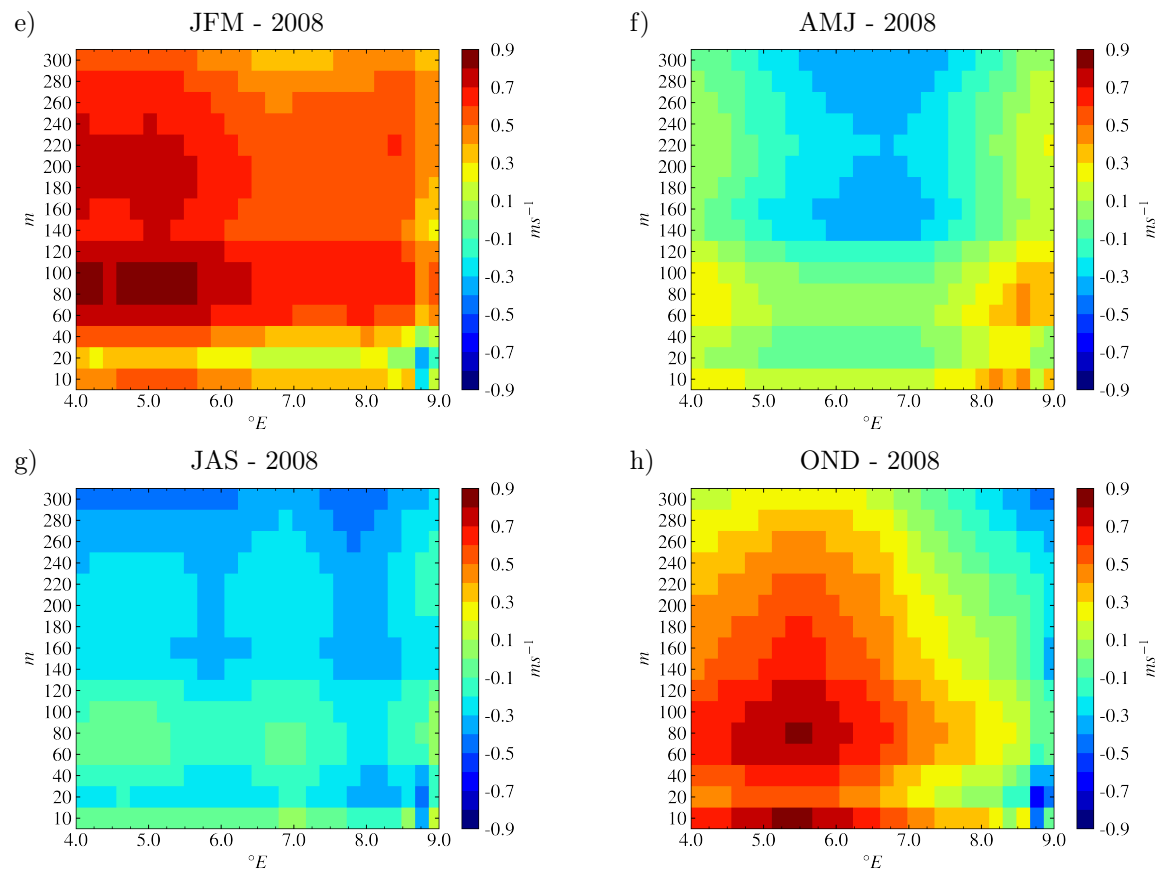


Figure 3.11: Meridional transects of seasonal mean wind speed differences for the lowest 300 m of the atmosphere between REMO49 and REMO27 for the simulation year 2008. Shown are mean absolute differences in ms^{-1} for JFM (e), AMJ (f), JAS (g) and OND (h) for the meridional transect as defined in Fig. 3.7. Analogous, images (a-d) on the previous page illustrate seasonal mean wind speed differences for the simulation year of 2010.

Regarding seasonal mean wind speed differences between REMO49 and REMO27, positive differences are observable during seasons showing strongest wind speeds (OND and JFM; see Fig. 3.11 d, e and h) and negative differences occur during seasons with lower wind speed (AMJ and JAS; see Fig. 3.11 b, f and g). This is an indication for higher intra-annual variability with increasing vertical resolution. In addition, the vertical wind speed patterns differ between both simulation years of 2010 (see Figs. A.5, A.6 and A.7 a-d) and 2008 (e-f), indicating inter-annual variability. Irrespective of the REMO simulation, this is most obvious for JFM where mean wind speed reaches $15.0 ms^{-1}$ in year 2008 (e) but amounts 3.0 to $5.0 ms^{-1}$ less during the same period in 2010 (a). Even though, the experimental setup comprising two individual simulation years does not provide the framework for a complete assessment of the intra-annual and inter-annual variability, the chosen snapshot years serve as a first guess impression about temporal variability.

Wind speed fluctuations (also referred to as turbulence intensity) positively contribute to the wind energy power production (*Emeis, 2015*). This short-term variability can be expressed in its standard deviation. The standard deviation over model output intervals (of one hour) is computed for all REMO simulations for additional height levels. The annual mean standard deviation for meridional transects of the first 300 m above ground is shown in Fig. 3.12. A continuous increase with height from about 0.18 ms^{-1} over ocean surface to about 0.25 ms^{-1} around 150 m is present for REMO27 (see Fig. 3.12 a-b), stabilising at these values across the remaining 150 m. With an increased vertical resolution, magnitudes increase, amounting to more than 15% for REMO49 (see Fig. 3.12 c-d) compared to REMO27. A further increase is observable for REMO-NH (see Fig. 3.12 e-f), reaching mean standard deviation values of more than 0.4 ms^{-1} at maximum in the vicinity of 40 to 120 m. Enhanced wind speed fluctuations can be expected for REMO-NH because of an increased horizontal resolution in addition to an increased vertical resolution, but might be to a substantial degree superimposed by fluctuations originating from a shorter model iteration time step of 6 s (used for REMO-NH) compared to 60 s (used for REMO27 and REMO49). Nevertheless, a better representation of simulated wind speed fluctuations in the lower PBL due to an increased number of vertical model levels is supported by observations: Records of annual mean standard deviations of wind speed from the meteorological measurement masts FINO1 and FINO3 located offshore in the German Bight indicate values in the range of 0.5 and 0.7 ms^{-1} , depending on their measurement height level (not shown).

As the friction decreases with distance from the surface and the influence of the stable geostrophic wind accelerates, wind speed fluctuations (in theory) reduce with height. An onset in the decrease of the mean wind speed standard deviation is hardly noticeable for REMO27 and REMO49, but for REMO-NH beyond around 200 m (see Fig. 3.12 e-f). The increased vertical and horizontal resolution as well as higher vertical velocities through non-hydrostatic motion might be attributable for this. However, the domain size affects the internal model variability, which is strongest central of the model domain where the largest vertical gradients in mean wind speed standard deviation occur. This might influence this finding.

In summary, increasing the vertical resolution from 27 to 49 atmospheric model levels significantly increases the resolution of the lower troposphere comprising the PBL. Because the prognostic variables for an increased number of vertical model levels get derived by REMO's vertical diffusion scheme in a physically and numerically consistent way, they provide a better approximation of the atmospheric state of the PBL with increasing vertical resolution. This is beneficial for wind energy applications as wind turbines harvest energy from wind in the lower PBL. While annual

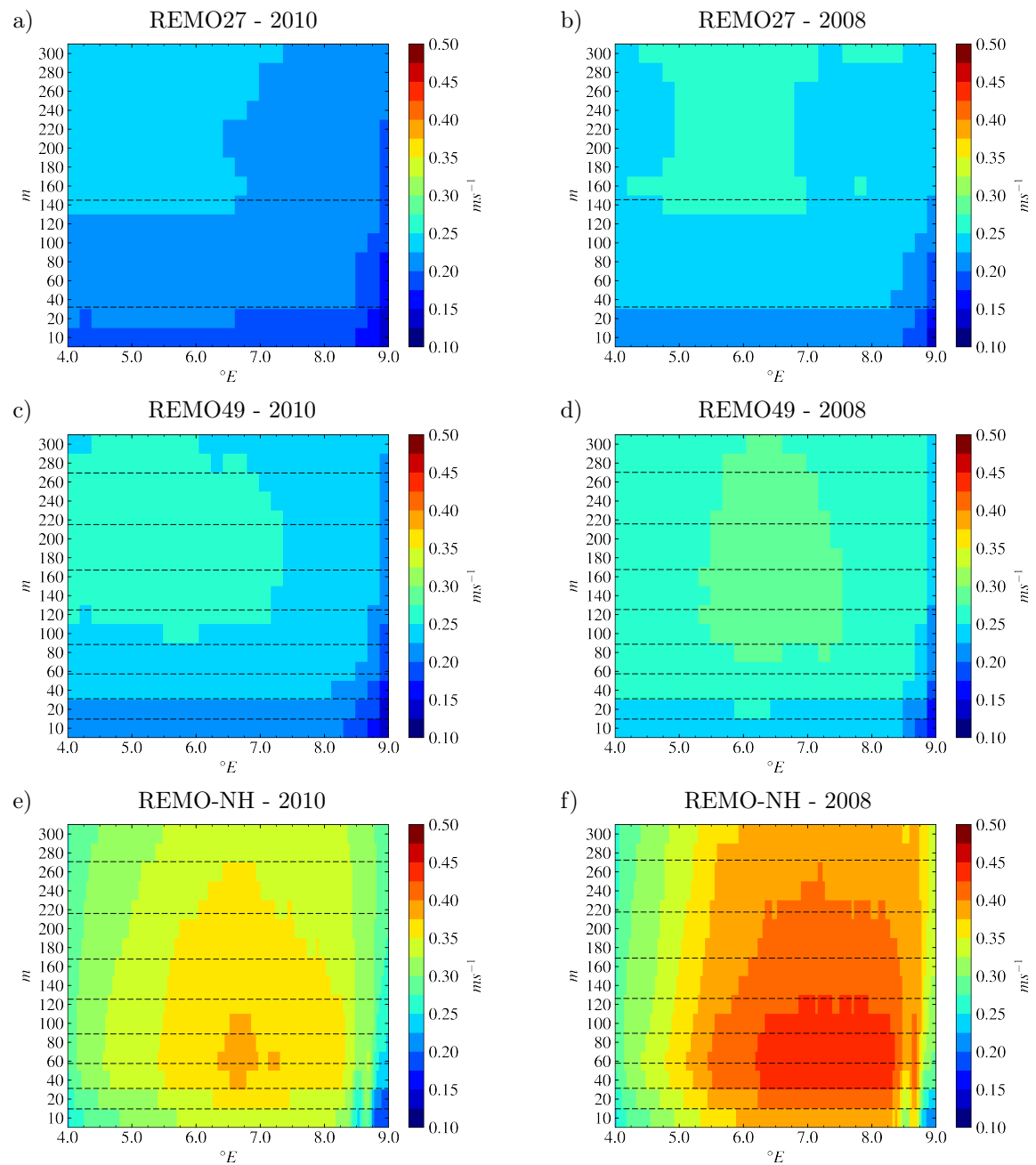


Figure 3.12: Meridional transects of annual mean wind speed standard deviation for the lowest 300 m of the atmosphere as simulated for the three different simulation setups. Shown are annual mean absolute values in ms^{-1} for REMO27 (a-b), REMO49 (c-d) and REMO-NH (e-f) for the respective simulation period covering the year 2010 (a, c, e) and 2008 (b, d, f) for the meridional transect as defined in Fig. 3.7. Dashed black lines refer to the average geometric height of model half-levels of the individual simulations where the horizontal wind components are defined.

mean wind speed patterns get not notably affected, the intra-annual variability in wind climate enhances. An indication for enhanced inter-annual variability in wind climate is present through the simulation of two individual snapshot years. Combining a higher vertical resolution with a higher resolved horizontal resolution as achieved with REMO-NH, structures as coastlines and topographic features get better resolved and provide additional fine-scale information. The effects are expected to express more intense for complex terrain with steep topographic gradients, but are of relevance for a better representation of frontal systems as well. While an increase in the vertical resolution better represents wind speed fluctuations in the lower PBL, this is enhanced further simulating at an additional higher horizontal resolution (as achieved with REMO-NH). Therefore, high-resolution non-hydrostatic simulations with the regional climate model REMO-NH are concluded as suitable to simulate and provide wind climate information of the PBL.

3.5.2 High Resolution Surrogate Climate Change Experiments

High-resolution non-hydrostatic simulations with the regional climate model REMO-NH are performed, following surrogate climate change experiments (see Sections 3.4.1 and 3.4.2), to study thermodynamically induced changes in wind climate, wind characteristics and wind energy conditions in the lower part of the PBL. These experiments use vertically variable temperature change signals based on long-term climate change projections following the RCPs 2.6 (see Fig. 3.3 a-b), 4.5 (see Fig. 3.3 c-d) and 8.5 (see Fig. 3.3 e-f), being imposed on the lateral and lower boundary conditions as described in Section 3.4.2.

The monthly mean temperature change signals of the surrogate climate change experiments (see Fig. 3.13) are in close agreement to the signals imposed on the boundary conditions of those experiments (cf. Fig. 3.3). Analogous, a warming of the troposphere and pronounced stratospheric cooling can be observed during almost all month of the year for all temperature change profiles of all surrogate climate change experiments (not shown). Throughout the troposphere, the warming rate increases with height up to the tropopause, while steepest gradients occur during summer. Distinct vertical gradients in the vicinity of the surface are not as pronounced as it is observable for the imposed daily-resolved temperature change signals (cf. Figs. 3.3 and 3.13). This is at least partly because of smoothing effects due to averaging in space as well as in time. Nonetheless, a vertical temperature change gradient can be observed during spring (AMJ) as well as summer (JAS) months, while the warming signal appears to be more homogeneous with height in particular during winter.

In line with the imposed temperature change signals, the shape of the profiles of the surrogate

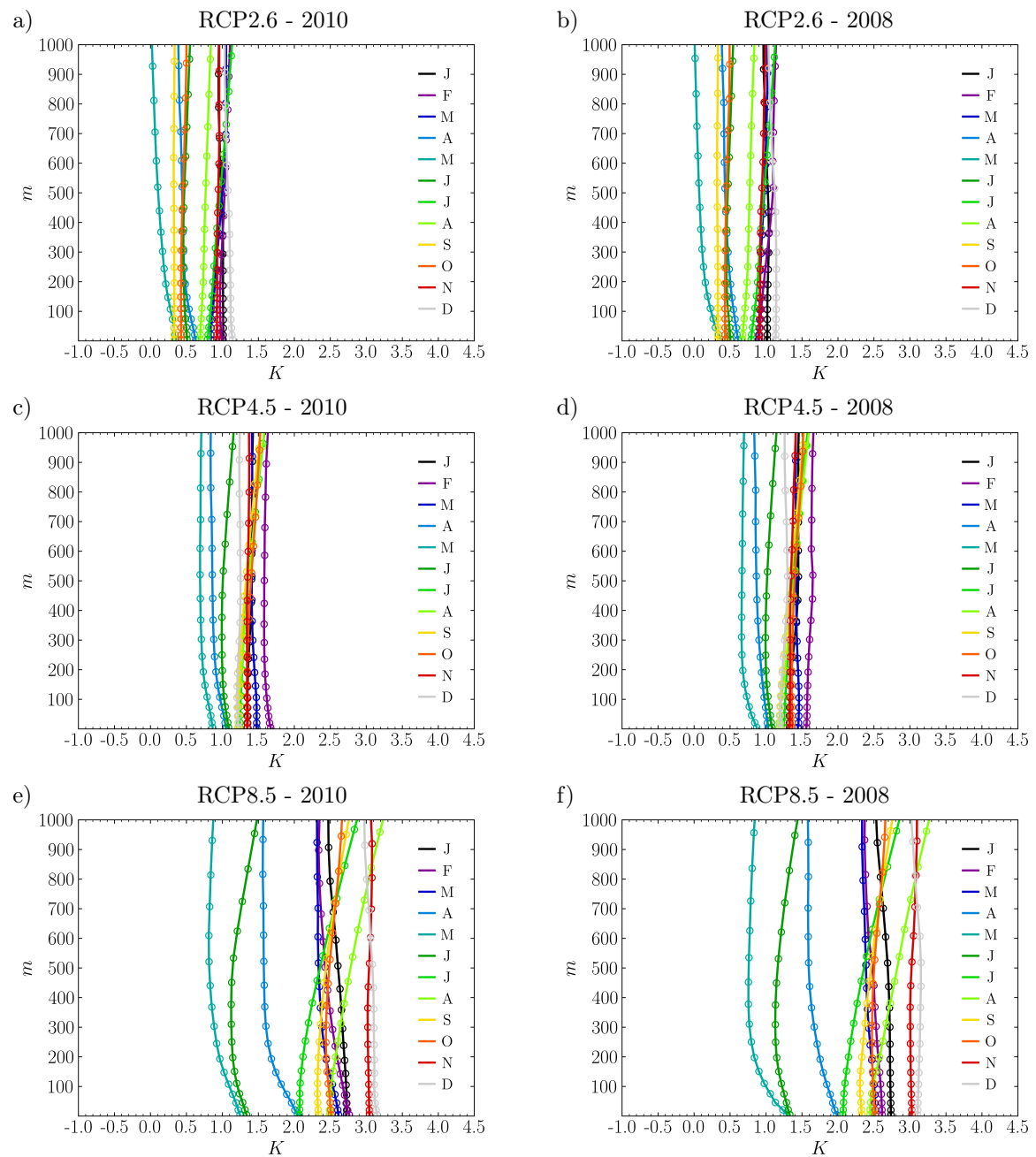


Figure 3.13: Vertical temperature change signals for the lowest 1000 m of the atmosphere as simulated for REMO-NH surrogate climate change experiments. The boundary forcing of the experiments is adjusted with vertically variable climate change signals based on long-term climate change projections following the RCPs 2.6 (a-b), 4.5 (c-d) and 8.5 (e-f) according to Fig. 3.3. The signals have been achieved by spatially averaging over the entire simulation domain of the German Bight and temporally aggregating to monthly profiles. Afterwards, the absolute differences between the surrogate climate change simulation and the reference simulation are computed. Shown are mean absolute change profiles in K for every month of a year, separately for the simulation years 2010 (a, c, e) and 2008 (b, d, f). Circles depict average model level heights for temperature (full levels).

climate change experiments vary with the degree of greenhouse gas forcing: Small and rather homogeneous changes can be observed for the RCP2.6 scenario (see Fig. 3.3 a-b), whereas the gradual warming within the troposphere as well as stratospheric cooling is more pronounced for RCP4.5 (see Fig. 3.3 c-d) and distinguishable strongest for the highest emission scenario RCP8.5 (see Fig. 3.3 e-f). Temperature change signals close to the surface vary between about 0.3 and 1.1 K (RCP2.6), 0.9 and 1.7 K (RCP4.5) and 1.3 and 3.1 K (RCP8.5) throughout the year. Least changes in the PBL compared to the remaining month of the year are observable during spring (AMJ) for RCP4.5 and 8.5, while this appears to be rudimentary for RCP2.6. Within the first 1000 m above ground, gradients in the temperature change signals can extend to more than 0.8 K. Besides the vertical temperature change signals, a homogeneous increase is observable for the vertical specific humidity change signals in the troposphere (not shown). According to the Clausius-Clapeyron relation, the specific humidity is adjusted such that the relative humidity is kept constant (cf. Section 3.4.1). Following the temperature dependency of equilibrium vapour pressure at saturation, this results in increased specific humidity values with higher temperatures. Furthermore, the geopotential height gets adjusted because of the modification of the temperature and specific humidity fields (following the surrogate climate change experimental setup in Section 3.4.1). Due to the increase in temperature and specific humidity, larger geopotential heights are present at model levels, being defined by their respective pressures (not shown). The simulated vertical temperature change signals as well as the change signals in specific humidity and geopotential height demonstrate the general capability of the surrogate climate change experimental setup to transfer temperature change information from climate change projections and simulate a thermodynamically adjusted atmosphere with REMO-NH. How a thermodynamically adjusted atmosphere is subject to change for wind and wind energy characteristics in the PBL is covered in the subsequent Section 3.5.3.

3.5.3 Wind and Wind Energy Characteristics under Surrogate Climate Change

Results of the surrogate climate change experiments are illustrated in the following. The surrogate climate change experiments use different intensities of temperature change perturbations following RCPs and are referred to as *scenarios* in the following. For clarification, those experiments do not represent a supplement to long-term climate change scenario projections but depict an alternative approach. Therefore, the term *scenario* is considered suitable as well. In this regard, the RCPs 2.6, 4.5 or 8.5 refer to surrogate climate change experiments using a climate change signal based on a climate projection with the regional climate model REMO following those

RCPs. These experiments enable to study the thermodynamic effect of temperature change perturbations according to these climate change signals. Simulated changes in wind speed and processes affecting wind speed as well as wind energy density across the lower part of the PBL are analysed to provide monthly-resolved wind resource change information for the financial modelling covered in Chapter 4.

Wind Speed in the Planetary Boundary Layer

Monthly mean wind speed changes of the surrogate climate change experiments for the lowest 300 m of the atmosphere are shown in Fig. 3.14. Associated to the changes in temperature of those experiments (see Section 3.5.2) are changes in simulated wind speed. The monthly mean wind speed profiles reveal non-uniform changes with height and in sign throughout the year. Change signals for the RCP2.6 (see Fig. 3.14 a-b) express relatively homogeneous, while they appear more pronounced for RCP4.5 (see Fig. 3.14 c-d) and form strongest for the high emission scenario RCP8.5 (see Fig. 3.14 e-f). The spread of the monthly-resolved signals is largest close to the surface, ranging from -1.4 to 2.3% (RCP2.6), -1.8 to 2.2% (RCP4.5) and -3.8 to 4.4% (RCP8.5). With stronger radiative forcing, induced through the temperature change signals of the respective RCP, tendencies towards increasing and decreasing wind speed values intensify. Even though the same boundary condition perturbations apply to the surrogate climate change experiments for both simulation years of 2010 (see Fig. 3.14 a, c and e) and 2008 (see Fig. 3.14 b, d and f), their individual weather events produce non-uniform change characteristics over the course of a year. Striking is a decrease in wind speed for the months of July, August and September, which is present for both simulation years and throughout all scenarios. While the maximum decrease close to the surface amounts to more than -1.9% for the simulation year 2010 (see Fig. 3.14 e; September), almost -3.8% are reached for the simulation year 2008 (see Fig. 3.14 f; August). As well, an increase is observable for the months of April, May and partly June. As for July, August and September, this tendency is present for both simulation years and throughout all scenarios. Here, the maximum increase close to the surface amounts to more than 4.4% for the simulation year 2010 (see Fig. 3.14 e; May), while more than 3.3% are reached for the simulation year 2008 (see Fig. 3.14 f; April). This degree of information of varying signals on a monthly to seasonal scale is not provided using annual mean values, where most of the opposing intra-annual signals average out (not shown). Noticeable for the months of April, May and June of both simulation years are pronounced gradients in the wind speed change signals across the lowest 150 m of the atmosphere, extending to more than 2.6% . A gradient is partly

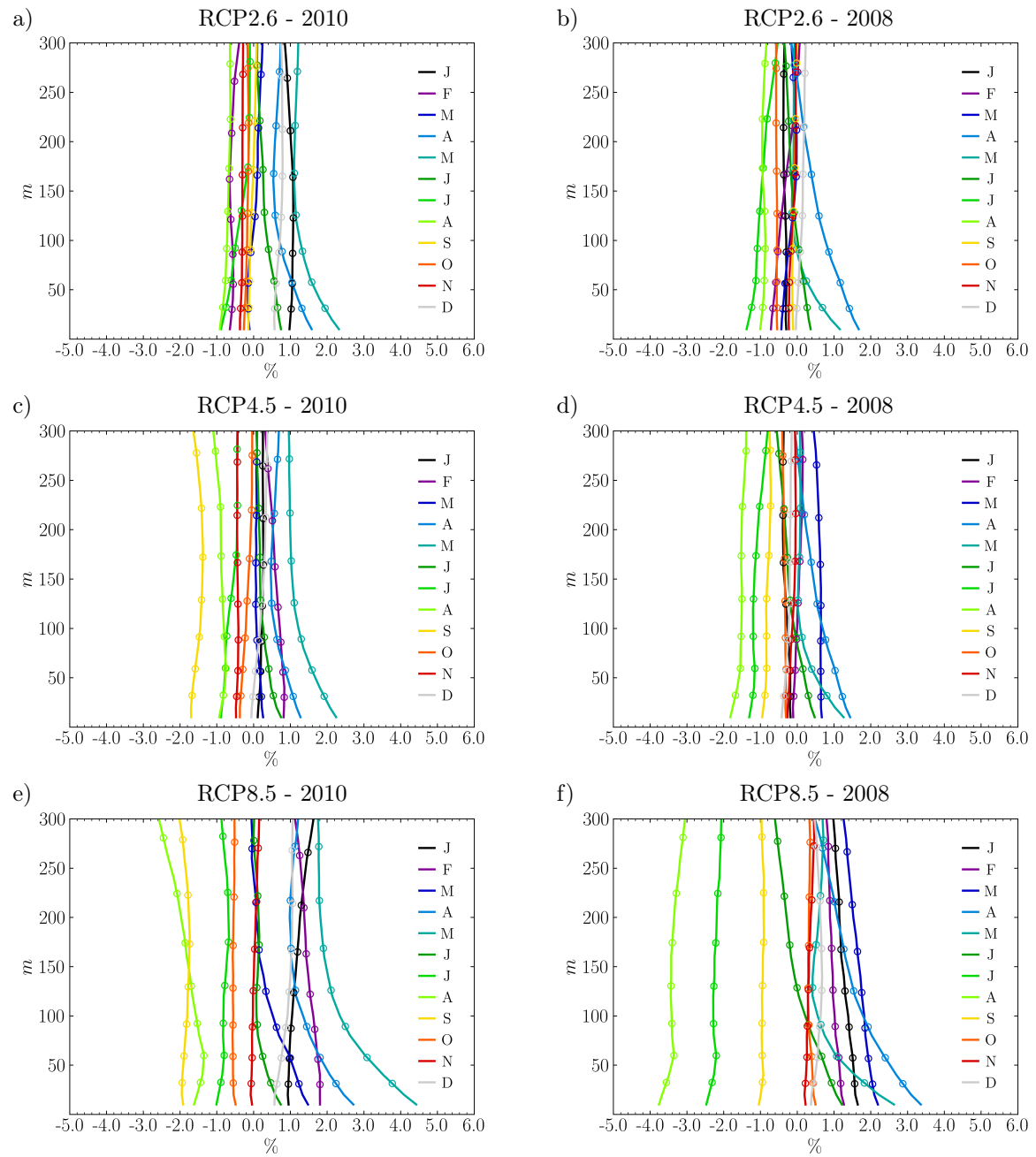


Figure 3.14: Vertical wind speed change signals for the lowest 300 m of the atmosphere as simulated for REMO-NH surrogate climate change experiments. The boundary forcing of the experiments is adjusted with vertically variable climate change signals based on long-term climate change projections following the RCPs 2.6 (a-b), 4.5 (c-d) and 8.5 (e-f) according to Fig. 3.3. The signals have been achieved by spatially averaging over a local area comprising 5×5 grid boxes centered in the middle of the domain in the German Bight (see Fig. 3.7) and temporally aggregating to monthly profiles. Afterwards, the relative differences between the surrogate climate change simulation and the reference simulation are computed. Shown are mean relative change profiles in % for every month of a year, separately for the simulation years 2010 (a, c, e) and 2008 (b, d, f). Circles depict average model level heights for wind speed above the lowest additional height level at 10 m (half levels).

observable for March of the simulation year 2010 under scenario RCP8.5 as well (see Fig. 3.14 e). However, a general tendency is not present for the remaining months of both simulated years. In comparison to climate projections with REMO carried out within the EURO-CORDEX framework (downscaling the first realisation of MPI-ESM's climate projections), the presented differing change signals of the surrogate climate change experiments for wind speed with height in combination with sub-yearly variability changes are (qualitatively) observable for long-term climate projections of the 21st century as well (cf. Figs. A.9 and A.10). Anyhow, up to now assessments of climate change and wind energy did not take the circumstance of differing climate change signals with height into account, because wind climate information are provided usually solely for the near surface (at 10 m height).

The illustrated changes in wind speed can not be linearly (and causally) related to temperature change intensities. More precisely, the observed increase in wind speed for the months of April, May and June is associated with the lowest temperature change signals, whereas the decrease during July, August and September is accompanied by temperature change signals situated neither at the upper nor at the lower intensity range. Moreover, it can not be clarified if the observed pronounced wind speed changes during those months depict a general feature. A hypothesis for this non-linear behaviour might be a diverging modulation of the dominating weather patterns of the respective months as a result of the change in temperature and associated thermodynamic effects. To identify possible physical processes being responsible for the observed changes, a profound analysis is necessary. A weather pattern clustering or in-depth analysis of single weather situations might clarify if certain weather patterns get thermodynamically modulated through the prevailing temperature change signals, leading to favouring lower or higher wind conditions. However, this is outside the scope of this thesis.

Atmospheric Stability in the Planetary Boundary Layer

The temperature change signals imposed on the boundary conditions of the surrogate climate change experiments is likely to affect atmospheric thermodynamics. Atmospheric stability is conditioned by thermodynamics and, in turn, influences prevailing wind conditions. Therefore, potential changes in atmospheric stability within the PBL are of relevance for wind power production. To quantify atmospheric stability, the Monin-Obukhov length L_* is used as stability indicator (see Section 3.4.2). When the dimensionless ratio of the geometric height z and L_* is negative, unstable atmospheric conditions prevail, while positive values describe stable atmospheric conditions. Neutral stratification is present for z/L_* around zero. The inverse of the Monin-

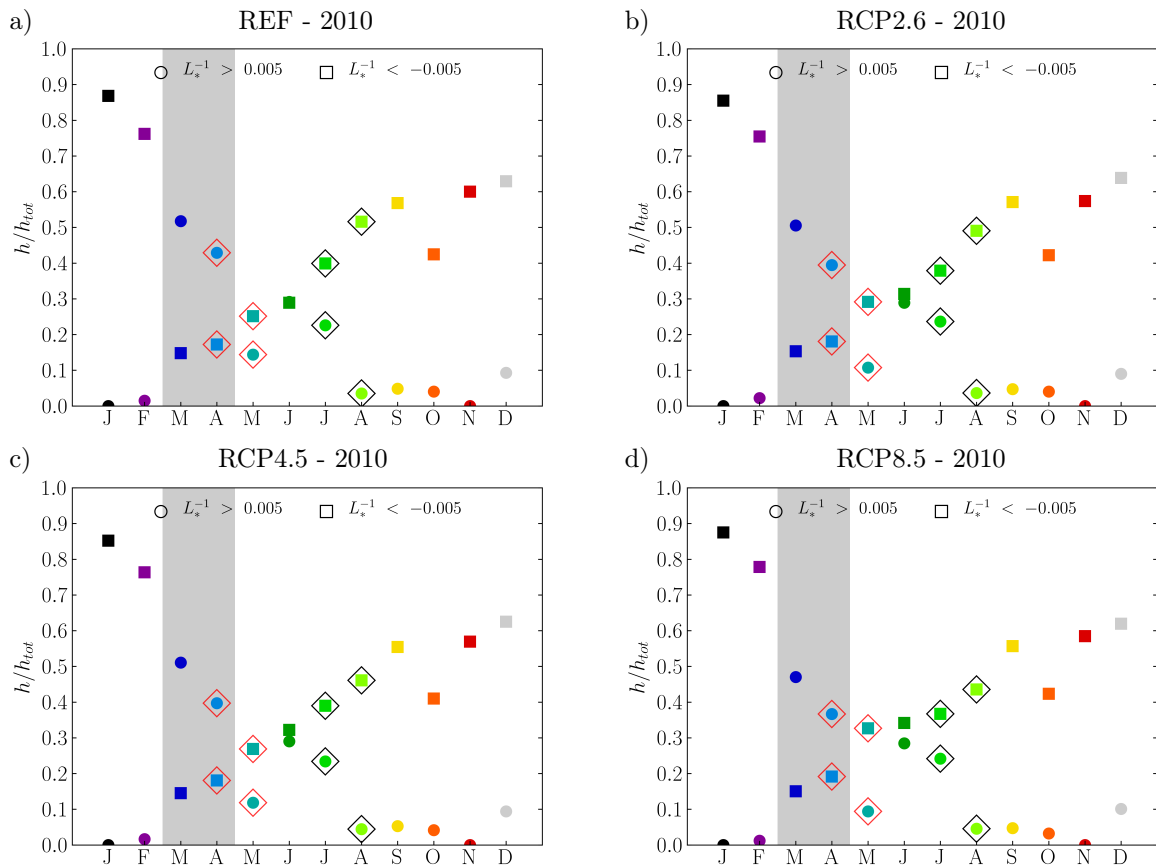


Figure 3.15: Fraction of stable and unstable atmospheric cases as simulated for REMO-NH surrogate climate change experiments for the simulation year 2010. The boundary forcing of the experiments is adjusted with vertically variable climate change signals based on long-term climate change projections following the RCPs 2.6 (b), 4.5 (c) and 8.5 (d) according to Fig. 3.3 and their reference simulations (a). Stable and unstable atmospheric conditions are identified using the inverse Monin-Obukhov length L_*^{-1} as stability indicator in combination with threshold values of $L_*^{-1} > 0.005$ for stable and $L_*^{-1} < -0.005$ for unstable conditions. Stability conditions are identified for every hour of the time series and occurrences are accumulated to monthly sums. These sums are then divided by the total hours of every individual month to achieve monthly fractions (h/h_{tot}). Shown are fractions of stable (circles) and unstable cases (squares) with respect to the total simulation period for every month of a year. Analogous, images (e-h) on the next page illustrate fractions of stable and unstable atmospheric cases for the simulation year of 2008.

Obukhov length (see Eq. 3.12) is used in combination with thresholds for stable ($L_*^{-1} > 0.005$) and unstable ($L_*^{-1} < -0.005$) atmospheric conditions to identify stable and unstable occurrences. The fraction of stable and unstable conditions for every month of a year, as simulated for the different surrogate climate change experiments and their reference simulations, is illustrated in Fig. 3.15. Unstable atmospheric conditions are detected more often compared to stable conditions

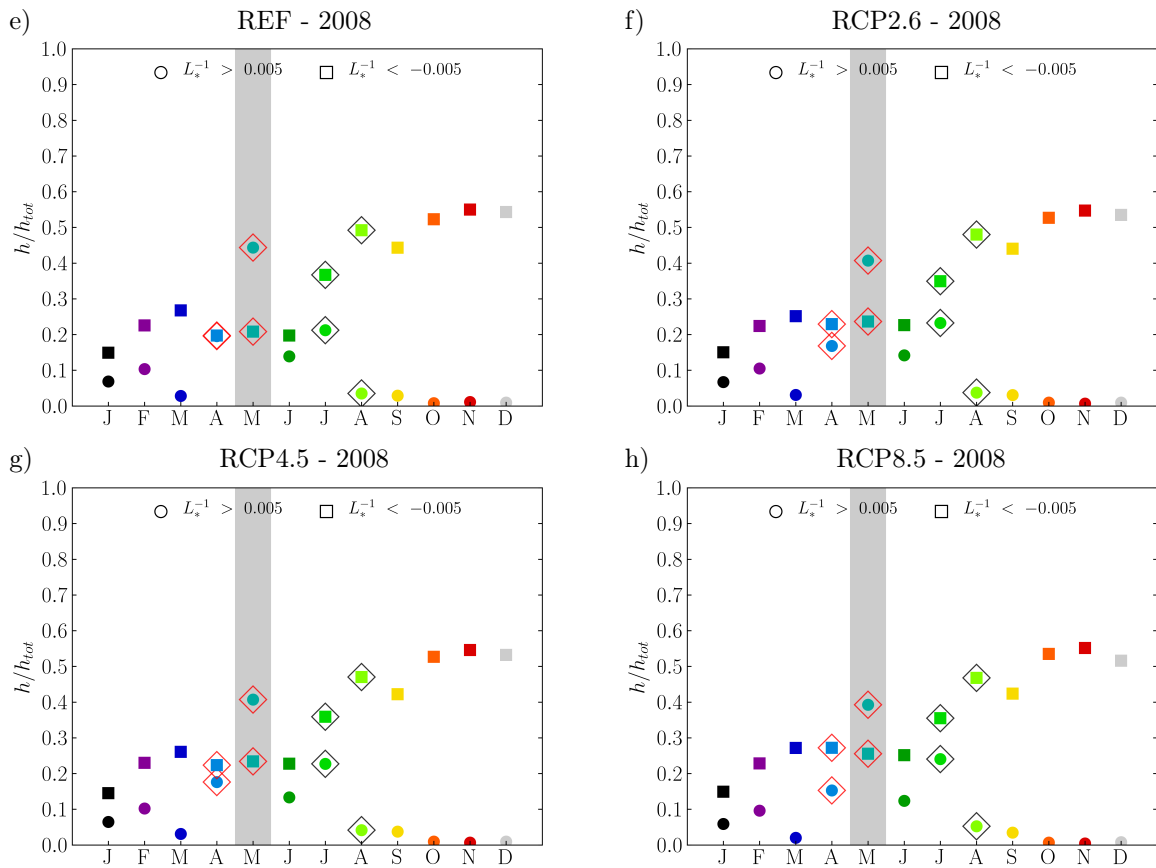


Figure 3.15: Fraction of stable and unstable atmospheric cases as simulated for REMO-NH surrogate climate change experiments for the simulation year 2008. The boundary forcing of the experiments is adjusted with vertically variable climate change signals based on long-term climate change projections following the RCPs 2.6 (f), 4.5 (g) and 8.5 (h) according to Fig. 3.3 and their reference simulations (e). Stable and unstable atmospheric conditions are identified using the inverse Monin-Obukhov length L_*^{-1} as stability indicator in combination with threshold values of $L_*^{-1} > 0.005$ for stable and $L_*^{-1} < -0.005$ for unstable conditions. Stability conditions are identified for every hour of the time series and occurrences are accumulated to monthly sums. These sums are then divided by the total hours of every individual month to achieve monthly fractions (h/h_{tot}). Shown are fractions of stable (circles) and unstable cases (squares) with respect to the total simulation period for every month of a year. Analogous, images (a-d) on the previous page illustrate fractions of stable and unstable atmospheric cases for the simulation year of 2010.

throughout the year, except for the months of March and April of the simulation year 2010 (see grey bar in Fig. 3.15 a-d) and May of the simulation year 2008 (see grey bar in Fig. 3.15 e-h). Only occasional stable atmospheric occurrences appear from August to February for both simulation years (see Fig. 3.15 a-h).

Associated to the observed changes in wind speed (see previous paragraph and Fig. 3.14), an

increase of unstable atmospheric conditions (up to about 7.5%) and a decrease of stable conditions (up to about -6.2%) is present for months with increasing wind speed (primarily April and May; see red diamonds in Fig. 3.15). Contrary, a tendency for decreasing unstable (up to about -8.0%) and increasing stable atmospheric conditions (up to about 2.8%) is observable for months with decreasing wind speed (primarily July and August; see black diamonds in Fig. 3.15). This relation between wind speed and atmospheric stability condition changes is striking for both simulation years. Furthermore, change signal magnitudes increase with rising scenario intensity. Analogous to changes presented for wind speed, no linear relationship to temperature change intensities (cf. Fig. 3.13) can be identified.

The Monin-Obukhov length is (amongst others) described by the counteracting quantities of frictional velocity (u_*) and turbulent heat flux (θ_* ; cf. Eq. 3.12). More precisely, it is proportional to the ratio of the turbulent heat flux and the square of the frictional velocity, whereas the turbulent heat flux is again dependant on the frictional velocity (cf. Eqs. 3.12 and 3.13). In this regard, the detected changes in atmospheric stability conditions (see previous paragraph) can get disassembled and related to changes in frictional velocity and turbulent heat flux.

The monthly mean change ratios between the scenarios and their reference for the frictional velocity (i.e. u_{*s}/u_{*r}) and the turbulent heat flux (i.e. θ_{*s}/θ_{*r}) are illustrated in Figs. 3.16 and 3.17. As presented above, unstable (stable) atmospheric conditions are simulated to increase (decrease) primarily for the months of April and May, while the contrary is observable for the months of July and August. Associated to the former, increasing frictional velocities (up to about 6.0%; see red diamonds in Fig. 3.16 e) and turbulent heat fluxes (up to more than a factor of two; see red diamonds in Fig. 3.17 f) are apparent, while decreasing frictional velocities (up to about -4.8% ; see black diamonds in Fig. 3.16 f) and turbulent heat fluxes (up to more than a factor of one third; see black diamonds in Fig. 3.17 f) are present for the latter. Again, increasing change signal magnitudes are observed with rising scenario intensity. In total, turbulent heat flux changes outweigh changes in friction velocity, leading to the prevailing changes in atmospheric stability conditions. This can be attributed to changes in the potential temperature flux ($\overline{\omega'\theta'}$), according to the formulation of the turbulent heat flux (see Eq. 3.13).

Vertical gradients of the temperature changes signals indicate larger signals close to the surface for April, May and June as well as lower signals close to the surface for July, August and September, compared to adjacent altitudes in the lower PBL (see Section 3.5.2 and Fig. 3.13). This seasonally reversed gradient in the temperature change signal across the lower PBL can explain the differing changes in the potential temperature flux among those months: As the heat flux is dependent

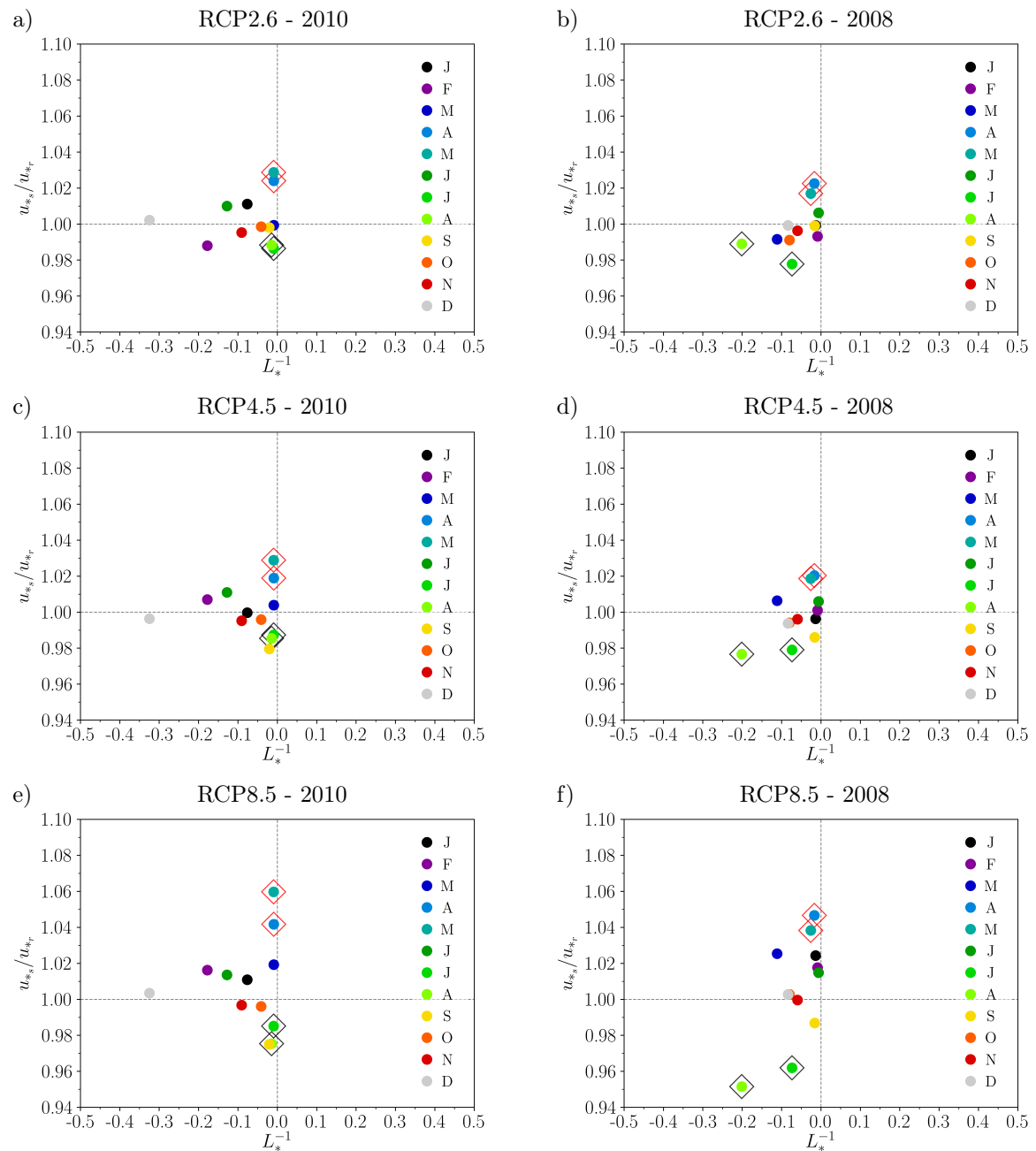


Figure 3.16: Change ratios of frictional velocity u_* as simulated for REMO-NH surrogate climate change experiments. The boundary forcing of the experiments is adjusted with vertically variable climate change signals based on long-term climate change projections following the RCPs 2.6 (a-b), 4.5 (c-d) and 8.5 (e-f) according to Fig. 3.3. Illustrated is the monthly mean change ratio of frictional velocity between the scenario and its reference (u_{*s}/u_{*r}) with respect to monthly mean stability described by the inverse of the Monin-Obukhov length L_*^{-1} . Increases in frictional velocity are depicted by values of u_{*s}/u_{*r} above one. Shown are change ratios of frictional velocity for every month of a year, separately for the simulation years 2010 (a, c, e) and 2008 (b, d, f).

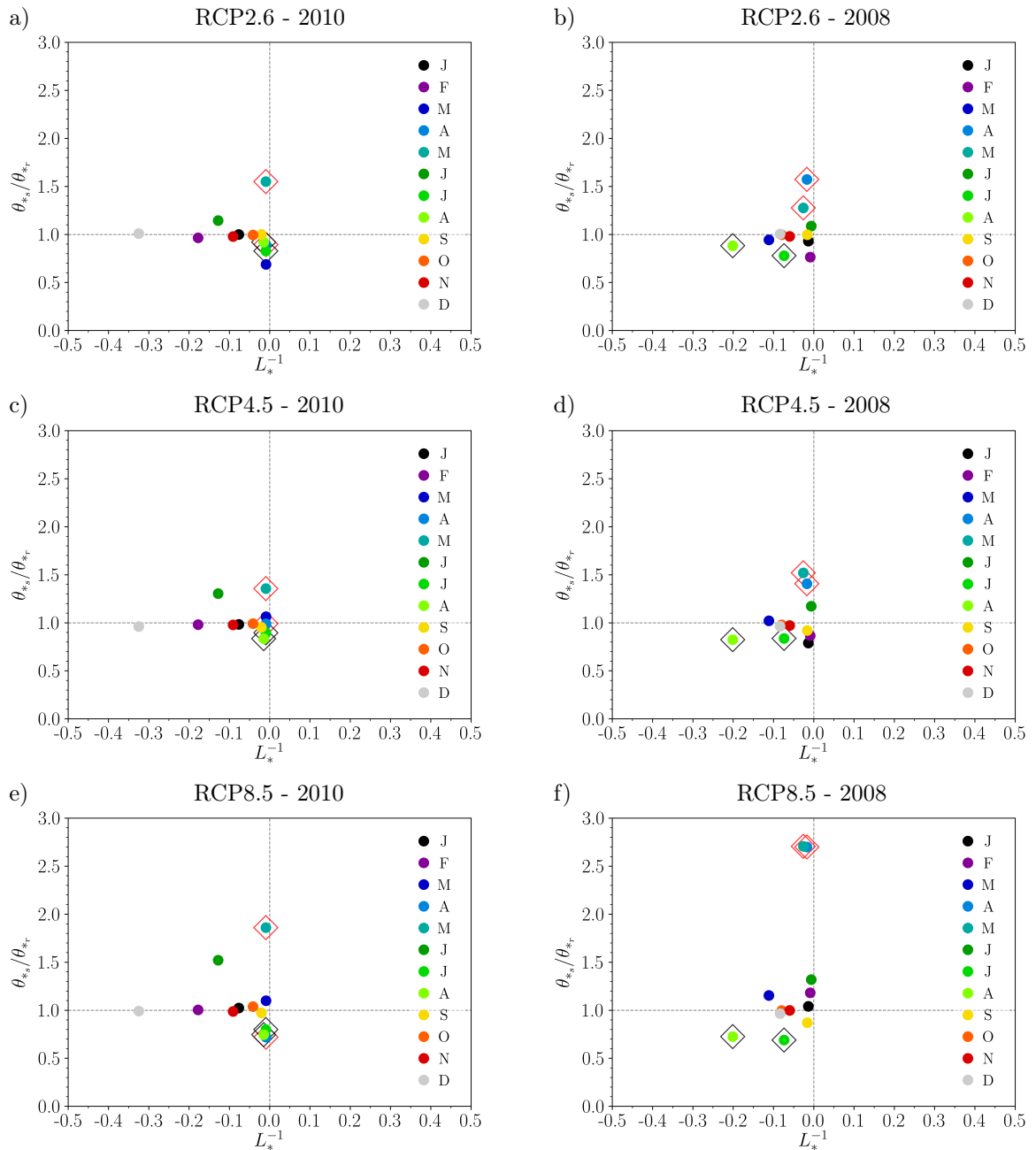


Figure 3.17: Change ratio of turbulent heat flux θ_* as simulated for REMO-NH surrogate climate change experiments. The boundary forcing of the experiments is adjusted with vertically variable climate change signals based on long-term climate change projections following the RCPs 2.6 (a-b), 4.5 (c-d) and 8.5 (e-f) according to Fig. 3.3. Illustrated is the monthly mean change ratio of turbulent heat flux between the scenario and their reference (θ_{*s}/θ_{*r}) with respect to monthly mean stability described by the inverse of the Monin-Obukhov length L_*^{-1} . Increases in turbulent heat flux are depicted by values of θ_{*s}/θ_{*r} above one. Shown are change ratios of turbulent heat flux for every month of a year, separately for the simulation years 2010 (a, c, e) and 2008 (b, d, f).

on the temperature gradient between the surface and adjacent model levels, a gradient in the vertical temperature change signal can intensify or weaken the potential temperature flux. This is independent of the absolute temperature change signals' intensities, which differ considerably among those months.

While observed changes in the monthly mean wind speed can not be linearly related to temperature change intensities (see previous paragraphs), a potential indirect coherence exists through atmospheric stability in the PBL: Changes in the occurrence of stability conditions appear to be attributable to changes in the potential temperature flux, which can be linked to the shape of the temperature change signal gradients. In turn, wind speed changes can be related to changes in stability condition occurrences. Therefore, thermodynamically induced changes in wind speed through the surrogate climate change experiments can be linked to vertical gradients of the temperature change signals, which alter atmospheric stability conditions in the PBL through changes in the potential temperature flux.

Wind Energy Density in the Planetary Boundary Layer

Wind power production is dependent on prevailing atmospheric conditions determining the wind resource. The wind energy density is a measure of the total kinetic energy per unit area being (potentially) extractable from atmospheric velocity. According to its definition, wind energy density is proportional to the cube of the wind speed and linearly related to air density (cf. Eq. 3.14). Therefore, wind energy density is prone to climate-induced changes of those atmospheric variables. As wind speed is subject to change according to the surrogate climate change experiments (see previous paragraphs), its impact on wind energy density is analysed in the following.

Monthly mean wind energy density change profiles for the lowest 300 m of the atmosphere are illustrated in Fig. 3.18. Because wind energy density is directly dependent on wind speed, changes in wind speed get imposed on the wind energy density change signals. Due to its cubic proportionality (cf. Eq. 3.14), wind energy density changes express even more intense. Analogous to the changes illustrated for wind speed (see Fig. 3.14), change signals for wind energy density manifest non-uniform with height and variable in sign throughout the year. With rising scenario intensity, change signal magnitudes tend to express more pronounced. The spread of the monthly mean wind energy density change signals is largest close to the surface, ranging from -4.8 to 6.4% (RCP2.6; see Fig. 3.18 a-b), -6.2 to 6.9% (RCP4.5; see Fig. 3.18 c-d) and -12.9 to 14.8% (RCP8.5; see Fig. 3.18 e-f).

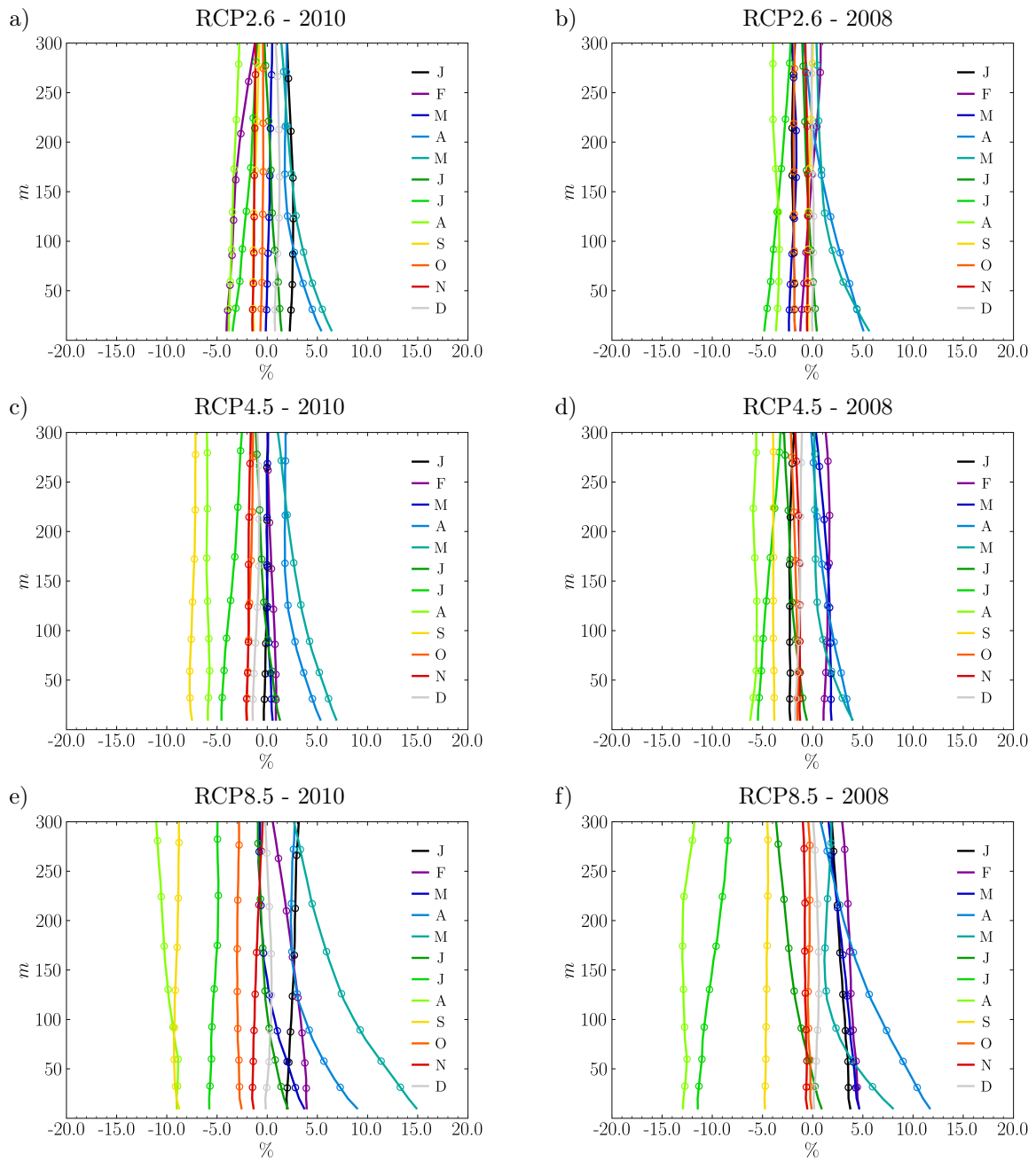


Figure 3.18: Vertical wind energy density change signals for the lowest 300 m of the atmosphere as simulated for REMO-NH surrogate climate change experiments. The boundary forcing of the experiments is adjusted with vertically variable climate change signals based on long-term climate change projections following the RCPs 2.6 (a-b), 4.5 (c-d) and 8.5 (e-f) according to Fig. 3.3. Wind energy density is derived according to Eq. 3.14. The signals have been achieved by spatially averaging over a local area comprising 5×5 grid boxes centered in the middle of the domain in the German Bight (see Fig. 3.7) and temporally aggregating to monthly profiles. Afterwards, the relative differences between the surrogate climate change simulation and the reference simulation are computed. Shown are mean relative change profiles in % for every month of a year, separately for the simulation years 2010 (a, c, e) and 2008 (b, d, f). Circles depict average model level heights for wind energy density above the lowest additional height level at 10 m (half levels).

Similar to the changes in wind speed, a decrease in wind energy density is observable for the months July, August and September, which is present for both simulation years and throughout all scenarios (see Fig. 3.18 a-h). The maximum decrease close to the surface amounts to almost -9.0% for the simulation year 2010 (August of RCP8.5; see Fig. 3.18 e), while about -12.9% are reached for the simulation year 2008 (August of RCP8.5; see Fig. 3.18 f). Contrary to the months July, August and September, an increase is observable for the months of April and May, which is present for both simulation years and throughout all scenarios. The maximum increase close to the surface amounts to more than 14.8% for the simulation year 2010 (May of RCP8.5; see Fig. 3.18 e) and to almost 11.7% for the simulation year 2008 (April of RCP8.5; see Fig. 3.18 f). This degree of information is not provided by annual mean wind energy density change signals where most of the opposing intra-annual signals cancel each other out (not shown). Noticeable are pronounced gradients in the wind energy density change signals expanding across the lowest 300 m of the atmosphere for the months of April and May (see Fig. 3.18 a-h). A gradient is partly detectable for March and June of the simulation year 2010 under scenario RCP8.5 as well (see Fig. 3.18 e), while no general tendency is observed to be present for the remaining months of both simulated years.

Even though wind speed change signals are reflected in the respective wind energy density change signals, these signals are not exclusively attributable to changes in wind speed. Exemplarily, for the months October, November and December a slight and more homogeneous increase in mean wind speed ranging from 0.2 to almost 0.7% is simulated across the lowest 300 m of the atmosphere for RCP8.5 of the simulation year 2008 (see Fig. 3.14 f). But the associated wind energy density signal for this experiment shows almost no change for December and even turns to decreasing values of about -1.0% for October and November (see Fig. 3.18 f). This shift towards lower wind energy density values can be explained by changes in air density. Because warmer air is merely able to carry less moisture, air density reduces with increasing temperature. This direct effect of temperature change is observable in simulated air density change signals.

Monthly mean air density change signals for the lowest 300 m of the atmosphere are illustrated in Fig. 3.19. A general decrease is observable, which expresses more pronounced with rising scenario intensity. The spread of the monthly mean change signals is rather uniform with height ranging from -0.05 to -0.45% (RCP2.6; see Fig. 3.19 a-b), -0.25 to -0.60% (RCP4.5; see Fig. 3.19 c-d) and -0.30 to -1.19% (RCP8.5; see Fig. 3.19 e-f). Intensities of air density changes reflect intensities of the associated temperature change signals (cf. Fig. 3.13). Exemplarily, the largest air density decreases are observable for November and December of RCP8.5, being in line with the

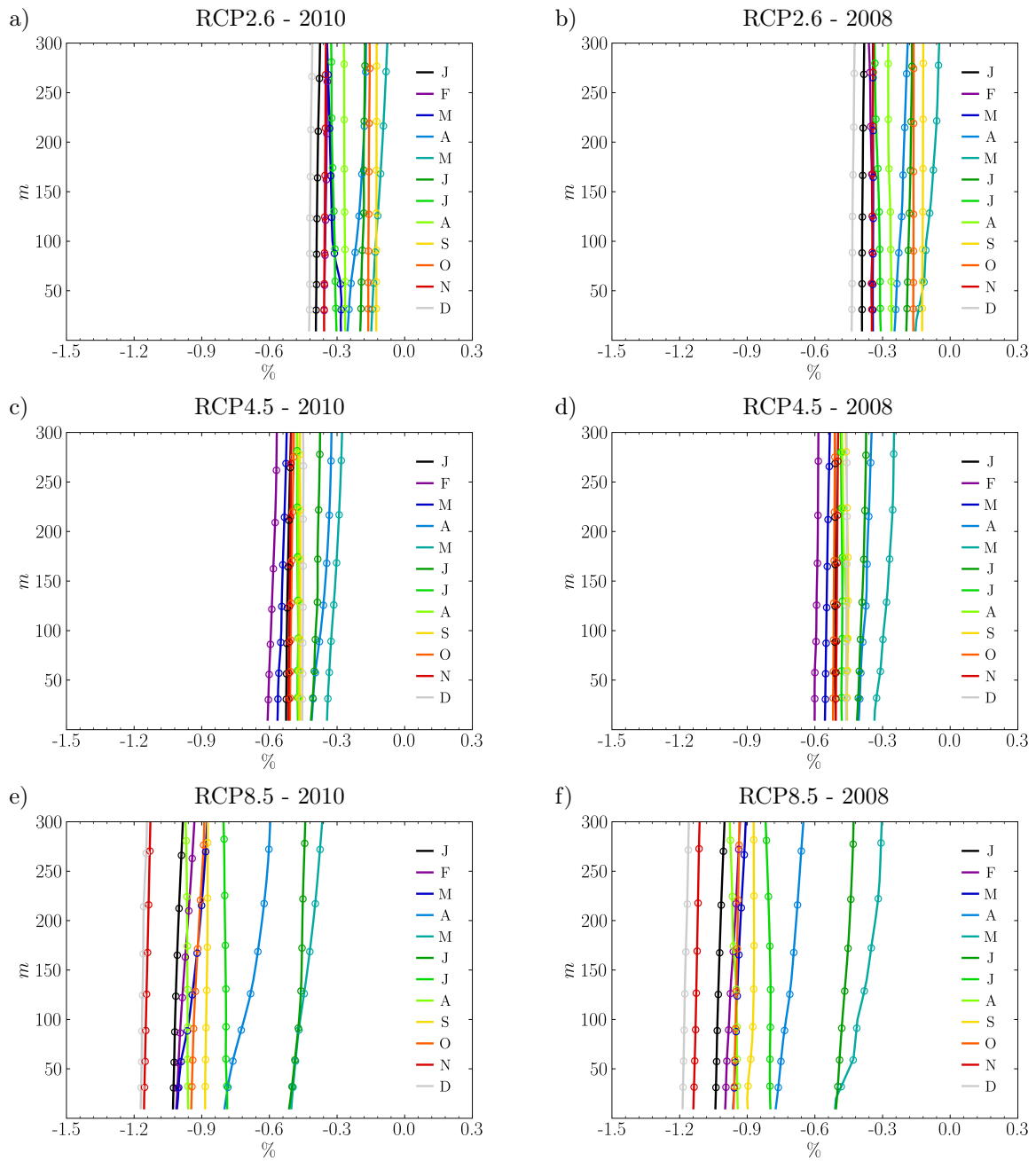


Figure 3.19: Vertical air density change signals for the lowest 300 m of the atmosphere as simulated for REMO-NH surrogate climate change experiments. The boundary forcing of the experiments is adjusted with vertically variable climate change signals based on long-term climate change projections following the RCPs 2.6 (a-b), 4.5 (c-d) and 8.5 (e-f) according to Fig. 3.3. Air density is derived according to Eq. 3.11. The signals have been achieved by spatially averaging over a local area comprising 5×5 grid boxes centered in the middle of the domain in the German Bight (see Fig. 3.7) and temporally aggregating to monthly profiles. Afterwards, the relative differences between the surrogate climate change simulation and the reference simulation are computed. Shown are mean relative change profiles in % for every month of a year, separately for the simulation years 2010 (a, c, e) and 2008 (b, d, f). Circles depict average model level heights for air density above the lowest additional height level at 10 m (half levels).

highest temperature change signals detected for those months. Contrary, the least temperature changes emerge from April to June for RCP4.5 and RCP8.5 (while this is rudimentary for RCP2.6), where air density changes occur to be smallest.

Changes in air density get frequently neglected in studies assessing wind energy and climate change (*Hueging et al.*, 2013; *Reyers et al.*, 2014, 2016; *Tobin et al.*, 2015, 2016; *Moemken et al.*, 2018). Even though wind energy density changes get determined by wind speed changes because of its cubic proportionality, a negative impact on wind energy density can be expected from air density decrease with increasing temperature (cf. *Pryor and Barthelmie*, 2010). In this regard, small changes in wind speed can get exceeded by larger changes in air density. Nonetheless, climate projections do not commonly provide (prognostic) information about air density. Also in the frame of this thesis, air density got newly introduced as additional output variable to REMO.

In summary, monthly mean vertical wind speed profiles reveal change signals varying in sign and intensity throughout the year. Striking are wind speed increases for the months of April to May and decreases for the months of July to September, which tend to evolve more pronounced with increased temperature change perturbation (i.e. rising scenario intensity). Additionally, distinct gradients in the wind speed change signals across the lower PBL are observable primarily for the former months. A linear relationship of those vertical wind speed change signals to temperature change intensities is not traceable. Nevertheless, a potential indirect dependency exists through the gradient of vertical temperature change signals. The gradient alters atmospheric stability conditions in the PBL through changes in the potential temperature flux. In turn, altered atmospheric stability conditions can be related to observed wind speed change signals. In addition to changes in wind speed, decreasing air density with increasing temperature are identified to negatively impact wind energy density changes, even though changes in wind energy density get primarily determined by wind speed changes.

3.6 Conclusions

According to current and prognoses of future wind turbine technology, the wind resource across the lowest 300 m of the atmosphere is of relevance for wind energy generation. From a theoretical perspective of boundary layer meteorology, physical processes determining the vertical wind speed profile are non-linear. Because physically consistent climate and climate change information across wind turbine operating altitudes are hardly available, extrapolation of near surface wind speed information to turbine hub heights is performed to approximate the wind resource for

energy generation. Even though commonly applied, such methodologies do not represent a physically consistent description. A suitable tool to achieve a physically consistent formulation of atmospheric motion is dynamical atmospheric modelling based on the Navier-Stokes equations. Dynamical climate models are constructed like this, while interactively simulating climate time scales. Therefore, such models are potentially capable to provide wind energy-specific climate and climate change information. With the recently developed non-hydrostatic extension of the regional climate model REMO, referred to as REMO-NH, convection-permitting scales of just a few kilometres are feasible. In addition, a vertical resolution sufficiently better resolving the PBL is achieved, complemented by wind energy-specific variable output across the lowest 300 m of the atmosphere. Based on this, a novel high-resolution experimental modelling framework is set up to generate climate and climate change information of the wind resource across wind turbine operation altitudes.

Convection-permitting configurations at the kilometre-scale comprising an increased horizontal as well as vertical model resolution depict a REMO setup which has not been investigated with respect to PBL characteristics until now. Therefore, the impact of resolution on simulated wind climate in the PBL is analysed using simulation setups of different horizontal and vertical resolution combinations, enabling to evaluate currently developed kilometre-scale simulations against state-of-the-art RCM configurations. An enhanced intra-annual variability (reaching almost $\pm 1.0 \text{ ms}^{-1}$) as well as an indication for extended inter-annual variability in wind climate could be observed as a result of an increased vertical resolution. Even though annual mean wind speed patterns are not substantially affected, the combination of enhanced intra-annual and inter-annual variability can lead to considerable variations in power production estimates. Therefore, an increased vertical resolution providing enhanced variability approximations is concluded as beneficial for wind energy applications.

Performed simulations with REMO-NH combine a higher vertical resolution with an increased horizontal resolution. Consequently, coastlines and topography get better resolved and provide additional fine-scale PBL information, being of importance for local-scale climate. In addition, wind speed fluctuations across the lower PBL get better represented at this higher resolution. These effects can be expected to express more intense over land surface and in particular over complex terrain, as the simulation domain is to a large extent covered by ocean being characterised by a comparably smooth surface with short roughness length and larger heat capacity. Overall, high-resolution non-hydrostatic simulations with the regional climate model REMO-NH are concluded as suitable to simulate and provide wind climate information of the PBL.

Climate projections at the kilometre-scale spanning several decades are economically not feasible at this instance of time. Therefore, the surrogate climate change methodology of *Schär et al.* (1996) and its extension by *Kröner et al.* (2017) is adopted to mimic a potential future climate by artificially adjusting the boundary conditions according to a temperature change signal, while the dynamics of the large-scale circulation remain unchanged. In this regard, surrogate climate change experiments are performed with REMO-NH using temperature change signals according to climate projection scenarios of different intensities for the end of the 21st century to consider a bandwidth of change. For the first time, this set up enables to study thermodynamically induced changes in wind climate, wind characteristics and wind energy conditions in the lower part of the PBL with the regional climate model REMO.

Monthly mean wind speed profiles reveal change signals varying in sign and intensity throughout the year. In particular the months of April to May (reaching 4.4%) and July to September (reaching -3.8%) evolve pronounced (with opposing signals), along with distinct gradients across the lower PBL. In this regard, change signal magnitudes increase with rising scenario intensity, but a linear relationship of those vertical wind speed change signals to temperature change intensities is not traceable. Nevertheless, a potential indirect dependency exists through the gradient of vertical temperature change signals. This gradient alters atmospheric stability conditions in the PBL through changes in the potential temperature flux. In turn, the altered atmospheric stability conditions can be related to the analysed wind speed change signals.

In addition to changes in wind speed, decreasing air density with increasing temperature (reaching -1.19%) are identified to negatively impact wind energy density changes. Even though changes in wind energy density get primarily determined by wind speed changes, larger changes in air density can exceed smaller changes in wind speed. Therefore, the consideration of air density information (in addition to wind speed) is concluded as necessary for a correct estimate of the wind energy resource under changing climate conditions.

Wind speed and air density conditions as well as their associated changes as generated through the surrogate climate change experiments get used to provide estimates about power production for the financial modelling covered in Chapter 4. Because a proper and sound uncertainty assessment encompasses measures of significance and robustness, and such statistical indicators can not be provided together with the performed experiments, only a rudimentary uncertainty estimate is included. This comprises a bandwidth of climate change scenario information of two individual simulation years. The simulation years are deliberately chosen to represent wind energy generation at the more upper and lower range with respect to the previous 10 years of production.

4 Financial Modelling of Wind Energy Project Financing

To evaluate the financial risk of wind energy with respect to climate change impacts, a financial model is set up and applied. Sensitivity experiments are performed making use of wind energy-specific climate and climate change information generated through surrogate climate change experiments as presented in Chapter 3. The applied modelling chain allows to identify potential impacts on the financing of wind energy being related to changes in the wind resource due to changing climate conditions.

An introduction to project financing and financial modelling is given in Section 4.1. Section 4.2 comprises a description of the financial model applied in the frame of this thesis. Furthermore, economic assessment criteria are presented, and the static economic and technical as well as variable meteorological assumptions for the financial modelling exercise are defined. The financial modelling results are presented in Section 4.3, followed by concluding remarks in Section 4.4.

4.1 Introduction

The term *financing* refers to the process of raising or the provision of monetary funding. In this context, external financial capital is usually tied to the realisation of a particular purpose, for example realising an investment. Large-scale infrastructure projects - such as renewable energy projects - require long-term financing (*Böttcher, 2010*). The revenues to be generated by such projects can be accounted isolated from the company's balance sheet. This allows for a financing structure which can be solely based upon the project's projected cash flows. Such a financing structure depicts a special type of financing, which is referred to as *project financing* (*FS-UNEP, 2017c*). As various stakeholders are involved in such financing constructs associated with time-consuming and cost demanding negotiation processes, transaction costs are high, independent of the project size. According to *FS-UNEP (2017c)*, this is why project financing is just of relevance for medium-scale to large-scale investment volumes beyond 25 mUSD.

In particular wind energy projects require large amounts of capital costs prior to the project realisation (*Blanco, 2009*). Because planned lifetimes of such projects span at least 20 to 25 years (*BMWi, 2018; Krohn et al., 2009*), most large-scale wind power plant projects are based on long-term financing and are realised through project financing (*Böttcher, 2013, 2012*). The corporate structure of project financed projects is organised in special purpose vehicles to legally isolate project investment volumes from sponsor's balance sheets, thus, protecting their assets from utilisation as collateral (*FS-UNEP, 2017c*). Therefore, a necessary condition for wind energy projects is to act as stand-alone projects with the ability to serve cash obligations solely from generated revenues. The provision of sufficient financial capital from lenders and sponsors for the realisation of such projects is, thus, solely based on the project's projected profitability and risk-return profile. To evaluate the project's profitability and risk-return profile, projections of the project cash flows are realised through financial modelling (*FS-UNEP, 2017a*).

Financial modelling, in terms of project financing, refers to the simulation of cash flows under certain economic and technical project assumptions. It is used as a tool to provide information about bankability as well as attractiveness (in terms of the risk-return profile) of a project in the financial decision process. Particularly sponsors and potential lenders base their decisions on investments and debt provision on such information. The financial outcome is influenced by a multitude of different and sometimes constantly changing interdependent parameters and variables, which need to be considered along the business plan preparation. A properly designed financial model is capable to perform sensitivity analyses (*FS-UNEP, 2017a*). As such, financial

outcomes can be simulated with differing parameter and variable assumptions. It is an important tool throughout the entire project development phase and complements the project business plan. Usually sponsors as well as lenders make use of a financial model alongside the project development and realisation. Even though interests of sponsors and potential lenders are generally opposed with respect to project assumptions, cash flow distribution and risk-return profiles, the underlying mechanics of such financial models are congruent and uniformly applicable (*FS-UNEP*, 2017a). Along the business plan preparation, a fairly simple and annually-resolved financial model is commonly elaborated by the project sponsor at an early stage to evaluate the projects' feasibility. As well, it is used to attract and negotiate with potential lenders. The level of detail of the financial model advances with project progress as more concrete information get disclosed with the various project stages, which can subsequently be included. Thus, it is applied primarily for the purpose of risk identification, allocation and mitigation (*FS-UNEP*, 2017a). Moreover, adequate capital structures, comprising debt and equity portions, are elaborated.

Project financing plans for large-scale wind power plant projects are based on assumptions of expected yield over project lifetimes spanning at least 20 to 25 years (*BMW*, 2018; *Krohn et al.*, 2009). Therefore, financial modelling is applied to project cash flows and evaluate the project's economic viability. Reaching climate relevant scales, information about climate and climate change with respect to the wind resource are of potential relevance for financial assessments of wind energy project financing, because expectations of the subsequent power production, which serve as model assumptions, might be affected. As the aim of this thesis is to assess climate change impacts on wind energy financing, financial modelling is applied as a tool in combination with wind energy-specific climate and climate change information (cf. Chapter 3).

4.2 Methodology

This section provides a description of the methodological approach to project financial cash flows with respect to the project financing of an imaginary offshore wind farm located in the German Bight. A description of the financial model applied in this thesis and an introduced extension to simulate monthly-resolved cash flows is presented in Section 4.2.1. To assess and evaluate the financial viability in terms of project profitability and financial risk, economic assessment criteria are specified in Section 4.2.2. Finally, Section 4.2.3 provides an overview of the simulation setup for sensitivity experiments performed with the financial model. In this regard, assumptions for static technical and economic parameters as well as for meteorological variables are illustrated.

4.2.1 Description of the Financial Model

A simplified but fully-fledged financial model is set up to simulate and project the financing cash flow of a particular project. The model is fully flexible with regard to the major financing assumptions, comprising technical and economic as well as meteorological boundary conditions. In this regard, the financial model is defined as a numerical spreadsheet processing a comprehensive list of input assumptions and providing transparent financial outcome, reflecting the complex interaction between boundary conditions and formulated interdependencies.

Organisation of the Financial Model

The financial model contains all necessary informational elements and assumptions to project the financial statements over the lifetime of the project. Principally, it is organised in a Microsoft[®]Excel-based spreadsheet comprised of different worksheets. An input worksheet contains various information about technical and economic as well as meteorological assumptions, which are usually based on a previously prepared business plan. These assumptions serve as boundary conditions and force the model. The interim calculation and output worksheet depicts the actual core of the financial model. It contains all interdependencies expressed in formulae and organises the various calculations. Once set up, this part of the model will not be subject to any adjustments, because changing assumptions are organised exclusively through the input worksheet. In this way, the model is capable to perform sensitivity analyses.

As a fully-fledged model, statements about profit and loan, balance sheet and cash flow are included. The balance sheet concept assures consistency of financial transactions through double-entry accounting. In this manner, liabilities and equity of an asset are always required to balance. Further crucial elements of a fully-fledged model are a balance sheet cash line calculation based on cash flow statements, an interactive linkage of assets and depreciation as well as an equity position considering discrete profit and dividend payments (*FS-UNEP*, 2017a).

The financial model used in the frame of this thesis is based on a financial model developed and taught within the course “Climate & Renewable Energy Finance” offered by the Frankfurt School of Finance & Management (www.frankfurt-school.de) in cooperation with the UNEP Collaborating Centre for Climate & Sustainable Energy Finance (<https://fs-unep-centre.org>). Due to reasons of copyright, a public disclosure of the financial model is not permitted. Therefore, only a description of the model is given - in addition to results of the financial modelling exercise presented in Section 4.3.

Computational Core of the Financial Model

The assumptions about technical and economic as well as meteorological information are translated by the core of the financial model, describing all interdependencies through numerical formulations. The simulation and projection of the financing cash flow is performed and discounted over the expected lifetime of the project at a continuous temporal resolution.

In the case of wind energy, meteorological information are translated into values of power production per generation unit, based on the wind energy resource availability and technical assumptions of the wind turbine (see Section 4.2.3 for details). Subsequently, the total electricity generation per time unit is determined for the entire asset. If applicable, this can be discounted with a constant system degradation factor to account for potential wear and tear. Furthermore, wind farm wake losses and downtime can be taken into account by (slightly) reducing the potential power production through constant factors. The revenues per unit of electricity produced are predefined but can be discounted with a constant expected tariff increase over the lifetime of the project. Finally, the total revenues per time unit are calculated as the product of the revenue per unit of electricity produced and the total power output.

Variable operating costs for maintenance, insurance, administration, land lease and other cost positions are predefined and summed to the total initial operational expenditure (OPEX). Thus, the operating costs are treated as a single cost position by the financial model. The OPEX can be discounted with a constant cost increase, representing rising expenditures with progressing operating life cycle of the asset.

The amount of total revenues minus operating costs represent the earnings before interests, taxes, depreciation and amortisation (EBITDA) of the profit and loan. Subtracting the depreciation from the EBITDA reveal the earnings before interests and taxes (EBIT). Here, the depreciation (and amortisation) of the asset is expressed as a linear depreciation rate by dividing the total investment costs less potential grants by the lifetime of the project. Allocating the EBIT with interest income and expenses provide information about the profit before taxes (PBT). Hence, a tax shield applies to the debt service. The PBT is used to calculate the tax charge by multiplication with the predefined tax rate. Finally, the surplus of the total revenues less operating costs and taxes represent the net operating cash flow. This can be complemented by an additional capital expenditure (CAPEX) for replacement of certain components after a predefined period. Thus, the net operating cash flow would form to a net operating and investing cash flow.

The financing cash flow is based on the net operating and investing cash flow, which serves as cash flow being available for debt service. Moreover, the financing cash flow is flanked by

a predefined capital structure composed of equity and a single debt tranche with a definite duration period (loan tenor). The regular debt service comprises the repayment of debt as well as interest expenses on outstanding debt. Project financing is usually comprised by a Debt Service Reserve Account (DSRA). This financial instrument serves as a structural mechanism to enhance creditworthiness by securing debt service during situations with insufficient revenue generation to cover repayment of debt. Furthermore, the financial model consists of a predefined minimum cash reserve. Before debt is repaid, interest income from those cash reserve accounts and interest expenses on outstanding debt are accounted to the cash flow available for debt service, based on predefined interest rates for cash and debt. Subsequently, debt repayment is proceeded from the remaining cash. The cash flow available after debt service is used for additions to the cash reserve accounts of DSRA and minimum cash reserve. Remaining profit is subject to profit sharing and gets distributed to equity holders as equity dividends. However, if a mandatory senior debt repayment is implemented in terms of a cash sweep, the dividend payments might be reduced by the predefined amount of the cash sweep. As profit gets fully distributed to equity holders as equity dividends, excess cash amounts to zero by definition.

Double-entry accounting (as realised through the balance sheet) serves as a security measure to assure balanced liabilities and equity of the asset. Moreover, modelling errors can be identified more easily by detecting balance mismatches compared to tracing back errors from the distilled financial modelling results.

The simulation and projection of cash flows with the financial model described above can be used to derive economic assessment criteria to assess and evaluate the financial viability. The economic assessment criteria, which are used to analyse the financial risk of wind energy with respect to climate change impacts, are presented in Section 4.2.2.

Simplifications of the Financial Model

Certain simplifications apply to the financial model described above, as illustrated in *FS-UNEP* (2017a). All cash flows are assumed to appear at the same instance in time. Resulting working capital requirements are covered through a minimum cash assumption. This reflects required capital for financing of working capital and compensates for different instances in timing of cash flows. Assets - in this case the wind farm - are regarded as fixed. Thus, no differentiation among various components of the asset and individual product cycles is made. The capital structure is composed of equity and a single debt tranche. Even though actual capital structures might include several debt portions of different duration periods, this would primarily cause an increase of the

model complexity, while the essential and most important elements of the financing mechanism are covered by the applied capital structure. All cash values are consistently expressed in a single currency throughout the model to prevent for currency mismatches. Statements of interest expenses and income are not subject to circular references but rather get calculated from the balances of the previous period. This simplification does not result in a major impact on the financial outcome but enhances the stability of the model.

The complexity of this financial model corresponds to an early stage of the project development phase, when assumptions are relatively rough. Besides the simplifications presented, this model is suitable to analyse financial viability with respect to the governing assumptions. Contrary, it is inappropriate to handle and provide sufficient detail which would be required during the negotiation phase with potential lenders.

Extension to Simulate Monthly-Resolved Cash Flows

The initial financial model is set up to cover and provide annually-based financials (*FS-UNEP*, 2017a). As being presented in Chapter 3, monthly-resolved climate and climate change information are of importance for wind energy applications to cover information about intra-annual variability and variability change. To allow the financial model to process monthly-resolved meteorological information as input, the computational core of the model is extended to cover monthly-resolved cash flow simulations. Therefore, the computation of the operating and investing cash flow is adjusted to comprise monthly variable electricity generation. In this regard, a potential system degradation is adapted to affect the electricity generation on a monthly scale as well. Moreover, the OPEX expressed in annual cash amounts, is linearly partitioned to monthly share rates. However, potential increases in revenue due to tariff increases and rising OPEX costs remain to apply on an annual basis. As well, profit and loan and the financing cash flow are extended to cover monthly-resolved cash flows. This does impact on depreciation rates, taxes, interests, debt as well as equity which are due on a monthly basis.

The extension to simulate monthly-resolved cash flows is balance sheet and quality-checked against the annually-resolving initial version of the financial model within a simulation setup using the same boundary conditions. The entailed adjustments mentioned above cause implications. The major impacts arise from the timing at which debt gets serviced. Because most of the liabilities which would be serviced once per year when annually-resolved, are due prior to the initial maturity date at the end of the year. This is why interest expenses get degraded and the regular debt service is slightly reduced. Moreover, the cash flow available after debt service is slightly increased

because of this behaviour and, thus, provides more cash being available for a potential cash sweep (which would accelerate the debt repayment even further) and equity dividends. Furthermore, the monthly-resolution causes the termination of liability duties and, thus, the release of the cash reserve accounts (of DSRA and minimum cash reserve) to occur at an earlier instance in time, compared to annually-based financials. This offers higher value to equity holders, according to the time value of money. Nonetheless, these implications are reasonable from an economic perspective and simply caused by the increase of the temporal resolution of the cash flow simulation.

The ratio of the free cash flow and the regular debt service, the Debt Service Cover Ratio (DSCR), is a fundamental economic assessment criteria to assess the financial viability of a project (see Section 4.2.2 for details). Here, the free cash flow is determined by the revenues generated from the power production, which, in turn, are subject to the uptime and vary with months due to their differing number of calendar days. This results in more variable DSCR values linked to the intra-annual variability of the power production, especially at the beginning of the project financing period when the regular debt service is largest.

Overall, with the extension to simulate monthly-resolved cash flows, the financial model is now capable to process monthly-resolved meteorological information as input. With this development, the debt service gets slightly accelerated and, thus, equity dividends slightly increase over the lifetime of the project, which is economically reasonable. Worth to mention is the effect on the DSCR which adds value to the financial outcome as intra-annual variability of the power production gets incorporated. This enables to incorporate and assess the financial risk of wind energy project financing with respect to intra-annual variability and variability change in the wind resource.

4.2.2 Economic Assessment Criteria

The principle of project financing is to provide long-term financing based on the cash flows projected for the particular project. To evaluate the financial viability of the projected cash flows of such projects, economic assessment criteria are used as measures. Those economic assessment criteria translate and distill the simulated cash flow information to comprehensible quantities. As such, they allow sponsors or commercial lenders and investors to judge on the bankability, the risk-return profile and attractiveness of the particular project. In the frame of this thesis, such economic assessment criteria are used to assess and evaluate the financial risk of wind energy with respect to intra-annual and variability change. Here, the financial risk is a measure of the profitability of an investment or project and its internal financial risk.

Project Profitability

A standard economic measure in financing to determine the profitability of an investment or project is the Net Present Value (NPV). The NPV describes the Present Value (PV) of future cash flows generated at a certain discount rate (*FS-UNEP*, 2017b). In practical terms, it is a measure of the surplus or shortcoming of future cash flows with regard to capital cost effects, translated into terms of present monetary value, thereby, taking into account the time value of money. To achieve the NPV, the calculated net cash flows for each monthly period are discounted at a monthly rate of return to determine its PV. The NPV is then the sum of these PVs over the expected lifetime of the project (see Eq. 4.1). Generally, an investment or project rated with a positive NPV is regarded to generate profit, while loss is associated with a negative NPV.

$$\text{NPV} = \text{CF}_0 + \frac{\text{CF}_1}{(1+r)^1} + \frac{\text{CF}_2}{(1+r)^2} + \dots + \frac{\text{CF}_t}{(1+r)^t} = \sum_{t=0}^N \frac{\text{CF}_t}{(1+r)^t} \quad (4.1)$$

where

- NPV : Net Present Value
- CF_t : net cash flow at time t
- r : discount rate
- N : total number of periods

However, the NPV is prone to the chosen discount rate, which needs to be determined based on assumptions of future development of the capital market. This is subject to economic uncertainty which grows with increasing time horizons and is, thus, of relevance for long-term capital required for project financing. To circumvent the determination of the discount rate for the calculation of the NPV, when assessing the profitability of an investment or project, the Internal Rate of Return (IRR) can be applied. The IRR is defined as the discount rate r for which the NPV $\stackrel{!}{=} 0$ (according to Eq. 4.1). Thus, the IRR represents the internal interest rate at which the cash value of the investment or project reaches zero. In practical terms, this reflects the margin where no internal profit would be generated anymore. The IRR is calculated directly within the Excel spreadsheet of the financial model, executing Excel's built-in IRR-function. Using this function, a goal seek is performed on the net operating and investing cash flow, which represents the free cash flow. As the cash flows are simulated on a monthly-resolution (following the extension presented in Section 4.2.1), but IRRs and IRR margins are usually defined on values based on annual cash flows, the IRR is upscaled to an IRR representative for annual cash flows while

keeping the temporal information of the simulated monthly cash flows (see Eq. 4.2).

As the IRR is a principal measure of the general profitability of a project or investment used and required by project sponsors and commercial lenders, equity holders might be interested in the IRR value specific to equity dividends. This Equity Internal Rate of Return (EIRR) is calculated analogous to the IRR, but using the cash flow to equity holders instead of the free cash flow.

$$\text{IRR}_a = (1 + \text{IRR}_m)^n - 1 \quad (4.2)$$

where

IRR_a : IRR value representative for annual cash flows

IRR_m : IRR value based on monthly cash flows

n : number of periods per year (here: 12 for monthly-resolution)

Financial Risk

In addition to the (long-term) project profitability, the credit worthiness of the project over its entire lifetime is crucial to commercial lenders. The Debt Service Cover Ratio (DSCR) is a key economic assessment criteria to determine the capability and efficiency to generate sufficient revenue for debt servicing and depicts a primary financial indicator for wind energy project financing (*Böttcher*, 2013, 2012, 2010). It is defined as the ratio of the free cash flow and the outstanding regular debt service at a specific instance of time (see Eq. 4.3). In practical terms, the DSCR is a measure of the ability to service debt at any time of the loan tenor. If a minimum DSCR value ≥ 1 is reached over the entire payback period of the project, sufficient coverage of debt service is achieved, thus, demonstrating financial validity of the project. Moreover, the debt service is rated more efficient, the higher the minimum DSCR. Commercial lenders often require specific minimum DSCR ratios including a certain safety cushion and loans are generally easier to acquire with higher coverage ratios of debt service (e.g. *Böttcher*, 2013).

$$\text{DSCR}_t = \frac{\text{EBIT}_t - \text{taxes}_t + \text{depreciation and amortisation}_t}{\text{interest on debt}_t + \text{debt repayment}_t} = \frac{\text{free cash flow}_t}{\text{regular debt service}_t} \quad (4.3)$$

where

DSCR_t : Debt Service Cover Ratio at time t

EBIT_t : earnings before interest and taxes at time t

In the frame of this thesis, the DSCR gets calculated on a monthly-basis. This, allows to study the effect of monthly varying cash flows, due to a variable power production, on the regular debt service. Thus, the financial risk of wind energy can be assessed with respect to intra-annual variability and variability change.

4.2.3 Simulation Setup

Financial model simulations are performed under different meteorological assumptions to assess the sensitivity of projected cash flows for project financing of wind energy with respect to intra-annual and variability change. Therefore, technical and economic assumptions specifying an imaginary offshore wind farm are defined, based on accessible key data of operational and planned offshore wind farms located in the German Bight, and iterated with external expert advise.

The financial model is sensitive to static and dynamic assumptions. Hence, a proper and meaningful simulation setup is key, as it is subject to garbage in-garbage out (*FS-UNEP*, 2017a). In this regard, it needs to be clarified that the chosen simulation setup assumptions presented in the following depict a deliberately chosen first guess, while the representativeness might be subject to discussion. Consultation of an experienced financial specialist in the field of renewable energy financing is received for advise concerning the technical and economic assumptions. In reality, assumptions vary among projects and with the intentions of project developers, which is why the financial model simulation results can strongly diverge. Therefore, a sensitivity analysis with respect to all technical and economic assumptions would be valuable to elaborate and evaluate different project and project financing scenarios. However, this is outside the scope of this thesis which focus is on the sensitivity of the financial model with respect to the meteorological assumptions affecting the power production.

Technical Assumptions

Analogous to operational and planned offshore wind farm projects in the German Bight (e.g. www.4coffshore.com for an overview), an imaginary offshore wind farm with a nominal system size of 400 MW is defined. This corresponds to a wind farm composed of 50 8.0 MW wind turbines. The associated system costs are chosen to account for 4 m€ per MW installed capacity, which is regarded as a realistic magnitude for current offshore wind energy (*J. Böttcher*, personal communication, August 27, 2018). Assuming contingencies to amount 1.0% of the system costs, the total initial CAPEX amounts to 1.616 bn€. A project lifetime of 20 years is expected for this imaginary offshore wind farm project. Over this lifetime, no additional CAPEX for replacement of

plant components nor system degradation is assumed, as both is expected to be incorporated and balanced by the operation and maintenance (O&M) costs (*J. Böttcher*, personal communication, August 27, 2018).

Operating cost assumptions for offshore wind energy are highly uncertain and no sufficient information is available because of lacking experience. However, O&M costs are assumed to roughly amount to as much as the total initial CAPEX over the project lifetime of 20 years (*Böttcher*, 2013). Basically three options exist to declare the operating costs: either as fixed costs per period (€ per year), as fixed costs per unit of power installed (€ per kW) or as variable costs per produced unit of power (€ per kWh). For simplicity reasons, O&M costs are expressed as fixed costs per unit of power installed. Operating cost assumptions are composed of maintenance costs, insurance, administration, land lease and any other costs. All operating cost positions are expressed as shares of the initial system costs and represent annual expenses. The maintenance costs are defined to amount 3.0% of the initial system costs. Insurance and administration is rated at 0.5% and land lease at 1.0% of the initial system costs. No additional cost position is utilised. Thus, the total initial OPEX amounts to 80 m€ per year, which corresponds to 200 k€ per MW installed capacity. For the O&M costs, an annual change rate of 2.0% is introduced to account for inflation.

Furthermore, assumptions concerning the operation of the wind farm are present. As wind turbines organised in a farm structure are prone to shadowing effects, a flat wind farm wake loss of 10.0% is used (*Hau*, 2014). As well, the operational uptime is defined to amount 95.0% due to regular maintenance and expected failure (*J. Böttcher*, personal communication, August 27, 2018). These assumptions for operational loss get directly allocated with the power production derived from the meteorological assumptions (see below).

A complete list of all technical assumptions, which serve as input parameters to the financial model simulations, are indicated in Tab. 4.1.

Economic Assumptions

The project financing of the imaginary offshore wind farm is realised with a financing structure of the total initial CAPEX being composed of 60.0% debt and 40.0% equity (e.g. *Böttcher*, 2013), whereas no grants or other sorts of subsidies apply. Debt is provided at a constant interest rate of 5.0% (e.g. *Fraunhofer ISI*, 2015), while the loan tenor has a duration period of 16 years (e.g. *Böttcher*, 2013). Here, the first year is treated as grace period, where the regular debt repayment gets waived to accelerate the filling of cash reserve accounts. The minimum cash reserve is set

Table 4.1: Technical assumptions serving as input parameters for the financial model simulations.

Initial investment		
System costs		1 600 000 k€
Contingencies	1.0%	16 000 k€
Total initial investment (CAPEX)		1 616 000 k€
Total initial investment per MW peak		4 040 k€/MW
Replacement CAPEX		
Amount of initial investment	0.0%	0 k€
Technical details		
Nominal system size		400 000 kW
Expected annual system degradation	0.0%	
Expected project lifetime		20 years
Operating assumptions		
Wind farm wake loss	10.0%	
Uptime	95.0%	
Operating cost assumptions		
Maintenance costs (as share of initial system costs)	3.0% p.a.	48 000 k€ p.a.
Insurance (as share of initial system costs)	0.5% p.a.	8 000 k€ p.a.
Administration (as share of initial system costs)	0.5% p.a.	8 000 k€ p.a.
Land lease (as share of initial system costs)	1.0% p.a.	16 000 k€ p.a.
Other costs (as share of initial system costs)	0.0% p.a.	0 k€ p.a.
Total initial operating costs (OPEX)		80 000 k€ p.a.
Total initial operating costs per MW peak		200 k€/MW p.a.
Annual change rate	2.0%	

to 5 m€ at a constant interest rate of 2.0%. The DSRA is required to cover debt service over a period of 6 months, which corresponds to a debt service reserve of approximately 56.5 m€. Furthermore, a cash sweep is implemented to allow 50.0% of the free cash flow available after debt service and changes to cash reserve accounts to be used for accelerated debt repayment. The remaining excess cash gets fully distributed to equity holders.

Expected revenues are tuned to reach values associated with a pursued IRR reaching at least 4.0% over the project lifetime of 20 years (J. Böttcher, personal communication, August 27, 2018) and an annual cash flow based minimum DSCR ≥ 1.0 to guarantee sufficient coverage of yearly debt service. Following these requirements, an initial electricity tariff of 12.5 €/ct/kWh is

Table 4.2: Economic assumptions serving as input parameters for the financial model simulations.

Expected revenues		
Initial electricity tariff		12.5 €cent/kWh
Annual tariff increase	2.0%	
Starting year of tariff increase		2 nd year
Tax rate	25.0%	
Financing structure		
Grants	0.0%	
Debt	60.0%	969 600 k€
Debt interest rate	5.0%	
Loan tenor		16 years
Grace period		1 year
Equity	40.0%	646 400 k€
Minimum cash reserve		5 000 k€
Cash interest rate	2.0%	
Required DSRA	6 months	56 560 k€
Cash sweep	50.0%	

chosen, accompanied with an annual tariff increase of 2.0%, which is put into effect after the first year of operation. This is in line with feed-in tariff ranges provided for offshore wind energy in Germany (e.g. *Böttcher*, 2013). The tax rate comes in at 25.0% according to German flat rate tax regulations.

A complete list of all economic assumptions, which serve as input parameters to the financial model simulations, are indicated in Tab. 4.2.

Meteorological Assumptions

Contrary to the technical and economic assumptions, which are expressed as static parameters, meteorological assumptions are provided as variables which are dynamic over the course of the year to incorporate intra-annual variability. The financial model - as presented in Section 4.2.1 - requires information about monthly power production. To achieve this, information about wind speed and air density are translated into amounts of total monthly power production by use of a power curve specific for an offshore wind turbine. Wind turbine power curves are provided by the turbine manufacturers and describe the energy output as a function of wind speed and power for a given reference air density ρ_0 .

In the frame of this thesis, the power curve of a Vestas V164 8.0 MW[®] is applied, which depicts a representative offshore wind turbine being commercially installed since 2017 and operating at wind farms across the German Bight, the North Sea and along the European coastline (*MHI Vestas Offshore Wind*, 2018b). With a turbine hub height exceeding 100 m, a rotor diameter of 164 m and a rated power of 8.0 MW (*MHI Vestas Offshore Wind*, 2018a), this turbine type offers technical specifications which are representative for most recent installed offshore wind turbines. Even though, future offshore wind turbines beyond the 12.0 MW class with rotor diameter dimensions reaching 200 m and hub heights of 120 m are expected by 2025 (*BMW*i**, 2018), and technical development might offer even larger turbine technology, power curve information for future turbine generations are not available yet. This is why technical specifications of a state-of-the-art offshore wind turbine are used.

In this regard, the applied power curve of a Vestas V164 8.0 MW[®] is provided through *The Wind Power Program* (2018). This power curve is characterised by cut-in wind speed at 4.0 ms⁻¹ and cut-out wind speed at 25.0 ms⁻¹, while rated power of 8.0 MW is reached at 13.0 ms⁻¹. Because the wind energy density is dependent on air density (see Eq. 3.14), the wind turbine power curve gets adjusted for varying air density values of the time series. Therefore, in a first step, the wind speed values describing the power curve are adjusted for air density according to the relation in Eq. 4.4, following the international standard IEC 61400-12 (*IEC-61400*, 2015). Thus, the provided manufacturers' energy output ($E_{\text{out}}(v_{\rho_0}, P_{\rho_0})$) is transferred to energy output as a function with adjusted wind speed values ($E_{\text{out}}(v_{\rho}, P_{\rho_0})$). Secondly, the power values of this relation are matched to the initial wind speed values v_{ρ_0} of the given manufacturer's power curve ($E_{\text{out}}(v_{\rho_0}, P_{\rho_0})$). Thus, consistency with respect to wind speed bins as well as cut-in and cut-out wind speed values is assured.

$$v_{\rho} = v_{\rho_0} \left(\frac{\rho_0}{\rho} \right)^{1/3} \quad (4.4)$$

where

v : velocity

ρ : air density

ρ_0 : reference air density of manufacturers wind turbine power curve

The provided manufacturers' turbine power curve for a given reference air density ρ_0 of 1.225 kgm⁻³ as well as resulting adjusted power curves for air density values representative for an upper and lower bound are visualised in Fig. 4.1. In agreement with Eq. 3.14, a lower air density results in a

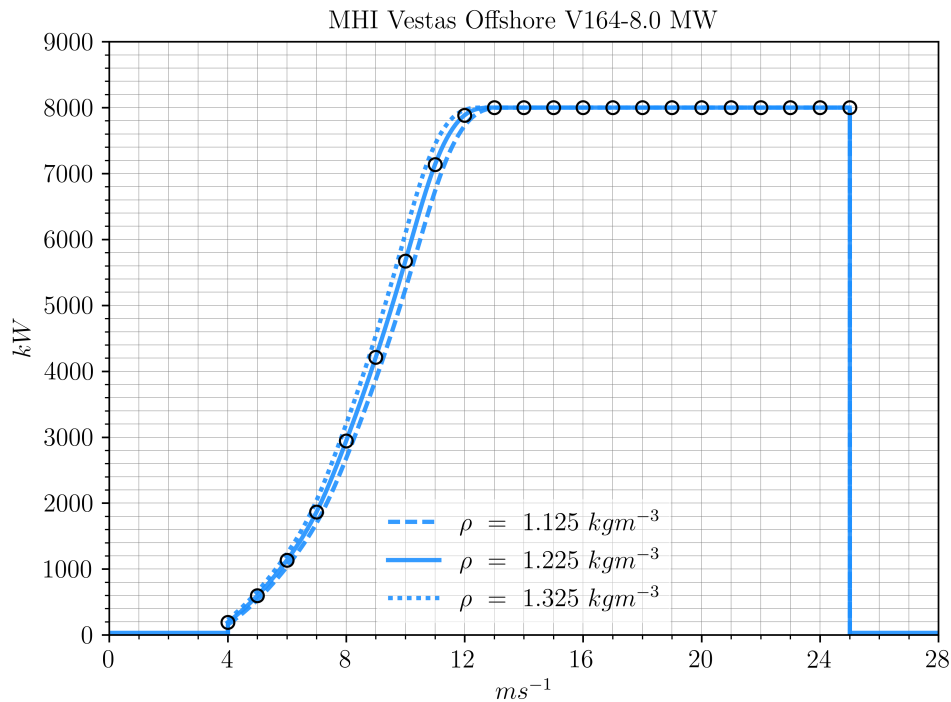


Figure 4.1: Power curve of a MHI Vestas Offshore V164-8.0 MW[®] offshore wind turbine. Rated power of 8.0 MW is reached at $13.0 ms^{-1}$, with cut-in wind speed at $4.0 ms^{-1}$ and cut-out wind speed at $25.0 ms^{-1}$, respectively. The manufacturers power curve is provided for an air density of $\rho = 1.225 kgm^{-3}$ (solid line). According to Eq. 4.4 the gained power curves for air densities of $\rho = 1.125 kgm^{-3}$ (dotted line) and $\rho = 1.325 kgm^{-3}$ (dashed line) are shown exemplarily. Circles depict provided manufacturers values from which the power curves are extrapolated to wind speed bins of $0.1 ms^{-1}$ using a spline fit to compute wind energy power production.

reduced power production and vice versa. Deviations in the power in the range of a few hundred kW are observable, emerging with the cut-in wind speed at $4.0 ms^{-1}$ and increasing with wind speed until rated power is reached at $13.0 ms^{-1}$.

The financial model allows to perform sensitivity analyses by changing certain input parameters, while retaining the remaining input. To analyse the impact of climate change on the financing of wind energy, simulations with the financial model are performed using climate and climate change information of different intensity as meteorological assumptions. Therefore, information about wind speed and air density as well as their associated changes, generated through the surrogate climate change experiments presented in Section 3.5.3, are used. A bandwidth of change for these meteorological variables is incorporated through the differing temperature change scenarios applied with the surrogate climate change experimental setup and through a rudimentary estimate

of inter-annual variability by means of two deliberately chosen simulation years, representing wind energy generation at the more upper and lower range with respect to the previous 10 years of production (*IWR*, 2018).

Information about wind speed and air density across altitudes where wind turbines operate are taken from the surrogate climate change experiments and translated into amounts of total monthly power production. This is achieved by computing the power production from the adjacent wind speed and the corresponding air density-adjusted power curve for every interval of the time series and every height level ranging from 20 to 220 m. Subsequently, the gained values get vertically average and aggregated to total monthly power production amounts. The gained total monthly power production for the two years of 2010 and 2008 and their associated changes corresponding to the surrogate climate change experiments are shown in Fig. 4.2. As the power curve (see Fig. 4.1) is defined to only produce energy at wind speeds between the cut-in wind speed of 4.0 ms^{-1} and cut-out wind speed of 25.0 ms^{-1} , solely climate and climate change information subject to this part of the wind speed distribution is reflected in the gained power production. This might lead to discrepancies in comparison to the potentially available wind energy density as presented and illustrated in Section 3.5.3 and Fig. 3.18, which is mainly a result of high wind speed events and the cubic relation of wind speed and wind energy density (see Eq. 3.14). Thus, events providing high wind energy densities but exceeding the operational range of the wind turbine do not produce any power. This circumstance depicts the realistic imprint of the technical feasibility of wind turbines to harvest energy from the available wind resource.

A complete list of the power productions gained from the surrogate climate change experiments and which serve as input parameters to the financial model simulations are indicated in Tab. A.7. These values represent the monthly energy generation of a single MHI Vestas Offshore V164-8.0 MW[®] wind turbine. Because the imaginary offshore wind farm is defined to have a nominal system size of 400 MW, the power output is upscaled corresponding to 50 of such 8.0 MW wind turbine types.

4.3 Results and Discussion

Financial model simulations are performed under different meteorological assumptions to assess the sensitivity of projected cash flows for project financing of an imaginary offshore wind farm with respect to wind resource change signals of different intensity. Here, the financial model presented in Section 4.2.1 serves as the tool to conduct those sensitivity experiments. Wind energy-specific

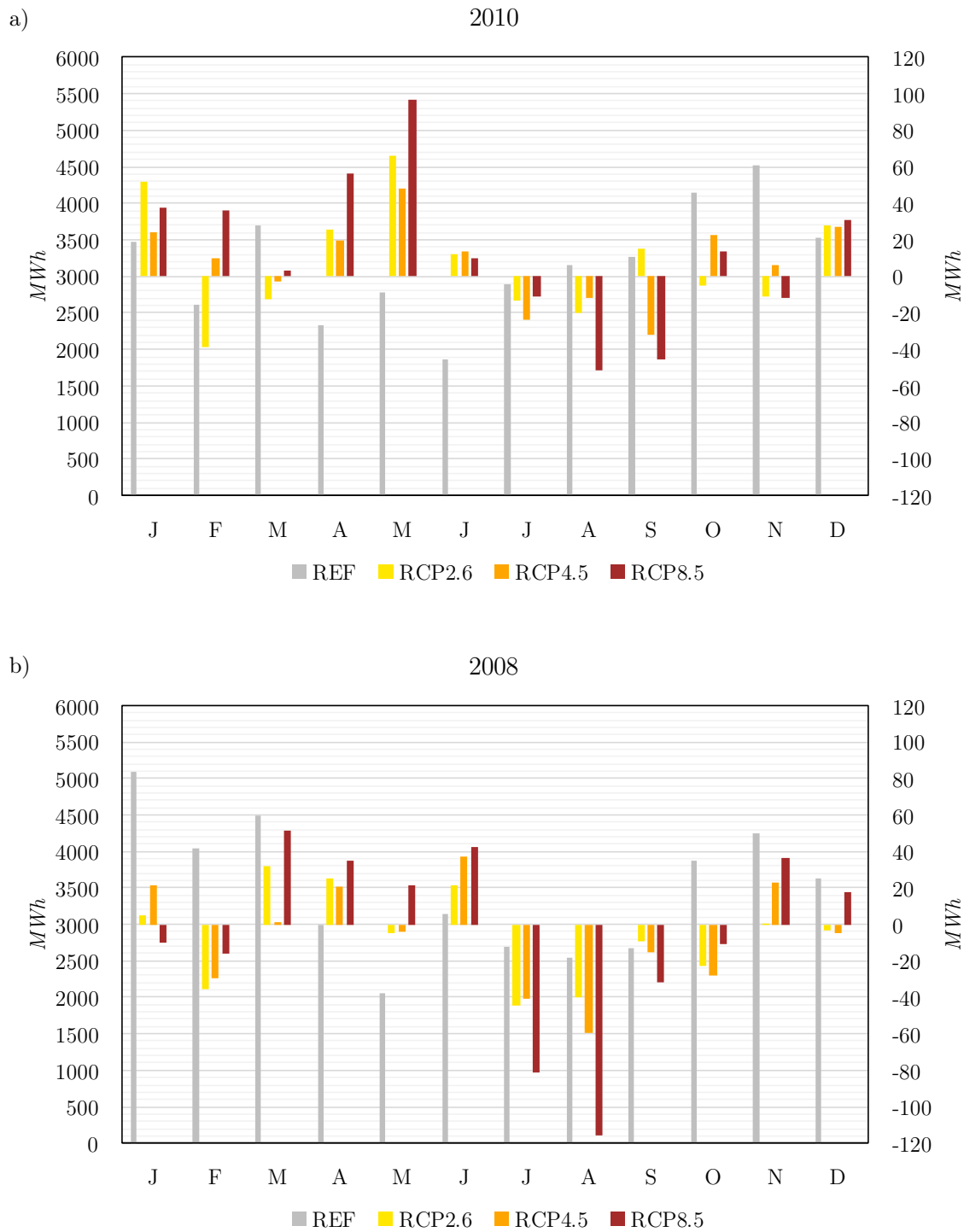


Figure 4.2: Total monthly energy output E_{out} of surrogate climate change experiments according to a ρ -corrected power curve of a MHI Vestas Offshore V164-8.0 MW[®] offshore wind turbine. The energy output in MWh is computed from hourly-resolved time series data of wind speed and air density taken and averaged over height levels ranging from 20 to 220 m. Shown are total monthly amounts for the reference (REF; grey) and their change values for the scenarios RCP2.6 (yellow), RCP4.5 (orange) and RCP8.5 (red) for both simulation years of 2010 (a) and 2008 (b).

climate and climate change information are taken from the simulation output of the surrogate climate change experiments (see Chapter 3) and get translated into meteorological assumptions (see Section 4.2.3). Technical and economic assumptions (see Tabs. 4.1 and 4.2) remain unchanged to solely analyse sensitivity with respect to differing meteorological assumptions.

The general behaviour and ability of the financial model to simulate financial cash flows for the project financing of an imaginary offshore wind farm are covered in Section 4.3.1. Subsequently, an assessment of the sensitivity of wind energy project financing with respect to wind resource change signals of different intensity is provided in Section 4.3.2.

4.3.1 Simulation of Wind Energy Project Financing Cash Flows

The performed financial model simulations project discounted monthly project cash flows of an imaginary offshore wind farm according to the technical, economic and meteorological assumptions presented in Section 4.2.3. In order to explore the general mechanism and behaviour of the financial model, the evolution of financial cash flows over the project lifetime are illustrated in terms of the free cash flow, the debt service and equity dividends. As well, the associated capital and cost structures are presented. In this first part of the results section, only analyses of current climate conditions are presented, while the impact of changing climate conditions with respect to the project financing of wind energy is subject to the subsequent Section 4.3.2. Analogous to the surrogate climate change experiments, the two simulation years of 2010 and 2008 are analysed to comprise inter-annual variability, as both years are characterised by differing total monthly power production amounts throughout the year as well as by differing total annual power production amounts (see Fig. 4.2). Due to reasons of visibility, only aggregated annual values from projected monthly-resolved cash flows are illustrated.

Free Cash Flow

The net operating and investing cash flow (cf. Section 4.2.1) represents the free cash flow of the project. The free cash flow is the cash portion of generated revenues being available for distribution among accounts payable (i.e. debt and equity holders). In practical terms, it describes the amount of cash which can be extracted from the project while securing its operation. The evolution of the free cash flow and generated revenues over the project lifetime for both simulation years of 2010 and 2008 are illustrated in Fig. 4.3.

Prior to the operational phase of the project (i.e. at year 0), a negative free cash flow of the amount of the total initial CAPEX of 1 616 m€ is accounted. Subsequently, stable positive free cash flows

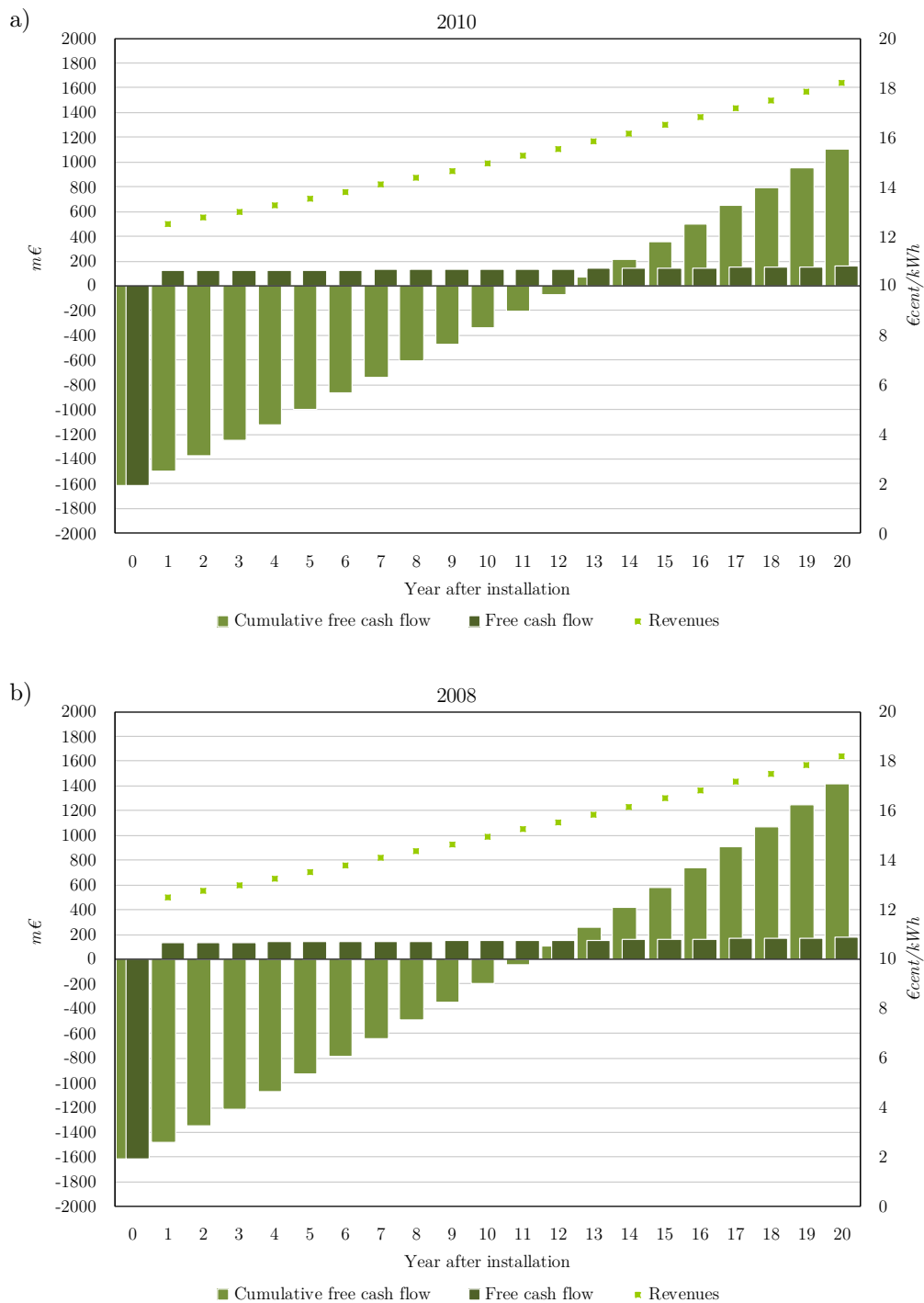


Figure 4.3: Projected free cash flow as simulated with the financial model. Technical and economic assumptions are chosen according to Section 4.2.3. Meteorological assumptions in terms of power production are processed from the reference surrogate climate change experiments for the years 2010 (a) and 2008 (b). Shown are annual as well as cumulative free cash flows in $m\text{€}$ over the lifetime of the project. In addition revenues per produced unit of electricity in €/cent/kWh are indicated. All values are aggregated from monthly-resolved cash flows, representing annual financial statements at the end of each period.

are generated throughout the project's operational phase. According to the annual electricity tariff increase of 2.0% per year, expected revenues increase from initially 12.5 €/cent/kWh to about 18.2 €/cent/kWh during the last year of planned operation. This is reflected by continuously increasing generated free cash flows. The cumulative sums of the free cash flows over the project lifetime reveal the instance of time when sufficient revenues are generated, such that the project reaches profitability. This moment is subject to the choice of meteorological assumptions only, as technical and economic assumptions are retained across the sensitivity experiments performed in the frame of this thesis.

Diverging meteorological assumptions result in differing amounts of total annual power production. Thus, the meteorological assumptions applied for the simulation year of 2010 result in a total annual power production of about 1 638 GWh (considering wind farm wake loss of 10.0% and operational uptime of 95.0%), while about 1 774 GWh is reached for the simulation year of 2008. This corresponds to an approximately 8.3% higher electricity generation for the simulation year 2008 in comparison to 2010. Because the generation of revenues is directly proportional to the power production, the adjacent free cash flow gets modified. While the same initial CAPEX and expected revenues per kWh apply to both simulation years, higher free cash flows in the range of 11 to 12% are projected for the simulation year 2008 (see Fig. 4.3 b) in comparison to 2010 (see Fig. 4.3 a), as a result of the higher power production. This circumstance leads to an accelerated return of the investment, where the project reaches profitability already during the 12th year after installation for the simulation year 2008 (see Fig. 4.3 b), while this is achieved about one year later for 2010 (see Fig. 4.3 a).

Debt Service

The evolution of the cash flow of debt service over the project lifetime for both simulation years of 2010 and 2008 is illustrated in Fig. 4.4. The total outstanding debt prior to the operational phase of the project amounts to 969.6 m€ (i.e. 60.0% of the total initial CAPEX). With progressing lifetime of the project, the outstanding debt reduces successively as debt gets repaid in a continuous manner. In addition, debt interests abate with decreasing outstanding debt amounts. The reduced interest payments transform into (additional) profit (cf. project cost structure in Fig. A.12). A cash sweep makes use of this surplus and, consequently, debt repayment accelerates with progressing project duration. The first year after installation is treated as grace period, where the regular debt repayment gets waived. During this year, the regular debt service consists only of interest expenses on outstanding debt. This is why the annual DSCR is relatively high

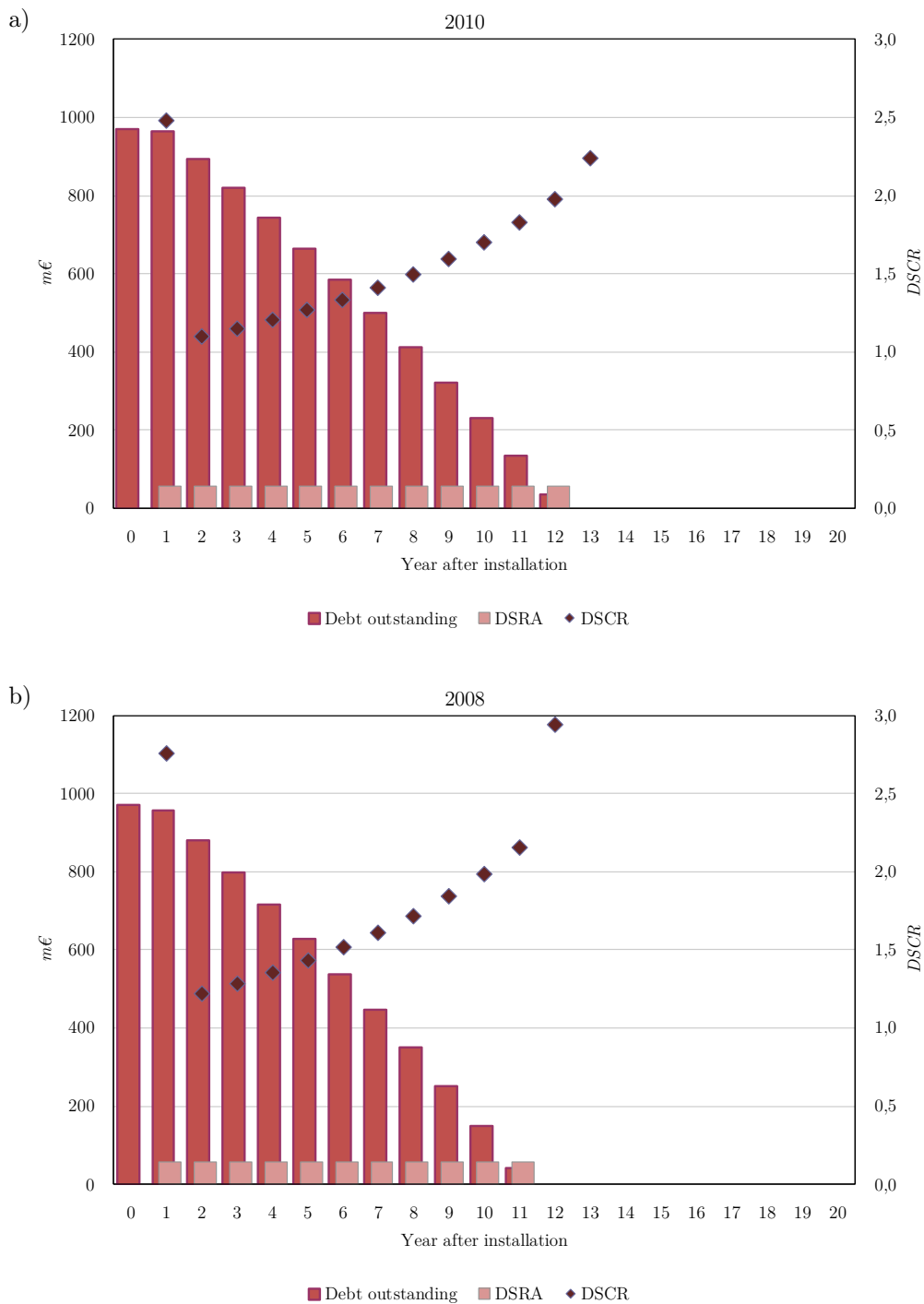


Figure 4.4: Projected cash flow of debt service as simulated with the financial model. Technical and economic assumptions are chosen according to Section 4.2.3. Meteorological assumptions in terms of power production are processed from the reference surrogate climate change experiments for the years 2010 (a) and 2008 (b). Shown are outstanding debt amounts as well as DSRA cash reserve in $m\text{€}$ over the lifetime of the project. In addition, the dimensionless annual mean DSCR is indicated. All values are aggregated or computed from monthly-resolved cash flows, representing annual financial statements at the end of each period.

during the first year of operation, before it drops to lowest DSCR values with the second year, when the regular debt service is complemented with repayment of debt. As the amount of the regular debt service reduces with progressing lifetime of the project, DSCR values increase. This reflects the highest credit risk to be present during the initial phase of the project (subsequently to the grace period), when regular debt service amounts are highest.

The projected higher free cash flows for the simulation year 2008 compared to 2010 (see previous paragraph) affect the projected cash flow of debt service: A higher free cash flow provides additional revenue, which is used by the cash sweep. Consequently, debt repayment accelerates further with higher free cash flows. As a result, the debt beg is fully repaid already during the 12th year after installation for the simulation year 2008, while this is achieved about one year later for 2010. However, repayment obligations are completely serviced prior to the end of the loan tenor of 16 years for both simulation years. In addition, annual DSCR values are continuously higher for the simulation year 2008 compared to 2010 as the amount of the regular debt service is reduced more quickly with progressing project duration due to further accelerated debt repayment.

Besides these effects related to the inter-annual variability of the meteorological assumptions, DSCR values are subject to intra-annual variability. The inherent sub-yearly variance of the power production (see Fig. 4.2) is getting superimposed on monthly-resolved DSCR values. In this regard, monthly DSCR values vary considerably and non-uniformly in magnitude over the course of the year for both simulation years (not shown). While minimum DSCR values based on accumulated annual cash flows are observable to reach sufficient coverage to service debt (i.e. $DSCR \geq 1.0$) at all times during the lifetime of the project, the monthly-resolved debt service cash flows reveal a total of 28 (2010) and 21 (2008) monthly occurrences, respectively, where the cash flow available for debt service is insufficient to (fully) cover debt repayment (see Tab. 4.4). At these occasions, additional cash from the DSRA cash reserve is released to secure regular debt service. Nonetheless, the DSRA is in balance at the end of each year during the operational phase for both simulation years and gets released with all repayment obligations cleared.

Equity Dividends

The evolution of the cash flow of equity dividends over the project lifetime for both simulation years of 2010 and 2008 is illustrated in Fig. 4.5. The equity portion prior to the operational phase of the project amounts to 646.4 m€ (i.e. 40.0% of the total initial CAPEX). Dividends to equity holders are disbursed subordinated after all other financial obligations are accounted.

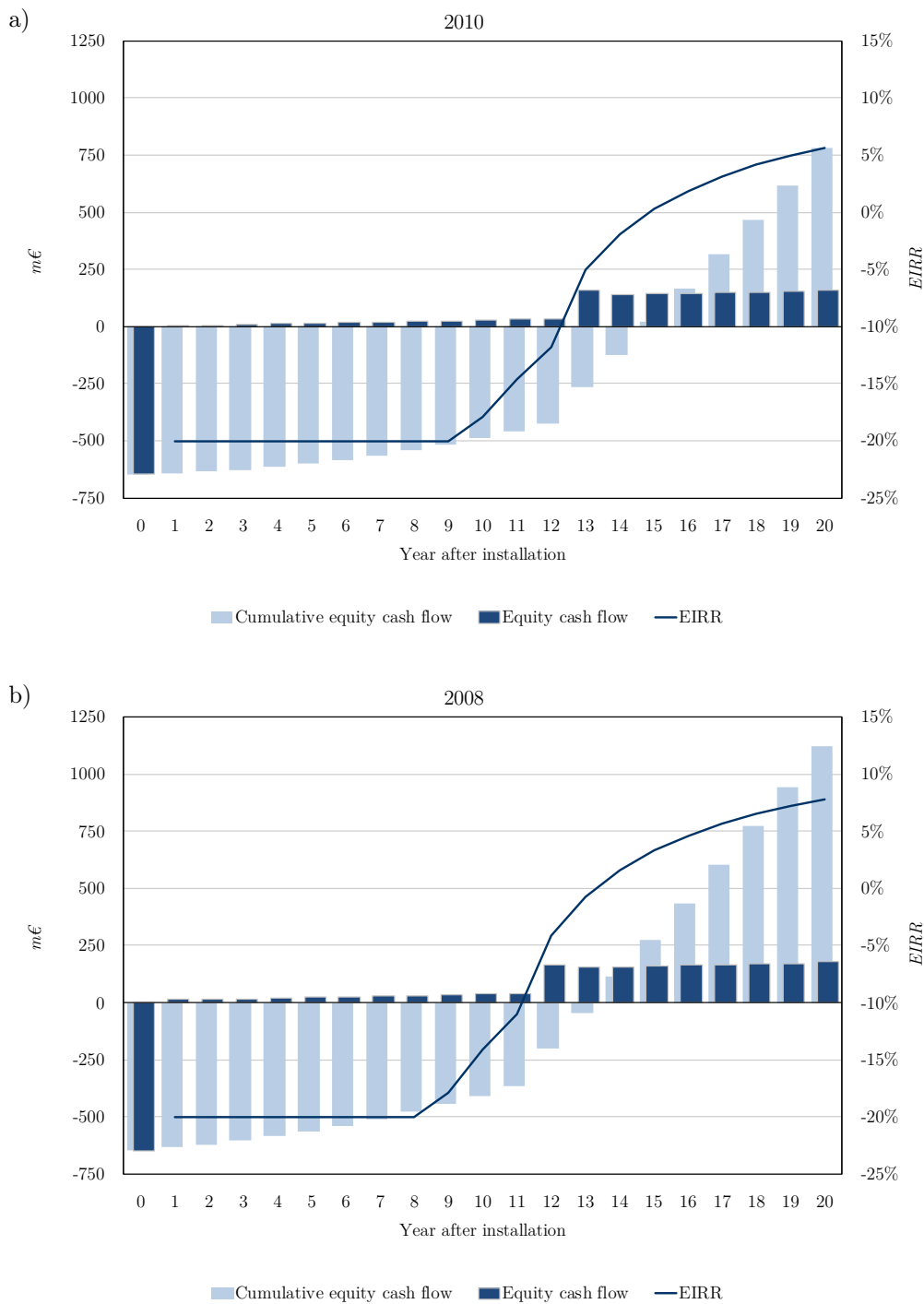


Figure 4.5: Projected cash flow of equity dividends as simulated with the financial model. Technical and economic assumptions are chosen according to Section 4.2.3. Meteorological assumptions in terms of power production are processed from the reference surrogate climate change experiments for the years 2010 (a) and 2008 (b). Shown are annual as well as cumulative equity cash flows in $m\text{€}$ over the lifetime of the project. In addition, the evolution of the EIRR is indicated in % (values below -20% are set constant due to visibility reasons). All values are aggregated or computed from monthly-resolved cash flows, representing annual financial statements at the end of each period.

This circumstance results in relatively small equity dividends until all repayment obligations are cleared. However, equity cash flows slightly increase as higher profit is generated with abating debt interest payments until the debt beg is fully repaid (cf. project cost structure in Fig. A.12). With all repayment obligations cleared, generated profit gets fully distributed among equity holders. Therefore, dividends to equity holders accelerate from that moment on. Furthermore, the DSRA cash reserve is released and feeds into the free cash flow. This results in a higher equity cash flow directly after the debt beg is fully repaid.

Analogous to the debt cash flow, the projected higher free cash flows for the simulation year 2008 compared to 2010 (see previous paragraph) affect the projected equity cash flow: A higher free cash flow provides additional revenue, which directly results in higher profit and, thus, increasing equity dividends (given that all other financial obligations are accounted). As a consequence, higher equity cash flows are observable for the simulation year 2008 in relation to 2010, converging to about 12.0% with progressing project duration (see Fig. 4.5 b). The cumulative sums of the equity cash flows over the project lifetime reveal the instance of time when sufficient revenues are generated, such that the equity investment reaches profitability. In agreement with higher equity cash flows for the simulation year 2008, the cumulative equity cash flow reaches profitability already during the 14th year after installation for 2008 (see Fig. 4.5 b), while this is achieved about one year later for 2010 (see Fig. 4.5 a). Analogous to the evolution of the cumulative equity cash flow, the equity investors perspective on the project profitability in terms of the EIRR over the lifetime of the project reaches 7.8% for the simulation year 2008 (see Fig. 4.5 b) compared to 5.6% for 2010 (see Fig. 4.5 a).

Striking is the fact, that the equity investment profitability is determined by the onset of accelerated equity cash flows with all repayment obligations cleared. Until this instance in time, only $\frac{2}{5}$ (2008) and $\frac{1}{3}$ (2010), respectively, of the equity investment are distributed as equity dividends. Not till then accelerated equity dividends pay off the equity investment. Therefore, a timely repayment of the debt beg is of interest for equity holders to increase the profitability of their investment.

4.3.2 Impact of Climate Change on Wind Energy Project Financing

To evaluate the financial risk of wind energy with respect to climate change impacts, the financial model presented in Section 4.2.1 is applied. With this financial model, sensitivity experiments for the individual simulation years of 2010 and 2008 are performed by making use of wind energy-specific climate and climate change information generated through the surrogate climate change

experiments as presented in Chapter 3. These climate change information imply temperature change signals of different intensity which represent a scenario bandwidth of change for the end of the 21st century. In this manner, four financial model simulations comprising three climate change scenarios of different intensity and their adjacent reference are performed for each simulation year (resulting in a total of eight sensitivity experiments). The financial model sensitivity experiments are achieved by processing climate and climate change information of wind speed and air density to power production amounts serving as meteorological assumptions, while technical and economic assumptions remain unchanged (see Section 4.2.3). Projected financial cash flows of these experiments are translated and distilled to economic assessment criteria, according to Section 4.2.2. These comprehensible quantities are used to assess and evaluate the financial risk, being specified as a measure of the profitability of an investment and the project's internal financial risk.

Varying the meteorological assumptions of the financial model with respect to an inherent climate change signal allows to analyse the sensitivity of simulated wind energy project financing cash flows with respect to these signals. Moreover, the extension of the financial model to project monthly-resolved cash flows (see Section 4.2.1) allows to specifically analyse the sensitivity of intra-annual variability changes on the financing of wind energy. A rudimentary estimate of inter-annual variability is included by means of the two deliberately chosen simulation years of 2010 and 2008.

Project Profitability

The general profitability of a project or investment is indicated by its IRR (see Section 4.2.2). The projected IRRs for the financial model sensitivity experiments are indicated in Tab. 4.3. For the reference simulations of the years 2010 and 2008, an IRR of 5.6% and 7.0% is computed over the lifetime of the project (see Tab. 4.3). The discrepancy between those values results from the difference in the total annual power production of the individual simulation years - being reflected in the projected free cash flows - which is about 8.3% higher for the simulation year of 2008 compared to 2010 (see Section 4.3.1). The associated IRR change signals amount to 0.1% (2010) and -0.1% (2008) at maximum (see Tab. 4.3). These contrary change signals result from the fact, that the change signals in the total annual power production are reversed: While the change signals of the total monthly power production are fluctuating in the range of about -1.6 to 3.5% (2010) and -4.5 to 1.3% (2008) (cf. Fig. 4.2), respectively, the change signals of the total annual power production account to approximately 0.4% (2010) and -0.2% (2008). Subsequently,

Table 4.3: Financial model simulation results representing project profitability. Listed are the return rates in % for the project (IRR) and project generated equity (EIRR) for sensitivity experiments performed with the financial model, using meteorological assumptions following wind resource change signals of different intensity (RCP2.6, RCP4.5 and RCP8.5) as well as their reference (REF) for the simulation years 2010 and 2008. The IRR is based on the free cash flow, while the EIRR is based on the cash flow to equity holders. IRR and EIRR values are obtained from monthly-resolved cash flows over the entire lifetime of the project. A definition for the IRR and EIRR is provided in Section 4.2.2.

	2010				2008			
	REF	RCP2.6	RCP4.5	RCP8.5	REF	RCP2.6	RCP4.5	RCP8.5
IRR	5.6%	5.6%	5.6%	5.7%	7.0%	6.9%	6.9%	6.9%
EIRR	5.6%	5.7%	5.7%	5.8%	7.8%	7.7%	7.7%	7.7%

annually accumulated free cash flows are projected to increase for the scenarios of the simulation year of 2010 and to decrease for the scenarios of the simulation year 2008 compared to their reference simulation, leading to the resulting contrary IRR change signals.

A similar behaviour is observable for the EIRR, representing the profitability with respect to the cash flow to equity holders. For the reference simulations of the years 2010 and 2008 an EIRR of 5.6% and 7.8% is computed over the lifetime of the project (see Tab. 4.3). Because the cash flow to equity holders is proportional to the free cash flow, the deviation between the individual simulation years can - analogous to the IRR - be related to the difference in the total annual power production. The associated EIRR change signals amount to 0.2% (2010) and -0.1% (2008) at maximum (see Tab. 4.3). As explored for the IRR, these contrary change signals are a result of reversed total annual power production change signals being present for the two simulation years. Both, the IRR and the EIRR are proportional to the power production. Nonetheless, with the onset of accelerated dividend distribution when all repayment obligations are cleared, the EIRR increases at a faster rate due to a smaller initial investment account (by definition, the free cash flow, the IRR is based on, comes in at the total initial CAPEX, while the cash flow to equity holders, the EIRR is based on, comes in at the equity portion). This is why the EIRR outperforms the IRR in the long-term, being observable in particular for the simulation year 2008 for which higher power production assumptions prevail. Nonetheless, IRR and EIRR change signals remain within the same order of magnitude.

Overall, the long-term profitability of wind energy project financing is not substantially affected by changing climate conditions, because the IRR and EIRR change signals express substantially smaller compared to the variation between the two simulation years. In this manner, the inter-

annual variability is of the order of one magnitude larger compared to the projected climate change signals of project profitability. However, this indicates the importance to incorporate information about natural climate variability in financial assessments related to wind energy.

Financial Risk

The financial risk of a project or investment is regarded as the risk of failing to meet financial obligations. In this manner, the credit worthiness of a project or its ability to service debt is indicated by the project's DSCR. The DSCR represents the ratio of the projected free cash flow and the regular debt service (see Section 4.2.2). Here, a $DSCR < 1.0$ indicates insufficient coverage to service regular debt obligations. Projected DSCRs for the financial model sensitivity experiments are indicated in Tab. 4.4. The technical and economic assumptions of the financial model sensitivity experiments are defined to represent a realistic wind farm scenario, while ensuring credit worthiness and profitability with respect to the reference meteorological assumptions (see Section 4.2.3). By making use of meteorological assumptions implying wind resource change signals of different intensity, the ability to sufficiently service debt is analysed under changing climate conditions. However, as a consequence, results of the reference simulations are meant to reflect sufficient debt service.

The average DSCR of monthly-resolved cash flows (\overline{DSCR}_m) as projected for the reference simulations of the years 2010 and 2008 amounts to 1.57 and 1.76 (see Tab. 4.4). As the DSCR represents the ratio of the projected free cash flow and the regular debt service, projected free cash flows are regarded as sufficient to service financial obligations with respect to the entire lifetime of the project and for both simulation years. The DSCR is proportional to the free cash flow since the regular debt service is continuous with the duration of the debt repayment. Because the projected free cash flows are higher due to a higher power production for the simulation year of 2008 compared to 2010 (see above and Section 4.3.1), the \overline{DSCR}_m values are higher as well, thus, explaining the discrepancy between those values for both simulation years. The minimum value of the DSCR over the entire payback period of the project provides information about the least coverage ratio of debt service. Regarding aggregated annual cash flows, minimum DSCRs (i.e. $DSCR_{a,min}$) of 1.10 (2010) and 1.23 (2008) are observable (see Tab. 4.4), revealing sufficient coverage to service debt (i.e. $DSCR_a \geq 1.0$) at the end of each year over the entire lifetime of the project. Nonetheless, minimum DSCR values of 0.37 (2010) and 0.47 (2008) are observable when regarding monthly-resolved cash flows (i.e. $DSCR_{m,min}$; see Tab. 4.4). The inherent sub-yearly variance of the power production (see Fig. 4.2) is getting superimposed on monthly-resolved

Table 4.4: Financial model simulation results representing financial risk. Listed are dimensionless DSCR values for sensitivity experiments performed with the financial model, using meteorological assumptions following wind resource change signals of different intensity (RCP2.6, RCP4.5 and RCP8.5) as well as their reference (REF) for the simulation years 2010 and 2008. DSCR values are obtained from either aggregated annual (a) or monthly-resolved (m) cash flows over the entire lifetime of the project. A definition of the DSCR is provided in Section 4.2.2.

	2010				2008			
	REF	RCP2.6	RCP4.5	RCP8.5	REF	RCP2.6	RCP4.5	RCP8.5
$\overline{\text{DSCR}}_m$	1.57	1.57	1.57	1.58	1.76	1.76	1.75	1.75
$\text{DSCR}_{a,\min}$	1.10	1.10	1.11	1.11	1.23	1.22	1.22	1.22
$\text{DSCR}_a < 1.0$	0	0	0	0	0	0	0	0
$\text{DSCR}_{m,\min}$	0.37	0.37	0.37	0.37	0.47	0.47	0.47	0.49
$\text{DSCR}_m < 1.0$	28	27	28	25	21	22	22	24

DSCR values through projected free cash flows. In this regard, monthly DSCR values vary considerably and non-uniformly in magnitude over the course of the year and for both simulation years. Consequently, a total of 28 (2010) and 21 (2008) occurrences are recorded, where the monthly free cash flow amount is not sufficient to cover regular debt service (i.e. $\text{DSCR}_m < 1.0$; see Tab. 4.4), despite the fact that financial obligations can be serviced on an annual basis and the DSRA cash reserve is in balance at the end of each year for both simulation years.

The climate change signals of the average DSCRs of monthly-resolved cash flows ($\overline{\text{DSCR}}_m$) as compared to the reference simulations of the years 2010 and 2008 amount to 0.01 and -0.01 at maximum (see Tab. 4.4). These contrary signals can be related to the change signals in the total annual power production, which determine the free cash flow and are reversed for the two simulation years. The same holds for the climate change signals of the minimum DSCRs of aggregated annual cash flows over the lifetime of the project ($\text{DSCR}_{a,\min}$), accounting to 0.01 (2010) and -0.01 (2008) at maximum (see Tab. 4.4). These change signals amount to less than one percent irrespective of the intensity of the underlying climate change scenario. Moreover, the discrepancy between the two simulation years is by one order of magnitude larger than the associated climate change signals.

Generally, the climate change signals of the minimum DSCRs of monthly-resolved cash flows over the lifetime of the project ($\text{DSCR}_{m,\min}$) are determined by monthly varying change signals inherent to the meteorological assumptions, expressed in changes of total monthly power production amounts. Despite changes of the total monthly power production in the range of about -1.6

to 3.5% (2010) and -4.5 to 1.3% (2008), depending on the scenario and month of the year (cf. Fig. 4.2), hardly any changes are observable for the $DSCR_{m,\min}$ (see Tab. 4.4). Primarily, this is due to the circumstance that the $DSCR_{m,\min}$ is determined by the month of the year with the least total power production. Subsequently, the change in the $DSCR_{m,\min}$ represents only the variation with respect to the lowest electricity generation. As such, it reflects just the change signal of a particular month and is not representative to evaluate intra-annual variability changes. A more meaningful measure to evaluate changes in financial risk with respect to monthly varying climate change signals is to detect changes in the occurrences with insufficient monthly free cash flow amounts to cover regular debt service. This is the case for $DSCR_m$ values < 1.0 and explicitly incorporates intra-annual variability changes when applying with monthly-resolved cash flows. The number of occurrences of $DSCR_m$ values < 1.0 decreases from a total of 28 to 25 at maximum for the simulation year 2010 over the lifetime of the project, while it increases from a total of 21 to 24 at maximum for the simulation year 2008 (see Tab. 4.4). In practical terms, the generated monthly free cash flow is not sufficient to cover regular debt service for this particular number of months. The general development of these contrary change signals is in line with the change signals in the total annual power production, which determine the free cash flow and are reversed for the two simulation years.

Projections of monthly-resolved cash flows provide additional information about changes in the free cash flows and subsequent DSCRs with respect to monthly varying climate change signals. This allows to trace back changes in the occurrences with insufficient monthly free cash flow amounts to cover regular debt service to the meteorological assumptions. In this regard, the monthly variations inherent to the meteorological assumptions (see Fig. 4.2) result in insufficient free cash flows to service interest expenses on outstanding debt and debt repayment during particular months. This is especially true during the initial phase of the project when interest expenses are highest and diminish with duration of the debt repayment as interest expenses reduce. For the simulation year of 2010 insufficient free cash flows for the months of February, April, May, June and July are projected, while this applies to the months of May, July, August and September for the simulation year of 2008 (not shown). This is observable for the reference simulations as well as for the climate change sensitivity experiments of both simulation years. Moreover, monthly varying climate change signals do not cause a reduction or any additional months besides those mentioned above, but rather affect the intensity of the power production of those respective months. This implies that the impact of monthly varying change signals on the recorded occurrences of $DSCR_m$ values < 1.0 is limited to these months.

The climate change signals associated to the meteorological assumptions (see Fig. 4.2 a) indicate for the simulation year of 2010 a decrease in power production for February (about 1.5% for RCP2.6) and July (less than 1.0% for all RCPs) with respect to its reference, whereas increasing values are present for February (about 0.4% to 1.4% for RCP4.5 and RCP8.5), April (in the range of 0.8% to 2.4% for all RCPs), May (in the range of 1.7% to 3.5% for all RCPs) and June (less than 1.0% for all RCPs). The degree of change in the occurrences of $DSCR_m$ values < 1.0 is tied to the intensity of these change signals. In this regard, the increase in power production for the months April, May, partly February and to a minor extent June outweigh the decrease for the month July. This results in a total record of 27 (RCP2.6), 28 (RCP4.5) and 25 (RCP8.5) occurrences with insufficient electricity generation and subsequent free cash flow to cover regular debt service (see Tab. 4.4). Because the increase in power production associated to the RCP4.5 is less pronounced for April and May, while its decrease for July is slightly higher compared to the change signal associated to the RCP2.6, a slightly higher occurrence record is observable for this scenario - despite the fact of a stronger temperature change signal inherent to the RCP4.5 scenario (cf. Figs. 3.3 c-d and 3.13 c). Nonetheless, the strongest change signal with respect to occurrences of $DSCR_m$ values < 1.0 is striking for the RCP8.5 scenario accounting to a total of three less events compared to its reference (equivalent to a decrease by about 10%; see Tab. 4.4). An analogous behaviour is observable on the simulation year of 2008. The climate change signals associated to the meteorological assumptions (see Fig. 4.2 b) indicate a decrease in power production for May (well below 1.0% for RCP2.6 and RCP4.5), July (in the range of 1.5% to 3.0% for all RCPs), August (in the range of 1.6% to 4.5% for all RCPs) and September (in the range of 0.4% to 1.2% for all RCPs) with respect to its reference for this simulation year, whereas increasing values are present for May only (about 1.0% for RCP8.5). This results in a total record of 22 (RCP2.6 and 4.5) and 24 (RCP8.5) occurrences with insufficient electricity generation and subsequent free cash flow to cover regular debt service (see Tab. 4.4). Even though a more intense decrease in the power production change signal is present for the RCP4.5 especially for the month August compared to the RCP2.6 (see Fig. 4.2 b), this additional decrease is not expressed in a more pronounced change signal in terms of occurrences of $DSCR_m$ values < 1.0 and both RCP scenarios are projected to be equally off. This can be attributed to a slightly enhanced accelerated debt repayment present for the RCP4.5 realised by the cash sweep. Again, the strongest change signal with respect to occurrences of $DSCR_m$ values < 1.0 is striking for the RCP8.5 scenario accounting to a total of three more events compared to its reference (equivalent to an increase by about 14%; see Tab. 4.4).

As the simulation year of 2010 is characterised by a lower total annual power production as well as a higher number of months with insufficient electricity generation to cover regular debt service compared to the simulation year of 2008, more occurrences of $DSCR_m$ values < 1.0 are recorded for this simulation year (see Tab. 4.4). In contrast, the climate change signals inherent to the meteorological assumptions for 2010 reflect an increase in the total annual power production and in particular for those months with insufficient electricity generation to cover regular debt service (see Fig. 4.2 a), whereas a decrease is present for 2008 (see Fig. 4.2 b). This results in the contrary change signals with respect to occurrences of $DSCR_m$ values < 1.0 for both simulation years (as illustrated above). Irrespective of the intensity of the underlying climate change signal, the discrepancy between the two simulation years exceeds the associated climate change signals. Because months with higher power production outweigh months with insufficient electricity generation and subsequent free cash flows to cover regular debt service, financial obligations can be serviced on an annual basis (i.e. $DSCR_a \geq 1.0$). During those months where the regular debt service can not be covered by the generated free cash flow, cash is released from the DSRA cash reserve to service financial obligations. Over the course of the year, the DSRA is restocked during profitable months such that it remains in balance at the end of each year (not shown). Hence, the DSRA cash reserve is providing sufficient liquidity at any time of the project period and independent of the climate change scenario for both simulation years.

Overall, the projected free cash flows are sufficient to service financial obligations with respect to the entire lifetime of the project, irrespective of the intensity of the underlying climate change signal and for both simulation years. Aggregated annual cash flows reveal sufficient coverage to service debt at all times during the lifetime of the project. However, the inherent sub-yearly variance in the power production projects occurrences where monthly free cash flow amounts are not sufficient to cover regular debt service. Meteorological assumptions with an underlying climate change signal indicate sensitivity with respect to these occurrences. In this regard, strongest changes are detected for the strongest intensity of the underlying climate change signal (i.e. RCP8.5) for both simulation years. Nonetheless, contrary change signals are observable for the two simulation years originating from reversed changes in the power production. However, the discrepancy between the two simulation years, reflecting natural climate variability, exceeds the associated climate change signals. Furthermore, financial obligations can be serviced on an annual basis and the compensative DSRA cash reserve remains in balance at the end of each year, irrespective of the underlying climate change signal and for both simulation years.

4.4 Conclusions

A simplified but fully-fledged financial model is set up to simulate and project the financing cash flows for an imaginary offshore wind farm located in the German Bight. The financial model is flexible with regard to the major financing assumptions, comprising technical and economic as well as meteorological boundary conditions. Moreover, the model's computational core is extended to cover monthly-resolved cash flow simulations. As such, monthly-resolved meteorological information can be processed as input. Additionally, this development enables to incorporate and assess the financial risk of wind energy project financing with respect to sub-yearly variations in the wind resource.

To assess climate change impacts on the financing of wind energy, sensitivity experiments with this financial model are performed using wind energy-specific climate and climate change information generated through surrogate climate change experiments (as presented in Chapter 3). This enables the evaluation of financial risk of wind energy project financing with respect to climate change impacts in terms of long-term and variability change. In this regard, financial risk is evaluated by translating and distilling simulated financial cash flow information to comprehensible quantities describing the project's profitability and internal financial risk.

The general sensitivity of the financial model to simulate wind energy project financing cash flows with respect to a bandwidth of current climate conditions is tested for an imaginary offshore wind farm located in the German Bight, by performing simulations with different sets of meteorological assumptions. Resulting sensitivity indicated for the evolution of the free cash flow (varying by about 11 to 12%), the debt service (full repayment of debt beg varies by about one year) and equity dividends (varying by about 2.2%) over the project lifetime can be exclusively accounted to the diverging total power production amounts inherent to the meteorological assumptions. Therefore, meteorological information (the meteorological boundary conditions of the financial modelling are based on) generally influence the profitability ratio and, thus, potentially affect decisions based on financial modelling exercises. This highlights the general importance of high-quality wind energy-specific climate data containing also information about the bandwidth of natural climate variability for accurate financial simulation results. Information about long-term natural climate variability has already been recognised as a significant measure to be incorporated in wind resource assumptions and adopted by practitioners (*Deloitte*, 2014). In addition to the sensitivity being subject to the meteorological assumptions, sensitivity is present with respect to the technical and economic assumptions as well. However, an assessment of the sensitivity of

these technical and economic boundary conditions is out of the scope of this thesis.

Utilising wind resource change signals of different intensity as meteorological assumptions, indicate the long-term profitability of wind energy project financing being not substantially affected by changing climate conditions. This is concluded because the bandwidth of natural climate variability exceeds the climate change signals related to the IRR (variation by 1.4% versus change signal of $\pm 0.1\%$) and EIRR (variation by 2.2% versus change signal of $\pm 0.2\%$), irrespective of the intensity of the underlying climate change scenario.

In addition to the project profitability, the impact of climate change signals of different intensity is examined with respect to the project's internal financial risk, by analysing the general ability to service all financial obligations from generated project cash flows. Over the entire lifetime of the project, free cash flows are sufficient to service financial obligations, irrespective of the intensity of the underlying climate change signal. As well, aggregated annual cash flows reveal sufficient coverage to service debt at the end of each year over the lifetime of the project. Nevertheless, inherent intra-annual variability in the meteorological assumptions disclose occurrences, where monthly free cash flow amounts are not sufficient to cover the regular debt service (up to 28 months over the entire lifetime of the project). These occurrences appear to be sensitive with respect to the underlying climate change signals. In this regard, strongest changes (exceeding -10% and 14%) are detected for the strongest intensity of the climate change signal. Even though the bandwidth of natural climate variability is in excess of this signal, this can be interpreted as a relevant impact, because the financial risk management is ultimately affected.

From a financiers perspective, the highest credit risk is present during the initial phase of a wind energy project, when regular debt service amounts are highest (expressed in lowest DSCR values). In contrast, the uncertainty associated to the climate change scenario and signal is lowest for the near future and increases with distance in time. Over the lifetime of a wind energy project, especially the financial risk within the initial project phase can, therefore, be concluded as being exposed to a lesser extend to changing climate conditions and associated uncertainties.

5 Conclusions and Outlook

After providing an introduction to the thesis' objective in Chapter 1, a procedure for assessing climate change impacts on wind energy financing is presented within the previous chapters. To the authors best knowledge, it is the first systematic attempt to interrelate climate information with economic project financing methodology and to investigate the financial risk of wind energy financing with respect to changing climate conditions. At first, the exposure of individual elements of wind energy financing to physical climate change is traced in Chapter 2. In the following Chapter 3, a novel high-resolution experimental modelling framework with the non-hydrostatic extension of the regional climate model REMO is set up to generate physically consistent climate and climate change information of the wind resource across wind turbine operating altitudes. Subsequently, the financial risk of wind energy project financing with respect to changing climate conditions is assessed in Chapter 4, by integrating the climate information generated in Chapter 3 with a financial model. In this final chapter, the guiding research questions formulated in Section 1.3 are answered by briefly summarising concluding remarks of the individual chapters, followed by an outlook.

- *Which cost elements of wind energy financing are affected most by changing climate conditions?*

The qualitative comparison of identified climate change impacts on capital costs, variable costs and wind energy revenue, provided in Chapter 2, leads to the overall conclusion that the revenue needs to be regarded as the essential component of the wind energy financing chain being exposed to changing climate conditions. This implies the wind resource (through the wind climate) to be of crucial interest for an assessment of climate change impacts on the financing of wind energy. With this finding, the second research question can be examined:

- *How do changing climate conditions affect the financial risk of wind energy financing?*

At first, climate and climate change information about the wind resource and wind energy

characteristics across wind turbine operating altitudes are essential to determine wind energy yield assumptions, on which the wind energy financing and financial risk assessment are based on. Therefore, surrogate climate change experiments with the non-hydrostatic regional climate model REMO-NH are performed in Chapter 3 to generate physically consistent and wind energy-specific climate and climate change information, using temperature change signals according to climate projection scenarios of different intensities. Change information about wind speed and air density are subsequently transferred to a simplified but fully-fledged financial model in Chapter 4 to assess the sensitivity of projected financing cash flows with respect to changing climate conditions. These experiments reveal the long-term profitability of wind energy project financing as not being substantially affected by changing climate conditions. Contrary, the project's internal financial risk, being expressed as the ability to service financial obligations from generated project cash flows, experiences relevant changes in occurrences with insufficient coverage of the regular debt service. The findings of this exercise lead to the final research question:

- *Should climate change impacts be considered as an additional influencing factor on wind energy financing?*

Overall, financiers and project managers face a variety of challenging issues, especially with respect to uncertain operational costs. Some of these challenging issues might have a more intense impact on the project financing, compared to the impact of projected changing climate conditions on wind power production. Nonetheless, the consideration of climate information, incorporating information about the bandwidth of natural climate variability, as well as climate change information, comprising a bandwidth of long-term and variability changes, depict a valuable ancillary information serving the uncertainty assessment and risk management for wind energy project financing. In particular, the ability to service financial obligations from generated project cash flows is vital for successful project financing and would be supported by information about intra-annual and inter-annual variability and associated changes. Moreover, financial measures - like a DSRA cash reserve - depict a necessary condition for successful project financing and could be adjusted to account for additional (uncertainty) risk to fail servicing financial obligations due to changing climate conditions. Therefore, the consideration of climate change impacts as an additional influencing factor on project financing of wind energy is proposed in terms of climate change bandwidth information for wind energy yield assumptions.

After summing up the most important results of this thesis, it is important to state that certain methodological and structural limitations apply to the experimental setup. Methodologically, the

generation of climate change information using surrogate climate change experiments as presented in Chapter 3 is limited to thermodynamical effects only. This is beneficial to disentangle climate change signals of different origin but does not provide a complete climate change assessment since dynamical effects get neglected. Following *Kröner et al. (2017)*, the choice of experiments could be extended to cover circulation effects (while still distinguishing between thermodynamic and dynamical effects). This would enable a complete climate change assessment, but requires additional decade-long simulations, which are not feasible at the kilometre-scale at this instance of time. Nevertheless, future technical development might enable such efforts.

The climate change signals used for the surrogate climate change experiments are based on climate projections of just a single GCM-RCM combination. An ensemble of climate model projections should be regarded to account for model as well as scenario uncertainty. This would require daily-resolved simulation output across the entire vertical atmosphere. If at all available, those data are usually exclusive to the modelling centres performing the climate projections. In this regard, data collection and homogenisation depicts an extensive effort.

Structurally, a proper and sound uncertainty assessment requires long-term climate projections of multiple climate models as well as multiple climate change scenarios. The generation of such information would be inevitable attainable through a community effort. Therefore, the provision of sufficiently resolved information of wind energy-specific variables (i.e. wind speed and air density) across wind turbine operating altitudes is proposed with future coordinated RCM downscaling experiments (e.g. CORDEX). This would allow to estimate uncertainties and provide the scientifically best possible climate information for wind energy applications.

An evaluation of the simulated wind climate against observations has not been performed. Even though this is addressed in previous research (e.g. *Larsén et al., 2010*), the latest development of the REMO model allowing to simulate non-hydrostatic regimes at convection-permitting resolutions might require readjustments of scale-dependant parameterisations (such as the turbulence scheme).

Concerning the financial modelling exercise in Chapter 4, technical and economic boundary conditions depict simplified assumptions. In this regard, technological development in combination with market mechanisms as well as risk profile and risk allocation reveal certain degrees of freedom. Therefore, the sensitivity of the financial model with respect to technical and economic assumptions should be assessed to contrast the sensitivity arising from changes in the meteorological assumptions against those of the remaining boundary conditions. This would enable to identify tipping points at which changes in the meteorological assumptions could not be compensated anymore by financial risk instruments (being defined through economic assumptions).

In addition to propagated limitations originating from the climate and climate change information being generated through the surrogate climate change experiments (see previous paragraph), additional constraints concerning the meteorological assumptions are present. The meteorological assumptions are based on individual simulation years. As such, projections of financial cash flows over the entire project lifetime are subject to wind energy conditions of a single year only and, thus, do neither incorporate long-term climate nor natural climate variability. Nonetheless, long-term climate projections providing physically consistent and wind energy-specific climate information of high spatial and temporal resolution (comparable to those gained through the surrogate climate change experiments) are not available at this instance of time, but are of importance to estimate realistic power production amounts and associated changes in wind climate. Future availability of such wind energy-specific climate information, spanning several decades as well as comprising multiple scenarios and various climate models, would enable a scientifically as well as statistically profound climate change and uncertainty assessment.

Financiers are used to estimate the resource uncertainty as part of the financial risk assessment, by performing financial simulations under meteorological assumptions representing different energy output occurrence probabilities. In this regard, usually an upside case for risk-affine lenders (p_{50} ; i.e. energy output reached with a probability of 50%) as well as more conservative cases for risk-averse lenders (p_{75} and p_{90}) get applied (Böttcher, 2013, 2012), in combination with certain safety cushions - defined as minimum DSCR hurdle rates - to these percentile values (FS-UNEP, 2017c). To perform the relevant statistics to distill such information, climate time series of an adequate temporal resolution are required. Again, future availability of wind energy-specific climate information would allow a scientifically as well as statistically profound climate change and uncertainty assessment, also matching the requirements of financiers. Such additional uncertainty information could be embedded along existing uncertainty propagation measures, as formulated in industry standards (cf. IEC-61400, 2015), resulting in modified safety cushions.

Overall, the identified and specified limitations concerning the experimental setup applied in Chapters 3 and 4 are potentially diminishable through additional efforts in combination with future technical development. This would advance the informational content and quality of wind energy-specific climate information as well as of subsequent financial modelling results relying on such data as meteorological assumptions. Moreover, the integration of wind energy-specific climate information as well as associated information about uncertainties into existing financial risk assessment procedures would illustrate a valuable contribution to climate services, thus, enabling climate change adaptation for wind energy.

References

- Antic, S., R. Laprise, B. Denis and R. de Elía (2006): Testing the downscaling ability of a one-way nested regional climate model in regions of complex topography. *Climate Dynamics*, **26**, 305–325. doi:10.1007/s00382-005-0046-z
- Asselin, R. (1972): Frequency filter for time integrations. *Monthly Weather Review*, **100**, 487–490. doi:10.1175/1520-0493(1972)100<0487:FFFTI>2.3.CO;2
- Barstad, I., A. Sorteberg and M. d. S. Mesquita (2012): Present and future offshore wind power potential in northern Europe based on downscaled global climate runs with adjusted SST and sea ice cover. *Renewable Energy*, **44**, 398–405. doi:10.1016/j.renene.2012.02.008
- Blackadar, A. (1962): The vertical distribution of wind and turbulent exchange in a neutral atmosphere. *Journal of Geophysical Research*, **67**(8), 3095–3102. doi:10.1029/JZ067i008p03095
- Blanco, M. I. (2009): The economics of wind energy. *Renewable and Sustainable Energy Reviews*, **13**(6-7), 1372–1382. doi:10.1016/j.rser.2008.09.004
- BMWi (2018): Vorbereitung und Begleitung bei der Erstellung eines Erfahrungsberichts gemäß §97 Erneuerbare-Energien-Gesetz - Teilvorhaben IIf: Windenergie auf See (Zwischenbericht). Report, Federal Ministry for Economic Affairs and Energy. https://www.erneuerbare-energien.de/EE/Redaktion/DE/Downloads/bmwi_de/bericht-eeg-7-wind-auf-see.pdf?__blob=publicationFile&v=6 (last access September 5, 2018)
- Bolton, D. (1980): The computation of equivalent potential temperature. *Monthly Weather Review*, **108**, 1046–1053. doi:10.1175/1520-0493(1980)108<1046:TCEOPT>2.0.CO;2
- Bosshard, T., S. Kotlarski, T. Ewen and C. Schär (2011): Spectral representation of the annual cycle in the climate change signal. *Hydrology and Earth System Sciences*, **15**, 2777–2788. doi:10.5194/hess-15-2777-2011
- Böttcher, J. (2010): Finanzierung von Erneuerbare-Energien-Vorhaben. Oldenbourg Wissenschaftsverlag. ISBN: 978-3-486-59974-9
- Böttcher, J. (2012): Handbuch Windenergie: Onshore-Projekte: Realisierung, Finanzierung, Recht und Technik. Oldenbourg Wissenschaftsverlag. ISBN: 978-3-486-71474-6
- Böttcher, J. (2013): Handbuch Offshore-Windenergie: Rechtliche, technische und wirtschaftliche Aspekte. Oldenbourg Wissenschaftsverlag. ISBN: 978-3-486-71776-1

- Brinkop, S. and E. Roeckner (1995): Sensitivity of a general circulation model to parameterization of cloud-turbulence interactions in the atmospheric boundary layer. *Tellus*, **47A**, 197–220. doi:10.1034/j.1600-0870.1995.t01-1-00004.x
- Charnock, H. (1955): Wind stress on a water surface. *Quarterly Journal of the Royal Meteorological Society*, **81**, 693–640. doi:10.1002/qj.49708134903
- Christensen, J. H., T. R. Carter and F. Giorgi (2002): PRUDENCE employs new methods to assess European climate change. *Eos*, **83**(13), 147–148. doi:10.1029/2002EO000094
- CORDEX (2015): CORDEX domains for model integrations. World Climate Research Programme (WCRP). http://wcrp-cordex.ipsl.jussieu.fr/images/pdf/cordex_regions.pdf (last access September 6, 2018)
- Cortekar, J. and M. Groth (2015): Adapting energy infrastructure to climate change - Is there a need for government interventions and legal obligations within the German "energiewende"? *Energy Procedia*, **73**, 12–17. doi:10.1016/j.egypro.2015.07.552
- Council of the European Union (2008): Council Directive 2008/114/EC on the identification and designation of European critical infrastructures and the assessment of the need to improve their protection. *Official Journal of the European Union*, **L 345**, 75–82. <http://data.europa.eu/eli/dir/2008/114/oj> (last access December 19, 2018)
- Dalili, N., A. Edrissy and R. Carriveau (2009): A review of surface engineering issues critical to wind turbine performance. *Renewable and Sustainable Energy Reviews*, **13**(2), 428–438. doi:https://doi.org/10.1016/j.rser.2007.11.009
- Davies, H. C. (1976): A lateral boundary formulation for multi-level prediction models. *Quarterly Journal of the Royal Meteorological Society*, **102**, 405–418. doi:10.1002/qj.49710243210
- Davies, T. (2014): Lateral boundary conditions for limited area models. *Quarterly Journal of the Royal Meteorological Society*, **140**, 185–196. doi:10.1002/qj.2127
- Dee, D. P., S. M. Uppala, A. J. Simmons, P. Berrisford, P. Poli, S. Kobayashi, U. Andrae, M. A. Balmaseda, G. Balsamo, P. Bauer, P. Bechtold, A. C. M. Beljaars, L. van de Berg, J. Bidlot, N. Bormann, C. Delsol, R. Dragani, M. Fuentes, A. J. Geer, L. Haimberger, S. B. Healy, H. Hersbach, E. V. Hólm, L. Isaksen, P. Kållberg, M. Köhler, M. Matricardi, A. P. McNally, B. M. Monge-Sanz, J. J. Morcrette, B. K. Park, C. Peubey, P. de Rosnay, C. Tavolato, J. N. Thépaut and F. Vitart (2011): The ERA-Interim reanalysis: Configuration and performance of the data assimilation system. *Quarterly Journal of the Royal Meteorological Society*, **137**, 553–597. doi:10.1002/qj.828
- Deloitte (2014): Establishing the investment case: Wind power. Report, Deloitte. <https://www2.deloitte.com/content/dam/Deloitte/global/Documents/Energy-and-Resources/gx-er-deloitte-establishing-the-wind-investment-case-2014.pdf> (last access June 9, 2018)
- Denis, B., R. Laprise, D. Caya and J. Côté (2002): Downscaling ability of one-way nested regional climate models: the Big-Brother Experiment. *Climate Dynamics*, **18**, 627–646. doi:10.1007/s00382-001-0201-0

- Denis, B., R. Laprise and D. Caya (2003): Sensitivity of a regional climate model to the resolution of the lateral boundary conditions. *Climate Dynamics*, **20**, 107–126. doi:10.1007/s00382-002-0264-6
- Di Luca, A., R. de Elía and R. Laprise (2012): Potential for added value in precipitation simulated by high-resolution nested regional climate models and observations. *Climate Dynamics*, **38**, 1229–1247. doi:10.1007/s00382-011-1068-3
- Di Luca, A., R. de Elía and R. Laprise (2013): Potential for added value in temperature simulated by high-resolution nested RCMs in present climate and in the climate change signal. *Climate Dynamics*, **40**, 443–464. doi:10.1007/s00382-012-1384-2
- Dickinson, R. E., R. M. Errico, F. Giorgi and G. T. Bates (1989): A regional climate model for the western United States. *Climatic Change*, **15**, 383–422. doi:10.1007/BF00240465
- EEA (2018): Renewable energy in Europe – 2018: Recent growth and knock-on effects. Report, European Environment Agency. doi:10.2800/03040
- Emeis, S. (2013): Wind Energy Meteorology - Atmospheric Physics for Wind Power Generation. Springer, 202 pp. ISBN: 978-3-642-30523-8
- Emeis, S. (2014): Current issues in wind energy meteorology. *Meteorological Applications*, **21**(4), 803–819. doi:10.1002/met.1472
- Emeis, S. (2015): Atmospheric boundary-layer wind phenomena which decisively impact the generation of electricity from the wind. *promet*, **39**(3), 151–162.
- Etling, D. (2008): Theoretische Meteorologie. Springer, 3rd ed., 379 pp. ISBN: 978-3-540-75978-2
- European Commission (2012): Energy Roadmap 2050. *COM*, **885**, 1–24. doi:10.2833/10759
- European Commission (2015): A European research and innovation roadmap for climate services. European Commission, Directorate-General for Research and Innovation, 56 pp. ISBN: 978-92-79-44341-1
- European Commission (2016): Proposal for a Directive of the European Parliament and of the Council on the promotion of the use of energy from renewable sources (recast). *COM*, **767**, 1–115. <https://eur-lex.europa.eu/legal-content/EN/TXT/PDF/?uri=CELEX:52016PC0767&from=EN> (last access December 19, 2018)
- European Commission (2018): Europe leads the global clean energy transition: Commission welcomes ambitious agreement on further renewable energy development in the EU. *Statement*, **18/4155**. http://europa.eu/rapid/press-release_STATEMENT-18-4155_en.pdf (last access December 19, 2018)
- Fichaux, N., J. Beurskens, P. H. Jensen and J. Wilkes (2011): UpWind: Design limits and solutions for very large wind turbines. Report, EWEA. http://www.ewea.org/fileadmin/files/library/publications/reports/UpWind_Report.pdf (last access September 5, 2018)
- Foken, T. (2008): Micrometeorology. Springer, 320 pp. ISBN: 978-3-540-74665-2

- Fraunhofer ISE (2019): Net public electricity generation in Germany in 2018. Report, Fraunhofer Institute for Solar Energy Systems. https://www.ise.fraunhofer.de/content/dam/ise/en/documents/News/Stromerzeugung_2018_2_en.pdf (last access January 9, 2019)
- Fraunhofer ISI (2015): Discount rates in energy system analysis. Report, Fraunhofer Institute for Systems and Innovation Research. http://bpie.eu/wp-content/uploads/2015/10/Discount_rates_in_energy_system-discussion_paper_2015_ISI_BPIE.pdf (last access November 17, 2018)
- Fraunhofer IWES (2017): Energiewirtschaftliche Bedeutung der Offshore-Windenergie für die Energiewende. Report, Fraunhofer Institute for Wind Energy Systems. https://www.offshore-stiftung.de/sites/offshorelink.de/files/documents/Studie_Energiewirtschaftliche_Bedeutung_Offshore_Wind.pdf (last access January 10, 2019)
- FS-UNEP (2017a): Certified Expert in Climate & Renewable Energy Finance – Unit 10: Business Plan Preparation & Financial Modelling. Script. Frankfurt School of Finance & Management, 3rd ed., 36 pp.
- FS-UNEP (2017b): Certified Expert in Climate & Renewable Energy Finance - Unit 5: Sources of Financing and Available Instruments. Script. Frankfurt School of Finance & Management, 1st ed., 97 pp.
- FS-UNEP (2017c): Certified Expert in Climate & Renewable Energy Finance - Unit 7: Renewable Energy Finance & the Role of Project Finance. Script. Frankfurt School of Finance & Management, 3rd ed., 60 pp.
- Giorgi, F. (1990): Simulation of regional climate using a limited area model nested in a general circulation model. *Journal of Climate*, **3**(9), 941–963. doi:10.1175/1520-0442(1990)003<0941:SORCUA>2.0.CO;2
- Giorgi, F., C. Jones and G. R. Asrar (2009): Addressing climate information needs at the regional level: The CORDEX framework. *World Meteorological Organization Bulletin*, **58**(3), 175–183.
- Giorgi, F., C. Torma, E. Coppola, N. Ban, C. Schär and S. Somot (2016): Enhanced summer convective rainfall at Alpine high elevations in response to climate warming. *Nature Geoscience*, **9**, 584–589. doi:10.1038/ngeo2761
- Göttel, H. (2009): Einfluss der nichthydrostatischen Modellierung und der Niederschlagsverdriftung auf die Ergebnisse regionaler Klimamodellierung. PhD thesis, University of Hamburg. doi:10.17617/2.994076
- Groth, M., S. Bender, J. Cortekar, T. Remke and M. Stankoweit (2018): Auswirkungen des Klimawandels auf den Energiesektor in Deutschland. *Zeitschrift für Umweltpolitik & Umweltrecht*, **3**, 324–355.
- Gryning, S. E., E. Batchvarova, B. Brümmner, H. Jørgensen and S. Larsen (2007): On the extension of the wind profile over homogeneous terrain beyond the surface boundary layer. *Boundary-Layer Meteorology*, **124**(2), 251–268. doi:10.1007/s10546-007-9166-9
- Haarsma, R. J., M. J. Roberts, P. L. Vidale, A. Catherine, A. Bellucci, Q. Bao, P. Chang, S. Corti, N. S. Fučkar, V. Guemas, J. Von Hardenberg, W. Hazeleger, C. Kodama, T. Koenigk, L. R. Leung, J. Lu, J. J. Luo, J. Mao, M. S. Mizieliński, R. Mizuta, P. Nobre, M. Satoh, E. Scoccimarro, T. Semmler, J. Small and J. S. Von Storch (2016): High Resolution Model Intercomparison Project (HighResMIP v1.0) for CMIP6. *Geoscientific Model Development*, **9**, 4185–4208. doi:10.5194/gmd-9-4185-2016

- Hau, E. (2014): Windkraftanlagen: Grundlagen, Technik, Einsatz, Wirtschaftlichkeit. Springer, 5th ed., 969 pp. ISBN: 978-3-642-28877-7
- Hewitt, C., S. Mason and D. Walland (2012): The global framework for climate services. *Nature Climate Change*, **2**, 831–832. doi:10.1038/nclimate1745
- Hewitt, C. D. and D. J. Griggs (2004): Ensembles-based predictions of climate changes and their impacts. *Eos*, **85**(52), 566–567. doi:10.1029/2004EO520005
- Hueging, H., R. Haas, K. Born, D. Jacob and J. G. Pinto (2013): Regional changes in wind energy potential over Europe using regional climate model ensemble projections. *Journal of Applied Meteorology and Climatology*, **52**, 903–917. doi:10.1175/JAMC-D-12-086.1
- IEC-61400 (2015): International Standard for Wind Turbines (IEC-61400). International Electrotechnical Commission, 1st ed., 1000 pp.
- IPCC (2013): Climate Change 2013: The Physical Science Basis. Contribution of Working Group I to the Fifth Assessment Report of the Intergovernmental Panel on Climate Change. Cambridge University Press, 1535 pp. ISBN: 978-1-107-66182-0
- IPCC (2014): Climate Change 2014: Impacts, Adaptation, and Vulnerability. Part A: Global and Sectoral Aspects. Contribution of Working Group II to the Fifth Assessment Report of the Intergovernmental Panel on Climate Change. Cambridge University Press, 1132 pp. ISBN: 978-1-107-64165-5
- IPCC SR (2012): IPCC Special Report on Renewable Energy Sources and Climate Change Mitigation. Cambridge University Press, 1076 pp. ISBN: 978-1-107-60710-1
- IWR (2018): IWR-Windtragsindex®. <https://www.iwr.de/wind/wind/windindex/index.html> (last access August 1, 2018)
- Jacob, D. (2001): A note to the simulation of the annual and inter-annual variability of the water budget over the Baltic Sea drainage basin. *Meteorology and Atmospheric Physics*, **77**(1-4), 61–73. doi:10.1007/s007030170017
- Jacob, D. and R. Podzun (1997): Sensitivity studies with the regional climate model REMO. *Meteorology and Atmospheric Physics*, **63**(1-2), 119–129. doi:10.1007/BF01025368
- Jacob, D., B. J. J. M. Van den Hurk, U. Andrae, G. Elgered, C. Fortelius, L. P. Graham, S. D. Jackson, U. Karstens, C. Köpken, R. Lindau, R. Podzun, B. Rockel, F. Rubel, B. H. Sass, R. N. B. Smith and X. Yang (2001): A comprehensive model inter-comparison study investigating the water budget during the BALTEX-PIDCAP period. *Meteorology and Atmospheric Physics*, **77**(1-4), 19–43. doi:10.1007/s007030170015
- Jacob, D., L. Bärring, O. B. Christensen, J. H. Christensen, M. De Castro, M. Déqué, F. Giorgi, S. Hagemann, M. Hirschi, R. Jones, E. Kjellström, G. Lenderink, B. Rockel, E. Sánchez, C. Schär, S. I. Seneviratne, S. Somot, A. Van Ulden and B. Van Den Hurk (2007): An inter-comparison of regional climate models for Europe: Model performance in present-day climate. *Climatic Change*, **81**, 31–52. doi:10.1007/s10584-006-9213-4

- Jacob, D., A. Elizalde, A. Haensler, S. Hagemann, P. Kumar, R. Podzun, D. Rechid, A. R. Remedio, F. Saeed, K. Sieck, C. Teichmann and C. Wilhelm (2012): Assessing the transferability of the regional climate model REMO to different coordinated regional climate downscaling experiment (CORDEX) regions. *Atmosphere*, **3**(1), 181–199. doi:10.3390/atmos3010181
- Jacob, D., J. Petersen, B. Eggert, A. Alias, O. B. Christensen, L. M. Bouwer, A. Braun, A. Colette, M. Déqué, G. Georgievski, E. Georgopoulou, A. Gobiet, L. Menut, G. Nikulin, A. Haensler, N. Hempelmann, C. Jones, K. Keuler, S. Kovats, N. Kröner, S. Kotlarski, A. Kriegsmann, E. Martin, E. van Meijgaard, C. Moseley, S. Pfeifer, S. Preuschmann, C. Radermacher, K. Radtke, D. Rechid, M. Rounsevell, P. Samuelsson, S. Somot, J. F. Soussana, C. Teichmann, R. Valentini, R. Vautard, B. Weber and P. Yiou (2014): EURO-CORDEX: new high-resolution climate change projections for European impact research. *Regional Environmental Change*, **14**(2), 563–578. doi:10.1007/s10113-013-0499-2
- Janjic, Z. I., J. P. Gerrity and S. Nickovic (2001): An alternative approach to nonhydrostatic modeling. *Monthly Weather Review*, **129**, 1164–1178. doi:10.1175/1520-0493(2001)129<1164:AAATNM>2.0.CO;2
- Keller, M., N. Kröner, O. Fuhrer, D. Lüthi, J. Schmidli, M. Stengel, R. Stöckli and C. Schär (2018): The sensitivity of Alpine summer convection to surrogate climate change: An intercomparison between convection-parameterizing and convection-resolving models. *Atmospheric Chemistry and Physics*, **18**, 5253–5264. doi:10.5194/acp-18-5253-2018
- Knutti, R., R. Furrer, C. Tebaldi, J. Cermak and G. A. Meehl (2010): Challenges in combining projections from multiple climate models. *Journal of Climate*, **23**(10), 2739–2758. doi:10.1175/2009JCLI3361.1
- Kotlarski, S. (2007): A subgrid glacier parameterisation for use in regional climate modelling. PhD thesis, University of Hamburg. doi:10.17617/2.994357
- Kotlarski, S., K. Keuler, O. B. Christensen, A. Colette, M. Déqué, A. Gobiet, K. Goergen, D. Jacob, D. Lüthi, E. Van Meijgaard, G. Nikulin, C. Schär, C. Teichmann, R. Vautard, K. Warrach-Sagi and V. Wulfmeyer (2014): Regional climate modeling on European scales: A joint standard evaluation of the EURO-CORDEX RCM ensemble. *Geoscientific Model Development*, **7**, 1297–1333. doi:10.5194/gmd-7-1297-2014
- Kotlarski, S., D. Lüthi and C. Schär (2015): The elevation dependency of 21st century European climate change: an RCM ensemble perspective. *International Journal of Climatology*, **35**(13), 3902–3920. doi:10.1002/joc.4254
- Krohn, S., P.-E. Morthorst and S. Awerbuch (eds.) (2009): The economics of wind energy. European Wind Energy Association (EWEA), 156 pp. <http://www.ewea.org/publications/reports/the-economics-of-wind-energy/> (last access November 9, 2015)
- Kröner, N., S. Kotlarski, E. Fischer, D. Lüthi, E. Zubler and C. Schär (2017): Separating climate change signals into thermodynamic, lapse-rate and circulation effects: theory and application to the European summer climate. *Climate Dynamics*, **48**, 3425–3440. doi:10.1007/s00382-016-3276-3
- Laprise, R. (1992): The Euler equations of motion with hydrostatic pressure as an independent variable. *Monthly Weather Review*, **120**, 197–207. doi:10.1175/1520-0493(1992)120<0197:TEEOMW>2.0.CO;2

- Laprise, R. (2008): Regional climate modelling. *Journal of Computational Physics*, **227**, 3641–3666. doi: 10.1016/j.jcp.2006.10.024
- Laprise, R., R. de Elía, D. Caya, S. Biner, P. Lucas-Picher, E. Diaconescu, M. Leduc, A. Alexandru and L. Separovic (2008): Challenging some tenets of regional climate modelling. *Meteorology and Atmospheric Physics*, **100**(1-4), 3–22. doi:10.1007/s00703-008-0292-9
- Larsén, X. G., J. Mann, J. Berg, H. Göttel and D. Jacob (2010): Wind climate from the regional climate model REMO. *Wind Energy*, **13**(4), 279–296. doi:10.1002/we.337
- Louis, J.-F. (1979): A parametric model of vertical eddy fluxes in the atmosphere. *Boundary-Layer Meteorology*, **17**(2), 187–202. doi:10.1007/BF00117978
- Lucas-Picher, P., F. Boberg, J. H. Christensen and P. Berg (2013): Dynamical downscaling with reinitializations: A method to generate finescale climate datasets suitable for impact studies. *Journal of Hydrometeorology*, **14**, 1159–1174. doi:10.1175/JHM-D-12-063.1
- Majewski, D. (1991): The EUROPA-MODELL of the Deutscher Wetterdienst. *ECMWF Seminar on Numerical Methods in Atmospheric Models*, pp. 147–191. <https://www.ecmwf.int/sites/default/files/elibrary/1991/10940-europa-modell-deutscher-wetterdienst.pdf> (last access May 16, 2018)
- MHI Vestas Offshore Wind (2018a): MHI Vestas Offshore Wind V164-8.0 MW[®] - Technical specifications. <https://en.wind-turbine-models.com/turbines/318-vestas-v164-8.0> (last access September 18, 2018)
- MHI Vestas Offshore Wind (2018b): MHI Vestas Offshore Wind V164-8.0 MW[®]. <http://www.mhivestasoffshore.com/category/v164-8-0-mw/> (last access September 18, 2018)
- Milan, P., M. Wächter and J. Peinke (2013): Turbulent character of wind energy. *Physical Review Letters*, **110**(13), 138701. doi:10.1103/PhysRevLett.110.138701
- Moemken, J., M. Meyers, H. Feldmann and J. G. Pinto (2018): Future changes of wind speed and wind energy potentials in EURO-CORDEX ensemble simulations. *Journal of Geophysical Research: Atmospheres*, **123**(12), 6373–6389. doi:10.1029/2018JD028473
- Moss, R. H., J. A. Edmonds, K. A. Hibbard, M. R. Manning, S. K. Rose, D. P. van Vuuren, T. R. Carter, S. Emori, M. Kainuma, T. Kram, G. A. Meehl, J. F. B. Mitchell, N. Nakicenovic, K. Riahi, S. J. Smith, R. J. Stouffer, A. M. Thomson, J. P. Weyant and T. J. Wilbanks (2010): The next generation of scenarios for climate change research and assessment. *Nature*, **463**, 747–756. doi:10.1038/nature08823
- MunichRE (2018): Powering growth - Innovative insurance solutions for on- and offshore wind power. Report, MunichRE. https://www.munichre.com/site/cip/get/documents_E-347956079/mr/assetpool.shared/Documents/3_Corporate_Insurance_Partner/Green-Tech-Solutions/Wind-Energy/MunichRe-On-Offshore-Windpower.pdf (last access November 15, 2018)
- Narapusetty, B., T. Delsole and M. K. Tippett (2009): Optimal estimation of the climatological mean. *Journal of Climate*, **22**(18), 4845–4859. doi:10.1175/2009JCLI2944.1

- Ørsted (2016): World's first offshore wind farm now dismantled. <https://orsted.com/en/Media/Newsroom/News/2017/09/Worlds-first-offshore-wind-farm-now-dismantled> (last access January 11, 2019)
- Peña, A., S. E. Gryning and C. B. Hasager (2010a): Comparing mixing-length models of the diabatic wind profile over homogeneous terrain. *Theoretical and Applied Climatology*, **100**, 325–335. doi:10.1007/s00704-009-0196-8
- Peña, A., S. E. Gryning, J. Mann and C. B. Hasager (2010b): Length scales of the neutral wind profile over homogeneous terrain. *Journal of Applied Meteorology and Climatology*, **49**, 792–806. doi:10.1175/2009JAMC2148.1
- Pfeifer, S. (2006): Modeling cold cloud processes with the regional climate model REMO. PhD thesis, University of Hamburg. doi:10.17617/2.994658
- Prein, A. F., W. Langhans, G. Fosser, A. Ferrone, N. Ban, K. Goergen, M. Keller, M. Tölle, O. Gutjahr, F. Feser, E. Brisson, S. Kollet, J. Schmidli, N. P. Van Lipzig and R. Leung (2015): A review on regional convection-permitting climate modeling: Demonstrations, prospects, and challenges. *Reviews of Geophysics*, **53**(2), 323–361. doi:10.1002/2014RG000475
- Pryor, S. C. and R. J. Barthelmie (2010): Climate change impacts on wind energy: A review. *Renewable and Sustainable Energy Reviews*, **14**(1), 430–437. doi:10.1016/j.rser.2009.07.028
- Pryor, S. C. and R. J. Barthelmie (2013): Assessing the vulnerability of wind energy to climate change and extreme events. *Climatic Change*, **121**, 79–91. doi:10.1007/s10584-013-0889-y
- Pryor, S. C., R. J. Barthelmie and E. Kjellström (2005): Potential climate change impact on wind energy resources in Northern Europe: Analyses using a regional climate model. *Climate Dynamics*, **25**, 815–835. doi:10.1007/s00382-005-0072-x
- Pryor, S. C., R. J. Barthelmie, N. E. Clausen, M. Drews, N. MacKellar and E. Kjellström (2012): Analyses of possible changes in intense and extreme wind speeds over northern Europe under climate change scenarios. *Climate Dynamics*, **38**, 189–208. doi:10.1007/s00382-010-0955-3
- Rechid, D. (2009): On biogeophysical interactions between vegetation phenology and climate simulated over Europe. PhD thesis, University of Hamburg. doi:10.17617/2.994074
- Rechid, D. and D. Jacob (2006): Influence of monthly varying vegetation on the simulated climate in Europe. *Meteorologische Zeitschrift*, **15**(1), 99–116. doi:10.1127/0941-2948/2006/0091
- Renewable Energy Directive (2009): Directive 2009/28/EC on the promotion of the use of energy from renewable sources. European Parliament & Council of the European Union. *Official Journal of the European Union*, **L 140**, 16–62. <http://data.europa.eu/eli/dir/2009/28/oj> (last access December 19, 2018)
- Reyers, M., J. G. Pinto and J. Moemken (2014): Statistical-dynamical downscaling for wind energy potentials: Evaluation and applications to decadal hindcasts and climate change projections. *International Journal of Climatology*, **35**(2), 229–244. doi:10.1002/joc.3975
- Reyers, M., J. Moemken and J. G. Pinto (2016): Future changes of wind energy potentials over Europe in a large CMIP5 multi-model ensemble. *International Journal of Climatology*, **36**(2), 783–796. doi:10.1002/joc.4382

- Roeckner, E., K. Arpe, L. Bengtsson, S. Brinkop, L. Dümenil, M. Esch, E. Kirk, F. Lunkeit, M. Ponater, B. Rockel, R. Sausen, U. Schlese, S. Schubert and M. Windelband (1992): Simulation of the present-day climate with the ECHAM model: Impact of model physics and resolution. Report, Max Planck Institute for Meteorology. https://www.mpimet.mpg.de/fileadmin/publikationen/Reports/MPI-Report_93.pdf (last access July 25, 2018)
- Roeckner, E., K. Arpe, L. Bengtsson, M. Christoph, M. Claussen, L. Dümenil, M. Esch, M. Giorgetta, U. Schlese and U. Schulzweida (1996): The atmospheric general circulation model ECHAM-4: Model description and simulation of present-day climate. Report, Max Planck Institute for Meteorology. https://www.mpimet.mpg.de/fileadmin/publikationen/Reports/MPI-Report_218.pdf (last access May 16, 2018)
- Rummukainen, M. (2010): State-of-the-art with regional climate models. *Wiley Interdisciplinary Reviews: Climate Change*, **1**(1), 82–96. doi:10.1002/wcc.8
- Rummukainen, M. (2016): Added value in regional climate modeling. *Wiley Interdisciplinary Reviews: Climate Change*, **7**(1), 145–159. doi:10.1002/wcc.378
- Schär, C., C. Frei, D. Lüthi and H. C. Davies (1996): Surrogate climate change scenarios for regional climate models. *Geophysical Research Letters*, **23**(6), 669–672. doi:10.1029/96GL00265
- Semmler, T. (2002): Der Wasser- und Energiehaushalt der arktischen Atmosphäre. PhD thesis, University of Hamburg
- Siemens (2016): Kosten für Offshore-Windstrom sinken weiter. <https://www.siemens.com/customer-magazine/de/home/specials/offshore-windenergie-eine-investition-fuer-die-zukunft/kosten-fuer-offshore-windstrom-sinken-weiter.html> (last access January 10, 2019)
- Stull, R. B. (1988): An Introduction to Boundary Layer Meteorology. Kluwer Academic Publishers, 670 pp. ISBN: 978-90-277-2769-5
- Taylor, K. E., R. J. Stouffer and G. A. Meehl (2012): An overview of CMIP5 and the experiment design. *Bulletin of the American Meteorological Society*, **93**(4), 485–498. doi:10.1175/BAMS-D-11-00094.1
- Teichmann, C. (2009): Climate and air pollution modelling in South America with focus on megacities. PhD thesis, University of Hamburg. doi:10.17617/2.993870
- Teichmann, C., B. Eggert, A. Elizalde, A. Haensler, D. Jacob, P. Kumar, C. Moseley, S. Pfeifer, D. Rechid, A. R. Remedio, H. Ries, J. Petersen, S. Preuschmann, T. Raub, F. Saeed, K. Sieck and T. Weber (2013): How does a regional climate model modify the projected climate change signal of the driving GCM: A study over different CORDEX regions using REMO. *Atmosphere*, **4**(2), 214–236. doi:10.3390/atmos4020214
- Termonia, P., A. Deckmyn and R. Hamdi (2009): Study of the lateral boundary condition temporal resolution problem and a proposed solution by means of boundary error restarts. *Monthly Weather Review*, **137**, 3551–3566. doi:10.1175/2009MWR2964.1
- The Wind Power Program (2018): Wind turbine power curve database. [http://www.wind-power-program.com/Downloads/Databasepowercurves\(May2017\).zip](http://www.wind-power-program.com/Downloads/Databasepowercurves(May2017).zip) (last access August 21, 2018)

- Tobin, I., R. Vautard, I. Balog, F.-m. Bréon, S. Jerez, P. M. Ruti, F. Thais, M. Vrac and P. Yiou (2015): Assessing climate change impacts on European wind energy from ENSEMBLES high-resolution climate projections. *Climate Change*, **128**, 99–112. doi:10.1007/s10584-014-1291-0
- Tobin, I., S. Jerez, R. Vautard, F. Thais, E. van Meijgaard, A. Prein, M. Déqué, S. Kotlarski, C. F. Maule, G. Nikulin, T. Noël and C. Teichmann (2016): Climate change impacts on the power generation potential of a European mid-century wind farms scenario. *Environmental Research Letters*, **11**, 034013. doi:10.1088/1748-9326/11/3/034013
- Torma, C., F. Giorgi and E. Coppola (2015): Added value of regional climate modeling over areas characterized by complex terrain - Precipitation over the Alps. *Journal of Geophysical Research: Atmospheres*, **120**(9), 3957–3972. doi:10.1002/2014JD022781
- Troccoli, A. (ed.) (2008): Management of Weather and Climate Risk in the Energy Industry. Springer, 361 pp. ISBN: 978-90-481-3692-6
- Troccoli, A., L. Dubus and S. E. Haupt (eds.) (2014): Weather Matters for Energy. Springer, 523 pp. ISBN: 978-1-4614-9221-4
- Troen, I. and E. Lundtang Petersen (1989): European Wind Atlas. Risø National Laboratory, 656 pp. ISBN: 87-550-1482-8
- UBA (2015): Vulnerabilität Deutschlands gegenüber dem Klimawandel. Report, Umweltbundesamt. <https://www.umweltbundesamt.de/publikationen/vulnerabilitaet-deutschlands-gegenueber-dem> (last access May 30, 2016)
- Vattenfall (2016): The first decommission in the world of an offshore wind farm is now complete. <https://corporate.vattenfall.com/press-and-media/press-releases/2016/the-first-decommission-in-the-world-of-an-offshore-wind-farm-is-now-complete/> (last access January 11, 2019)
- von Storch, H. and F. W. Zwiers (1999): Statistical Analysis in Climate Research. Cambridge University Press, 1st ed., 495 pp. ISBN: 978-0-511-61233-6
- Warner, T. T. (2011): Numerical Weather and Climate Prediction. Cambridge University Press, 550 pp. ISBN: 978-0-521-51389-0
- Warner, T. T., R. A. Peterson and R. E. Treadon (1997): A tutorial on lateral boundary conditions as a basic and potentially serious limitation to regional numerical weather prediction. *Bulletin of the American Meteorological Society*, **78**(11), 2599–2618. doi:10.1175/1520-0477(1997)078<2599:ATOLBC>2.0.CO;2
- WindEurope (2018a): Wind in power 2017 - Annual combined onshore and offshore wind energy statistics. Report, WindEurope. <https://windeurope.org/wp-content/uploads/files/about-wind/statistics/WindEurope-Annual-Statistics-2017.pdf> (last access December 21, 2018)
- WindEurope (2018b): Offshore Wind in Europe - Key trends and statistics 2017. Report, WindEurope. <https://windeurope.org/wp-content/uploads/files/about-wind/statistics/WindEurope-Annual-Offshore-Statistics-2017.pdf> (last access December 21, 2018)

WMO (2017): WMO Guidelines on the Calculation of Climate Normals. WMO-No. 1203. World Meteorological Organization, 2017th ed., 29 pp. ISBN: 978-92-63-11203-3

List of Abbreviations

CAPEX	capital expenditure
CF	cash flow
CMIP5	Coupled Model Intercomparison Project Phase 5
CMIP6	Coupled Model Intercomparison Project Phase 6
CORDEX	Coordinated Regional Climate Downscaling Experiment
DSCR	Debt Service Cover Ratio
DSRA	Debt Service Reserve Account
EBITDA	earnings before interests, taxes, depreciation and amortisation
EBIT	earnings before interests and taxes
EEG	German Renewable Energy Sources Act
EIRR	Equity Internal Rate of Return
ESGF	Earth System Grid Foundation
EU	European Union
EURO-CORDEX	European branch of the Coordinated Regional Climate Downscaling Experiment
GCM	global climate model
IRR	Internal Rate of Return
LBC	lateral boundary condition

LES	large eddy simulation
MSLP	mean sea level pressure
NPV	Net Present Value
O&M	operation and maintenance
OPEX	operational expenditure
PBL	planetary boundary layer
PBT	profit before taxes
PV	Present Value
RCM	regional climate model
RCP	representative concentration pathway
RMSE	root mean square error
WCRP	World Climate Research Programme

List of Figures

2.1	Schematic of different phases of wind energy project	8
2.2	Schematic of the wind energy financing chain	10
2.3	Schematic of climate change impacts on the wind energy financing chain	14
3.1	Schematic of an Arakawa-C grid	28
3.2	Schematic of a σ -coordinate system	28
3.3	Vertical temperature change signals following the emission scenarios RCP2.6, RCP4.5 and RCP8.5 to be used for surrogate climate change experiments	37
3.4	Bandwidth of EURO-CORDEX ensemble temperature change signals at 850 hPa and 500 hPa following the emission scenarios RCP2.6, RCP4.5 and RCP8.5	38
3.5	Simulation domains	42
3.6	Mean sea level pressure sensitivity to lateral boundary condition update intervals	43
3.7	Analysis setup for meridional transects and vertical profiles	49
3.8	Horizontal patterns of annual mean wind speed at 10 m height	51
3.9	Meridional transects of annual mean wind speed for the lowest 1000 m of the atmosphere	53
3.10	Meridional transects of annual mean wind speed for the lowest 300 m of the atmosphere	54
3.11	Meridional transects of seasonal mean wind speed differences for the lowest 300 m of the atmosphere	56
3.12	Meridional transects of annual mean wind speed standard deviation for the lowest 300 m of the atmosphere	59
3.13	Vertical temperature change signals for the lowest 1000 m of the atmosphere as simulated for REMO-NH surrogate climate change experiments	61

3.14	Vertical wind speed change signals for the lowest 300 m of the atmosphere as simulated for REMO-NH surrogate climate change experiments	64
3.15	Fraction of stable and unstable stability cases with respect to the total simulation period as simulated for REMO-NH surrogate climate change experiments	66
3.16	Change ratio of frictional velocity as simulated for REMO-NH surrogate climate change experiments	69
3.17	Change ratio of turbulent heat flux as simulated for REMO-NH surrogate climate change experiments	70
3.18	Vertical wind energy density change signals for the lowest 300 m of the atmosphere as simulated for REMO-NH surrogate climate change experiments	72
3.19	Vertical air density change signals for the lowest 300 m of the atmosphere as simulated for REMO-NH surrogate climate change experiments	74
4.1	Power curve of a MHI Vestas Offshore V164-8.0 MW [®] offshore wind turbine . . .	94
4.2	Total monthly energy output E_{out} of the surrogate climate change experiments according to a MHI Vestas Offshore V164-8.0 MW [®] wind turbine power curve . .	96
4.3	Projected free cash flow as simulated with the financial model	98
4.4	Projected cash flow of debt service as simulated with the financial model	100
4.5	Projected cash flow of equity dividends as simulated with the financial model . .	102
A.1	Vertical temperature change signals following the emission scenarios RCP2.6, RCP4.5 and RCP8.5 spatially averaged over the EURO-CORDEX domain	138
A.2	Bandwidth of EURO-CORDEX ensemble temperature change signals at 850 hPa and 500 hPa following the emission scenarios RCP2.6, RCP4.5 and RCP8.5 spatially averaged over the EURO-CORDEX domain	139
A.3	Horizontal patterns of annual mean wind speed at 100 m height	144
A.4	Horizontal patterns of seasonal mean wind speed differences at 10 m height . . .	145
A.5	Meridional transects of seasonal mean wind speed for the lowest 300 m of the atmosphere as simulated for REMO27	147
A.6	Meridional transects of seasonal mean wind speed for the lowest 300 m of the atmosphere as simulated for REMO49	149
A.7	Meridional transects of seasonal mean wind speed for the lowest 300 m of the atmosphere as simulated for REMO-NH	151

A.8 Meridional transects of seasonal mean wind speed standard deviation differences for the lowest 300 m of the atmosphere	153
A.9 Horizontal patterns of seasonal mean wind speed climate change signals of REMO EURO-CORDEX simulations over the German Bight	155
A.10 Difference between upper air and near surface seasonal mean wind speed climate change signals over the German Bight from REMO EURO-CORDEX simulations	157
A.11 Projected capital structure as simulated with the financial model	158
A.12 Projected cost structure as simulated with the financial model	159

List of Tables

- 4.1 Technical assumptions used for the financial model simulations 91
- 4.2 Economic assumptions used for the financial model simulations 92
- 4.3 Financial model simulation results representing project profitability 105
- 4.4 Financial model simulation results representing financial risk 107

- A.1 List of EURO-CORDEX ensemble simulations 140
- A.2 List of REMO model levels according to 27 vertical atmospheric levels 141
- A.3 List of REMO model levels according to 49 vertical atmospheric levels 142
- A.4 List of REMO variables to be adjusted for surrogate climate change experiments 160
- A.5 List of wind energy-specific variables introduced to REMO 161
- A.6 List of REMO simulation experiments 162
- A.7 Total monthly energy output of surrogate climate change experiments according
to a MHI Vestas Offshore V164-8.0 MW[®] offshore wind turbine power curve . . . 163

A Appendix

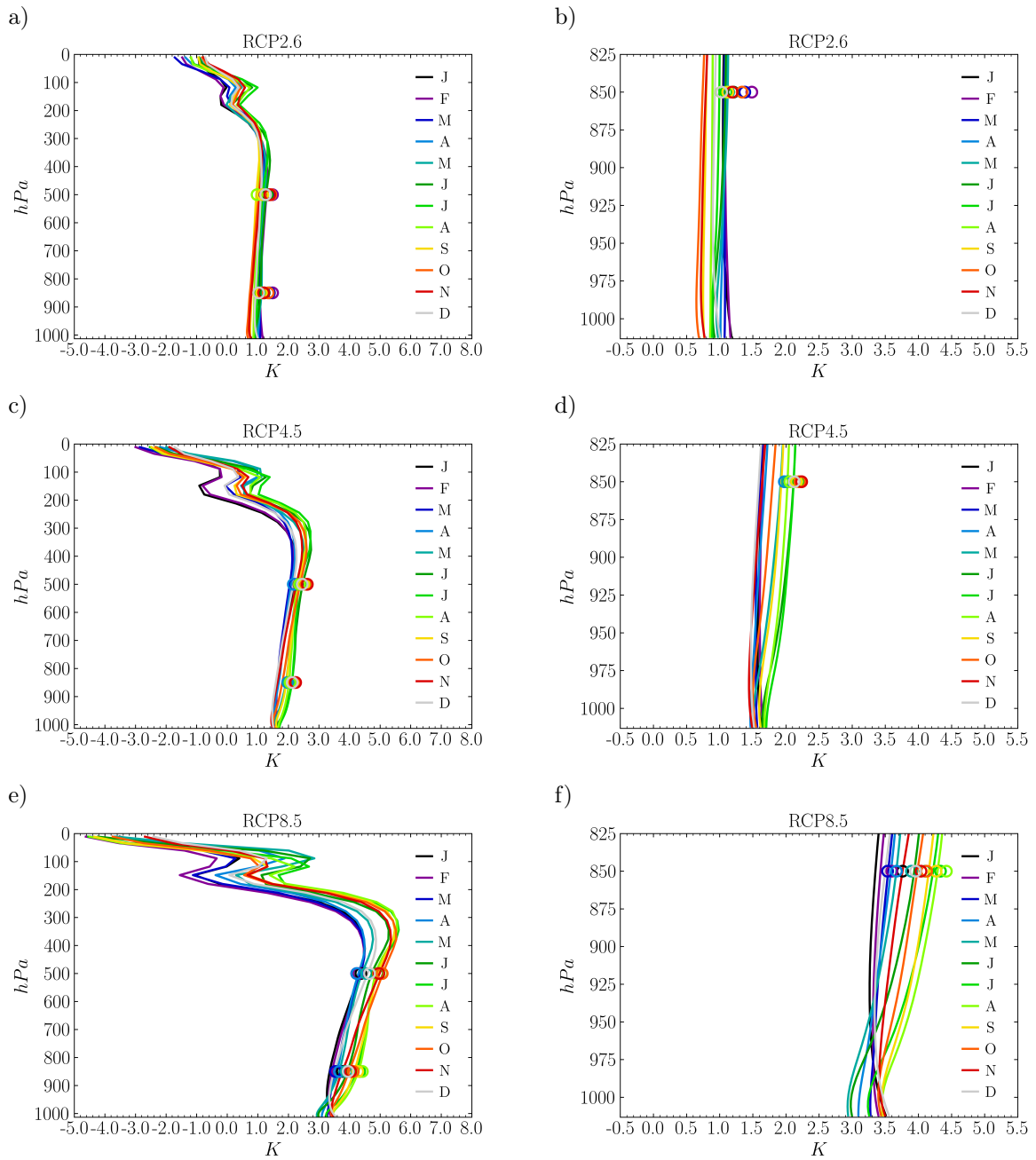


Figure A.1: Vertical temperature change signals spatially averaged over the EURO-CORDEX domain. Shown are signals following the emission scenarios RCP2.6 (a-b), RCP4.5 (c-d) and RCP8.5 (e-f) for the entire (a, c, e) and lower atmosphere (b, d, f; up to 825 hPa) as simulated by REMO. The signals are achieved analogues to Fig. 3.3 but 30-year periods of daily temperature values are spatially averaged and spectrally filtered over the entire simulation domain (i.e. EURO-CORDEX; see Fig. 3.5) to gain smoothed annual temperature cycles for every model level separately. Change signals for the end of the 21st century are computed from these annual cycles and reconstructed to daily-resolved vertical temperature change profiles over a year (only the mid-month days for each month are shown due to visibility reasons). The vertical profiles range from 1013.25 hPa until 25 hPa where REMO's atmospheric top is capped. Circles depict median temperature change values of the EURO-CORDEX ensemble (see Tab. A.1) at 850 hPa and 500 hPa, while the color code matches the monthly scaling.

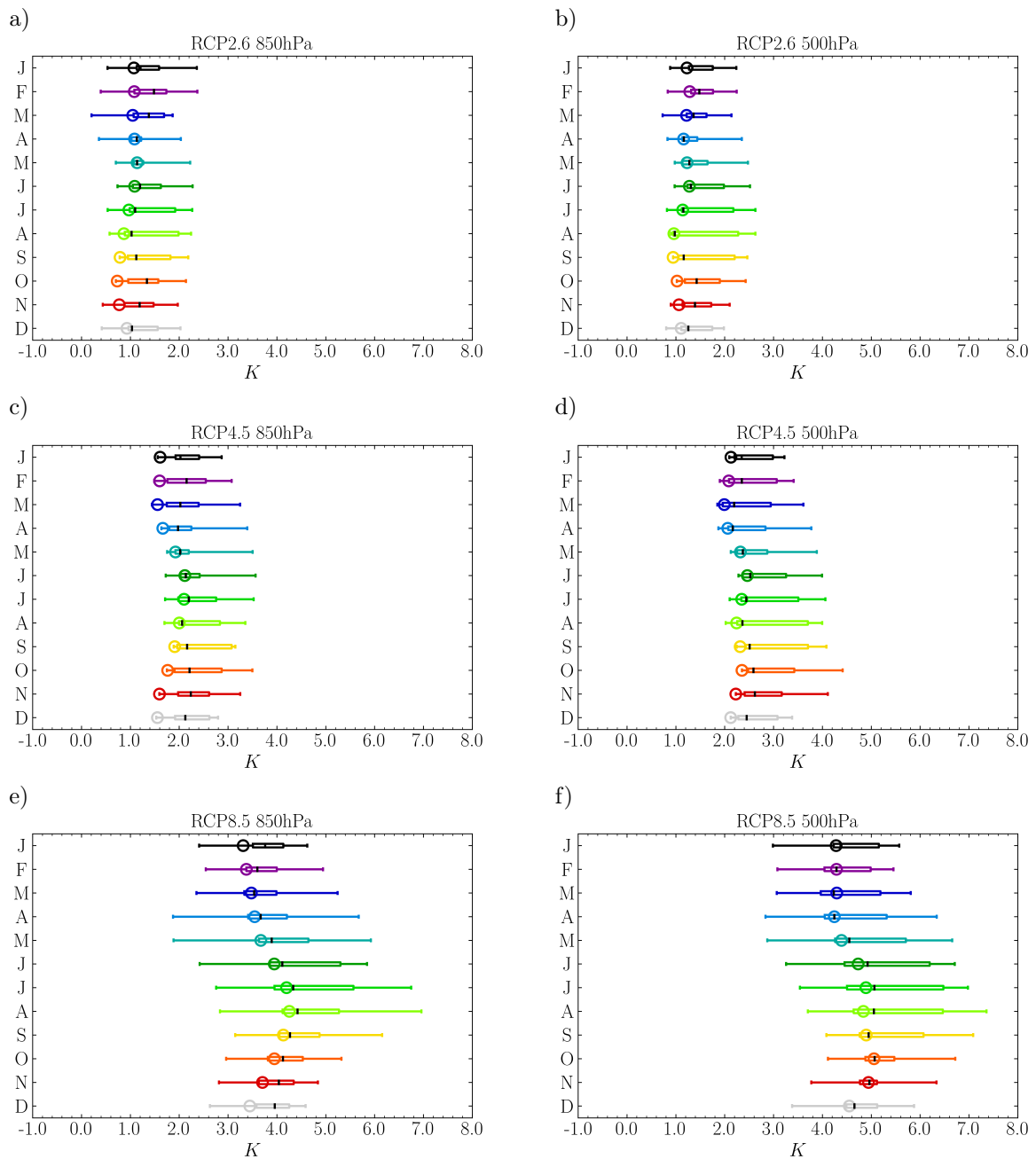


Figure A.2: Bandwidth of EURO-CORDEX ensemble temperature change signals spatially averaged over the EURO-CORDEX domain. Shown are signals at 850 hPa (a, c, e) and 500 hPa (b, d, f) following the emission scenarios RCP2.6 (a, b), RCP4.5 (c, d) and RCP8.5 (e, f) for the end of the 21st century. The signals are achieved analogous to Fig. 3.4 but spatially averaged over the entire EURO-CORDEX simulation domain. The methodological procedure is as described in Section 3.4.1 and Fig. A.1 but applied to the EURO-CORDEX ensemble. Monthly-resolved box and whisker plots indicate the ensemble median (black bars), interquartile range (boxes; i.e. range between 25th and 75th percentile) as well as minimum and maximum values (whisker edges; i.e. full ensemble range). Circles depict the REMO model simulation (according to Fig. A.1).

Table A.1: List of EURO-CORDEX ensemble members. Simulations are carried out within the WCRP CORDEX initiative (*Giorgi et al., 2009*) and provide regional downscaled climate and climate change information for Europe. Combinations of regional climate model (RCM) and forcing global climate model (GCM) realisations are clustered by representative concentration pathway (RCP) scenarios. The (current) EURO-CORDEX ensemble consists of 15 members for RCP2.6, 17 members for RCP4.5 and 25 members for RCP8.5, being composed of 9 different GCMs (12 different GCM realisations) and 6 different RCMs (7 different RCM versions). Only high-resolution EURO-CORDEX simulations (EUR-11) providing atmospheric temperature at pressure levels of 850 hPa and 500 hPa are listed.

RCP2.6		RCP4.5		RCP8.5	
RCM	GCM	RCM	GCM	RCM	GCM
				CCLM4.8	CanESM r1
				REMO2015	CanESM r1
		CCLM4.8	CNRM-CM5 r1	CCLM4.8	CNRM-CM5 r1
		RCA4	CNRM-CM5 r1	RCA4	CNRM-CM5 r1
				REMO2015	CNRM-CM5 r1
CCLM4.8	EC-EARTH r12	CCLM4.8	EC-EARTH r12	CCLM4.8	EC-EARTH r12
HIRHAM5	EC-EARTH r3	HIRHAM5	EC-EARTH r3	HIRHAM5	EC-EARTH r3
		RACMO2.2	EC-EARTH r1	RACMO2.2	EC-EARTH r1
RACMO2.2	EC-EARTH r12	RACMO2.2	EC-EARTH r12	RACMO2.2	EC-EARTH r12
RCA4	EC-EARTH r12	RCA4	EC-EARTH r12	RCA4	EC-EARTH r12
REMO2015	EC-EARTH r12			REMO2015	EC-EARTH r12
REMO2015	GFDL-ESM r1				
		CCLM4.8	HadGEM2 r1	CCLM4.8	HadGEM2 r1
				HIRHAM5	HadGEM2 r1
RACMO2.2	HadGEM2 r1	RACMO2.2	HadGEM2 r1	RACMO2.2	HadGEM2 r1
RCA4	HadGEM2 r1	RCA4	HadGEM2 r1	RCA4	HadGEM2 r1
REMO2015	HadGEM2 r1			REMO2015	HadGEM2 r1
		RCA4	IPSL-CM5A r1	RCA4	IPSL-CM5A r1
REMO2015	IPSL-CM5A r1				
		WRF3.3.1	IPSL-CM5A r1	WRF3.3.1	IPSL-CM5A r1
				CCLM4.8	MIROC5 r1
REMO2015	MIROC5 r1			REMO2015	MIROC5 r1
CCLM4.8	MPI-ESM r1	CCLM4.8	MPI-ESM r1	CCLM4.8	MPI-ESM r1
RCA4	MPI-ESM r1	RCA4	MPI-ESM r1	RCA4	MPI-ESM r1
REMO2009	MPI-ESM r1	REMO2009	MPI-ESM r1	REMO2009	MPI-ESM r1
REMO2009	MPI-ESM r2	REMO2009	MPI-ESM r2	REMO2009	MPI-ESM r2
		HIRHAM5	NorESM1 r1	HIRHAM5	NorESM1 r1

Table A.2: List of REMO model levels according to 27 vertical atmospheric levels. Model levels are defined through AK and BK values. Pressures of the model levels in Pa are derived through Eq. 3.4 for half ($p_{k-\frac{1}{2}}$) and Eq. 3.5 for full model levels (p_k) using standard atmospheric pressure of 1013.25 hPa.

k	$AK_{k-\frac{1}{2}}$	$BK_{k-\frac{1}{2}}$	$p_{k-\frac{1}{2}}$ [Pa]	p_k [Pa]
1	0.00000000	0.00000000	0.00000000	2500.00000000
2	5000.00000000	0.00000000	5000.00000000	7500.00000000
3	10000.00000000	0.00000000	10000.00000000	11800.00000000
4	13600.00000000	0.00000000	13600.00000000	15197.59717787
5	14736.35546875	0.02031916	16795.19435575	18115.43953825
6	15689.20703125	0.03697486	19435.68472075	20864.93960938
7	16266.60937500	0.05948764	22294.19449800	23832.57862637
8	16465.00390625	0.08789498	25370.96275475	27015.29981587
9	16297.62109375	0.12200361	28659.63687700	30404.64726038
10	15791.59765625	0.16144150	32149.65764375	33988.90499725
11	14985.26953125	0.20570326	35828.15235075	37754.66588850
12	13925.51953125	0.25418860	39681.17942625	41687.88563012
13	12665.29296875	0.30623537	43694.59183400	45774.42072712
14	11261.23046875	0.36114502	47854.24962025	50000.00094562
15	9771.40625000	0.41820228	52145.75227100	54349.69500362
16	8253.21093750	0.47668815	56553.63773625	58806.84315588
17	6761.33984375	0.53588659	61060.04857550	63351.43713463
18	5345.91406250	0.59508425	65642.82569375	67957.98676122
19	4050.71777344	0.65356457	70273.14782869	72592.84838556
20	2911.56933594	0.71059442	74912.54894244	77211.02003061
21	1954.80517578	0.76540524	79509.49111878	81752.41262993
22	1195.88989258	0.81716698	83995.33414108	86137.56677743
23	638.14892578	0.86495584	88279.79941378	90262.86769656
24	271.62646484	0.90771586	92245.93597934	93995.20153298
25	72.06358337	0.94421321	95744.46708662	97166.09674494
26	0.00000000	0.97298521	98587.72640325	99565.32469538
27	0.00000000	0.99228150	100542.9229875	100933.96149375
28	0.00000000	1.00000000	101325.00000000	

Table A.3: List of REMO model levels according to 49 vertical atmospheric levels. Model levels are defined through AK and BK values. Pressure values in Pa are derived through Eq. 3.4 for half ($p_{k-\frac{1}{2}}$) and Eq. 3.5 for full model levels (p_k) using standard atmospheric pressure of 1013.25 hPa.

k	$AK_{k-\frac{1}{2}}$	$BK_{k-\frac{1}{2}}$	$p_{k-\frac{1}{2}}$ [Pa]	p_k [Pa]
1	0.00000000	0.00000000	0.00000000	1117.62322588
2	2235.24645176	0.00000000	2235.24645176	3487.58881636
3	4739.93118096	0.00000000	4739.93118096	6092.99185308
4	7446.05252520	0.00000000	7446.05252520	8880.03011615
5	10314.00770710	0.00000000	10314.00770710	11813.54117855
6	13313.07465000	0.00000000	13313.07465000	14865.07736516
7	16417.08008032	0.00000000	16417.08008032	18009.90669029
8	19602.73330026	0.00000000	19602.73330026	21225.79132188
9	22848.84934350	0.00000000	22848.84934350	24493.36290478
10	25990.44656456	0.00145502	26137.87646606	27797.43730502
11	28619.07079148	0.00826970	29456.99814398	31124.73512246
12	30500.39927595	0.02262100	32792.47210095	34460.86068872
13	31597.69332800	0.04472298	36129.24927650	37790.51424138
14	32007.22576651	0.07347203	39451.77920626	41098.45832647
15	31870.98302968	0.10731956	42745.13744668	44370.41450017
16	31324.24597291	0.14479591	45995.69155366	47593.50295845
17	30477.44407275	0.18469154	49191.31436325	50756.33954425
18	29415.21714276	0.22606610	52321.36472526	53848.97973595
19	28201.07674588	0.26820151	55376.59474663	56862.81731445
20	26882.66651028	0.31054896	58349.03988228	59790.47964768
21	25496.08645684	0.35268525	61231.91941309	62625.73340572
22	24069.08485511	0.39428041	64019.54739836	65363.39730217
23	22623.31437424	0.43507459	66707.24720599	67999.26524149
24	21175.90328599	0.47486188	69291.28327699	70530.03219282
25	19740.54980465	0.51347872	71768.78110865	72953.22438033
26	18328.29132300	0.55079572	74137.66765200	75267.13243429
27	16948.05346584	0.58671151	76396.59721659	77470.74369509
28	15607.04982184	0.62114819	78544.89017359	79563.67910690

Table A.3: List of REMO model levels according to 49 vertical atmospheric levels. Model levels are defined through AK and BK values. Pressure values in Pa are derived through Eq. 3.4 for half ($p_{k-\frac{1}{2}}$) and Eq. 3.5 for full model levels (p_k) using standard atmospheric pressure of 1013.25 hPa.

29	14311.07977146	0.65404775	80582.46804021	81546.13168857
30	13064.75608067	0.68536925	82509.79533692	83418.80768161
31	11871.68345355	0.71508647	84327.82002630	85182.86833346
32	10734.60228336	0.74318593	86037.91664061	86839.87512569
33	9655.50722077	0.76966520	87641.83361077	88391.73892619
34	8635.74709686	0.79453143	89141.64424161	89840.67198595
35	7676.11067729	0.81780004	90539.69973029	91189.14149886
36	6776.90134018	0.83949353	91838.58326743	92439.82836429
37	5938.00283839	0.85964047	93041.07346114	93595.58843908
38	5158.93767802	0.87827452	94150.10341702	94659.41658556
39	4438.91922085	0.89543361	95168.72975410	95634.41397273
40	3776.89833086	0.91115914	96100.09819136	96523.75935411
41	3171.60519135	0.92549534	96947.42051685	97330.68336285
42	2621.58678735	0.93848862	97713.94620885	98058.44424791
43	2125.24045897	0.95018704	98402.94228697	98710.30694592
44	1680.84386987	0.96063980	99017.67160487	99289.52479855
45	1286.58169247	0.96989683	99561.37799222	99799.32420172
46	940.56928122	0.97800840	100037.27041122	100242.89042012
47	640.87358228	0.98502479	100448.51042903	100623.35531315
48	385.53151053	0.99099599	100798.20019728	100943.78820908
49	172.56600987	0.99597148	101089.37622087	101207.18811044
50	0.00000000	1.00000000	101325.00000000	

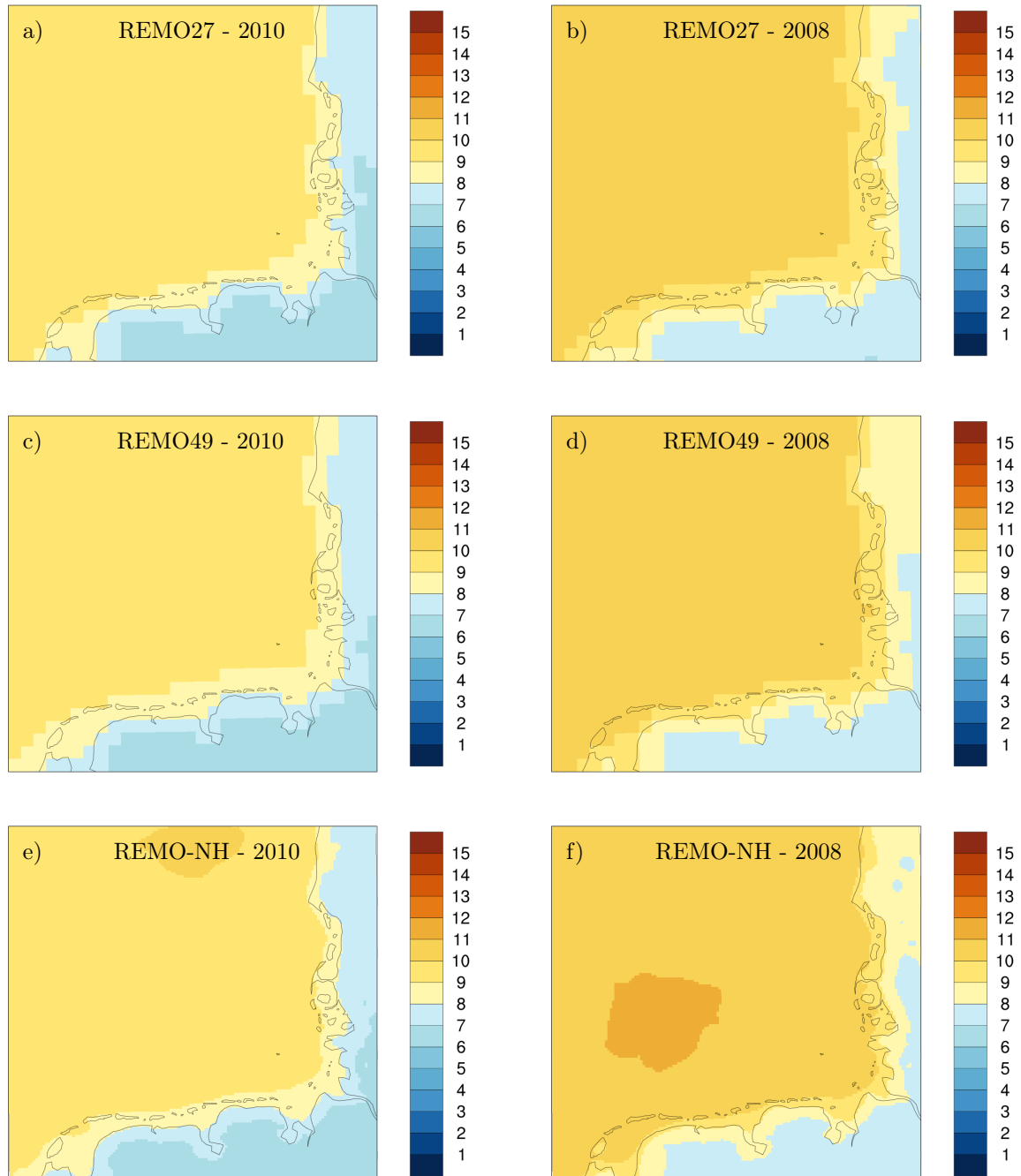


Figure A.3: Horizontal patterns of annual mean wind speed at 100 m height as simulated for the three different simulation setups. Shown are annual mean absolute values in ms^{-1} for REMO27 (a-b), REMO49 (c-d) and REMO-NH (e-f) for the respective simulation periods covering the year 2010 (a, c, e) and 2008 (b, d, f).

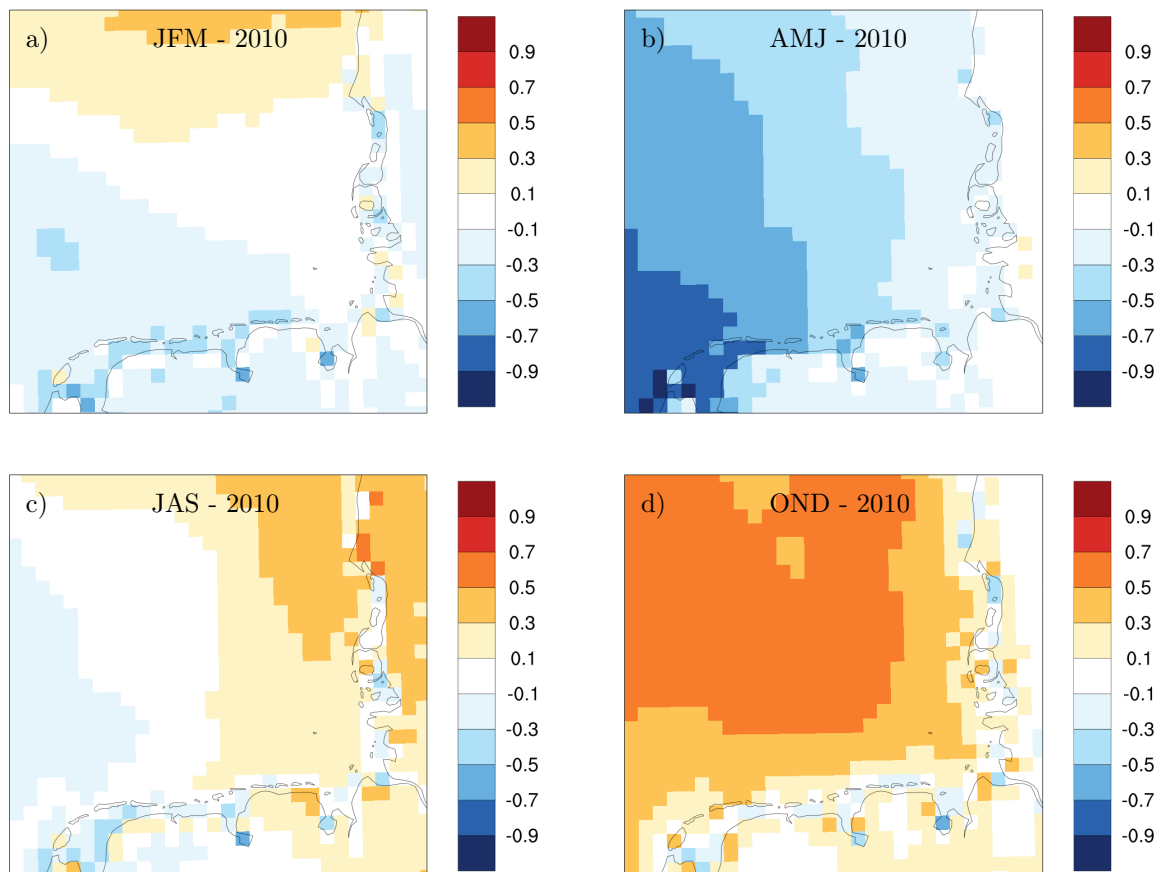


Figure A.4: Horizontal patterns of seasonal mean wind speed differences at 10 m height between REMO49 and REMO27 for the simulation year 2010. Shown are mean absolute differences in $m s^{-1}$ for JFM (a), AMJ (b), JAS (c) and OND (d). Analogous, images (e-h) on the next page illustrate seasonal mean wind speed differences for the simulation year of 2008.

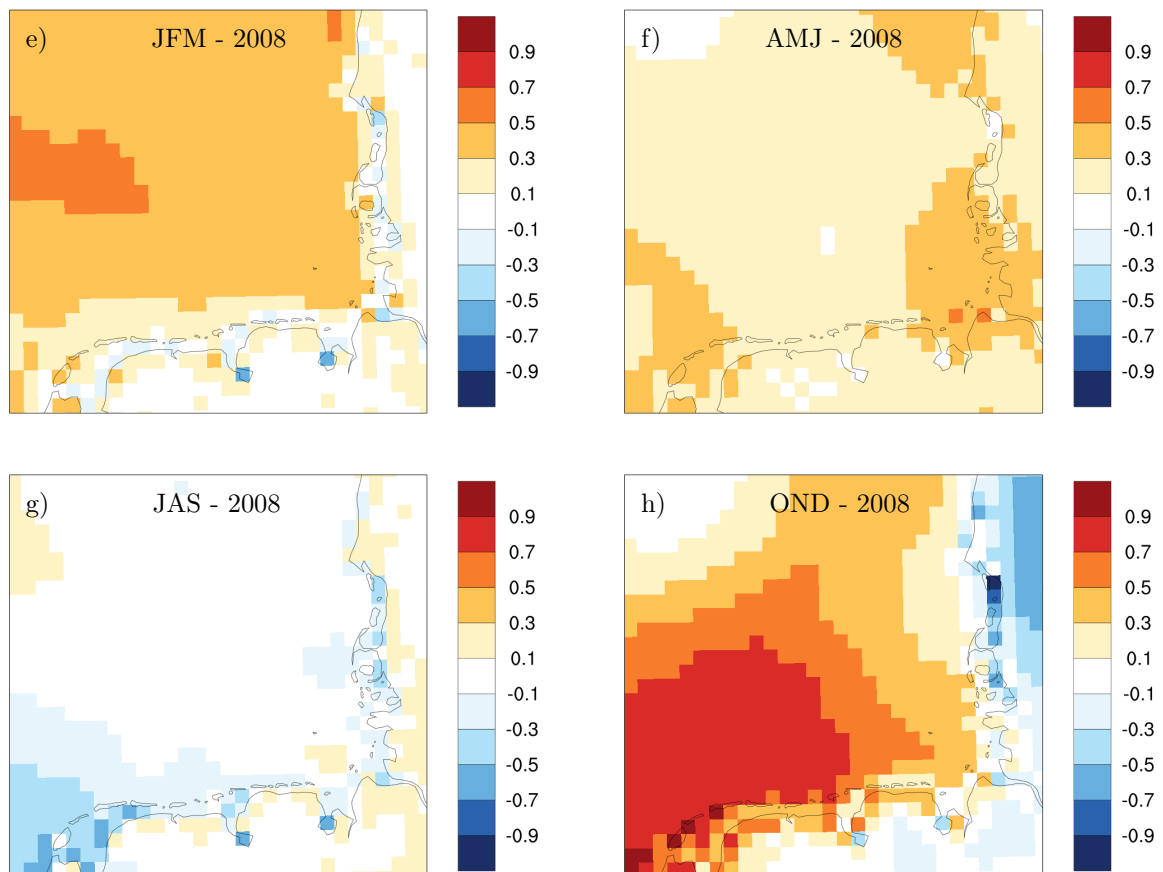


Figure A.4: Horizontal patterns of seasonal mean wind speed differences at 10 m height between REMO49 and REMO27 for the simulation year 2008. Shown are mean absolute differences in $m s^{-1}$ for JFM (e), AMJ (f), JAS (g) and OND (h). Analogous, images (a-d) on the previous page illustrate seasonal mean wind speed differences for the simulation year of 2010.

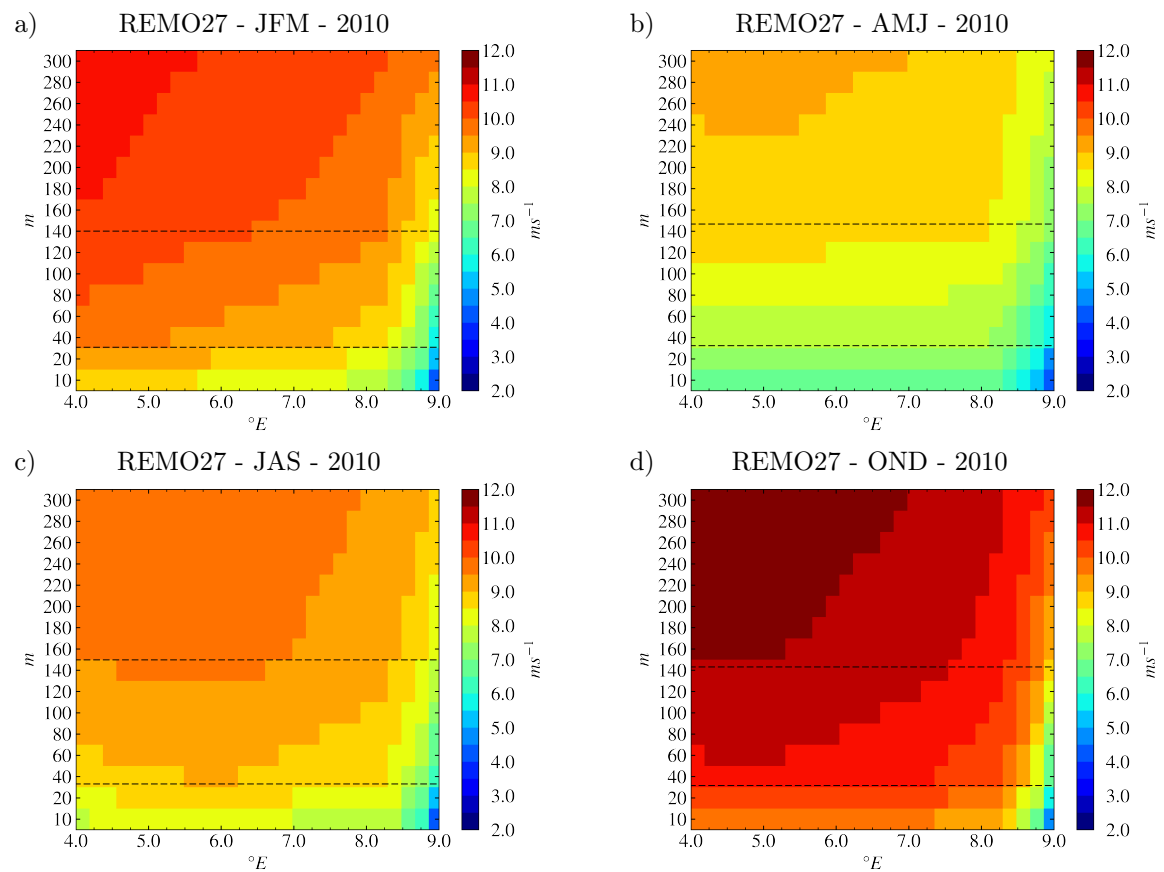


Figure A.5: Meridional transects of seasonal mean wind speed for the lowest 300 m of the atmosphere as simulated for REMO27 for the simulation year 2010. Shown are mean absolute values in $m s^{-1}$ for JFM (a), AMJ (b), JAS (c) and OND (d) for the meridional transect as defined in Fig. 3.7. Dashed black lines refer to the average geometric height of model half-levels of the individual simulations where the horizontal wind components are defined. Analogous, images (e-h) on the next page illustrate seasonal mean wind speed differences for the simulation year of 2008.

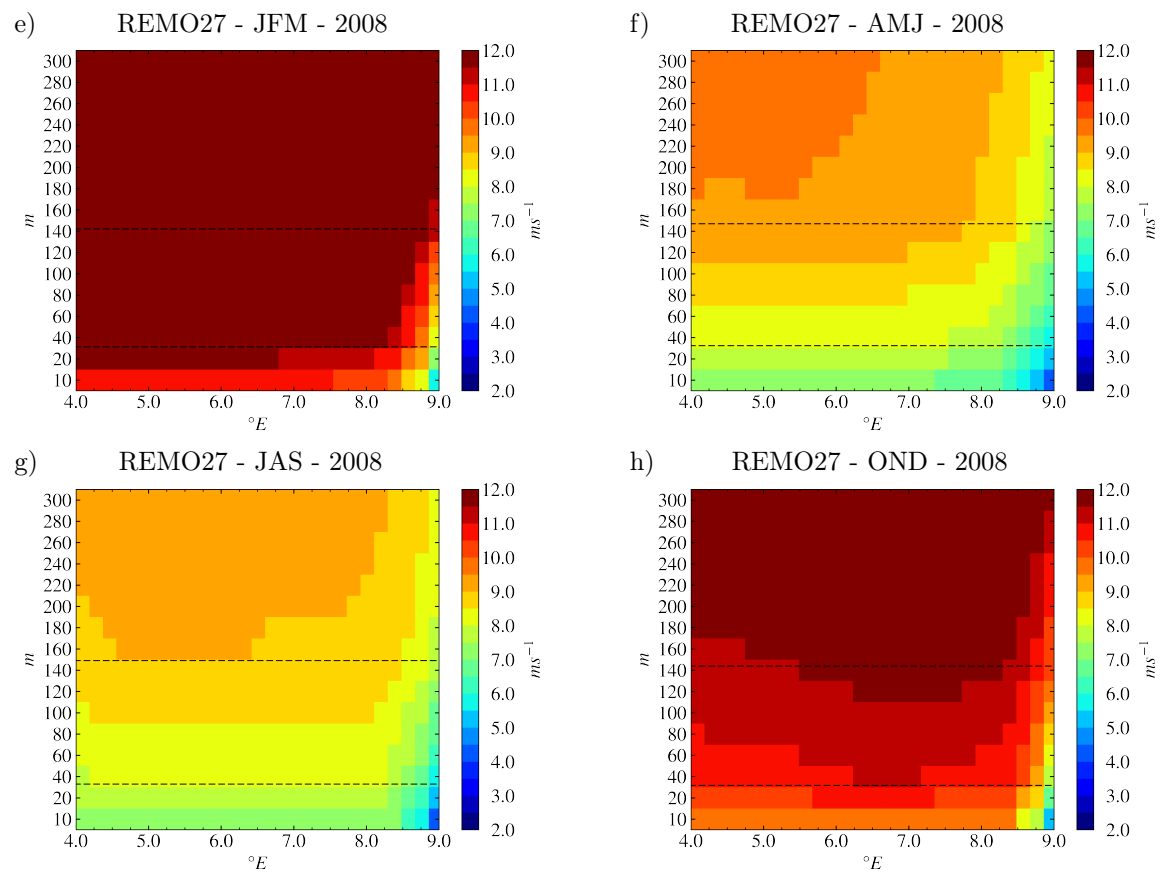


Figure A.5: Meridional transects of seasonal mean wind speed for the lowest 300 m of the atmosphere as simulated for REMO27 for the simulation year 2008. Shown are mean absolute values in $m s^{-1}$ for JFM (e), AMJ (f), JAS (g) and OND (h) for the meridional transect as defined in Fig. 3.7. Dashed black lines refer to the average geometric height of model half-levels of the individual simulations where the horizontal wind components are defined. Analogous, images (a-d) on the previous page illustrate seasonal mean wind speed differences for the simulation year of 2010.

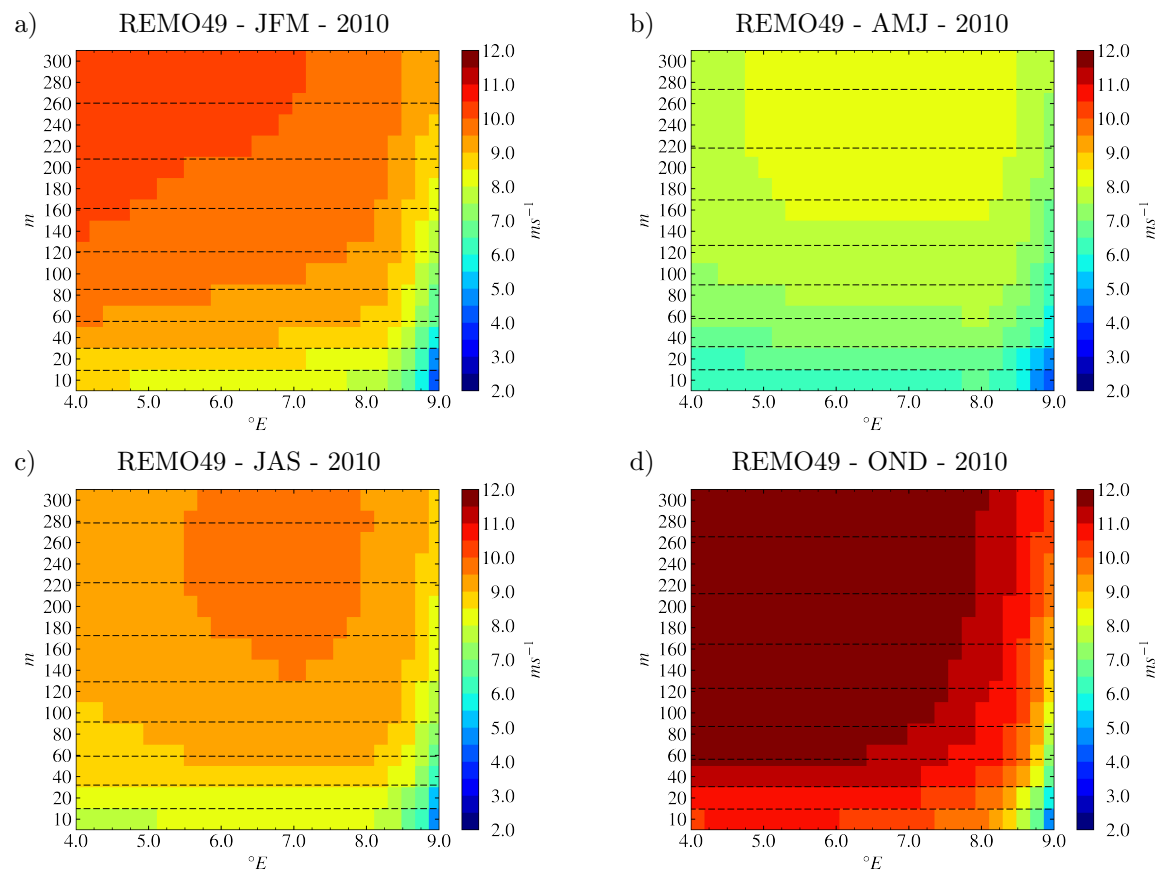


Figure A.6: Meridional transects of seasonal mean wind speed for the lowest 300 m of the atmosphere as simulated for REMO49 for the simulation year 2010. Shown are mean absolute values in $m s^{-1}$ for JFM (a), AMJ (b), JAS (c) and OND (d) for the meridional transect as defined in Fig. 3.7. Dashed black lines refer to the average geometric height of model half-levels of the individual simulations where the horizontal wind components are defined. Analogous, images (e-h) on the next page illustrate seasonal mean wind speed differences for the simulation year of 2008.

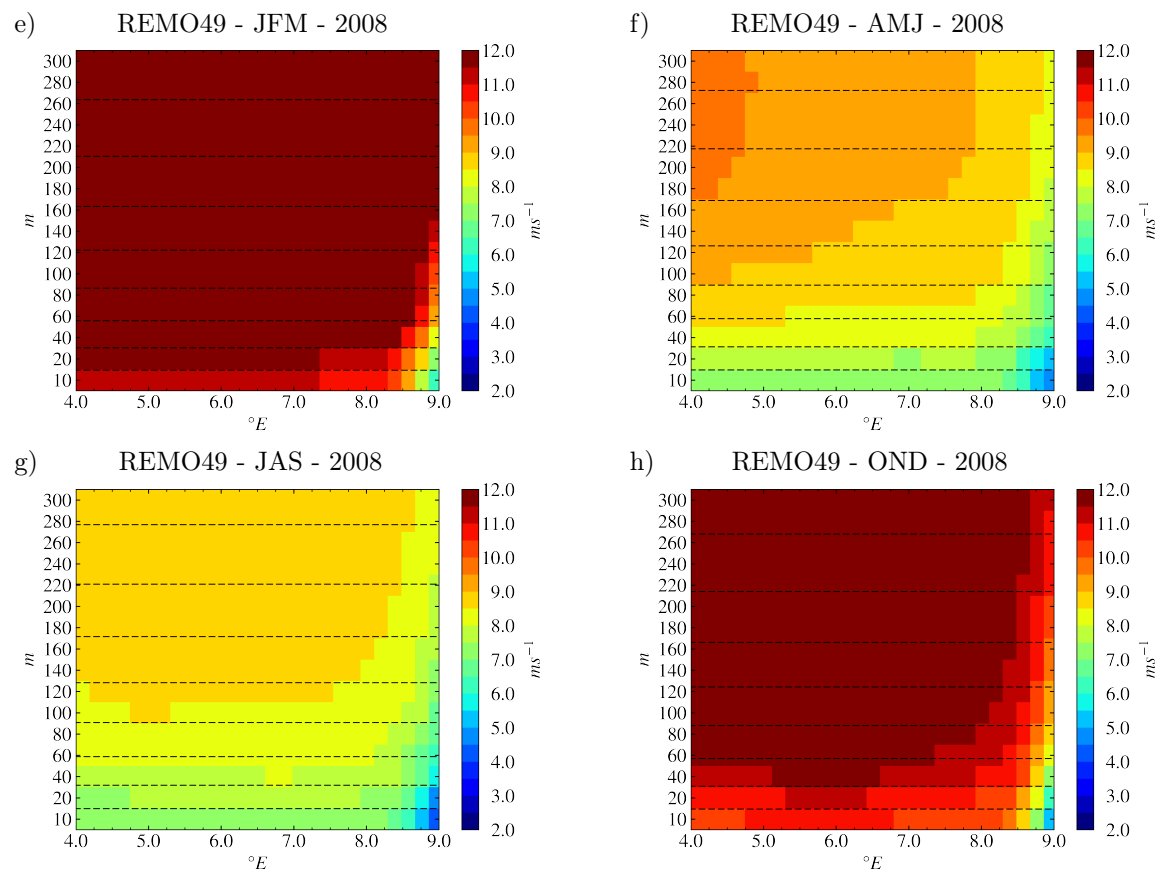


Figure A.6: Meridional transects of seasonal mean wind speed for the lowest 300 m of the atmosphere as simulated for REMO49 for the simulation year 2008. Shown are mean absolute values in $m s^{-1}$ for JFM (e), AMJ (f), JAS (g) and OND (h) for the meridional transect as defined in Fig. 3.7. Dashed black lines refer to the average geometric height of model half-levels of the individual simulations where the horizontal wind components are defined. Analogous, images (a-d) on the previous page illustrate seasonal mean wind speed differences for the simulation year of 2010.

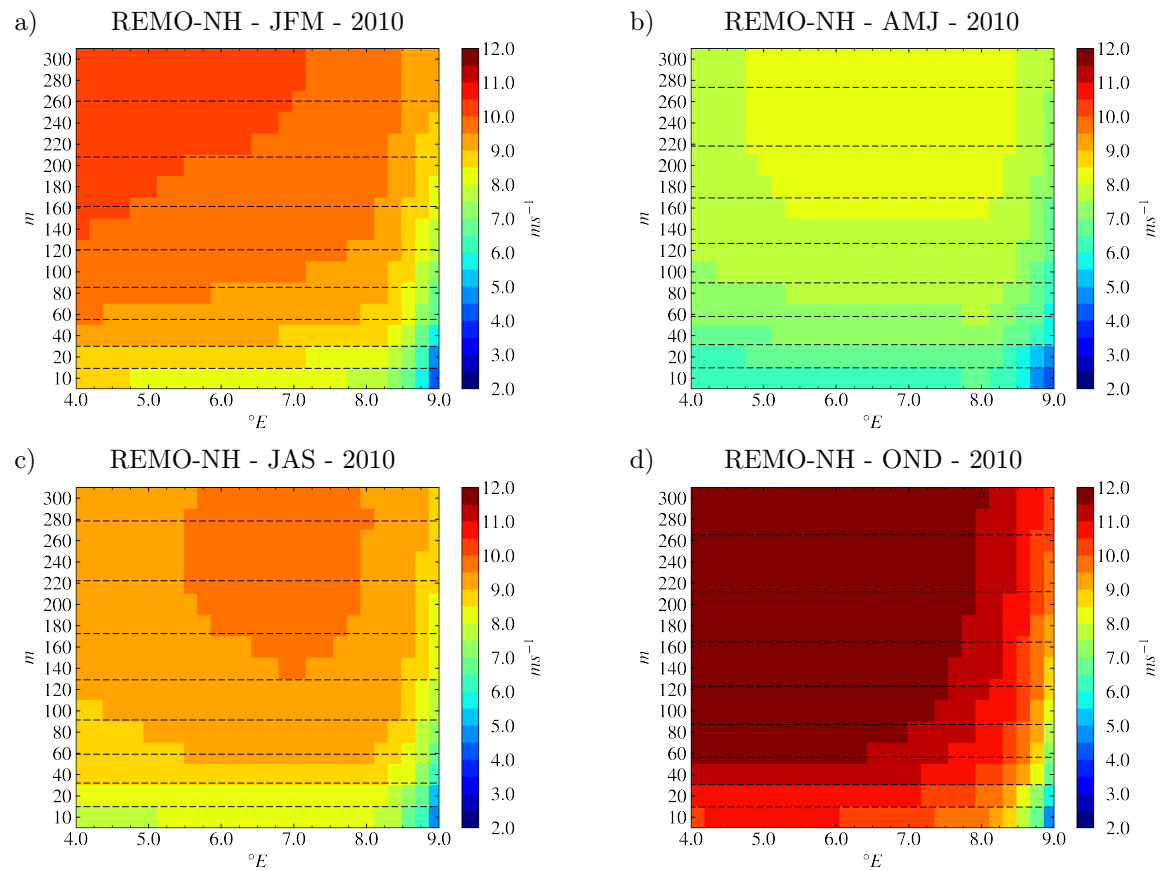


Figure A.7: Meridional transects of seasonal mean wind speed for the lowest 300 m of the atmosphere as simulated for REMO-NH for the simulation year 2010. Shown are mean absolute values in $m s^{-1}$ for JFM (a), AMJ (b), JAS (c) and OND (d) for the meridional transect as defined in Fig. 3.7. Dashed black lines refer to the average geometric height of model half-levels of the individual simulations where the horizontal wind components are defined. Analogous, images (e-h) on the next page illustrate seasonal mean wind speed differences for the simulation year of 2008.

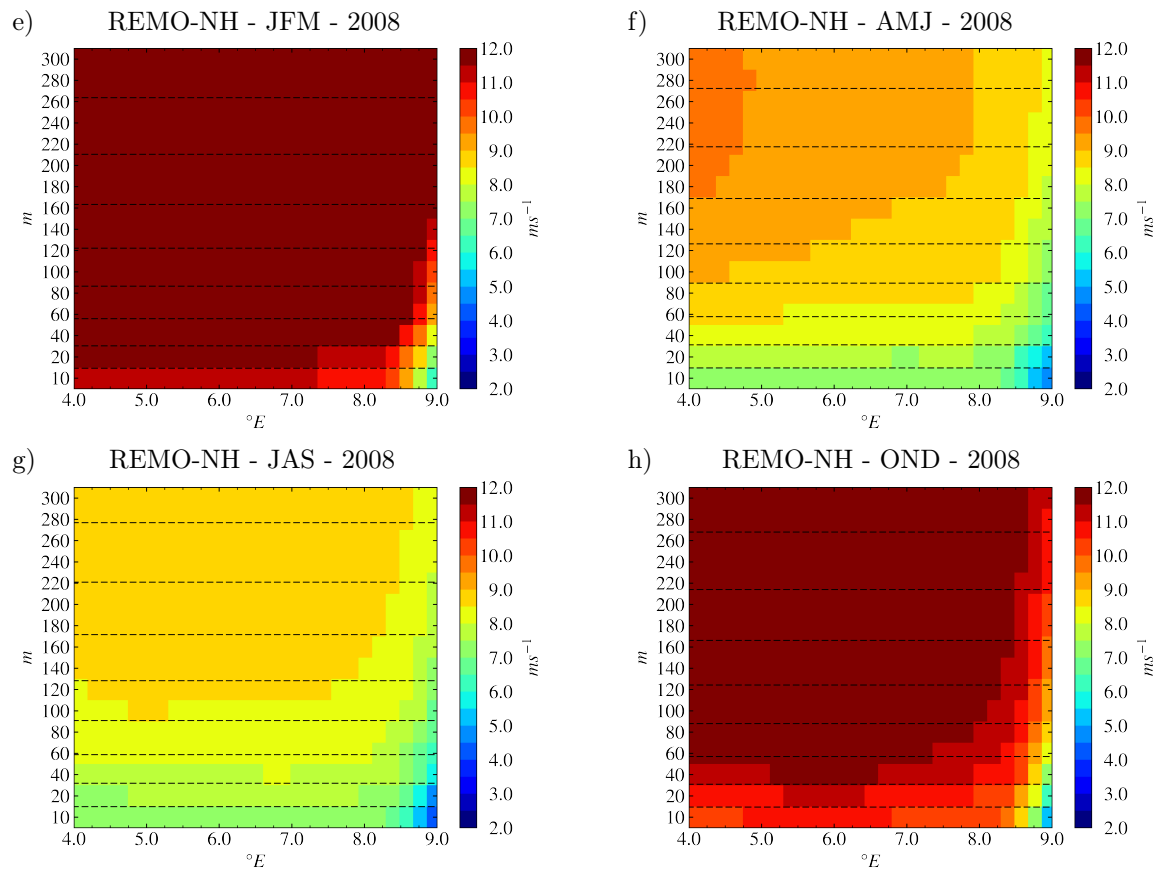


Figure A.7: Meridional transects of seasonal mean wind speed for the lowest 300 m of the atmosphere as simulated for REMO-NH for the simulation year 2008. Shown are mean absolute values in $m s^{-1}$ for JFM (e), AMJ (f), JAS (g) and OND (h) for the meridional transect as defined in Fig. 3.7. Dashed black lines refer to the average geometric height of model half-levels of the individual simulations where the horizontal wind components are defined. Analogous, images (a-d) on the previous page illustrate seasonal mean wind speed differences for the simulation year of 2010.

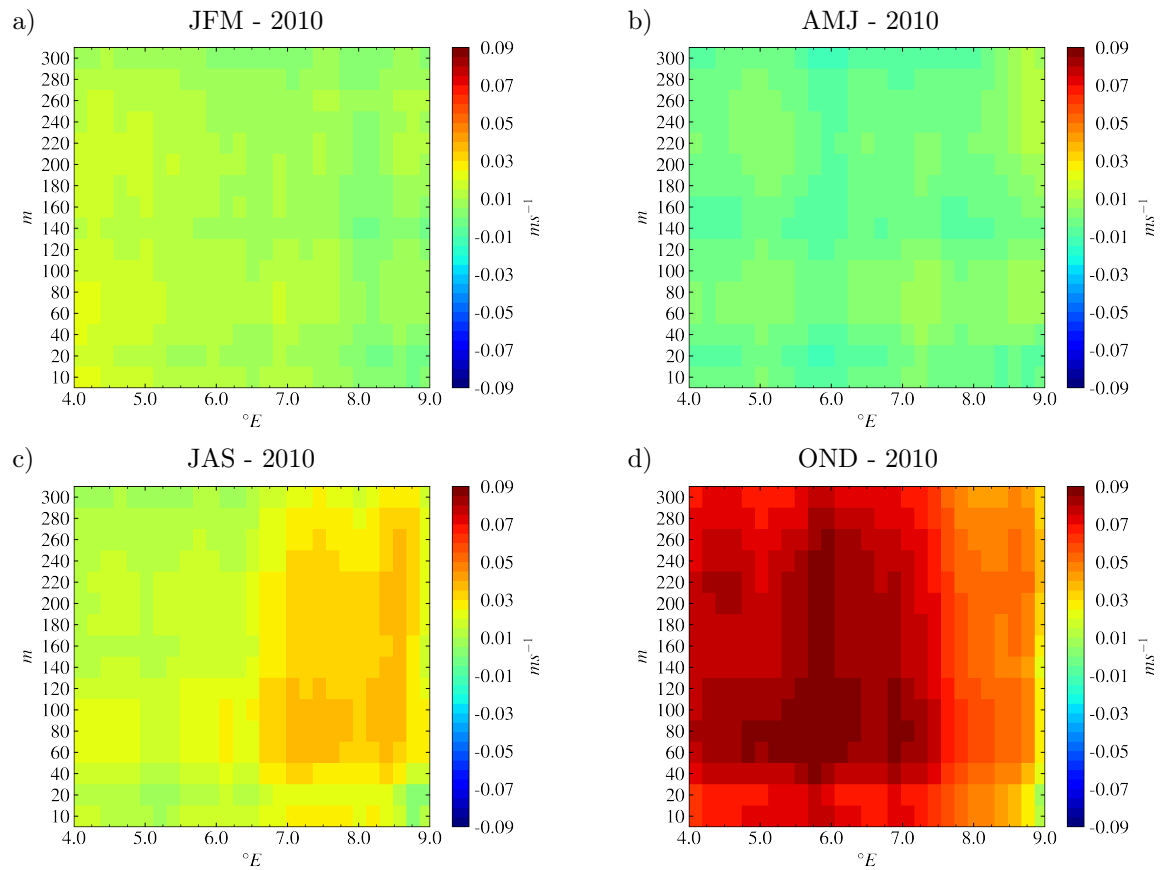


Figure A.8: Meridional transects of seasonal mean wind speed standard deviation differences for the lowest 300 m of the atmosphere between REMO49 and REMO27 for the simulation year 2010. Shown are mean absolute differences in $m s^{-1}$ for JFM (a), AMJ (b), JAS (c) OND (d) for the meridional transect as defined in Fig. 3.7. Analogous, images (e-h) on the next page illustrate seasonal mean wind speed standard deviation differences for the simulation year of 2008.

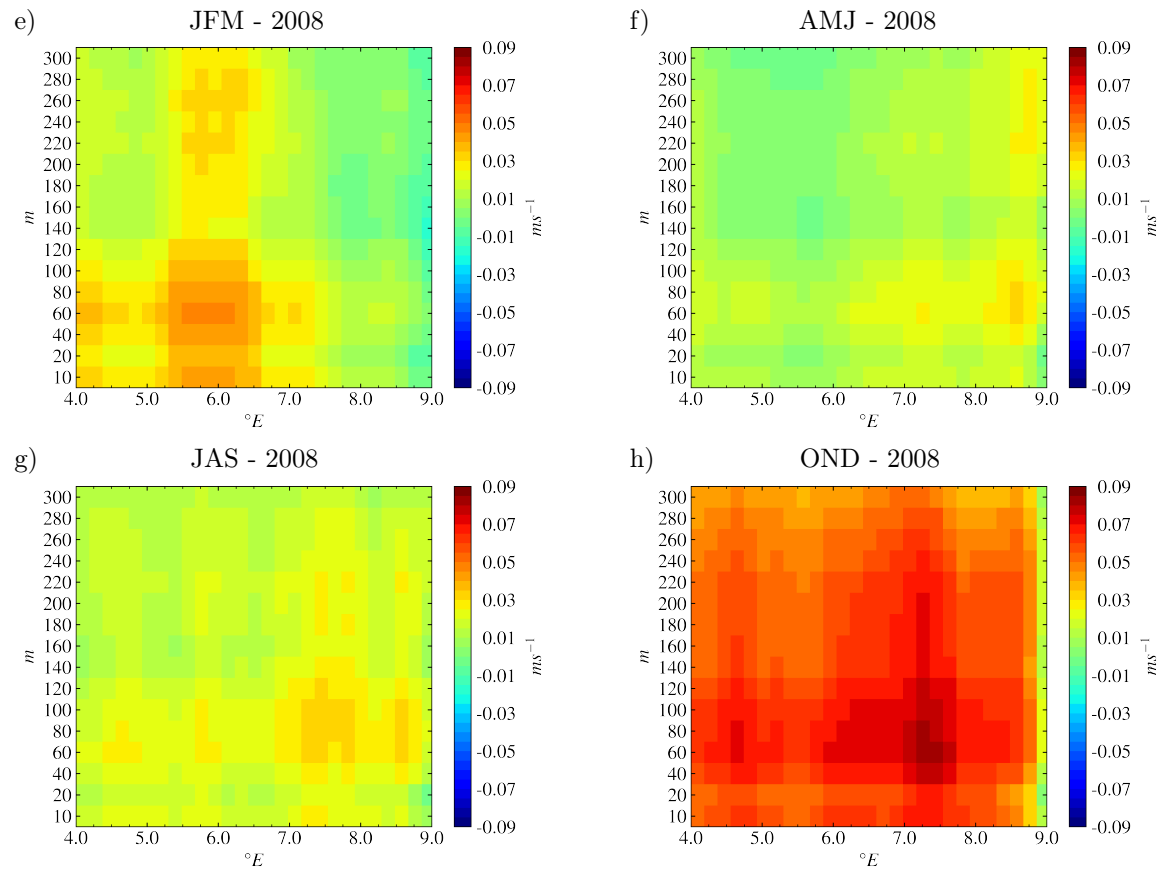


Figure A.8: Meridional transects of seasonal mean wind speed standard deviation differences for the lowest 300 m of the atmosphere between REMO49 and REMO27 for the simulation year 2008. Shown are mean absolute differences in $m s^{-1}$ for JFM (e), AMJ (f), JAS (g) OND (h) for the meridional transect as defined in Fig. 3.7. Analogous, images (a-d) on the previous page illustrate seasonal mean wind speed standard deviation differences for the simulation year of 2010.

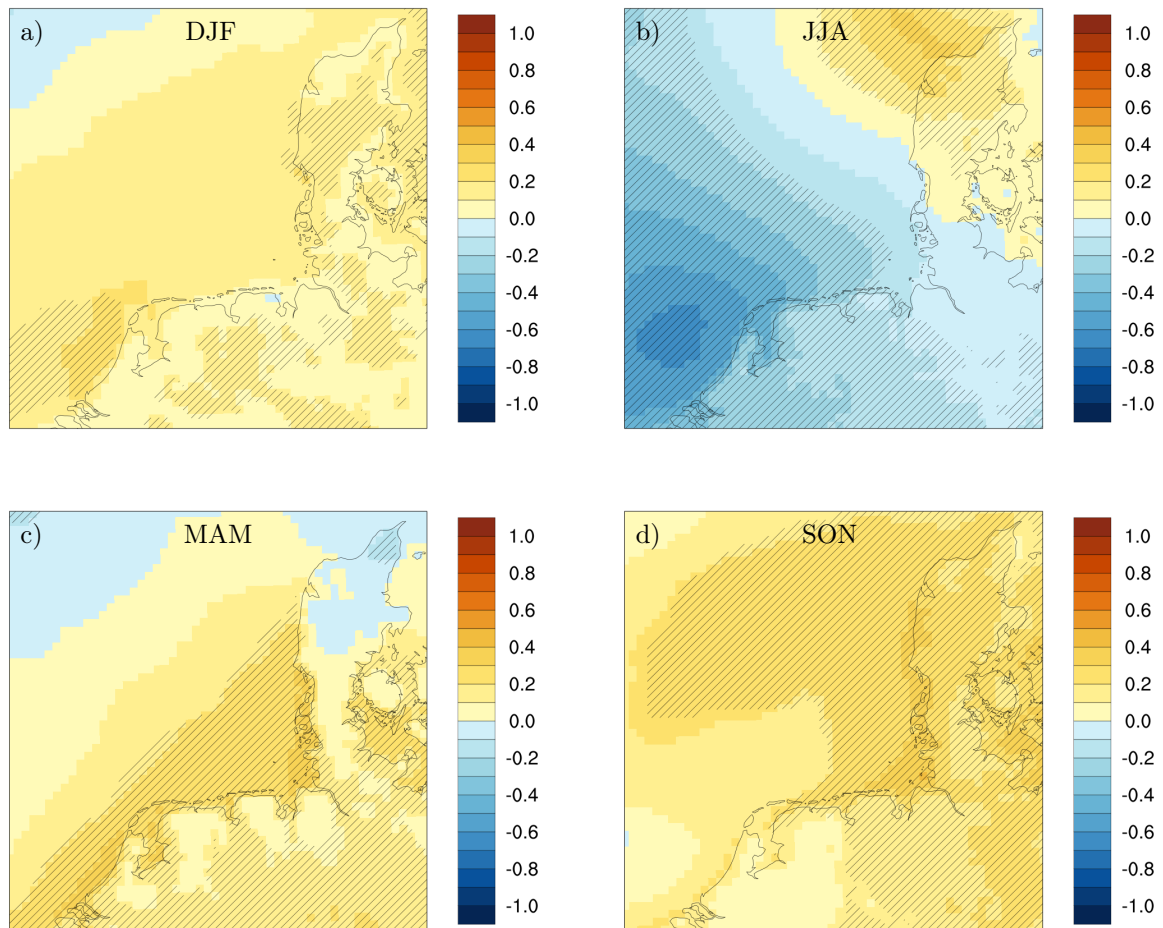


Figure A.9: Horizontal patterns of seasonal mean wind speed climate change signals of REMO EURO-CORDEX simulations over the German Bight at the end of the 21st century. Shown are absolute signals in $m s^{-1}$ for DJF (a), JJA (b), MAM (c) and SON (d) of 2071 to 2100 compared to the reference period 1971 to 2000. Significance to the reference time period is indicated by hashed areas applying a Mann-Whitney-U-test using a significance level of 0.95. Analogous, images (e-h) on the next page illustrate associated relative seasonal mean wind speed change signals.

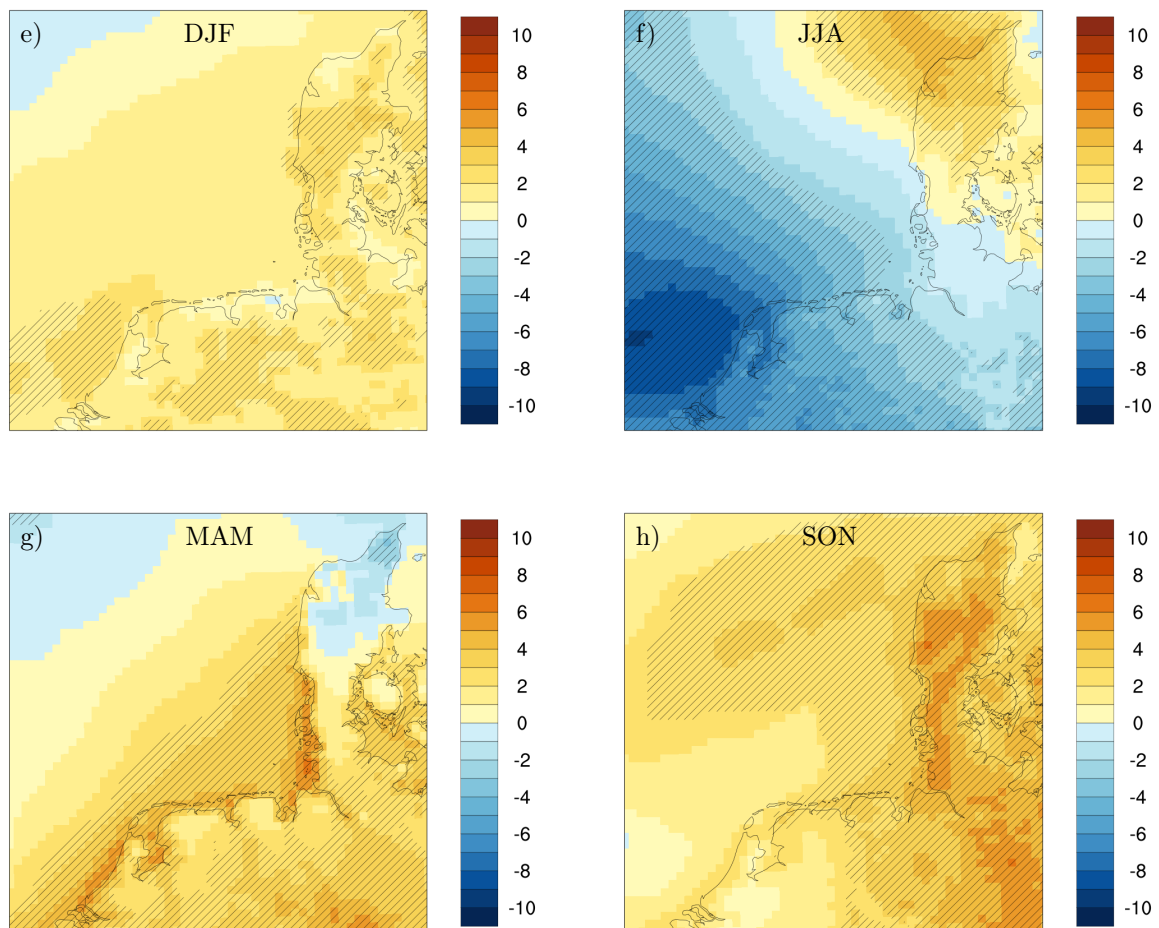


Figure A.9: Horizontal patterns of seasonal mean wind speed climate change signals of REMO EURO-CORDEX simulations over the German Bight at the end of the 21st century. Shown are relative changes in % for DJF (e), JJA (f), MAM (g) and SON (h) of 2071 to 2100 compared to the reference period 1971 to 2000. Significance to the reference time period is indicated by hashed areas applying a Mann-Whitney-U-test using a significance level of 0.95. Analogous, images (a-d) on the previous page illustrate associated absolute seasonal mean wind speed change signals.

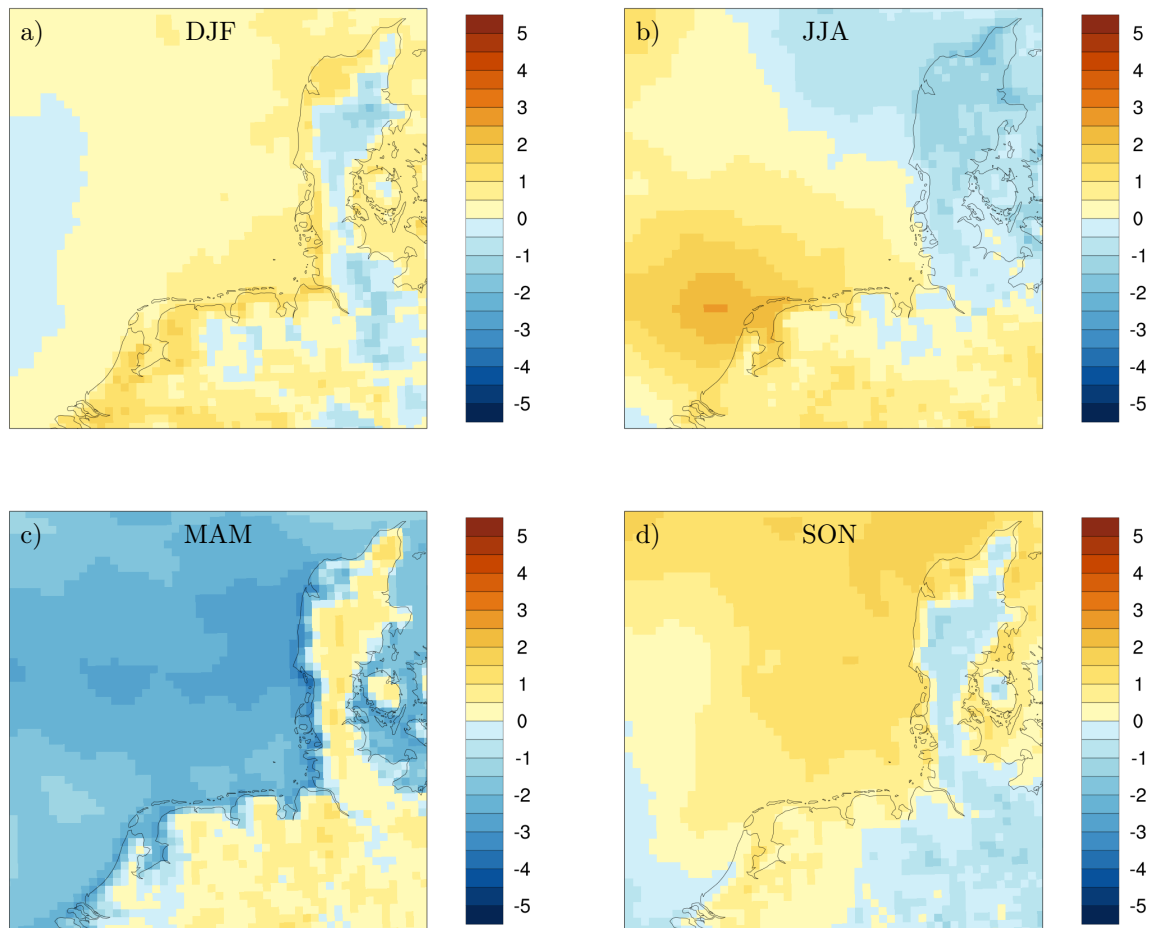


Figure A.10: Difference between upper air and near surface seasonal mean wind speed climate change signals of REMO EURO-CORDEX simulations over the German Bight at the end of the 21st century. Upper air wind speed is taken from the 2nd lowest model level situated at an altitude of approximately 150 m, while the near surface wind speed is defined at 10 m above ground. Shown are relative differences in % for DJF (a), JJA (b), MAM (c) and SON (d). The climate change signals for wind speed comprise 2071 to 2100 compared to the reference period 1971 to 2000.

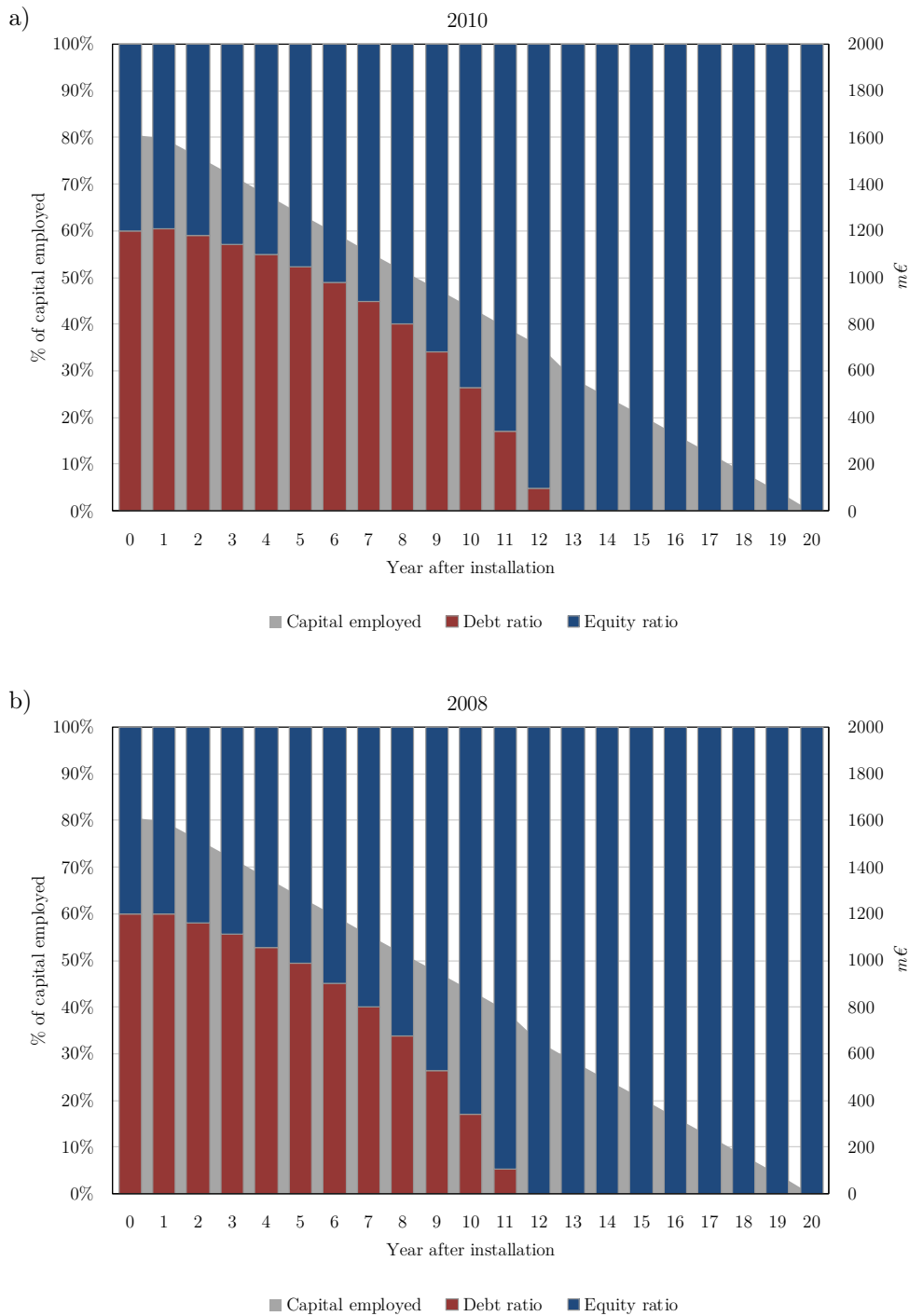


Figure A.11: Projected capital structure as simulated with the financial model. Technical and economic assumptions are chosen according to Section 4.2.3. Meteorological assumptions in terms of power production are processed from the reference surrogate climate change experiments for the years 2010 (a) and 2008 (b). Shown is the capital structure in terms of debt and equity ratio in % of the employed capital at the end of each year. In addition, the total amount of employed capital in m€ is indicated. All values are aggregated from monthly-resolved cash flows, representing annual financial statements at the end of each period.

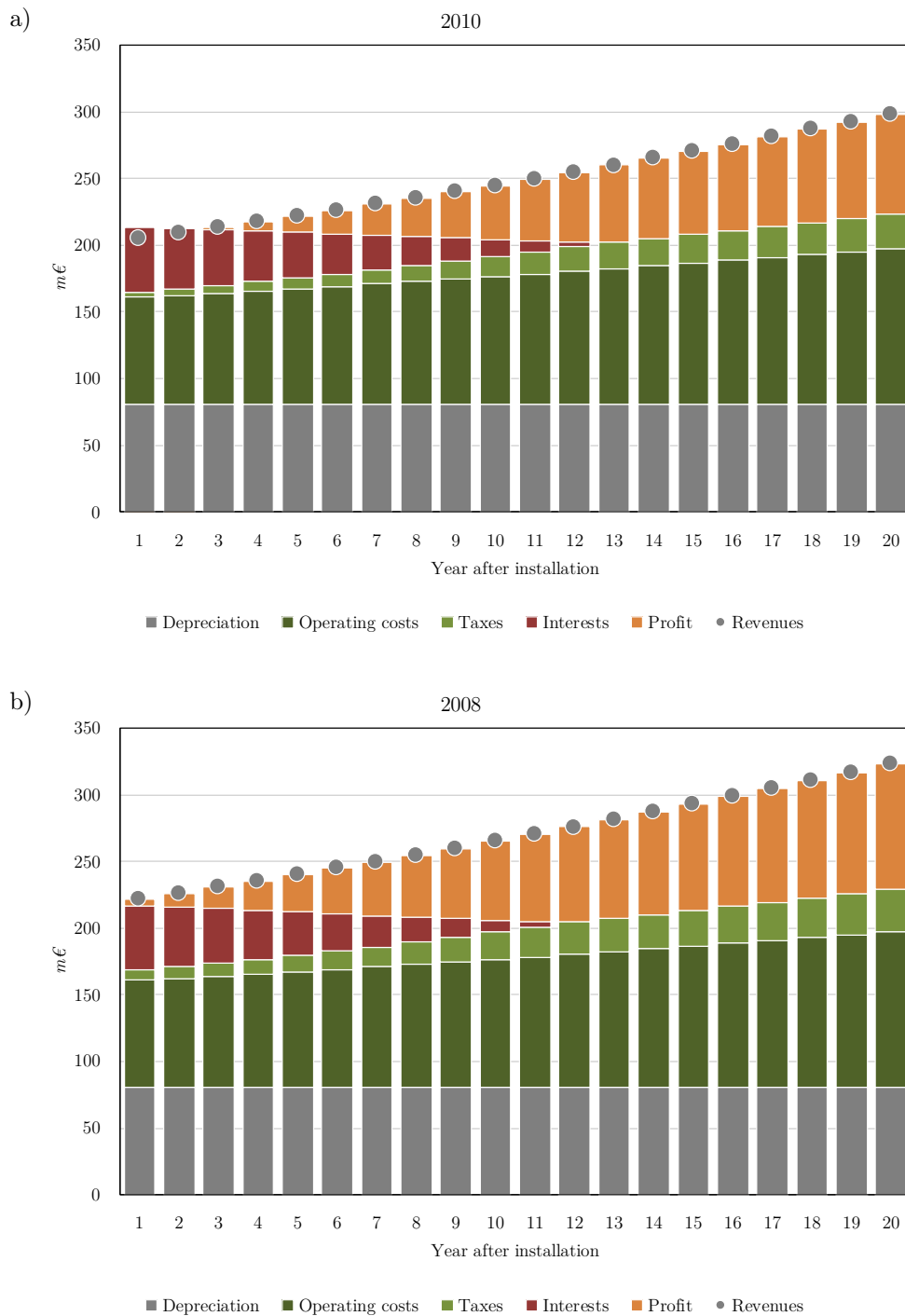


Figure A.12: Projected cost structure as simulated with the financial model. Technical and economic assumptions are chosen according to Section 4.2.3. Meteorological assumptions in terms of power production are processed from the reference surrogate climate change experiments for the years 2010 (a) and 2008 (b). Shown is the cost structure in terms of depreciation, operating costs, taxes, interests, profit and revenue in $m\text{€}$ at the end of each year. All values are aggregated from monthly-resolved cash flows, representing annual financial statements at the end of each period.

Table A.4: List of REMO variables to be adjusted for surrogate climate change experiments.

Code	Long name	Unit	Dimension
54	surface skin temperature (land)	<i>K</i>	2-D
55	surface skin temperature (water)	<i>K</i>	2-D
56	surface skin temperature (ice)	<i>K</i>	2-D
139	surface temperature (mean over gridbox)	<i>K</i>	2-D
207	soil temperature (level 2)	<i>K</i>	2-D
208	soil temperature (level 3)	<i>K</i>	2-D
209	soil temperature (level 4)	<i>K</i>	2-D
170	deep soil temperature	<i>K</i>	2-D
183	soil temperature	<i>K</i>	2-D
206	temperature of snow layer	<i>K</i>	2-D
130	temperature	<i>K</i>	3-D
133	specific humidity	<i>kgkg⁻¹</i>	3-D

Table A.5: List of wind energy-specific variables introduced to REMO. *klev* depict model levels while *hlev* depict additional height levels within the PBL at which those variables get interpolated to (i.e. from 20 m to 300 m in 20 m intervals). These additional variables are stored at hourly output intervals in the frame of this study.

Variable	Long name	Unit	Level
uhlev	u-velocity at height level <height>	ms^{-1}	hlev
vhlev	v-velocity at height level <height>	ms^{-1}	hlev
windhlev	windspeed at height level <height>	ms^{-1}	hlev
wimaxhlev	maximum windspeed at height level <height> (w/o gusts)	ms^{-1}	hlev
wiminhlev	minimum windspeed at height level <height>	ms^{-1}	hlev
wistdhlev	windspeed standard deviation at height level <height>	ms^{-1}	hlev
tkeklev	turbulent kinetic energy (TKE)	m^2s^{-2}	klev
wklev	w-velocity (non-hydrostatic REMO only)	ms^{-1}	klev
thetaklev	potential temperature (θ)	K	klev
rhoklev	air density (ρ)	kgm^{-3}	klev
ghklev	geographical height	m	klev
monoblen	inverse Monin-Obukhov length (L_*^{-1})	m^{-1}	2-D
ustar	friction velocity (u_*)	ms^{-1}	2-D
thetastar	turbulent heat flux (θ_*)	K	2-D
ghpblcon	geopotential height of the dry convective height level of the PBL	m	2-D
ghpbldyn	geopotential height of the dry dynamical height level of the PBL	m	2-D
fmcm	turbulent transfer coefficient of momentum at the surface	1	2-D
fmch	turbulent transfer coefficient of heat at the surface	1	2-D
ftkvm	turbulent transfer coefficient of momentum in the atmosphere	1	klev-1
ftkvh	turbulent transfer coefficient of heat in the atmosphere	1	klev-1

Table A.6: List of REMO simulation experiments carried out in the frame of this thesis.

Name	Model version	Setup	Domain	Horizontal resolution	Number of vertical levels	Period	Boundary conditions
REMO27	REMO2015	hydrostatic	EURO-CORDEX	0.11°	27	2008-2009 2010-2011	ERA-Interim
REMO49	REMO2015	hydrostatic	EURO-CORDEX	0.11°	49	2008-2009 2010-2011	ERA-Interim
REMO-NH	REMO2015	non-hydrostatic	German Bight	0.022°	49	2008-2010 2010-2011	REMO49 + RCP4.5
						2008-2010 2010-2011	REMO49 + RCP8.5

Table A.7: Total monthly energy output E_{out} of surrogate climate change experiments according to a ρ -corrected power curve of a MHI Vestas Offshore V164-8.0 MW[®] offshore wind turbine. The energy output in *MWh* is computed according to Eq. 4.4 from hourly-resolved time series data of wind speed and air density taken and averaged over height levels ranging from 20 m to 220 m. Shown are total monthly amounts for the reference (REF) and the scenarios RCP2.6, RCP4.5 and RCP8.5 of the individual simulation years of 2010 and 2008.

Month	E_{out} [MWh]							
	2010				2008			
	REF	RCP2.6	RCP4.5	RCP8.5	REF	RCP2.6	RCP4.5	RCP8.5
January	3476.6	3528.2	3500.8	3514.5	5099.0	5103.7	5120.1	5088.7
February	2612.7	2574.3	2622.6	2648.8	4050.1	4014.6	4020.4	4034.4
March	3695.8	3683.2	3693.1	3698.9	4487.7	4519.7	4489.2	4539.3
April	2340.1	2366.0	2359.8	2396.3	3001.2	3026.7	3021.6	3035.8
May	2786.1	2852.3	2834.2	2882.5	2052.3	2047.6	2048.4	2073.5
June	1871.2	1883.6	1885.0	1881.4	3141.0	3162.3	3178.3	3183.2
July	2897.2	2883.9	2873.4	2885.9	2685.0	2640.2	2644.1	2603.5
August	3160.6	3140.3	3148.8	3109.2	2548.5	2508.2	2488.7	2432.6
September	3275.5	3291.0	3243.2	3229.7	2678.0	2668.8	2662.5	2646.6
October	4144.6	4139.6	4167.3	4158.1	3877.5	3854.9	3849.5	3866.7
November	4523.0	4511.9	4528.9	4511.2	4245.6	4245.8	4268.7	4282.1
December	3522.3	3550.0	3549.7	3552.8	3620.8	3617.3	3615.9	3638.4

Acknowledgements

First and foremost, I would like to thank my supervisor Daniela Jacob for encouraging me in the choice to conduct a doctoral thesis as well as for her support in developing my thesis topic. Moreover, I would like to thank her for sharing her valuable and inspirational thoughts. Aside, I am deeply grateful for the various opportunities to get involved beyond my own research. I am honestly thankful to Kevin Sieck and Thomas Raub for their scientific advice concerning REMO model development, and to Lars Buntmeyer for providing support during all kinds of technical problems that arose. My thanks to Nico Kröner for sharing scientific insights on the surrogate climate change methodology. Likewise, I would like to thank Jörg Böttcher for sharing his knowledge on assumptions for wind energy project financing from a financiers' perspective. I especially thank Kevin Sieck and Markus Groth for reading parts of my thesis, fruitful discussions on the results and their helpful suggestions.

Working at GERICS was a great pleasure to me at any time. I would like to thank the entire staff and doctoral students for providing an inspiring and fun work environment representing an indispensable part of the institutes' spirit. A special thank-you goes to Marius for great support in all circumstances and motivational companionship as well as to Juliane for her invaluable attitude of a good soul.

I would like to thank my family for their great support over all these years, for their encouragement, for their patience, for putting their own needs on hold and simply for being there. Just as important, I am deeply grateful for solid and invaluable friendship - may it be over geographical distance, a longer or shorter period of time.

Last but not least, I am thankful, though humbled, to be privileged to educate myself in academia and research for more than a decade. I am well aware that this is an opportunity not available to everybody.